博士論文

Evaluation and Enhancement of Photoelectrochemical Activity of $SrTiO_3$ Based on a Model Photocatalyst Approach (モデル光触媒研究を基礎とした $SrTiO_3$ の光電気化学特性の評価と高効率化)

東京大学大学院

新領域創成科学研究科 物質系専攻

リップマー ミック 准教授 研究室

川崎 聖治

2016 年 2 月

Contents

Chapter 1

Introduction

1.1 Energy and environmental demands for solar fuel production

Problems related to global ecological sustainability have become increasingly severe in the 21st century due to the release of massive amounts of carbon dioxide into the atmosphere. The consumption of very large quantities of fossil fuels has continued at an increasing pace ever since the start of the industrial revolution.

The power consumption of the current (2014) global population of 7.3 billion people is 18 TW. These numbers have been estimated to increase to $\sim$ 9 billion and 30 TW by 2050. Fossil fuels, which currently provide about 80% of our energy supply, will be unable to keep up with this increase in demand. However, based on the current consumption rate, estimated reserves range from 150-400 years for coal, 40-80 years for oil, and 60-160 years for natural gas. Nuclear power generation with the present uranium-based reactor technology will not be able to replace the fossil fuel supply due to a limited uranium supply, unsolved long-term waste handling problems, and due the unreliability of the technology, as witnessed by dramatic accidents at Fukushima and elsewhere.

Global development and population growth has led to various forms of environmental disruption, with global warming being the most serious. The emission of greenhouse gases, CO_2 in particular, has increased in step with the increase of the consumption of fossil fuels. The current (2015) CO_2 level in the atmosphere has risen to 400 ppm from the former the base level of 280 ppm in 1750s, and continues to increase at a rate of $\sim$ 2 ppm/year. According to the International Panel on Climate Change (IPCC), CO_2 level above 450 ppm carries a high risk of causing global warming by more than 2°C, which would impact various ecosystems and the human society [1]. As an attempt to solve the issue, just recently, in December 2015 at the Paris climate conference (COP21), 195 countries adopted a universal, legally binding climate deal "the Paris agreement" with a long-term goal of keeping the increase in global average temperature below 2°C by reducing further CO_2 emissions.

In order to solve the global energy-related issues and move towards a sustainable society, a different type of energy resource that is a clean, safe, cheap, and a practical alternative to fossil fuels is necessary, besides a reduction of global energy consumption. That is important not only for solving energy and environmental issues but also for finding solutions to other problems facing humanity, such as health, food, and military conflicts. The largest energy supply available to us is the Sun. Using sunlight directly, or any of the renewable intermediaries, such as wind, rain, biomass, ocean waves etc., is therefore becoming ever more essential in this century. Using solar energy to replenish a readily-usable fuel supply is a particularly attractive alternative, as it solves problems related to solar energy harvesting and storage. Solar fuels are chemical fuels produced with the help of sunlight through artificial photosynthesis or a thermochemical reaction. Biomass is, of course, the best known solar fuel, but other options that offer a renewable and carbon-neutral energy resource are becoming available as well. Hydrogen is probably the most widely studied solar fuels and a candidate as a next-generation energy carrier. Hydrogen itself is an essential chemical resource for industrial productions of various useful products such as ammonia and methanol. In addition, it can be used as a fuel to generate electricity through with the help of a fuel cell. The production of hydrogen utilizing solar energy has been extensively in the last few decades.

Photoelectrochemical solar fuel production, which is the focus of this thesis work, is a way to generate solar fuels by directly utilizing solar energy in an electrochemical reaction. Photoelectrochemical solar water splitting in particular has attracted considerable attention since the discovery of the photoelectrochemical water splitting activity of TiO_2 by Fujishima and Honda in 1972 [2]. Photoelectrochemical solar water splitting is an ideal clean system which uses only sunlight and water for producing hydrogen and oxygen via photoelectrochemical reactions. An idea of large-scale solar hydrogen production using photocatalysts has been proposed by Maeda and Domen [3]. Solar water splitting has considerable potential as a pathway to overcome the global energy supply and environmental sustainability issues.

1.2 Photoelectrochemical solar fuel production

Harvesting solar energy to produce useful chemicals and fuels is one of the most important technology challenges in this century. There are several ways to produce chemical fuels by utilizing solar energy, e.g., photosynthesis and thermochemical reactions. The typical biological photosynthesis process stores solar energy in biomass with $0.1 \sim 8$ % sunlight-to-biomass efficiency. Biotechnology using microalgae such as *Botryococcus braunii* is one strong candidate for producing hydrocarbon equivalents of petroleum [4]. Solar thermochemical cycles utilize solar heat for producing hydrocarbons in two steps. In the first step, concentrated sunlight is used to heat a reactor to $\sim 1500^{\circ}C$ for driving two-step metal oxide redox reactions that produce H_2 and CO from H_2O and CO_2 [5]. In the second step, the synthesized gas (so-called syngas) can

be converted to liquid hydrocarbons by Fischer-Tropsch or similar catalytic reactions. Artificial photosynthesis has been achieved by photochemical reaction of organic compounds [6] and metal organic complexes [7], by semiconductor photoelectrodes or photocatalysts [1,8–15], and also by a combined system of photovoltaic cells and electrolytic cells.

Photoelectrochemical fuel production using a photoelectrochemical cell or powdered photocatalysts in water is the target of this thesis. Many books and review articles discuss the fundamental principles of photoelectrochemical water splitting [1,8–15]. Water splitting and CO_2 reduction are the most widely studied target reactions in the field of photoelectrochemical fuel production. Analogous to the photosynthesis in natural plants, these chemical reactions require positive Gibbs energy changes, storing solar energy in the form of chemical fuels via photoelectrochemical systems. Photoelectrochemical solar fuel production can thus be considered to be an artificial form of photosynthesis (Fig. 1.1). Solar water splitting requires ΔG^0 = 237 kJ/mol to split water into hydrogen and oxygen. It is known that direct photolysis of water is possible under strong light radiation at a wavelength less than 190 nm (> 6.5 eV) to sever the H-O bonds of a H_2O molecule [16]. A semiconductor photoelectrode creates a new reaction pathway and reduces the activation energy for the water splitting reaction, making it possible to split water even under visible light irradiation on the surface of a photoelectrode. Organic material synthesis, such as producing HCOOH from CO_2 and H_2O via photocatalysis, has also been achieved using hybrid materials consisting of a metal-organic complex and a semiconductor photoelectrode, as reported in 2011 [17].

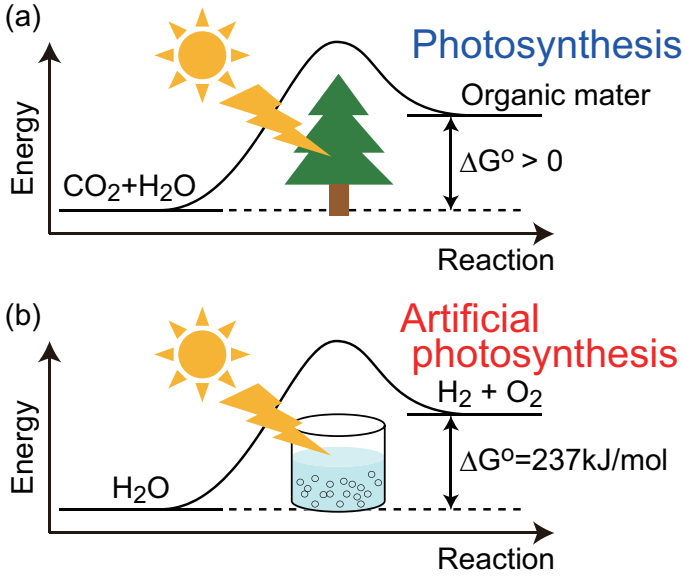

Figure 1.1: Reaction energy diagram of (a) photosynthesis by natural plants and (b) solar water splitting with powdered photocatalysts.

Photoelectrochemical solar water splitting has been studied since late 1960s [18]. A system based on a photoelectrochemical cell uses semiconductor photoelectrodes to absorb light and directly utilizes the photo-generated carriers to drive a certain electrochemical reaction, which can be recognized as a single device directly combining a photovoltaic cell and an electrode for water splitting. Gerischer, Memming, Pleskov, and coworkers pioneered the semiconductor electrochemistry and photoelectrochemistry, and studied the fundamental reaction mechanisms that occur at water/semiconductor interfaces [14, 15, 18]. They studied typical semiconductor materials such as Si, GaAs, CdS, and ZnO, but found that these semiconductors suffer from photocorrosion. Later, a *Nature* article [2] published by Fujishima and Honda in 1972 drew attention to photoelectrochemical water splitting as a form of an artificial photosynthesis at the time when the oil shocks of early 1970s hit the world economy.

Fig. 1.2 illustrates the operating principle of the photoelectrochemical water splitting process. The photoelectrode type depends on the position of the Fermi level (E_F) of a semiconductor. An *n*-type semiconductor works as a photoanode and forming an upward band bending space charge region at the water interface, while a *p*-type material works as a photocathode that exhibits downward band bending. In a photoelectrochemical cell using a photoanode connected with a metal counter electrode (CE) as shown in Fig. 1.2(a), photo-generated holes are driven to the surface of the photoanode by the internal band bending and oxidize water into oxygen, while photo-generated electrons flow to the CE and reduce water into hydrogen. The ratio of the evolved oxygen and hydrogen is $O_2/H_2 = 1/2$, following the electrochemical reactions

$2H_2O + 2e^- \rightarrow H_2 + 2OH^-$,

$2H_2O + 4h^+ \rightarrow O_2 + 4H^+$.

In total:

$2H_2O \rightarrow 2H_2 + O_2$.

On the other hand, in a system using a photocathode (Fig. 1.2(b)), a photo-reduction reaction occurs at the surface of the photocathode, and oxidation at the counter electrode. The current flow direction (J_{ph}) is opposite to that of the photoanode system. Since the redox potentials of H^+/H_2 and O_2/H_2O are 0 and 1.23 V vs a reversible hydrogen electrode (RHE), respectively, electrolysis of water in principle requires an applied potential over 1.23 V. To split water in a photoelectrochemical cell without any external bias, a semiconductor photoelectrode should have a band gap over 1.23 eV with suitable band positions, where the valence band maximum (VBM) is lower than the redox potential of O_2/H_2O and the conduction band minimum (CBM) is higher than the redox potential of H^+/H_2.

Photoelectrochemical water splitting with powdered semiconductor photocatalysts has been studied since the late 1970s. Schrauzer et al. [19] demonstrated in 1977 that photocatalytic gaseous water splitting can proceed with the help of TiO_2-based photocatalysts. Bard *etal*. provided the fundamental mechanism of powdered semiconductor photocatalysis in 1978 [20–22]. In 1980, Domen et al. [23] and Lehn *etal*.. [24] reported that $SrTiO_3$ loaded with metal

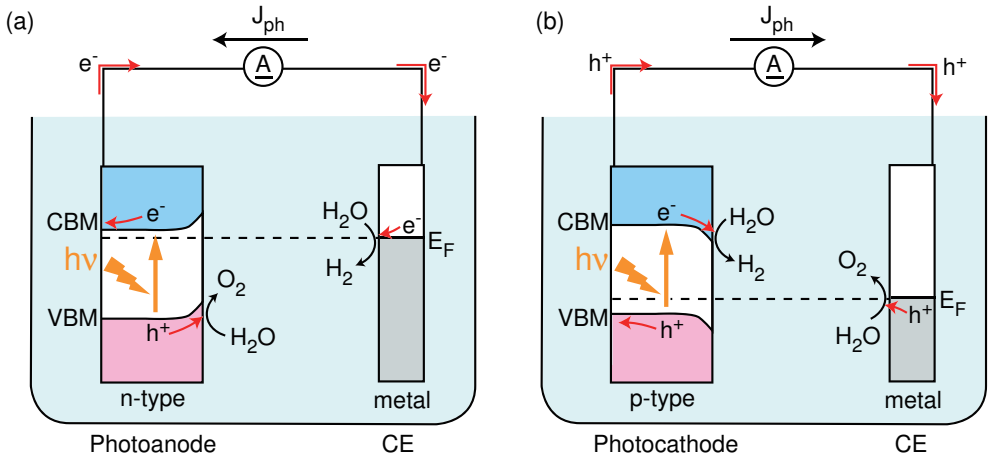

Figure 1.2: Schematic illustration of photoelectrochemical cells using (a) n-type semiconductor as a photoanode and (b) p-type semiconductor as a photocathode connected to a counter metal electrode (CE). h^+ and e^- represent holes and electrons. CBM and VBM mark the conduction band minimum and valence band maximum positions of the semiconductor photoelectrode. The current flow direction (J_{ph}) is opposite in the two cases.

nanoparticles can work as a photocatalyst and split water in an aqueous solution. Since then, metal nanoparticles, so-called cocatalysts, have been recognized as an essential component for obtaining efficient photocatalysts. Domen *etal*.. [23] reported that $SrTiO_3$ powders alone are not active for water splitting, whereas $SrTiO_3$ loaded with NiO/Ni core shell nanoparticles is active for splitting water to hydrogen and oxygen. Cocatalysts create catalytic reaction sites, lowering the required overpotential, or activation energy, for electrochemical water splitting.

Fig. 1.3 shows a schematic illustration explaining the operating principle of photocatalytic water splitting. The advantage of this system is its simplicity and scalability. The system requires only a water vessel and photocatalyst powders, producing hydrogen and oxygen from water under light irradiation. The photocatalytic water splitting is triggered by a photo-generated electron-hole pair, where the photoelectron reduces water to hydrogen and the photohole oxidizes water to oxygen, similarly to the system of a photoelectrochemical cell. Semiconductor photocatalyst powders are often modified with one or two cocatalysts on the surface. In order to achieve overall water splitting, the electronic structure of photocatalysts should have a VBM lower than the redox potential of O_2/H_2O and a CBM higher than the redox potential of H^+/H_2, similarly to that of a photoelectrode.

A powder photocatalyst can be recognized as a localized photoelectrochemical cell where a photoelectrode and a counter metal electrode are directly combined on nanoscale, although one cannot apply an electric bias on a powder particle. As illustrated in Fig. 1.4, the fundamental

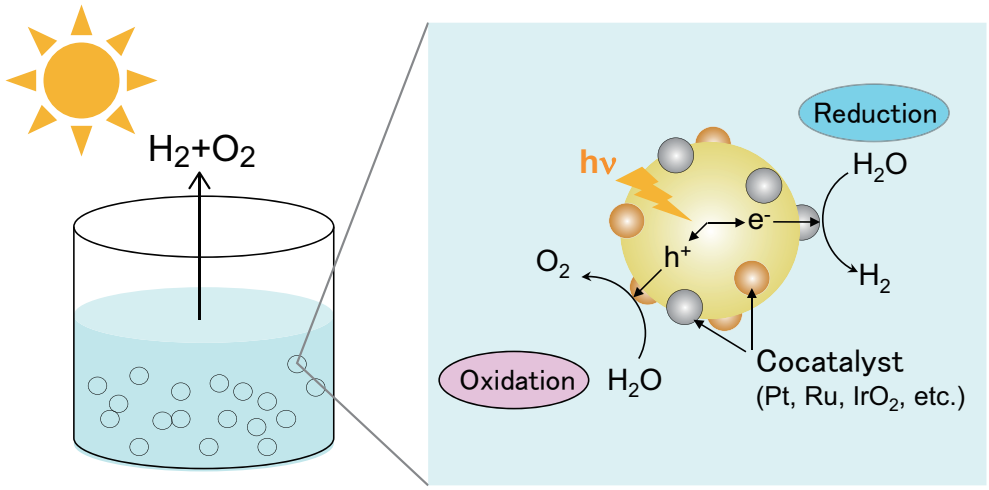

Figure 1.3: Schematic illustration showing the basic operating principle of photocatalytic water splitting.

process in both systems can be divided into three steps including light absorption, charge transport of photocarriers from bulk to surface, and a surface electrochemical reaction. The photocurrent density (J_{ph}) flowing in the system is given by

$$J_{ph} = eJ_{ab} \times \eta_{ct} \times \eta_{sr}, \tag{1.1}$$

where e is the elementary charge and J_{ab}, η_{ct}, and η_{sr} are the absorbed photon flux, and the efficiencies of carrier transport and surface reaction, respectively. Therefore, there are three main strategies for improving the activity of a photoelectrochemical water splitting cell. The first is to select a semiconductor that has a large visible light absorption coefficient or to decorate the semiconductor surface with dyes or metal nanoparticles showing a localized surface plasmon resonance, i.e., a suitable absorption of sunlight, to improve J_{ab}. The second approach is to improve η_{ct} in the bulk of the semiconductor This can be achieved by modifying the morphology of the semiconductor to increase the specific surface area or by making metal-semiconductor or semiconductor-semiconductor heterojunctions to accelerate the photocarrier migration along the band bending in the space charge region. The third strategy is to decorate the photoelectrode surface with an efficient electrocatalyst for the water splitting reaction, reducing the overpotential that is needed for the electrochemical reaction to occur, thus improving η_{sr}. To achieve efficient photoelectrochemical water splitting, these approaches have been studied for various types of materials and nanostructures [1, 8–15].

Mimicking the Z-scheme system of biological photosynthesis with two photoexcitation centers, Z-scheme type water splitting by combining two types of semiconductors has also been proposed in late 1970s [22]. This system, in principle, has the advantage to utilize semicon-

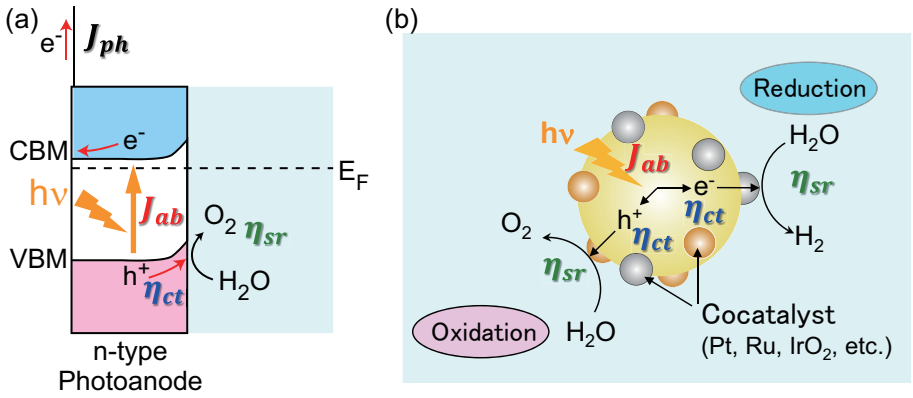

Figure 1.4: Basic principles of photoelectrochemical water splitting via (a) a photoelectrochemical cell and (b) powder photocatalysts.

ductors that have band gaps smaller than 1.23 eV, and can therefore harvests a larger fraction of photons coming from the Sun than a system using a single photoexcitation process. This point is actually very important for harvesting a large fraction of the solar spectrum, because as seen in Fig. 1.5 a large number of photons in the solar spectrum have energies below 2 eV with a peak at 0.78 eV. Bolton *etal*.. [25] estimated the maximum theoretical efficiencies for various photoelectrochemical water splitting setups, pointing out that a two-photon process will be able to achieve a higher efficiency than a single-photon process.

Fig. 1.6 shows schematic energy diagrams of the photosynthesis of natural plants, a photoelectrochemical cell using dual photoelectrodes, and a Z-scheme water splitting system using two types of powdered photocatalysts. The photosynthesis in natural plants utilizes two different photo-excitation centers, P680 and P700, which are coupled with redox mediators, oxidizing water to oxygen while reducing CO_2 to biomass (Fig. 1.6(a)). Since the electron transport pathway in this system resembles the alphabetical character "Z", the process is called a Z-scheme. Similarly, by using a suitable pair of two different semiconductors that are electrically coupled to each other, Z-scheme type water splitting can be achieved. Fig. 1.6(b) shows a photoelectrochemical cell using a photoanode and a photocathode coupled with wiring, where water oxidation occurs at the photoanode while water reduction occurs at the photocathode. An O_2-evolving photocatalyst and a H_2-evolving photocatalyst can also be coupled with a redox mediator for achieving Z-scheme type water splitting (Fig. 1.6(c)). The two different powdered photocatalysts can be electrically coupled with suitable redox mediators, such as Fe^{2+}/Fe^{3+} [27], IO_3^-/I^- [28], and graphene [29], or directly combined without mediators [30].

Still, practical application of photoelectrochemical water splitting have proven to be elusive even though almost half a century has passed since the original discovery. The poor efficiency and severe instability due to photocorrosion have to be overcome to fulfill the dream, as Hodes

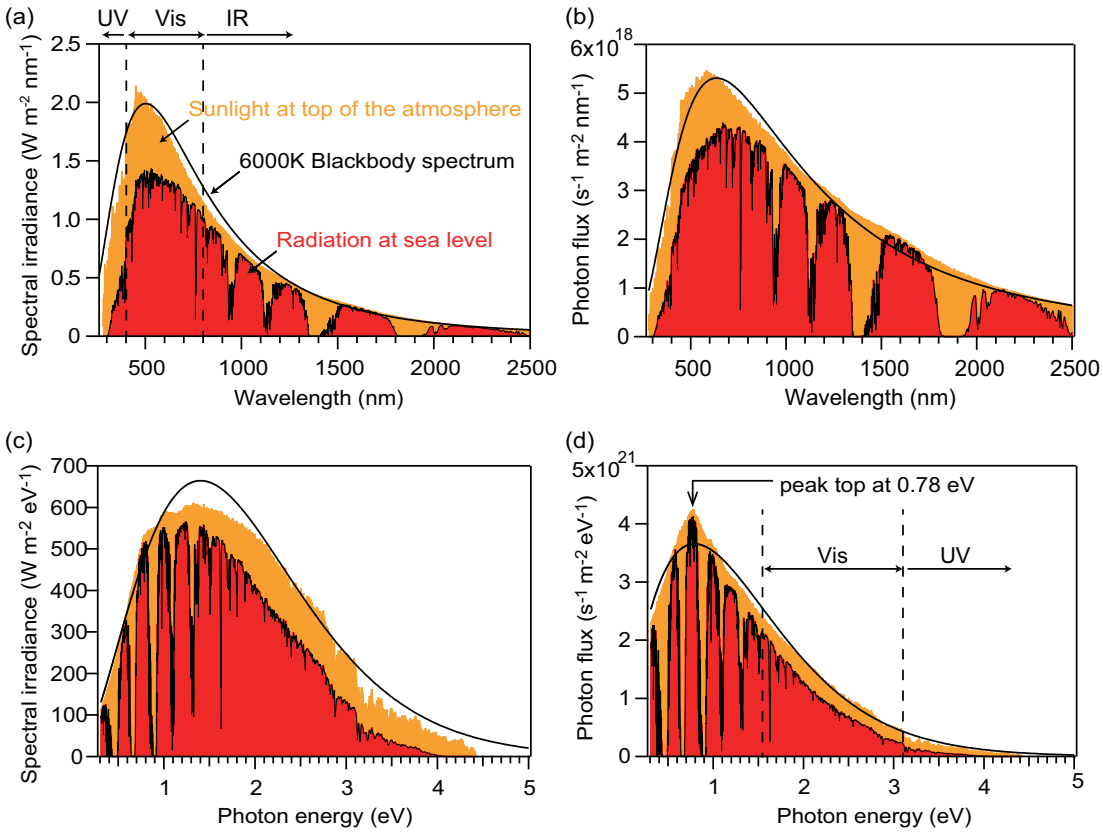

Figure 1.5: Solar spectra at the top of the atmosphere (AM0) and at sea level (AM1.5), with a plot of 6000 K blackbody spectrum. The data for the solar spectrum is from Ref. 26. (a) Spectral irradiance and (b) photon flux as a function of wavelength of light. (c) and (d) are plotted as a function of photon energy.

etal.. [31] have pointed out in a discussion of the fundamental constraints of the photoelectrochemical energy conversion process.

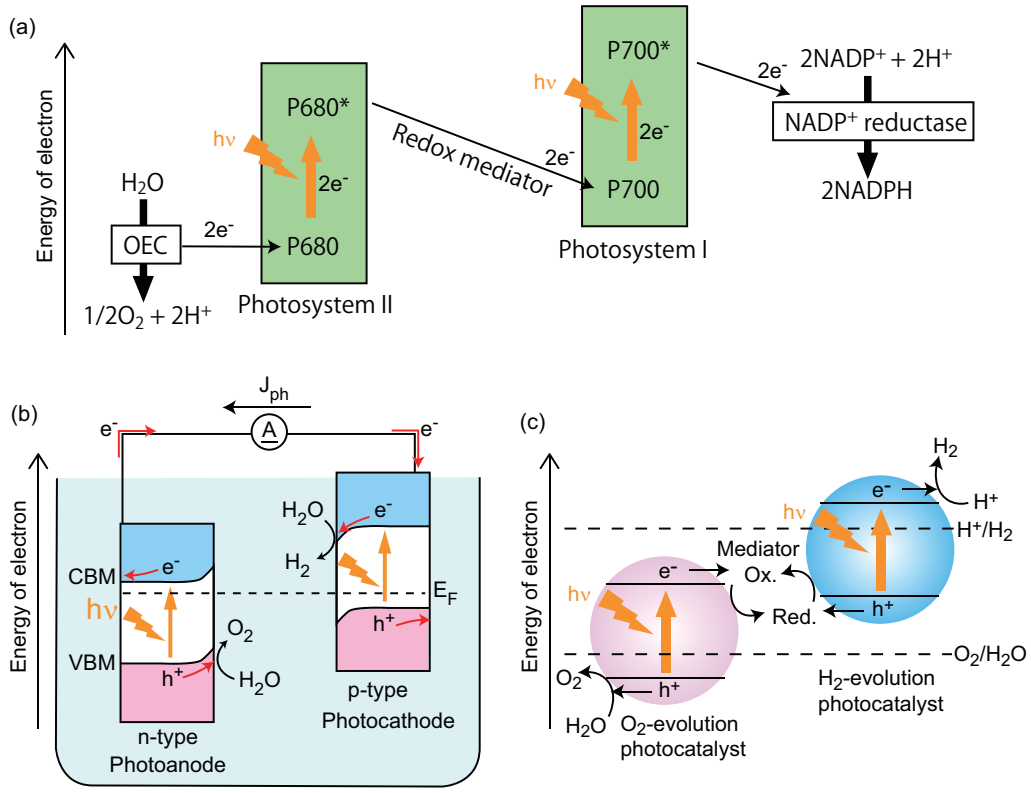

Figure 1.6: Schematic energy diagrams of (a) photosynthesis in natural plants, (b) a photoelectrochemical cell using dual photoelectrodes, and (c) Z-scheme water splitting using powdered photocatalysts.

1.3 Photoelectrochemical environmental purification

It has been known for a long time, at latest since the 1920s [32,33], that TiO_2 shows the photo-oxidation effect under sunlight and decomposes pigments that are used in paints [34,35].

Contemporaneously with the invention of photoelectrochemical water splitting, studies on photocatalytic decomposition of organic compounds for environmental cleaning started in the early 1970s, pioneered by Teichner *etal*.. [36]. Since oxide photocatalysts, especially TiO_2, have high photo-oxidation activity and can produce reactive oxygen due to the deep valence band position of 2.5 $\sim$ 3 eV vs RHE, they are useful for environmental surface cleaning by decomposing organic pollutants [37]. Photocatalytic organic decomposition has considerable advantages, such as cleanliness without any secondary pollutants, complete decomposition of organic pollutants, low energy cost, and simplicity of the system. TiO_2 has recently been used as a coating material for building exteriors because it works as a self-cleaning material that automatically decomposes organic substances, the cause of dirt, under sunlight [37].

In addition to the strong photocatalytic oxidation activity, TiO_2 shows an interesting phenomenon called "photo-induced superhydrophilicity". This is a phenomenon where the hydrophilicity of a surface increases and the water contact angle decreases to nearly 0° by light irradiation. The effect is often observed on oxide photocatalyst surfaces and has been known since the original discovery on a TiO_2 surface in 1997 [38]. This unique property assists the removal of organic contaminants, and has found practical use in antifogging applications. However, the mechanism of photo-induced superhydrophilicity has not been completely understood yet and it is not clear if the phenomenon affects the photocatalytic behavor of a surface. Two competing hypotheses have been proposed to explain why a surface becomes superhydrophilic; "surface reconstruction model" and "contamination model". The surface reconstruction model proposed by Hashimoto *etal*.. [39] explains the strong hydrophilicity by the appearance of a surface reconstruction that includes surface hydroxyl groups and oxygen vacancies that are induced by a reaction with water under light. In contrast, the contamination model considers photocatalytic oxidative decomposition of organic contaminants on a surface as the dominant mechanism for photo-induced superhydrophilicity, since the hydrophilicity of most oxide surfaces should be intrinsically very high due to the large surface energy, which was proposed independently by Anpo *etal*. [40] and Yates, Jr. *etal*. [41].

The clarification of the mechanism of photo-induced superhydrophilicity is important not only for understanding the phenomenon itself but also for determining the photocatalytic reaction dynamics. Assuming that the surface reconstruction model is true and there is actually a photo-induced surface state, the reconstruction would affect the surface electronic structure, which affects surface band bending, overpotential, and thus photocatalytic activity. The clarification of the mechanism of the photo-induced superhydrophilicity is also one of the targets of this thesis work.

1.4 Materials design for efficient photoelectrochemical solar water splitting

Here, I discuss the material design aspects of designing efficient photoelectrodes and photocatalysts for solar water splitting. Although there are many parameters affecting the photoelectrochemical activity, the electronic structure of a semiconductor photoelectrode (or photocatalyst) is a critical factor determining the activity. From the viewpoint of electrochemistry, a semiconductor photocatalyst needs to have a conduction band edge higher than the redox potential of H^+/H_2 and a valence band edge that is lower than the redox potential of O_2/H_2O, as shown in Fig. 1.7(a). If a semiconductor meets these conditions, photogenerated electrons and holes would, in principle, be able to electrolyze water to hydrogen and oxygen. In order to reduce water to hydrogen, photoelectrons in the conduction band should have a potential higher than the redox potential of H^+/H_2, while photoholes in the valence band should have a potential lower than the redox potential of O_2/H_2O in order to oxidize water to oxygen. In contrast, semiconductors with a conduction band edge that is lower than the H^+/H_2 potential and a valence band edge that is lower than the O_2/H_2O potential cannot achieve overall water splitting. The same is true if the conduction band edge is higher than H^+/H_2 and the valence band edge is also higher than O_2/H_2O, as illustrated in Fig. 1.7(b) and (c). Such semiconductors are only active for either water oxidation or reduction and can be used in photoelectrodes if an external electric bias is applied or in Z-scheme type water splitting cells.

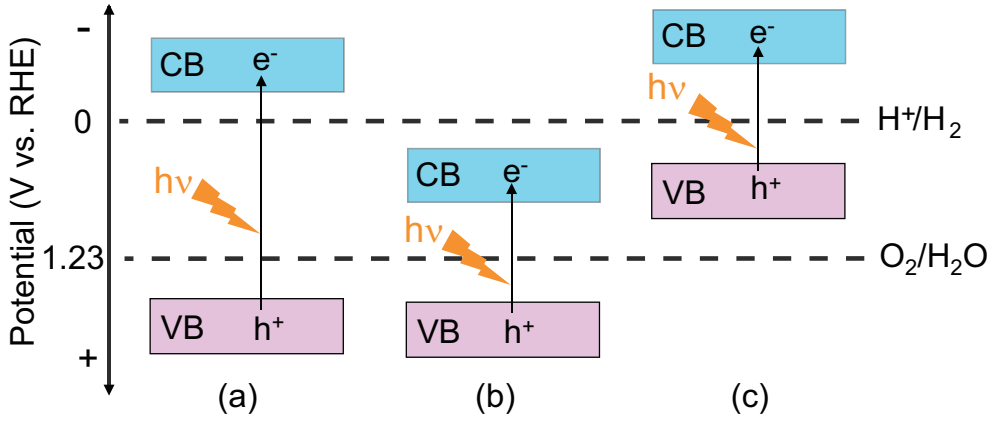

Figure 1.7: Band structures of a semiconductors: (a) The conduction band is higher than H^+/H_2 and a valence band lower than O_2/H_2O, overall water splitting is possible. (b) The conduction band is lower than H^+/H_2 and the valence band is lower than O_2/H_2O, only water oxidation is possible. (c) The conduction band is higher than H^+/H_2 and the valence band is higher than O_2/H_2O, only water reduction is possible.

The electronic structure is also important in the process of photocarrier generation. The absorbed photon flux is

$$J_{ab} = \int_{E_g}^{\infty} (1 - R_E)\{1 - \exp(-\alpha_E d)\}\phi_E dE, \tag{1.2}$$

where E is the photon energy, E_g and d are the band gap and the thickness of the semiconductor, R_E and α_E are the reflectance and absorption coefficients of the semiconductor at the photon energy of E, and ϕ is the incident photon flux. The band gap thus determines the threshold energy of light absorption. The absorption coefficient is determined by the dipole moment associated with the transition from the valence band (or HOMO) to the conduction band (or LUMO). Since sunlight includes a large fraction of photons in the energy range less than 3 eV, in order to improve J_ab under sunlight, a narrow E_g and a large α_E over a wide energy range are preferable. However, it is also known that if the overpotential for water oxidation or reduction is small, the water electrolysis proceeds very slowly or not at all. The valence and conduction bands of a photocatalyst should therefore be at energies that leave a sufficient overpotential for the photocarriers relative to the redox potential of water. Even though the overpotential corresponds to a loss of energy, a certain amount of overpotential has to be applied for both water oxidation and reduction to accelerate water splitting. There is clearly a trade-off between light absorption and the rate of electrochemical reactions. While 1.23 eV is the minimum threshold for the band gap required for water splitting, Bolton *etal*.. [25] have estimated that the optimum band gap of a photoelectrode (or a photocatalyst) for a practical water splitting system is ~ 2 eV by considering a ~ 0.8 eV loss from overpotentials. As shown by Eq. 1.2, light absorption can be improved by reducing R_E, i.e., coating a photoelectrode with an antireflection layer or by modifying the surface morphology of a semiconductor.

Since the discovery of stable photoelectrochemical water splitting on TiO_2 in 1972 [2], a huge number of semiconducting materials have been tested in photoelectrochemical reactions. Band positions of typical semiconductors studied in photoelectrochemistry are shown in Fig. 1.8. The data was taken from Ref. 9, 42, 43. Considering the band gaps and band positions, CdS and CdSe seem to be suitable for water splitting. However, semiconductors such as Si, CdS, GaAs and ZnO are known to be unstable against photocorrosion [18]. The photocorrosion reactions occurs due to photo-generated holes inside the semiconductors as

$Si + 2H_2O + 4h^+ \rightarrow SiO_2 + 4H^+$,

$CdS + 2h^+ \rightarrow Cd^{2+} + S$,

$ZnO + 2h^+ \rightarrow Zn^{2+} + 1/2O_2$,

where photoholes react with the semiconductor, rather than water, and degrade the semiconductor in a self-oxidation reaction. This instability against photocorrosion is a severe problem for almost all semiconductor materials, especially for non-oxide materials, because the photoexcitation process is, in principle, equivalent to bond breaking (or weakening). Even TiO_2,

a typical stable photocatalyst, has been reported to show surface roughening under UV light irradiation [44]. In order to prevent such photocorrosion, protecting the semiconductor with a corrosion-resistant layer is one strategy for obtaining an efficient and stable photoelectrode (or photocatalyst) [45,46].

Oxide semiconductors are relatively stable in water, and most oxide semiconductors containing d^0 (Ti^{4+}, V^{5+}, Zr^{4+}, Nb^{5+}, Ta^{5+}, and W^{6+}) or d^{10} (Zn^{2+}, Ga^{3+}, Ge^{4+}, In^{3+}, Sn^{4+}, and Sb^{5+}) metal cations work as stable photoelectrodes (or photocatalysts) for water splitting. Although TiO_2, $SrTiO_3$, and $NaTaO_3$ work well under UV light irradiation, these materials are very poor light absorbers under sunlight [11]. The valence band of most relevant oxides is composed of O2*p* orbitals that are usually at ~ 3 V vs. RHE [47] due to the large electronegativity of oxygen atoms. In order to satisfy the condition that the conduction band should be higher than the redox potential of H^+/H_2 (0 V vs. RHE), the semiconductors have to possess a band gap that is larger than 3 eV. This unavoidably leads to a problem of poor light absorption under sunlight, because 3 eV corresponds to a wavelength of 413 nm and the fraction of solar irradiance in the energy range above 3 eV is less than 5%.

WO_3, α-Fe_2O_3, and $BiVO_4$ are some narrow band gap oxide semiconductors that can work as photoelectrodes (or photocatalysts) for water oxidation under visible light and have long-term stability. But, since the conduction band edge is below the redox potential of H^+/H_2, these oxides do not have a potential to reduce water to hydrogen. To achieve overall water splitting, the photoelectrodes of these materials require external electric bias [48], and photocatalysts based on these materials have to be coupled with H_2-evolving photocatalysts to construct a Z-scheme water splitting setup [11].

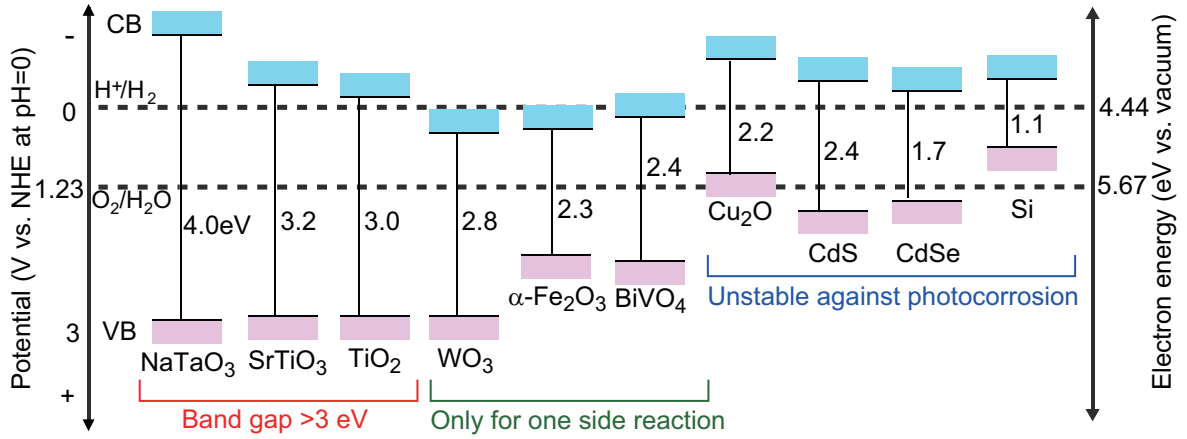

Figure 1.8: Band positions of typical semiconductors studied in photoelectrochemistry. The data was taken from Ref. 9,42,43. 0 V vs. NHE at pH = 0 corresponds to 4.44 eV vs. the vacuum level [49].

Band engineering by modifying the chemical composition of semiconductors is a commonly used technique to obtain stable visible-light-driven photocatalysts. Chemical doping and valence band control effectively reduce the energy gap of a wide band gap semiconductor [11]. Fig. 1.9 shows the strategy to obtain a narrow gap semiconductor photocatalyst by doping a wide-gap material. Chemical doping generally forms impurity levels within the band gap region. If such impurity levels are close to the valence band top or the conduction band minimum, the effective energy gap required for the photocarrier generation can be reduced. Doped TiO_2 and doped $SrTiO_3$ among the most common doped semiconductors used for photocatalysts [11]. N:TiO_2 [50, 51], Ni/Ta:TiO_2 [52], Cr/Sb:TiO_2 [53], Rh/Sb:TiO_2 [54], N:$SrTiO_3$ [55, 56], N/La:$SrTiO_3$ [57], Rh:$SrTiO_3$ [59], Rh/Sb:$SrTiO_3$ [60, 61, 64], Ir:$SrTiO_3$ [59], Cr:$SrTiO_3$ [53, 62, 63, 65–67], Cr/La:$SrTiO_3$ [58], Cr/Ta:$SrTiO_3$ [53], Cr/Sb:$SrTiO_3$ [68] are some examples that have relatively high photocatalytic activity in the H_2 or O_2 evolution reactions under visible light irradiation. Chemical doping often has positive effects on structural [69], electronic [70, 71], optical [72], and morphological [73] properties. However, doping also has a major disadvantage in that impurities often works as photocarrier trap sites, shortening the photocarrier diffusion length, as pointed out by Herrmann *etal*.. [74]. A technique called valence band control is a method to incorporate elements that form a new valence band higher than the level of the O2*p* orbitals. Metal elements that have electron configurations of either d^{10} (Cu^+, Ag^+) or $d^{10}s^2$ (Sn^{2+}, Pb^{2+}, Bi^{3+}), and anions with smaller electronegativity than oxygen (N, S) are often used for this purpose. Typical examples are $BiVO_4$ [75], SnM_2O_6(M = Nb, Ta) [76, 77], $MTaO_2N$(M = Ca, Sr, Ba) [78], and $LaTiO_2N$ [79].

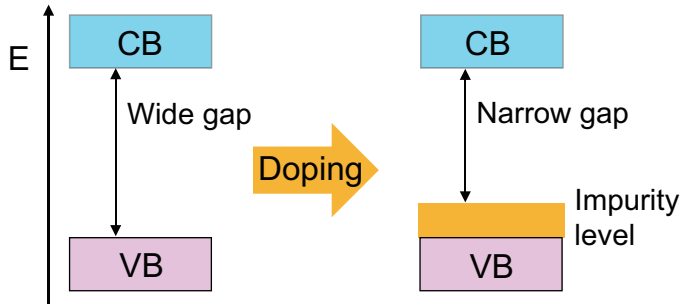

Figure 1.9: Strategy for obtaining a narrow-gap semiconductor photocatalyst by doping a wide-gap semiconductor. Doping with a suitable element creates an impurity level at the top of the valence band, narrowing the energy gap to improve the photocarrier generation efficiency.

The light absorption can also be modified by decorating the semiconductor with a sensitizer such as dyes (metal organic compounds) [80], quantum dots [81], and metal nanoparticles showing a localized surface resonance [82,83]. Interestingly, the idea of dye-sensitized photocatalysts triggered the invention of dye-sensitized solar cell as proposed by Grätzel in 1991 [84].

The electronic structure also has strong influence on photocarrier transport and surface reaction processes. Especially the photocarrier mobility and lifetime are affected by the characters of the valence and conduction bands and also the presence of any in-gap levels formed by defects and impurities. The band dispersion of the valence and conduction bands determine the carrier mobility in an intrinsic semiconductor. Defects and impurities generally work as trap sites, accelerating photocarrier recombination and suppressing photocarrier transport from the bulk to the surface. This suggests that high crystallinity and low trap densities are generally preferable for efficient photocarrier utilization. In addition, the internal band bending in a semiconductor plays an important role for the photocarrier transport from the bulk to the surface [85–87]. Photoelectrons and photoholes generated in the space charge region can separate from each other along the internal electric field gradient associate with the band bending, whereas photocarriers generated in the region where the band is flat cannot effectively separate and thus quickly recombine inside the semiconductor because there is no driving force to separate the photocarriers. In this sense, controlling the morphology of semiconductors [88] and utilizing heterojunctions [89] are feasible methods for increasing the specific surface area and the volume fraction of space charge regions.

The electronic structure of surface states affects the water splitting surface reactions by changing the activation energy (overpotential in the sense of electrochemistry) for water splitting. Electrocatalytic surface states may lead to faster electrochemical reactions. To make an efficient photoelectrode (or photocatalyst), the semiconductor surface is often decorated with cocatalysts that provide suitable surface reaction sites. Generally, good electrocatalysts for water splitting work as cocatalysts and accelerate the rate of electrochemical reactions. For the water oxidation reaction, IrO_2, RuO_2, and Co-oxides are often used as cocatalysts. For the water reduction reaction, Pt, Rh, Ru, and Ni are used as cocatalysts. Surface states also affect the bulk band bending and surface photocarrier recombination rates. Cocatalysts therefore affect not only the surface reactions but also the bulk band bending and surface photocarrier recombination.

Understanding and engineering the electronic structure are thus critically important tasks for creating suitable materials to achieve efficient photoelectrochemical solar water splitting.

1.5 Doped $SrTiO_3$

A wide variety of doped photocatalyst materials have been studied so far. Titanium oxides, especially TiO_2 and $SrTiO_3$, are often employed as host materials for doping in the study of photocatalyst [11]. That is because the band gap of TiO_2 (3.00 eV for rutile, 3.13 eV for brookite, and 3.21 eV for anatase [90]) and $SrTiO_3$ (3.2 eV [91]) is relatively small compared to other oxide materials, such as Ta- and Nb-based oxides.

Doped $SrTiO_3$, which is the target material in this thesis work, is a good starting point for studying fundamental aspects of photocatalysts. Non-doped $SrTiO_3$ has a cubic perovskite structure (ABO_3) with a band gap of 3.2 eV and it shows photocatalytic water splitting activity under UV light irradiation. The basic physical properties of $SrTiO_3$, e.g., permittivity, electronic structure, and carrier dynamics, have been widely studied from the viewpoint of solid-state physics. Since perovskites can accommodate a diverse selection of dopant elements, doped $SrTiO_3$ can be used to modify a variety of material properties such as the light absorption spectrum, carrier density, and magnetism. The perovskite lattice of $SrTiO_3$ can accommodate many types of guest atoms, which is why most elements in the periodic table can be chemically doped into a perovskite lattice (Fig. 1.10).

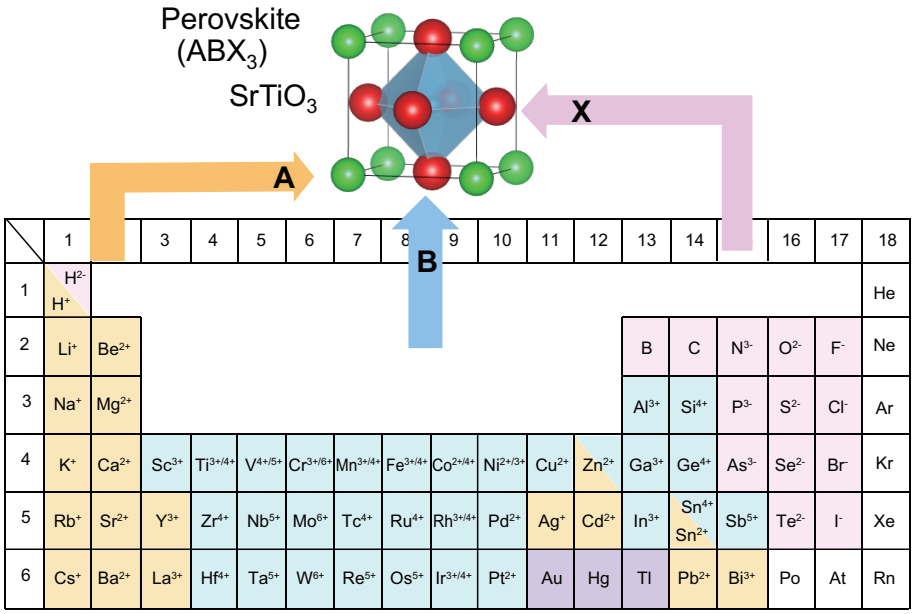

Figure 1.10: Diverse selection of dopant elements that can be used in $SrTiO_3$. The elements colored yellow, blue, and red substitute at the perovskite A-site (Sr in the case of $SrTiO_3$), B-site (Ti in $SrTiO_3$), and X-site (O in $SrTiO_3$), respectively. The elements colored purple have not been studied well. The noble gases cannot be chemically doped in the lattice.

In particular, Rh^{3+}- [59], Cr^{3+}- [53, 62, 63, 65–67], and N^{3-} [55, 56]-doped and Rh^{3+}/Sb^{5+}- [60, 61, 64], Cr^{3+}/La^{3+}- [58], Cr^{3+}/Ta^{5+}- [53] N^{3+}/La^{3+} [57]-codoped $SrTiO_3$ have been reported to show relatively high photoelectrochemical activity under visible light. Especially, Rh:$SrTiO_3$ has attracted considerable attention because this material is a rare *p*-type $SrTiO_3$ derivative, showing a photocathodic photoelectrochemical response [92] and high H_2-evolution activity under visible light [59]. Rh:$SrTiO_3$ works as an efficient H_2-evolving photocatalyst when coupled with an O_2-evolving photocatalyst in Z-scheme water splitting [93]. Still, despite the favorable band structure, the maximum solar conversion efficiency is ~ 0.1% [94].

A unique property of Rh:$SrTiO_3$ is a characteristic color change behavior that has been observed in the induction period during the early stage of the photocatalytic reaction. Only after the induction period does Rh:$SrTiO_3$ become active in a photocatalytic reaction under visible light irradiation (Fig 1.11 (A)) [59, 95]. The color change is known to be caused by a Rh valence change during a photocatalytic reaction. The as-prepared Rh:$SrTiO_3$ powders normally contain only Rh^{4+} ions, but conversion to Rh^{3+} occurs during the induction period in the photocatalytic reaction. The Rh valence shift is visually detectable as a color change from purple Rh^{4+}:$SrTiO_3$ to yellow Rh^{3+}:$SrTiO_3$. The overlapping absorption and action spectra (1.11 (B)) indicate that the photocatalytic activity is caused by light absorption related to a transition from a Rh^{3+} donor level to the conduction band of $SrTiO_3$.

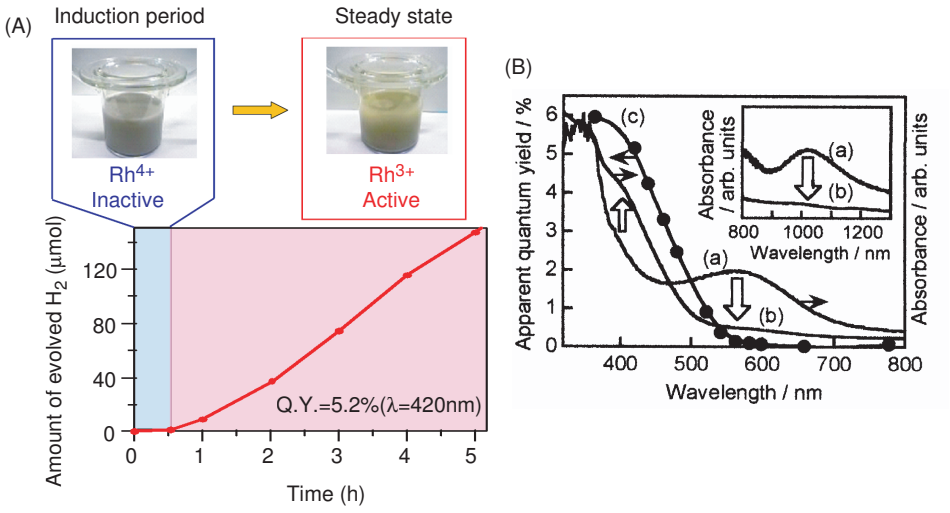

Figure 1.11: (A) Photocatalytic activity of Pt (0.1 wt%) loaded Rh(1 at%):$SrTiO_3$. A Rh valence change can be observed as a color change from purple to yellow after an induction period during photocatalytic reaction. Solution: 10 vol% MeOH aq. Light source: 300 W Xe lamp with L42-filter ($\lambda \geq 420$ nm). The data was taken from ref. [95]. (B) Absorption spectra of Rh:$SrTiO_3$ photocatalyst (a) before and (b) after the induction period, together with (c) action spectrum of its photocatalytic activity for the H_2 evolution reaction [59].

In addition to promising photocatalytic activity, it has been reported that Rh:$SrTiO_3$ can work as a photocathode for H_2 evolution from water under visible light irradiation [92]. Although non-doped $SrTiO_3$ is a typical *n*-type material that would be expected to form an upward band bending region at the water interface and thus function as a photoanode for the O_2 evolution reaction under UV light irradiation [96], the fact that Rh:$SrTiO_3$ can work as a photocathode indicates that a downward band bending region is formed at the water interface and Rh:$SrTiO_3$ thus has a *p*-type character (See Fig. 1.12 (A)). The cathodic photocurrent corresponding to H_2 evolution reaction was observed regardless of the doping level of Rh. Fig. 1.12 shows the photoelectrochemical response of Rh:$SrTiO_3$ as a function of the Rh doping level from 0.5 to 10 at%, indicating that the optimum doping level is 5 ~ 7 at% [92,97]. In spite of the attractive photocatalytic activity and electric *p*-type character of Rh:$SrTiO_3$, the electronic structure and the relationship between the photocatalytic activity and the electronic structure had not been fully understood until my work.

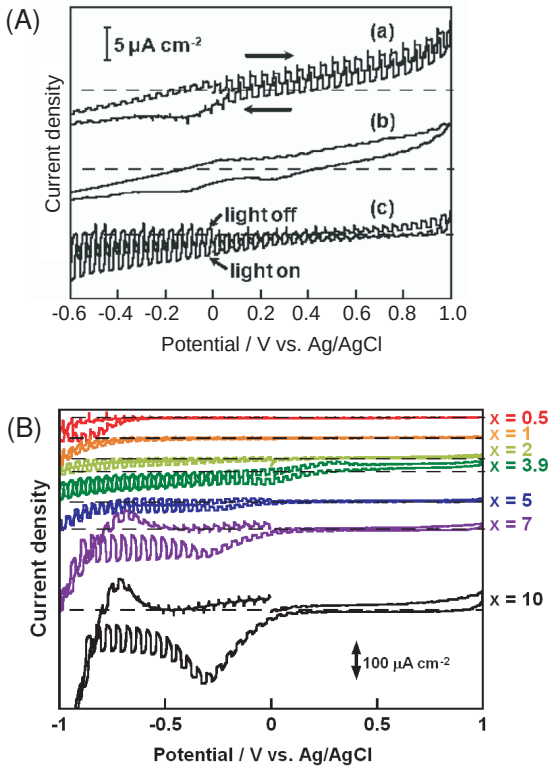

Figure 1.12: (A)Cyclic-voltammetry curves of (a) $SrTiO_3$ ($\lambda > 300$ nm), (b) $SrTiO_3$ ($\lambda > 420$ nm), and (c) Rh(1 at%):$SrTiO_3$ ($\lambda > 420$ nm) electrodes. Electrolyte, 0.1 M aqueous K_2SO_4 solution; sweep rate 20 mV/s; light source, 300 W Xe lamp [92]. (B)Cyclic-voltammetry curves of $SrTiO_3$ doped with Rh(x at%) under 300 W Xe lamp illumination through an L42-filter ($\lambda > 420$ nm), for x = 0, 0.5, 1, 2, 3.9, 5, 7, and 10 [97].

Ir:$SrTiO_3$ has also been reported to be a visible-light-driven photocatalyst, although the photocatalytic activity is lower than that of Rh:$SrTiO_3$ [59]. One advantage of this material is the capability to utilize light with wavelength up to 600 nm, which is potentially favorable for solar energy conversion. A characteristic color change during the induction period in the early stage of the photocatalytic reaction, similarly to Rh:$SrTiO_3$, has been reported by Matsumoto [98]. This color change is supposed to be caused by an Ir valence change from Ir^{4+} to Ir^{3+} [98, 99]. The availability of Ir:$SrTiO_3$ for solar water splitting has been studied, but the detailed material properties of Ir:$SrTiO_3$, including the electronic structure have not been fully understood yet. In this study, the electronic structure and the photoelectrochemical property of Ir:$SrTiO_3$ were investigated and discussed by comparing with Rh:$SrTiO_3$ to determine the difference between 4*d* and 5*d* transition metal doping (Ir and Rh are in the same group in the periodic table).

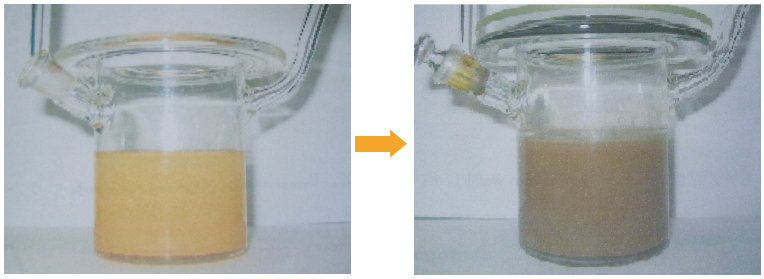

Figure 1.13: Characteristic color change behavior observed during the induction period in the early stage of a photocatalytic reaction. As-prepared Ir:$SrTiO_3$ is yellow (a), but the color changes to brown after the induction period while the material becomes active for the photocatalytic reaction. Photocatalyst; Ir(0.2%):$SrTiO_3$ 0.3 g suspended in 150 mL of 10 vol% MeOH aq. Light source: 300 W Xe lamp with an L42-filter. [98]

In this study, I clarified the relationship between the electronic structure and the photoelectrochemical activity of doped $SrTiO_3$, based on a model photocatalyst approach.

1.6 Model photocatalyst

Practical catalysts are usually in a polycrystalline form. Polycrystalline materials have the advantage of lower synthesis cost and a large specific surface area. However, the difficulty of analyzing detailed material properties of a polycrystalline specimen makes it difficult to clarify the reaction dynamics of catalytic reactions. Due to this fact, the performance of catalytic materials have often been optimized by chemical composition and surface modifications based on a large number of trial-and-error experiments without clarifying the true reaction dynamics at a microscopic level. It is clear that clarification of the catalytic reaction mechanism helps us to improve the catalytic activity and develop practical applications. For understanding the reaction dynamics at an atom level, using a well-defined single crystals or epitaxial thin film as a "model catalyst" is a way to analyze the detailed catalytic performance by surface scientific analytical techniques. Samples with well-defined surfaces are prepared by using an ultrahigh vacuum system and have an ideally clean atomically flat surface with good crystal quality. Various kinds forms of spectroscopy and microscopy can be used to analyze the surface structures on an atom level.

Extending the concept of a "model catalyst" to the study of photocatalysts, using a well-defined single crystal or epitaxial thin film as the "model photocatalyst" is a good starting point for analyzing the detailed photocatalytic performance by surface scientific and also semiconductor analytical techniques (Fig. 1.14). Water / semiconductor interfaces have been extensively studied from the point of view of photoelectrochemical solar water splitting since the 1960s [18]. A physical model of a semiconductor photoelectrode has been established based on semiconductor device physics, similarly to solar cells [1,14,15]. While typical semiconducting materials such as Si, GaAs, CdS, and ZnO were studied in early work on photoelectrochemical water splitting, the discovery of photoelectrochemical activity of TiO_2 [2] directed interest toward oxides. The TiO_2 surface has attracted much attention and it has been studied from various viewpoints because it is a cheap, abundant, stable, and non-toxic material with good photocatalytic performance [100]. Comprehensive review papers on the properties of TiO_2 surface have been published by Henderson and Diebold [101–103]. Currently, TiO_2 is recognized as a prototypical photocatalyst and it is widely studied not only for photoelectrochemical water splitting but also for photocatalytic organic decomposition and photo-induced hydrophilicity. The development of vacuum and thin film technologies have led to the availability of high quality epitaxial oxide thin films. TiO_2 epitaxial thin films have been fabricated since 1990s by various vapor deposition processes such as MOCVD [104], PLD [105], and MBE [106]. Such atomically controlled epitaxial thin films have expanded the availability of research techniques. As an example, Matsumoto *etal*.. have investigated the activity difference of SrO-terminated and TiO_2-terminated $SrTiO_3$(001) surfaces for photocatalytic organic decomposition [107] and photo-induced hydrophilicity [108] by using atomically controlled epitaxial thin films fabri-

cated by PLD. They also studied the effect of surface states of TiO_2(110) on electrochemical performance by using atomically flat TiO_2 photoelectrodes [109].

In this study, single crystals and epitaxial thin films were used as model photocatalysts to investigate both bulk and surface properties of oxide photocatalysts.

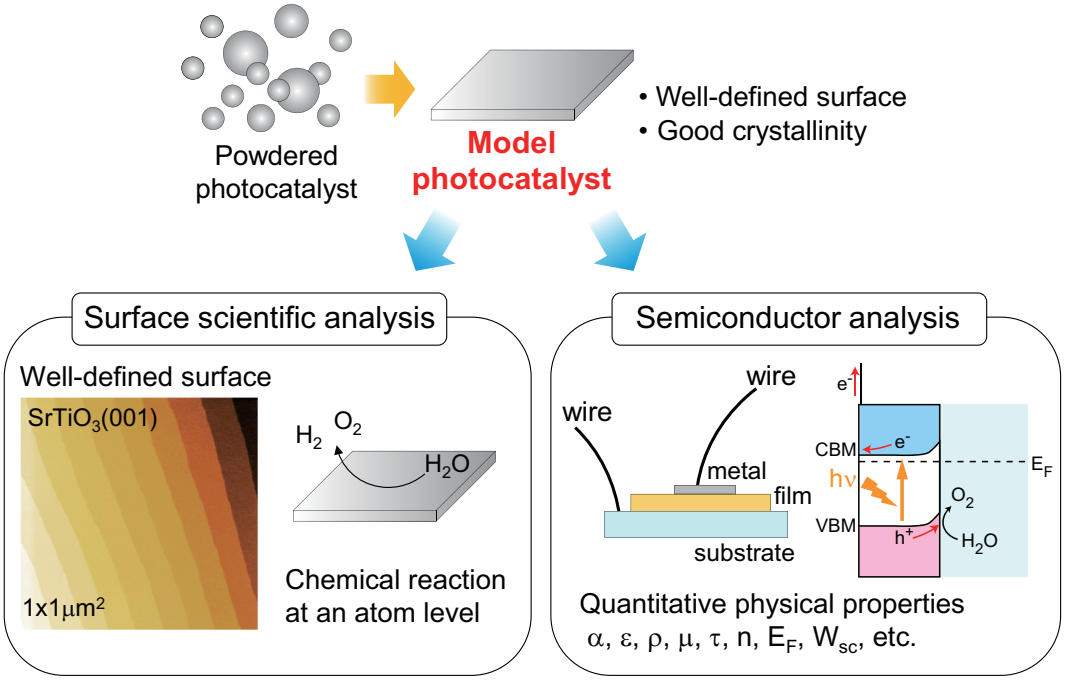

Figure 1.14: Concept of the model photocatalyst approach. By using a well-defined single crystal or epitaxial thin film as a model photocatalyst, one can apply surface scientific and semiconductor analytical techniques to investigate the detailed material properties for both surface catalytic properties and bulk semiconductor properties.

1.7 Aim of this study

The motivation of this study was to clarify some of the fundamental physical mechanisms in photocatalysts and photoelectrodes that limit the efficiency of photoelectrochemical activity, and to propose new routes for developing an efficient solar-to-fuel conversion system. Well-defined single crystal substrates and epitaxial thin films can be used as model photocatalysts (or photoelectrodes) to investigate the dynamics of photoelectrochemical reactions. In this study, $SrTiO_3$ (and Nb:$SrTiO_3$) single crystal substrates and doped $SrTiO_3$ epitaxial thin films were used to clarify the mechanism of photo-induced superhydrophilicity and the relationship between the electronic structure (especially the impurity level positions) and photoelectrochemical activity.

Theoretical limitations of solar energy conversion efficiency in doped $SrTiO_3$ were analyzed and proposals are presented for innovative material designs that improve the photoelectrochemical efficiency of oxide photoelectrodes. This study was based on a model photocatalyst approach, but fruitful stimuli from collaboration with researchers in various fields such as solid state physics, surface science, thin film technology, and device physics helped to reach several fundamentally important conclusions. An overview of topics covered in this thesis is schematically shown in Fig. 1.15. Chapter 1 explains the social demand for solar fuel production. As one promising candidate, photoelectrochemical water splitting is discussed with the basic material design as well as the introduction of model photocatalyst approaches. Chapter 2 briefly describes the methods and techniques used in this work. The main results are discussed in Chapters 3, 4, and 5. Chapter 3 is on the clarification of the mechanism of photo-induced superhydrophilicity. Hydrophilicity on an atomically flat oxide surface was precisely analyzed. The results showed that oxide surfaces are intrinsically highly hydrophilic, indicating that the mechanism of photo-induced superhydrophilicity can be explained purely by the contamination model. In Chapter 4, the relationship between photoelectrochemical activity and electronic structure of doped $SrTiO_3$ photocatalysts are investigated. The electronic structure formed by dopants was elucidated by X-ray spectroscopy and the photoelectrochemical activity was measured with high quality epitaxial thin film photoelectrodes made of doped $SrTiO_3$. The effect of dopant valence on the photoelectrochemical activity of Rh- and Ir- doped $SrTiO_3$ was clearly understood by considering the influence of the impurity level positions on photocarrier transport and light absorption. The results clarified the peculiarity of the Rh^{3+} dopant for $SrTiO_3$ in terms of impurity level positions. The contents of this work have been partially published in three papers (See publication lists). However, these findings suggested that doped $SrTiO_3$ photocatalysts are problematic due to a fundamental trade-off between visible light absorption and photocarrier transport efficiencies. In order to overcome this problem, Chapter 5 proposes a novel nanostructure design using self-assembled epitaxial metal nanopillars for improving the photocarrier transport efficiency in doped $SrTiO_3$. This nanostructure includes noble metal nanopillars embedded in a thin film photoelectrode, forming 3-dimensional Schottky junctions between $SrTiO_3$ and metal nanopillars owing to the large work function of noble metals. Nanocomposite Ir:$SrTiO_3$ films with embedded Ir metal nanopillars showed over 80% internal quantum efficiency over a wide range of visible light region. The thesis work is concluded in Chapter 6.

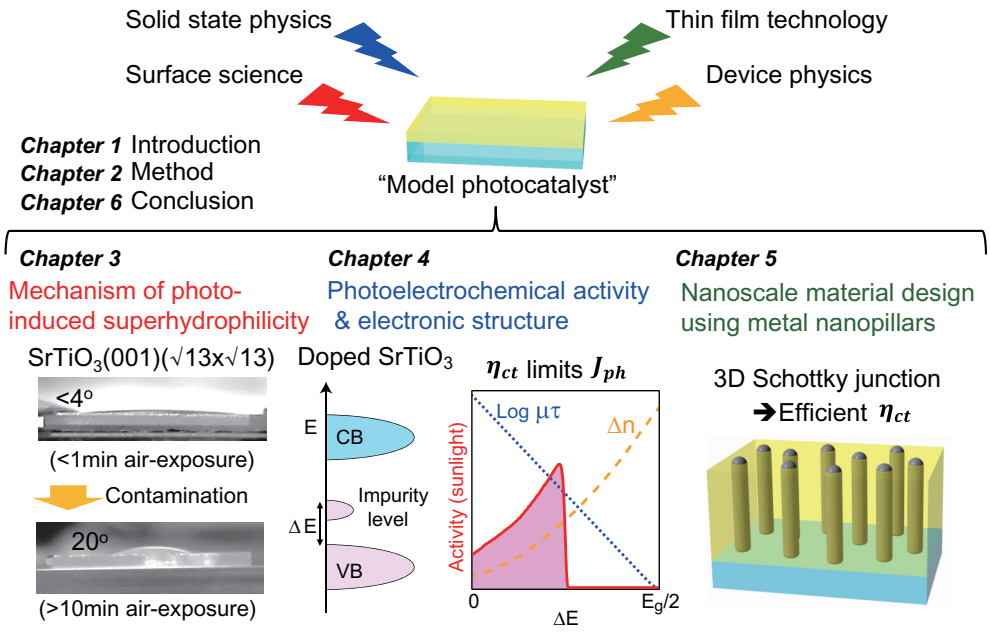

Figure 1.15: Illustration showing the construction of this thesis.

Chapter 2

Methods and techniques

The main sample fabrication methods and characterization techniques are introduced in this section. Most of the work is based on thin films that were fabricated by Pulsed Laser Deposition (PLD). The growth rate and the surface roughness of the films were characterized by reflection high-energy electron diffraction (RHEED) during film growth and annealing treatments. Conventional symmetric X-ray Diffraction (XRD) was used for verifying that the samples did not contain unwanted crystallographic phases and for characterizing the crystallinity of the samples. Various forms of X-ray spectroscopy were used for determining the electronic structure and the dopant valence, including laboratory and synchrotron source X-ray Photoemission Spectroscopy (XPS), X-ray Absorption Spectroscopy (XAS), and X-ray Emission Spectroscopy (XES). Most films were analyzed by Atomic Force Microscopy (AFM) to measure the surface flatness, infer the growth modes, and to check for segregation. Frequency-Modulation Atomic Force Microscopy (FM-AFM) was used to observe the atomic-scale surface structure of reconstructed crystal surface and to study the hydration structure in a water environment. Optical absorption spectra of the films were measured with a UV-Vis-NIR spectrometer. For powder samples, equivalent data was obtained by Diffuse Reflection Spectroscopy (DRS). The photoelectrochemical performance of the film samples was measured by standard photoelectrochemical techniques, including cyclic-voltammetry, chronoamperometry, and Mott-Schottky analysis.

2.1 Pulsed laser deposition

The thin film samples were grown by PLD, which has been used widely for oxide thin film growth. The technique is technically relatively simple and can be used to grow films of complex oxides with the desired stoichiometry relatively easily [110–112]. A schematic illustration of the PLD system used in this work is shown in Fig. 2.1. The films were grown on single-crystal substrates that were mounted on a nickel sample holder and heated with an infrared Nd:YAG laser (λ = 1064 nm). PLD works by evaporating a bulk ceramic pellet with a short ultraviolet laser pulse, creating a plasma plume that transports material from the target to the substrate surface. In this case, several targets were placed a few centimeters below the substrate on a carousel that could be used to conveniently switch between different target materials for film growth. The ablation was done with a pulsed KrF excimer laser (Lambda Physik COMPex 102 or COMPex 201), operating at λ = 248 nm. The short wavelength and a high peak power of the laser ensured nearly stoichiometric evaporation from the target surface. The excimer laser pulses were focused onto the target surface at a fluence of approximately 1 J/cm^2. The fluence was adjusted to control the amount of material evaporated with a single pulse, which in turn controlled the film growth rate. Growth rate adjustment was essential for some of the film growth experiments where the growth kinetics plays an important role, such as the formation of the embedded metal nanopillar structures. Fig. 2.2 shows a photo of the inside of the PLD chamber during thin film growth. The oxygen gas pressure in the deposition chamber was controlled with a variable leak valve from the chamber base pressure of about 5×10^{-9} Torr to 1 Torr. The biggest advantage of PLD for growing complex oxides is the nearly stoichiometric transfer of material from target pellet to the film surface due to the extremely high temperature created at the target surface by the pulsed laser. For the growth of complex oxides like the perovskite-type materials used in this work, where two or more different elements are included in a unit cell, however, slight off-stoichiometry of thin films grown by PLD has been reported for several materials, such as $SrTiO_3$ [113, 114], $YBa_2Cu_3O_7$ [115], $LiCoO_4$ [116] and $SrRuO_3$ [117]. It is therefore important to control the laser fluence in a repeatable way. A simple single-lens focusing setup was combined with an optical attenuator and in situ laser pulse energy monitoring for fluence control.

Most oxide thin films need to be grown at a high temperature to obtain good crystallinity. A special oxygen-compatible high-temperature sample holder was used for growth temperature control. A sandwich structure was used to clamp together a substrate crystal, heat-transfer metal foils (5 μm-thick Ni sheets, Nilaco, 99%), an oxidized Ni heat absorber (100 μm) and a sapphire support. The heat absorber was heated with a Nd:YAG laser from outside of the chamber. This design ensured homogeneous heating and could reach a maximum temperature of about 1400°C in oxygen. The sample temperature was monitored with an optical pyrometer (Japan Sensor; FTC2) focused onto the sample surface. Besides being oxygen compatible, the

laser heating technique can be used to heat and cool the sample very rapidly, due to the very small heat capacity of the sample holder. [118].

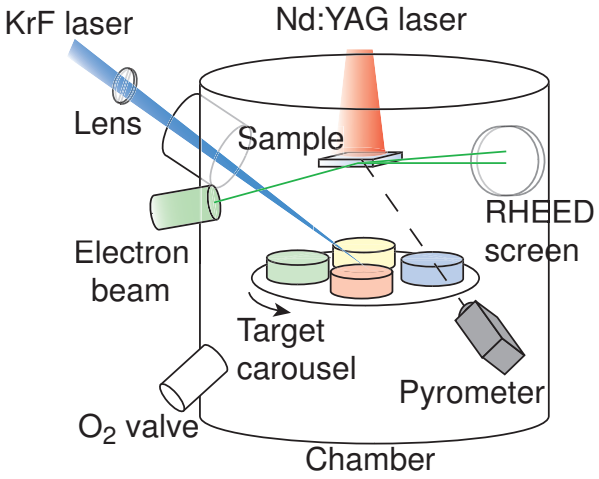

Figure 2.1: Schematic of the PLD system.

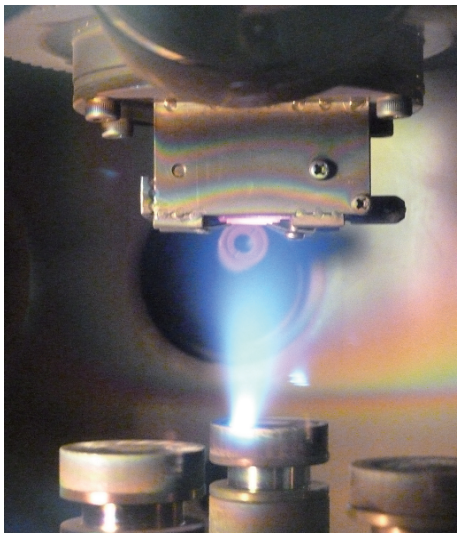

Figure 2.2: A photograph of the inside of the PLD chamber during thin film growth.

2.2 Reflection high-energy electron diffraction (RHEED)

One of the difficult issues with fabricating oxide films by PLD is the variability of the surface morphology and film crystallinity due to minor variations in the substrate surface or the deposition conditions, such as the sample temperature or the ablation laser fluence. A convenient method for in-situ analysis of growth dynamics, surface morphology, and surface reconstructions is reflection high-energy electron diffraction (RHEED). It is a diffraction technique where a sample surface is probed with a high-energy electron beam ($\sim$ 25 keV) at grazing incidence (0.5 to 2.5° from the surface). RHEED is suitable for surface analysis in a PLD chamber because differential pumping in two pumping stages separated by pinholes can ensure that the electron gun remains at high vacuum conditions while the deposition part of the chamber can be filled with oxygen to a pressure of up to about 500 mTorr. The use of the grazing incidence geometry means that the electron gun and the phosphor screen used for diffraction pattern observation do not interfere with the mechanics of the sample holder or the targets. The low incident angle and the use of electrons instead of X-rays mean that RHEED is extremely surface sensitive and ideal for surface structure analysis. The electron beam is scattered from sample surface and forms a diffraction pattern on a phosphor screen. The image is captured with a CCD camera and analyzed in real time during film deposition. Besides observing the diffraction pattern, the intensity of the specular reflection beam carries important information about the atomic-scale roughness of the crystal surface. An atomically flat surface gives a strong reflected beam, while local roughness leads to electron scattering and reduced specular intensity. When the specular beam intensity is measured a function of time, the intensity profile can be used to determine the growth mode of a thin film.

There are three relevant growth modes that can be distinguished by RHEED specular intensity analysis during pulsed laser deposition: layer-by-layer growth, 3-dimensional growth, and step-flow growth. Static image analysis is used for distinguishing between layer-by-layer and 3-dimensional growth modes. During layer-by-layer growth, which is normally preferred, the diffraction pattern shows diffraction spots and possibly streaks arranged on Laue circles. If the surface roughness increases due to the formation of 3-dimensional grains, a transmission pattern appears, with a regular rectangular array of diffraction spots.

During layer-by-layer growth, the surface roughness is proportional to the fractional layer coverage of the topmost unit-cell layer. Fig. 2.3 shows the variation of the specular RHEED beam intensity as a function of surface roughness during near-perfect layer-by-layer growth of homoepitaxial $SrTiO_3$. The intensity behavior can be understood in terms of step-edge scattering of electrons. If the initial surface is flat, the specular intensity is high, but starts to decrease rapidly when the deposition starts, as adatoms nucleate and form small single unit cell high islands ($A \rightarrow B \rightarrow C$). The minimum intensity is reached close to half monolayer coverage (C), after which the reflected electron beam intensity starts to increase again, until the

topmost molecular layer is completed and the specular beam intensity recovers to the original level ($C \rightarrow D \rightarrow E$). The number of laser pulses needed to fill one unit cell layer is usually in the range from 10 to 100, and it may take a few tens of seconds to grow a single unit cell layer.

Due to the pulsed deposition, where the adatom density increases instantaneously after each deposition pulse and relaxes during the interval between pulses, the specular RHEED intensity also carries information about this pulse-by-pulse relaxation process. At very high temperatures, when the relaxation process is completed between each deposition pulse, the film growth mode changes from layer-by-layer to step flow. The step flow mode can be detected by spike-like intensity changes in the RHEED intensity.

The RHEED intensity oscillations are mostly determined by the variation of the film surface morphology, but other factors should also be considered. For example, even small changes in the electron beam incident angle can affect the intensity oscillation amplitude and phase [120, 121]. Especially the intensity oscillation phase shifts need to be considered carefully when attempting to measure the thickness of very thin layers of a few unit cells.

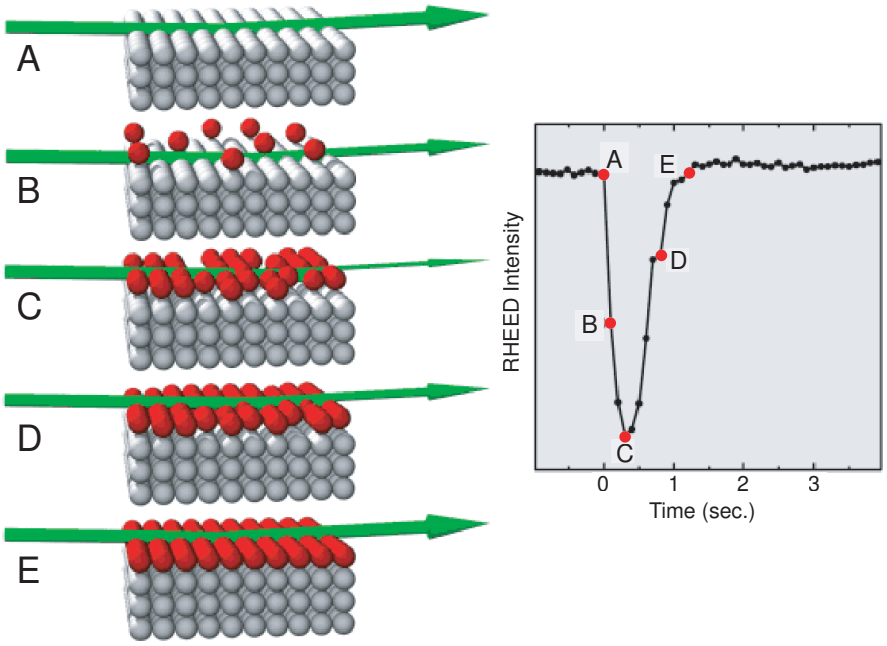

Figure 2.3: RHEED specular intensity oscillation for the layer-by-layer growth mode during the deposition of a single unit cell layer of $SrTiO_3$ [119].

2.3 X-ray diffraction (XRD)

The crystallinity, orientation, and the presence of secondary phases in the films was analyzed by XRD. Either a conventional powder-type (Rigaku; SmartLab) or a 4-circle (Philips; X'Pert-MRD) diffractometer was used for measuring the out of plane lattice parameter of the films, as schematically illustrated in Fig. 2.4. The presence of strain, the effect of dopants, stoichiometry errors, and the density of oxygen vacancies can be estimated from the lattice parameter of a thin film, which is calculated from the diffraction angle of a film peak in a $2\theta/\theta$ scan. The atomic layer distance can be calculated from Bragg's law,

$$2d_{hkl} \sin\theta = n\lambda, \tag{2.1}$$

where λ is the X-ray wavelength, n is an integer diffraction order, d_{hkl} is the lattice spacing, and θ is the diffraction angle. In this work, all measurements were done with Cu K_α X-ray sources that emit Cu $K_{\alpha1}$ = 1.54054 Å and Cu $K_{\alpha2}$ = 1.54432 Å radiation.

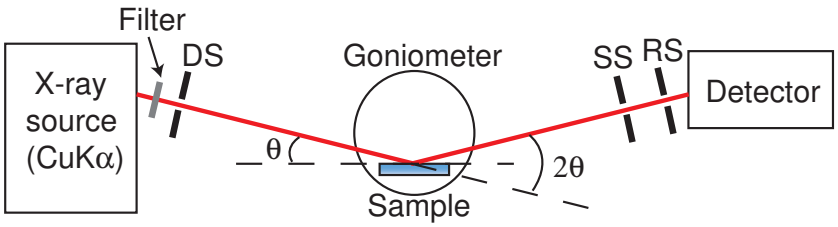

Figure 2.4: Schematic of a $\theta/2\theta$ XRD measurement. DS, SS, and RS correspond to divergence slit, scattering slit, and receiving slit, respectively.

Conventional X-ray diffraction, i.e., symmetric scans where the incident and scattering angles are equal, can be used to measure only the out-of-plane lattice spacings in a crystal. For single-crystal samples, such as epitaxial thin films, it is necessary to measure the in-plane lattice parameters independently due to the presence of epitaxial strain imposed by the substrate. Reciprocal space mapping was therefore used to measure the X-ray scattering intensity distributions in the vicinity of certain reciprocal lattice points. In reciprocal space mapping, it is more convenient to use the scattering vector Q, with Q_x being the in-plane component and Q_z the out-of-plane component. The relations between the diffractometer incident and scattering angles, ω and 2θ, and the scattering vector components, Q_x and Q_z, is given by

$$Q_x = K[cos(\theta - \omega) - cos(\theta + \omega)] \qquad Q_z = K[sin(\theta - \omega) + sin(\theta + \omega)], \tag{2.2}$$

where $K = 1/\lambda$ is the radius of the Ewald sphere. Not all reciprocal space points can be mapped, because for some lattice plains the necessary incident or scattering directions would be below the surface of the sample. The reciprocal lattice points that can be mapped fall within

a hemispheres in the Q space having $-2K \leq Q_x \leq 2K$ and obeying $Q_x^2 + Q_z^2 \leq 4K^2$. The area of reflection is divided from the area of transmission by two other hemispheres of radius K that are centered at $Q_x = -K$ and K. The combined plot of the scattering vector (Q_x, Q_z) and the position of the Bragg peaks for the $SrTiO_3$ (001) orientation in reciprocal space is shown in Fig. 2.5. A conventional symmetric $\theta/2\theta$ scan would follow a vertical line along the Q_z axis in reciprocal space. The materials studied in this work have either a pseudo-cubic or a tetragonal structure, which means that the reciprocal space points, such as (103) and (303), are suitable for investigating the in-plane lattice parameter when considering the extinction rules.

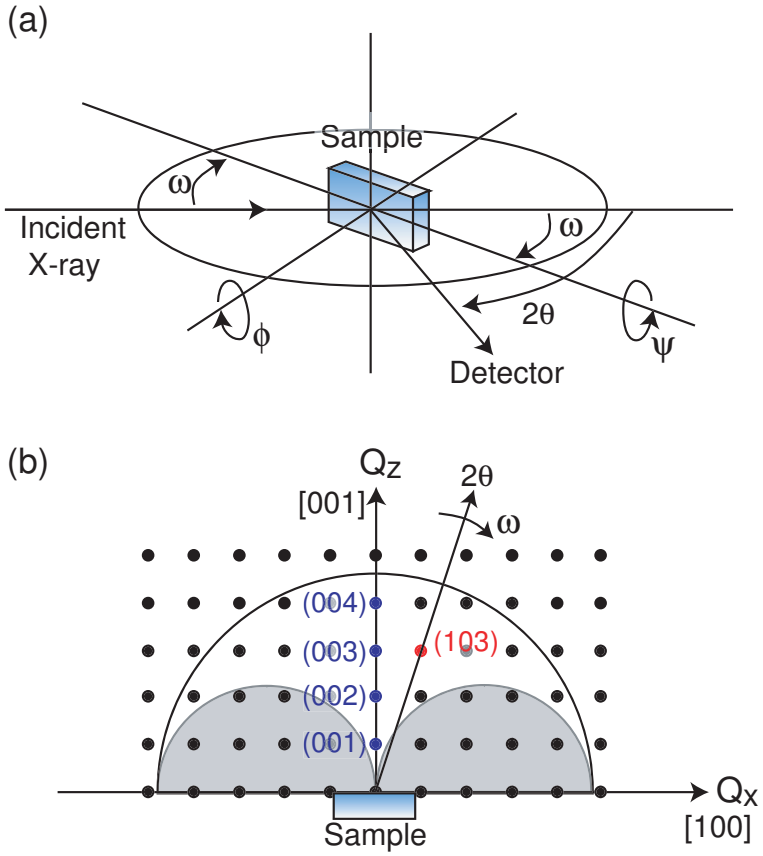

Figure 2.5: (a)Sample position and measuring angles (2θ, ω, ϕ, ψ) in real space for 4-axis XRD and (b) combined plot of (Q_x, Q_z) and the positions of Bragg peaks for $SrTiO_3$ (001) in reciprocal space.

2.4 X-ray photoelectron spectroscopy (XPS)

XPS was used mostly for determining the valence of the dopant elements in the oxide thin film samples. In an XPS measurement, a monochromatic X-ray beam is used extract electrons from a solid by the photoemission effect. Both core and valence levels of the atoms close to the film surface can be analyzed. The core levels refer to the inner electron shells that have no direct role in chemical bonding but chemical bonding affects the precise energy of the core levels. Measuring the exact core level energies or the distribution of core level energies can be used to determine the valence of a particular atomic species in a sample. The purpose of XPS measurements was to determine the valence of dopant atoms. For samples that contained dopants with several different valence states, deconvolution of the photoemission spectra was used to determine the ratios of the different valence species. The kinetic energy of photoemitted electrons is given by:

$$E_{kinetic} = h\nu - \Phi - E_{binding}, \tag{2.3}$$

where $E_{kinetic}$ is the kinetic energy of the emitted electrons, $h\nu$ is the incident X-ray energy, Φ is the work function of the surface, and $E_{binding}$ is the binding energy of a particular electron energy level. In an XPS measurement, $h\nu$ and Φ are known, and $E_{kinetic}$ is measured with an electron energy analyzer, which means that $E_{binding}$ can be calculated.

Since XPS uses electrons emitted from the sample surface, it is obviously a very surface sensitive technique. The detection depth depends on the inelastic mean free path (IMFP) of electrons, usually labeled λ, which is defined as the distance an electron can travel before its intensity decays to $1/e$ or (1/2.718) of its initial value. The IMFP is thus a good measure for how deep layers can be probed by XPS. In this study, the IMFP was approximated by using Fig. 2.6 [122].

Since electrons are emitted from a sample during an XPS measurement, a static charge would build up in an insulating sample due to the electron loss. A conducting sample is therefore required to avoid charging effects. Film samples used in XPS measurements were therefore grown on conducting Nb(0.05 wt%):$SrTiO_3$ substrates.

Most of the XPS measurements were carried out at the beamline BL-13A [123] and BL-2A [124] at the Photon Factory (PF) of the High Energy Accelerator Organization (KEK). Standard data processing tools were used for XPS feature extraction. The background was subtracted by the Shirley algorithm and peak deconvolution was done by nonlinear least squares fitting of spectral shapes with multiple semi-Gaussian peaks. Synchrotron sources were used due to the high x-ray intensity, greatly shortening the measurement time over conventional laboratory X-ray sources. The monochromatized X-rays from an undulator also have very high spectral purity, which increases the XPS energy resolution.

Several samples were also measured with a conventional XPS system (JEOL; JPS-9010MC)

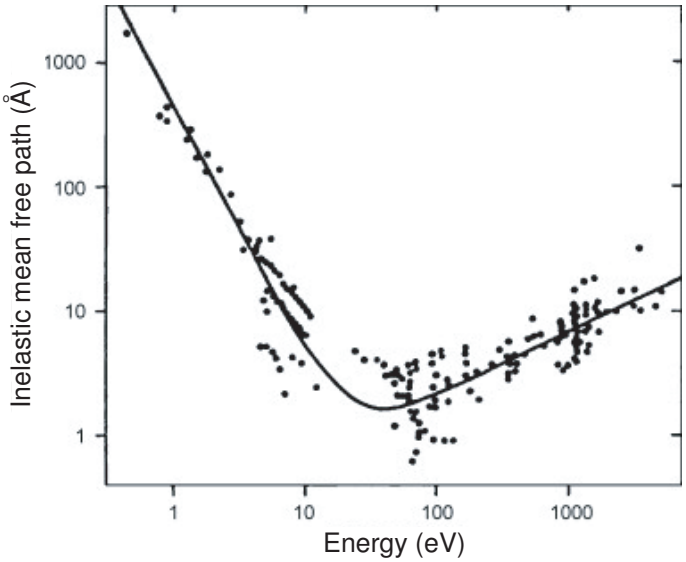

Figure 2.6: The universal curve, showing the relation between photoelectron kinetic energy and inelastic mean free path (IMFP) [122].

at Kudo laboratory in Tokyo University of Science. The X-ray source was a Mg K_α = 1253.6 eV lamp, operating at a source current of 10 mA at 12 kV.

2.5 X-ray absorption and emission spectroscopy (XAS/XES)

Photocarrier generation and transport are important characteristics of photocatalytic materials. Closer analysis of photoexcited carrier behavior requires an accurate electronic structure model for both occupied and unoccupied states. To build such model for the model photocatalysts, a combination of X-ray absorption spectroscopy (XAS) and X-ray emission spectroscopy (XES) was used.

A schematic diagram in Fig. 2.7 explains the difference between these two spectroscopic techniques. In XAS, a core-level electron is lifted into an unoccupied state just above the Fermi level. As the excited electron relaxes, a photon emitted and can be detected. By measuring the fluorescence yield as a function of the incident X-ray energy, the absorption spectrum can be mapped. Since the initial state is constant in a single absorption spectrum, the fluorescence yield is proportional to the absorption cross section of the unoccupied states.

If a high-resolution X-ray monochromator is used to analyze the energy of the emitted fluorescence photons, it is possible to map out the density of occupied states as well, following the excitation scheme shown in Fig. 2.7b. In this case, the fluorescence signal of interest is generated by valence band electrons repopulating an empty core-level state. This is known as X-ray emission spectroscopy and it can be used to measure the density of occupied states. It should be noted that while the density of occupied states can, in principle, be measured by XPS or UPS, these techniques require a conducting sample to prevent sample charging. Both XAS and XES are X-ray in - X-ray out techniques, making them insensitive to sample charging. Even materials with very low conductivity can thus be used in measurements. An additional benefit of XAS/XES is that samples do not need to be held in vacuum, but in operando measurements in air or even in liquid electrolytes is possible.

The X-ray absorption and emission intensities are proportional to the transition probability between the initial and final states in the electron transition process. This relation is known as Fermi's golden rule:

$$P \propto |\langle \psi_f | r | \psi_i \rangle|^2 \delta(E_f - E_i - h\nu), \tag{2.4}$$

where ψ_i and ψ_f are the initial and final states in an electron transition process and $|\langle \psi_f | r | \psi_i \rangle|$ is the electric dipole moment. δ is the delta function, limiting transitions only to cases where the photon energy equals the energy difference between the initial and final states.

A combined XAS and XES ultrahigh-resolution soft X-ray emission spectrometer at the undulator beamline BL07LSU at SPring-8 was used for measuring O1s spectra [125, 126]. Fluorescence yield mode was used for XAS spectra, avoiding any charging artefacts from possible charge-up effects in $SrTiO_3$. A photodiode detector (IRD AXUV-100) was positioned in front of the sample at a 45° angle to the incident beam to detect the fluorescence x-rays. The photoelectron background was eliminated by applying a -550 V retarding bias relative to the sample

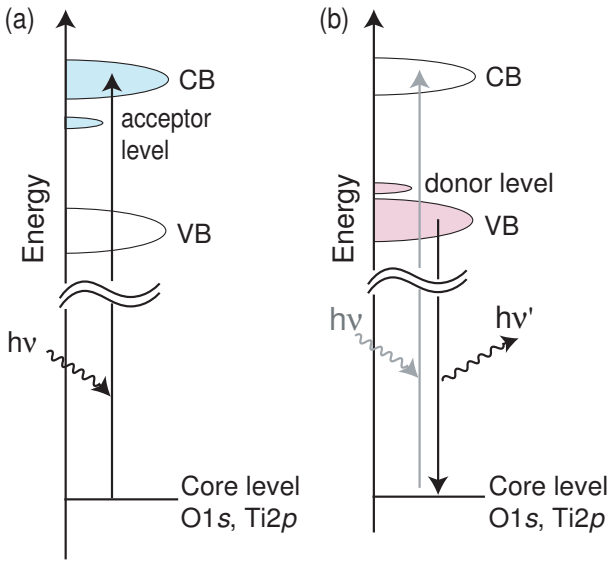

Figure 2.7: Energy level diagrams for the electron transitions probed by XAS and XES for a doped $SrTiO_3$ sample.

surface on a gold mesh in front of the detector.

The XES spectra were measured with a long baseline x-ray grating monochromator optimized for ultrahigh energy resolution. The energy resolution of the spectrometer was around 50 meV at the O1*s* edge. The total energy resolution, $E/\Delta E$, was 3500 ($\Delta E \sim 0.15$ eV) at 530 eV for both XAS and XES measurements. The incident photon energy was calibrated against Xe $5p_{3/2}$ photoemission lines. The X-ray emission energy calibration was based on elastic scattering lines.

2.6 Atomic force microscopy (AFM)

Atomic force microscopy (AFM) is a scanning probe techniques used for measuring the morphology of surfaces with atomic-scale accuracy. A Shimadzu SPM-9600 microscope was used in this study to record the surface morphology of thin film samples, and to map the conductivity of metallic nanopillars embedded in a thin film.

The essential elements of a contact-mode AFM are illustrated in Fig. 2.8. The scanning probe sensor consists of a sharp probe needle that is attached to a flexible cantilever. A tube-shaped piezoelectric actuator is used to raster scan the sample under the sharp needle and to adjust the sample height so as to maintain the cantilever at a constant average height. The deflection of the cantilever, i.e., the height of the sharp needle, is measured by detecting the shift of a laser beam reflected from the backside of the cantilever. The detector is a four-segment photodiode that is used to measure the vertical and horizontal shifts of the laser beam. A vertical shift of the beam indicates a change in the sample height. A feedback system automatically adjusts the sample stage height to return the cantilever to the equilibrium position. Horizontal shifts of the laser beam indicate that the cantilever is tilting, which can be caused by lateral friction forces in contact-mode measurements. The friction force between the surface and the tip is dependent on the chemical nature of the surface. Although the friction signal is not quantitative, a friction force contrast between two areas on a sample surface indicates that those two areas are chemically different. [127, 128]. A big advantage of AFM is that the sample does not to be conductive and therefore it can be used to measure the morphology of all types of film samples. The main drawback is the limited spatial resolution, which is set by the 10 nm radius of the AFM probe needle.

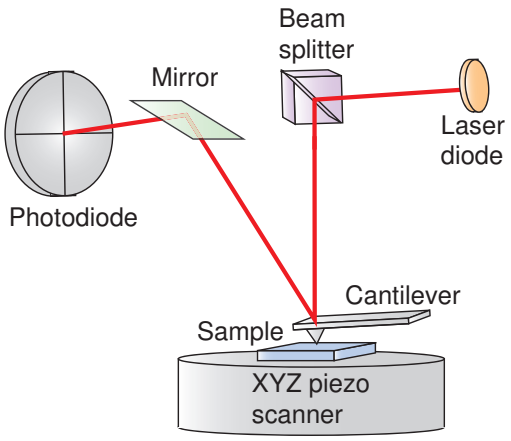

Figure 2.8: Schematic illustration of an atomic force microscope (AFM).

2.7 Frequency-Modulation Atomic force microscopy (FM-AFM)

In conventional non-contact AFM measurements the tip is vibrated close to its mechanical resonance frequency with a small excitation piezo actuator and approached to the surface being imaged. The interaction force between the tip and the sample surface causes the phase and the amplitude of the cantilever to change and both parameters are detected by the microscope feedback system. The height information is obtained by adjusting the vertical sample position piezo to maintain constant tip vibration amplitude.

In frequency-modulation atomic force microscopy (FM-AFM), the frequency shift of the cantilever is used to detect short-range contact forces with the sample surface. The FM mode has been developed to a point where ultrahigh, atomic-scale resolution can be achieved in vacuum and even in liquid environments [129]. A high-resolution FM-AFM machine was used in this work to observe the atomic-scale surface structure of oxide crystal surfaces in a liquid electrolyte and to study the solvation structure near the solid surface [130, 131]. The frequency shift detected by FM-AFM can be due to the proximity of a surface, but in a liquid, the FM signal can be detected even when the tip is not close to a solid surface. Instead, the microscope can detect a local liquid density change near the liquid/solid interface [132], as shown in Fig. 2.9. The force exerted on the tip can be calculated from the measured frequency shift as reported by Sader *etal*. [133].

In this study, the surface structure of $SrTiO_3$ and the hydration structure on a $SrTiO_3$ surface were investigated by FM-AFM. The microscope was a modified Shimadzu SPM9600, modified with a low-noise optical deflection sensor at Onishi laboratory in Kobe University. In order to stabilize the power of laser diode (LD), the LD was modulated with ~1 GHz frequency.

The deflection noise was less than 20 fm/Hz$^{1/2}$. A schematic illustration of the FM-AFM equipment is shown in Fig. 2.10. An AFM cantilever is oscillating by the excitation from an automatic gain control (AGC). The frequency shift is detected by phase locked loop (PLL), and the signal is feedback to XYZ scanner to control the frequency shift of the cantilever. More detailed information is described in Ref.129. Si cantilevers (BudgetSensors; Tap300GD-G) with a nominal spring constant of 40 N/m were used in liquid environments. The resonant frequency was typically 130~150 kHz and the quality factor (Q) of resonance was ~10 in water. The oscillation amplitude was 0.1 to 0.2 nm.

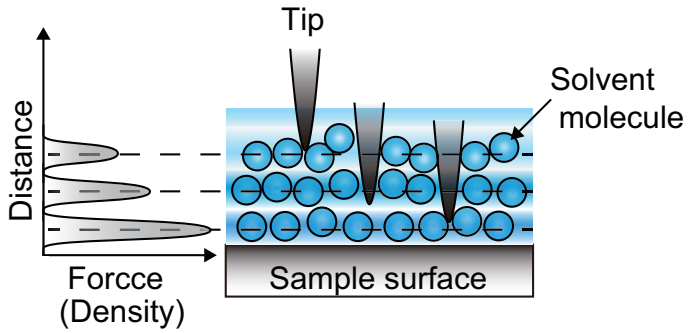

Figure 2.9: Schematic illustration showing the observation of solvation structure by FM-AFM. The force exerted on a tip reflects the information of density distribution of solvation molecules near a solid surface.

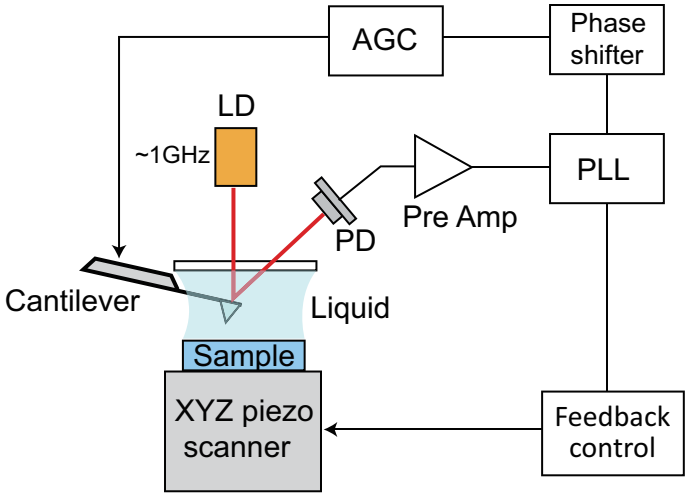

Figure 2.10: Schematic illustration of an FM-AFM equipment. LD: laser diode. PD: photodiode. AGC: automatic gain control. PLL: phase locked loop.

2.8 Optical absorbance measurement

The absorption spectra of thin film samples were measured with a Jasco V-570 UV-Vis-NIR spectrometer. The instrument can automatically switch between ultraviolet and visible-near-infrared light sources, conveniently measuring the whole optical response from the band gap absorption edge of the semiconductor samples to near infrared range. The absorbance is calculated by using the Lambert-Beer law:

$$\alpha = \frac{\log_{10}(I_0/I)}{l}, \tag{2.5}$$

where α is the measured absorption coefficient, I_0 and I are the intensities of the incident and transmitted light, and l is the film thickness. To avoid scattering, double-side-polished $SrTiO_3$ (001) substrates were used to fabricate samples for optical spectroscopy. Since the bandgaps of all films used in this work were lower than the nondoped $SrTiO_3$ substrates, fully epitaxial films, equivalent to the samples used in other characterization experiments, could be used. A bare annealed double-side-polished $SrTiO_3$ substrate was used as a reference for background correction.

The absorbance of powder samples cannot be measured in simple transmission geometry due to strong scattering. For powder samples, diffuse reflectance spectroscopy (DRS) was used instead. This method is based on the equation:

$$\%A + \%T + \%R = 100, \tag{2.6}$$

where %A is the absorbance, %T is the transmittance, and %R is the reflectance of the sample. For a completely opaque sample, %T is zero and %A can therefore be directly calculated by measuring %R. As shown in a schematic illustration in Fig. 2.11 diffuse reflectance spectroscopy is based on measuring the intensity of light diffusely scattered from the sample surface within a half-sphere solid angle. The specular reflection is ignored in DRS. The diffuse reflection intensity is collected with an integrating sphere and the absorbance is calculated from the Kubelka-Munk equation:

$$f(R_\infty) = \frac{(1-R_\infty)^2}{2R_\infty} = \frac{k}{s}, \tag{2.7}$$

where $f(R_\infty)$ is the Kubelka-Munk function and $R_\infty = R_{sample}/R_{standard}$ [134, 135]. The s and k parameters are the Kubelka-Munk scattering and absorption coefficients. The sample thickness is assumed to be infinite and can be ignored. Reflectance at a given wavelength is a function of the k/s ratio rather than of the absolute values of k and s. The k and s values cannot therefore be determined independently from Eq. 2.11. $BaSO_4$ was used as a standard material in the RDS measurements, since it is known to have negligible absorbance in the measurement range.

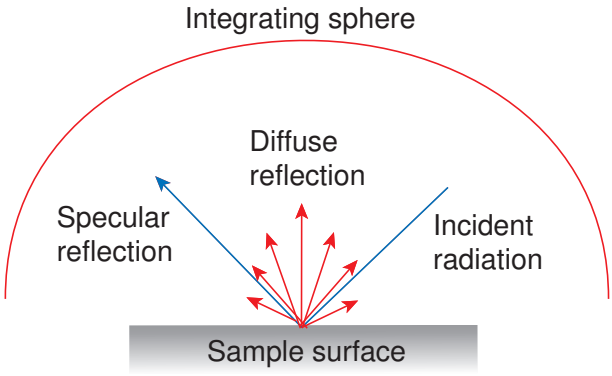

Figure 2.11: Schematic of diffuse reflectance spectroscopy (DRS).

2.9 Photoelectrochemical measurement

The photoelectrochemical response of the photocatalyst samples was analyzed by a combination of cyclic voltammetry (CV), chronoamperometry (CA), and Mott-Schottky analysis using Hokuto Denko HZ-5000 and Bio-Logic SP-150 potentiostats. A self-made photoelectrochemical cell was used for thin film measurements (Fig. 2.12). Polytetrafluoroethylene (PTFE) was used as the cell material due to its good chemical stability since the cell needs to operate with either acidic or alkaline electrolytes. The measurements were done in a standard three-electrode configuration with a Pt (99.98%, Nilaco) counter electrode and a Ag/AgCl sat. KCl (TOA DKK; HS-205C, or eDAQ; ET072) reference electrode. The aqueous electrolyte solutions were bubbled with pure N_2 gas for at least 30 min to remove dissolved O_2 before each measurement run. The electrochemical cell was filled with the oxygen-free solution flowing through PTFE tubing connected with the bubbling cell. An external nitrogen gas supply was used to pressurize the system and drive the liquid circulation in the cell.

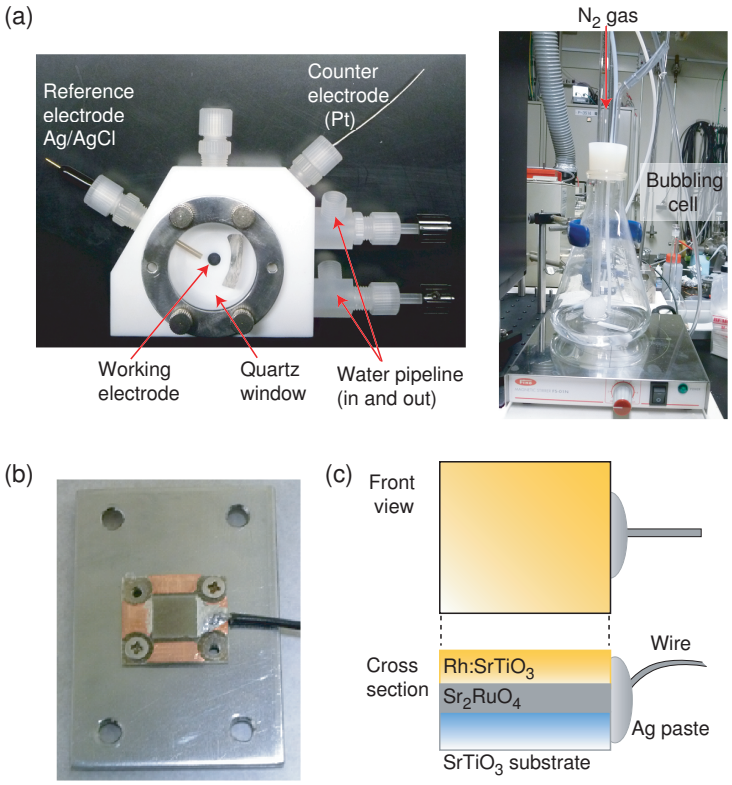

Figure 2.12: Photoelectrochemical measurement setup: (a) photoelectrochemical cell with a bubbling cell, (b) sample holder, (c) schematic of a $Rh:SrTiO_3/Sr_2RuO_4/SrTiO_3$ sample. Silver paste was used to attach a working electrode lead to the Sr_2RuO_4 layer to complete the necessary electric circuit for the potentiostat.

The potentiostat requires an Ohmic contact to the sample. Since most Rh:$SrTiO_3$ and Ir:$SrTiO_3$ films are nearly insulating, the films were grown either on conducting Nb:$SrTiO_3$ substrates or on a metallic electrode layer. Epitaxial Sr_2RuO_4 films were used as the electrode layer for Rh:$SrTiO_3$ films since it can be grown epitaxially on $SrTiO_3$ and it is stale to the highest temperatures used for the photocatalyst film growth ($\approx$ 1100°C). The heterostructure sample design is illustrated in Fig. 2.12(c). Conducting Nb(0.05wt%):$SrTiO_3$(001) substrates were used as a back electrode for the Ir:$SrTiO_3$ films. Silver paste (Fujikurakasei; D-550) was used for making Ohmic contacts between $SrRuO_3$ the external wiring. An InGa alloy (In (Nilaco; 4N) 1 g and Ga (Nilaco; 6N) 3 g, alloyed at 50°C) was used for the Nb:$SrTiO_3$ contacts.

Mott-Schottky analysis was used for determining the flat-band potential and the carrier concentration of the photocatalyst films. The sample capacitance is given by

$$\frac{1}{C^2} = \frac{2}{e\epsilon_0\epsilon_{SC}N_D}(U - U_{fb} - \frac{kT}{e}), \tag{2.8}$$

where C, U, and U_{fb} are the differential capacitance formed in the semiconductor at the semiconductor/water interface, electrode potential, and flat-band potential, respectively. The constants e, ϵ_0, ϵ_{SC}, N_D, k, and T are the elementary charge $e = 1.60217 \times 10^{-19}$ C, vacuum permittivity $\epsilon_0 = 8.85418 \times 10^{-12}$ F/m, relative permittivity of the semiconductor, carrier density, the Boltzmann constant $k = 1.38065 \times 10^{-23}$, and the temperature, respectively. This equation is only applicable when the semiconductor surface is atomically flat and the carrier concentration is homogeneous in the depth direction [136].

The incident photon to current efficiency (IPCE) and absorbed photon to current efficiency (APCE) were evaluated from:

$$\begin{aligned} IPCE(\%) &= \frac{[Numberofphotocarriersusedforelectrochemicalreaction(1/cm^2)]}{[Incidentphotonflux(1/cm^2)]} \times 100(\%) \\ &= \frac{hc}{e}\frac{[Photocurrentdensity(mA/cm^2)]}{[Wavelength(nm)] \times [Lightintensity(mW/cm^2)]} \times 100(\%), \end{aligned} \tag{2.9}$$

$$\begin{aligned} APCE(\%) &= \frac{[Numberofphotocarriersusedforelectrochemicalreaction(1/cm^2)]}{[Absorbedphotonflux(1/cm^2)]} \times 100(\%) \\ &= \frac{hc}{e}\frac{[Photocurrentdensity(mA/cm^2)]}{[Wavelength(nm)] \times [Lightintensity(mW/cm^2)] \times [1 - 10^{-\alpha d}]} \times 100(\%), \end{aligned} \tag{2.10}$$

where h, c, and e are the Planck constant, the speed of light, and the elementary charge, respectively, and $hc/e = 1240$. α and d are light absorption coefficient and film thickness of the sample. A 100 W Xe-lamp (Asahi Spectra; LAX-101 or LAX-102) with band-pass filters and a 1 kW Xe-lamp (Ushio Lighting; UXL-1000D) with a double monochromator were used as light sources for measuring the wavelength-dependent quantum efficiencies. The number of incident photons was calculated from the average optical power density measured with calibrated power meters (OPHIRA; PD300-UV or THORLABS; S120VC).

Chapter 3

Mechanism of photo-induced superhydrophilicity

In this chapter, I describe the studies of the water and oxide photocatalyst interfaces. The Water / photocatalyst interface is of crucial importance for understanding the dynamics of photocatalytic reactions and photo-induced superhydrophilicity. Water stability of semiconductor photocatalysts is another important aspect because it is one of the basic requirements for practical use of a photocatalytic solar energy converter with long-term operational stability. However, most photocatalysts, even oxides, are not stable and corrode in water under light irradiation. Atomic-scale investigation of the water / photocatalyst interface is thus necessary to understand and overcome the water stability issues. This study focused on the clarification of the mechanism of photo-induced superhydrophilicity of oxide photocatalysts. Two competing hypotheses have been proposed; the "surface reconstruction model" and the "contamination model".

Here, ($\sqrt{13}\times\sqrt{13}$)-R33.7° $SrTiO_3$ (001) surface was studied in detail because the titanium-rich surface associated with this particular surface reconstruction was found to be stable in water. The surface structure and the hydration structure that forms on the ($\sqrt{13}\times\sqrt{13}$)-$SrTiO_3$ (001) surface were investigated by RHEED and AFM. The hydration structure was also simulated by DFT-MD and classical-MD calculations, which supported the experimental observation that the ($\sqrt{13}\times\sqrt{13}$)-$SrTiO_3$ (001) surface is stable in water and has low levels of dissociative adsorption of water molecules. Even such a stable surface showed superhydrophilicity if the surface is cleaned of contamination. The intrinsic superhydrophilicity was also confirmed on several other oxide surfaces, TiO_2, Al_2O_3, $NdGaO_3$, and LSAT. Based on a physical model of the contact angle of a water droplet on a solid surface, ionic surfaces having large surface energy (> 200 mJ/m^2) should be intrinsically superhydrophilic. Since oxide surfaces have large surface energies, it is natural that the clean surfaces are intrinsically superhydrophilic. The fact that TiO_2 and $SrTiO_3$ surfaces showed superhydrophilicity just by removing the surface contamination suggests that

the "contamination model" gives a more appropriate description of the superhydrophilicity phenomenon on oxide photocatalyst surfaces than the "surface reconstruction" model. Along with previous related reports, I discussed the mechanism of photo-induced superhydrophilicity.

3.1 Introduction

Understanding the behavior of the water / photocatalyst interface under light illumination is necessary to clarify the dynamics of photocatalytic reactions. The water / photocatalyst interface is important as it is the reaction field where water splitting occurs. The reaction dynamics have been studied extensively by various surface-sensitive analysis techniques using scanning probe microscopes and spectroscopic tools, along with theoretical simulations [100]. The stability of photocatalysts against photo-corrosion is one important subject and also one of the minimum requirements for obtaining long-term operational stability of photoelectrochemical systems. Photo-corrosion has been recognized as a severe problem in most semiconductors, particularly in non-oxides [31]. Even oxide semiconductors like ZnO and TiO_2 show photo-corrosion in water under light irradiation [44, 137, 138]. The management of photocatalyst surface stability against photo-corrosion is thus one of the topics studied in the research field of photoelectrochemical solar water splitting [45]. The water interface has also attracted considerable attention due to applications in antifogging and antifouling materials since the original discovery of photo-induced superhydrophilicity of TiO_2 photocatalysts in 1997 [38].

This study focused on the clarification of the mechanism of photo-induced superhydrophilicity. Photo-induced superhydrophilicity is a phenomenon where the hydrophilicity of a surface increases and the water contact angle decreases to nearly 0° by light irradiation. The effect is often observed on oxide photocatalyst surfaces and has been known since the original discovery on a TiO_2 surface [38]. However, the mechanism of photo-induced superhydrophilicity has not been completely understood yet. Two competing hypotheses have been proposed; one is the "surface reconstruction model", which explains the strong hydrophilicity by the appearance of a surface reconstruction that includes surface hydroxyl groups and oxygen vacancies that are induced by a reaction with water under light [39]. The other is a "contamination model", which considers photocatalytic oxidative decomposition of organic contaminants on a surface as the dominant mechanism for photo-induced superhydrophilicity, since the hydrophilicity of most oxide surfaces should be intrinsically very high due to the large surface energy [40, 41]. The difficulty of in-situ experimental observation of surface atomic configurations at the water/oxide interface prevents direct proof of either hypothesis. However, several studies of TiO_2 single crystals as a model photocatalyst have revealed no clear photo-induced changes in surface hydroxyl groups in vibrational spectra [40, 41, 139–142], in ambient pressure XPS measurements [141], and in TPD spectra [143], whereas a lower density of organic contaminants has been shown to result in a faster appearance of photo-induced superhydrophilicity [41]. It is known that the presence

of O_2 is essential for photo-induced hydrophilicity change to occur and oxygen has been recognized as being essential for photocatalytic oxidation of organic contaminants [40, 41]. The contamination model therefore has stronger support than the surface reconstruction model. A combined model has also been proposed [144]. The model combines the surface reconstruction model and the contamination model in a way that explains the appearance of photo-induced superhydrophilicity in two phases. In the first phase, hydrophilicity is increased to a certain level with a water contact angle $\sim 10^\circ$ by removing organic contamination. The process is driven by photocatalytic oxidation of organic contaminants. Subsequently, a UV-light-induced surface reconstruction forms and produces a metastable superhydrophilic surface state. In fact, two different time constants of the transition of water contact angle under light irradiation have been reported [145]. However, there is another fundamental difficulty in clarifying the true mechanism. Since light irradiation induces both photocatalytic decomposition of organic contaminants [146] and the formation of oxygen vacancies on the TiO_2 surface [44, 147], it is almost impossible to distinguish between the two influences. The removal of surface contamination and surface roughening generally occur at the same time, which makes it particularly difficult to elucidate the true mechanism of photo-induced superhydrophilicity. One possible and plausible way to clarify the true mechanism of the emergence of superhydrophilicity is to investigate the intrinsic hydrophilicity of oxide surfaces that have been cleaned of surface contamination. If the intrinsic surface is superhydrophilic, the mechanism can be totally explained by the contamination model, and if not, the surface reconstruction model is supported. Still, there is no comprehensive study of intrinsic hydrophilicity of oxide surfaces, which would be needed to determine the true mechanism of superhydrophilicity. In this work, the intrinsic hydrophilicity of oxide surfaces was investigated and the mechanism of superhydrophilicity is discussed. The results support the contamination model.

3.2 Stability of the ($\sqrt{13} \times \sqrt{13}$)-R33.7° $SrTiO_3$ (001) surface

Here, I propose the use of the reconstructed ($\sqrt{13} \times \sqrt{13}$)-R33.7° $SrTiO_3$ (001) surface as an ideal surface to study the intrinsic hydrophilicity of Ti-oxide surfaces. This surface was found to have an atomic structure stable even in water, where water molecularly adsorbs without chemical reactions. It is thus suitable for investigating the water/oxide interface on an atomic scale.

Various types of reconstructions have been reported to form on $SrTiO_3$(001) surfaces [148–150]. Among the large variety of surface reconstructions, ($\sqrt{13} \times \sqrt{13}$)-R33.7° (hereafter referred to as ($\sqrt{13} \times \sqrt{13}$) is one of the most stable atomic structures on $SrTiO_3$(001). This surface has an excess TiO_x layer on top of TiO_2-terminated $SrTiO_3$(001) [151]. M. Naitoh *etal*. reported that ($\sqrt{13} \times \sqrt{13}$) can be obtained by furnace annealing in an oxygen atmosphere, indicating that the surface structure is stable in air [152]. This is unusual, since most reconstructed surface structures deteriorate when exposed to air. The lattice constant of the ($\sqrt{13} \times \sqrt{13}$) reconstructed surface is 1.408 nm and the structure is shown in Fig. 3.1, following the model reported in Ref. 151.

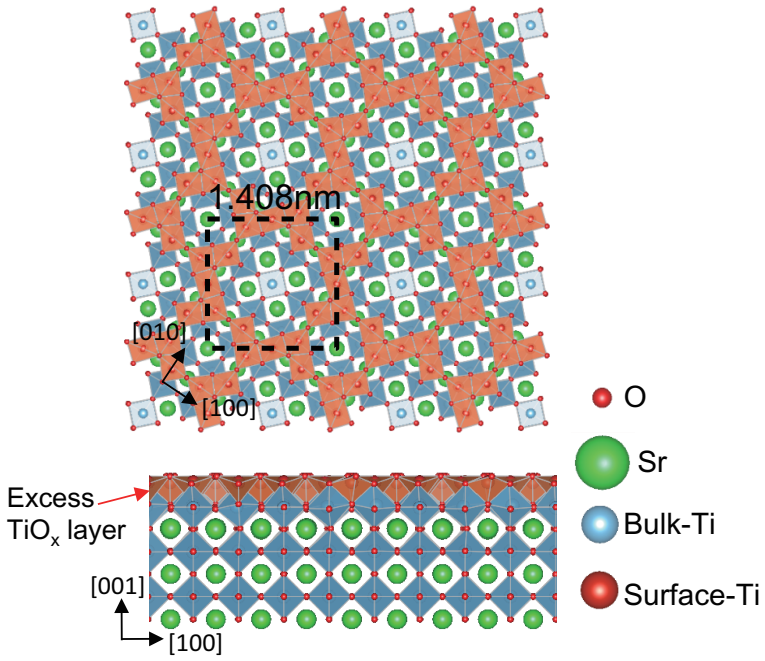

Figure 3.1: Plan-view and cross-sectional structure of the ($\sqrt{13} \times \sqrt{13}$) reconstructed surface. Oxygen, Sr, bulk-Ti, and surface-Ti are represented by red, green, blue, and orange spheres, respectively.

The ($\sqrt{13} \times \sqrt{13}$) reconstructed surface was reproducibly fabricated by a programed annealing procedure illustrated in Fig. 3.2(a). The temperature program was adapted from a report by

R. Shimizu *etal*. [153]. In this process, a $SrTiO_3$ (001) substrate (Shinkosha) was firstly annealed at 500°C under an oxygen pressure of 10^{-5} Torr for 10 min to remove the carbon contamination from the surface. The crystal was then annealed at 850°C for 30 min to stabilize the ($\sqrt{13} \times \sqrt{13}$) reconstructed structure, and subsequently heated to 1000°C for 3 min to sharpen the step-and-terrace surface morphology. After the brief high-temperature phase, a finally anneal at 850°C for 10 min was used to stabilize the ($\sqrt{13} \times \sqrt{13}$) reconstructed structure. The sample heating and cooling rates were 50°C/min. The presence of the ($\sqrt{13} \times \sqrt{13}$) reconstruction was confirmed after the annealing procedure by RHEED (Fig. 3.2(b)). The RHEED pattern was consistent with previous reports [152, 153]. AFM showed a clear step-and-terrace surface morphology where the step height was ~ 4 Å, corresponding to the lattice constant of $SrTiO_3$ (Fig. 3.2(d)). RHEED images were observed after immersing the sample in water for a few minutes and re-loading the crystal back into the vacuum chamber. Although the RHEED intensity became weaker after water and air exposure, the characteristic RHEED pattern of the ($\sqrt{13} \times \sqrt{13}$) surface still remained visible, even after water exposure (Fig. 3.2(c)), indicating that the surface atomic order of the ($\sqrt{13} \times \sqrt{13}$) reconstruction is stable against water exposure. The reason for the intensity drop of RHEED intensity was surface contamination. Small unidentified particles were often observed on the surface when the crystals were studied in water by FM-AFM (Fig. 3.2(e)), though such particles were never observed on as-prepared samples in air. The step-and-terrace structure was also stable in water.

As suggested by RHEED, the atomic structure of ($\sqrt{13} \times \sqrt{13}$) remained intact even in water and this was confirmed by FM-AFM. The sample surface and the AFM cantilever were immersed in a 50 mM KCl aqueous solution for the FM-AFM measurements. Fig. 3.3 shows a topographic FM-AFM image of the ($\sqrt{13} \times \sqrt{13}$) reconstructed surface. The atomic structure was not clear in a raw topographic image (Fig. 3.3(a)), but four-fold symmetric spots with 1.4 nm periodicity were visible in the 2-dimensional Fourier-transformed image (Fig. 3.3(b)). Fig. 3.3(c) is the filtered image restored by an inverse Fourier transform of (d). The 1.4 nm periodicity was clearly observed and the lattice direction was 33.7° rotated from the $SrTiO_3$[100] direction, consistent with the expected ($\sqrt{13} \times \sqrt{13}$)-R33.7° structure. Therefore, the atomic structure of ($\sqrt{13} \times \sqrt{13}$) reconstructed $SrTiO_3$ (001) surface is stable even in water, as confirmed by RHEED and AFM observations.

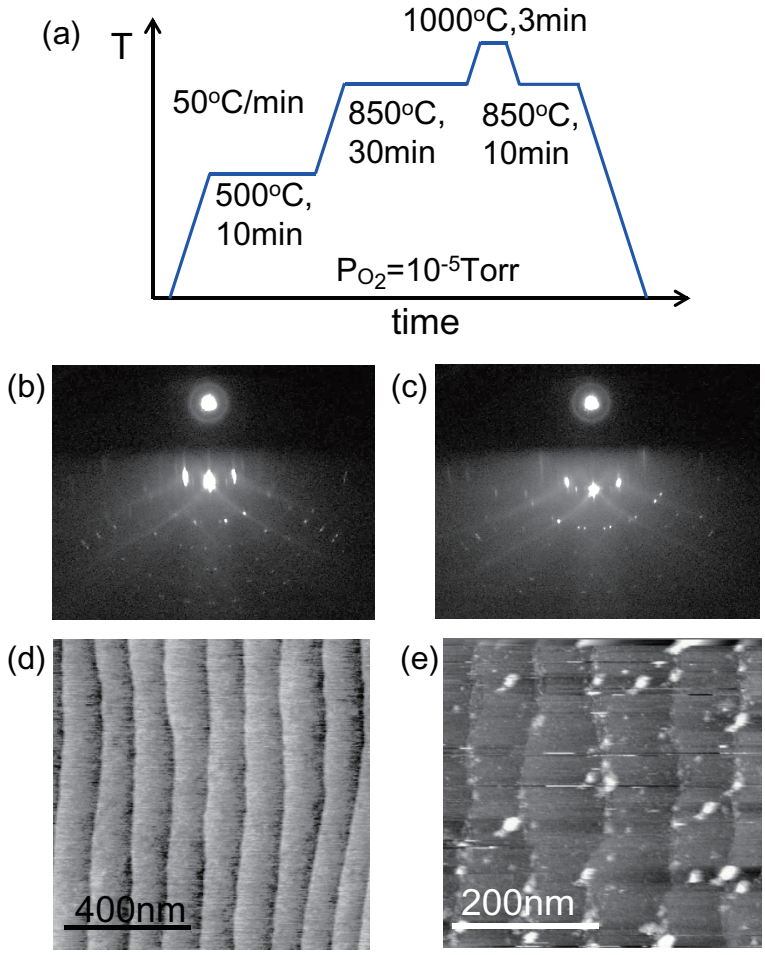

Figure 3.2: (a) Annealing procedure of a $SrTiO_3$ (001) substrate for preparing a reconstructed ($\sqrt{13} \times \sqrt{13}$) surface. RHEED patterns of the ($\sqrt{13} \times \sqrt{13}$) reconstructed surface (b) before and (c) after water exposure. AFM images of the ($\sqrt{13} \times \sqrt{13}$) reconstructed surface measured (d) in the atmosphere and (e) in water. (d) was measured in air with dynamic mode AFM. (e) was measured in a 50 mM KCl aqueous solution with FM-AFM (Δf = 130 Hz).

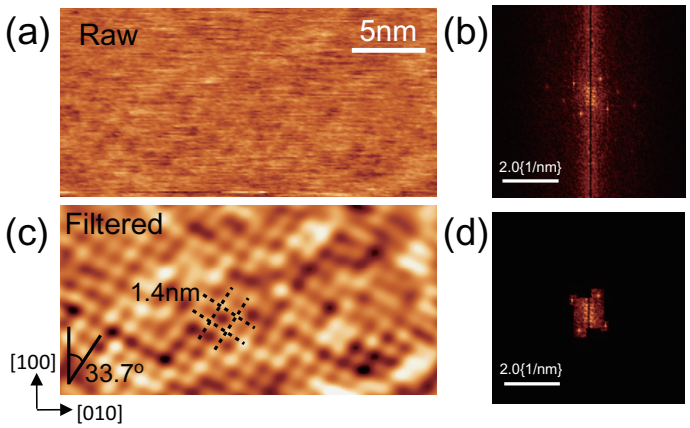

Figure 3.3: (a) FM-AFM topography of ($\sqrt{13} \times \sqrt{13}$) surface observed in a 50 mM KCl aqueous solution. The cantilever oscillation amplitude and the frequency shift were 0.2 nm and +150 Hz, respectively. (b) 2-dimensional Fourier-transformed image of (a). (c) An image of (a) after a procedure of 2-dimensional Fourier filtering and the corresponding Fourier-transformed image (d).

The relationship between macroscopic hydrophilicity and the microscopic hydration structure is of great scientific interest. Here, the hydration structure on the ($\sqrt{13} \times \sqrt{13}$)-$SrTiO_3$ (001) surface was investigated by FM-AFM and supported by theoretical simulations. FM-AFM has recently been developed for visualizing the solvation structure on an atomic scale [131]. The resonance frequency shift (Δf) of a cantilever in FM-AFM, which is often observed at liquid/solid interfaces, reflects the density distribution of solvent molecules [132]. The hydration structure was observed on the ($\sqrt{13} \times \sqrt{13}$)-$SrTiO_3$ (001) surface. Fig. 3.4(a) shows a Δf map obtained by measuring the variation of the cantilever frequency shift as a function of the distance from the surface and the lateral position. The measurement was done on a ($\sqrt{13} \times \sqrt{13}$)-$SrTiO_3$(001) surface in a 50 mM KCl aqueous solution. The KCl solution was prepared by dissolving KCl (Nakarai, 99.5 %) in Millipore purified water. The KCl solution was needed to minimize the electric double layer force, which may otherwise dominate over force modulations caused by the hydration structure. Fig. 3.4(b) shows an averaged force-distance curve and the corresponding Δf-distance curve. Force oscillations were observed near the $SrTiO_3$ surface. Force minima were observed at ~ 0.2 and ~ 0.5 nm from the surface. The oscillation period is in good agreement with the expected thickness of a water molecule layer (0.2 ~ 0.4 nm) [131]. This is the first 3-dimensional hydration structure observation on a $SrTiO_3$ surface so far.

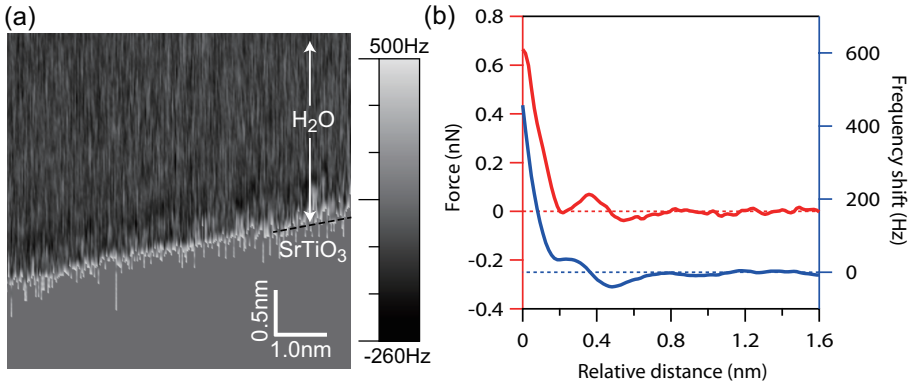

Figure 3.4: (a) FM-AFM Δf distribution observed in a xz scan above the ($\sqrt{13} \times \sqrt{13}$)-$SrTiO_3$(001) surface in a 50 mM KCl aqueous solution. (b) Averaged force-distance and the corresponding Δf-distance curves. The cantilever oscillation amplitude was 0.1 nm.

It should be noted that the surface hydrophilicity of ($\sqrt{13} \times \sqrt{13}$)-$SrTiO_3$ (001) varied strongly between samples. The water contact angle on the $SrTiO_3$ surfaces was clearly different. In addition, when the surface showed strong hydrophilicity (some $SrTiO_3$ samples showed superhydrophilicity without UV-light irradiation), the contrast of the hydration structure was sharp, as in Fig. 3.4, whereas when the surface was weakly hydrophilic, the contrast of the hydration structure was weak, as shown in Fig. 3.5(a). The force curve in Fig. 3.5(c), taken by integrating

over the area shown in (a), decreased monotonically as a function of distance from the $SrTiO_3$ surface and no clear force modulation was observed. This indicates that the hydration structure was weak. The weak hydrophilicity and the weak hydration structure might be caused by surface contamination, as discussed later.

It was found that UV light irradiation changes the hydration structure on a $SrTiO_3$ surface. There are two possible reasons why UV light irradiation might affect the hydration structure. One would be a surface reconstruction that may be induced by UV-light irradiation and the other would be the removal of surface contamination. But, according to the analysis of hydrophilicity discuss later, I conclude that the effect of surface contamination was dominant. The UV light irradiation induces decomposition of contaminants on the $SrTiO_3$ surface by photocatalytic oxidation reactions. The contrast of the hydration structure became sharper after UV light irradiation (λ = 365 ± 5 nm, 60 mW/cm^2, 30 min) from a LED lamp (ASAHI SPECTRA, POT-365). Fig. 3.5(b) shows the Δf distribution observed on the same sample surface as (a) after UV irradiation. The difference in the hydration structures before and after UV irradiation is clearly visible in the Δf distribution. Averaged force-distance curves calculated from the Δf distribution in the range marked with red dotted lines in Fig. 3.5(a) and (b) are shown in (c) and (d), respectively. Several Δf-distance curves are displayed in Fig. 3.6. After UV light irradiation, the sample surface became superhydrophilic, i.e., the surfaces showed photo-induced superhydrophilicity, and clear oscillatory force modulations were observed near the surface with a $\sim$ 0.4 nm period. The fact that the contrast of the hydration structure became sharper after UV light irradiation indicated that the interaction between $SrTiO_3$ and water became stronger after UV exposure.

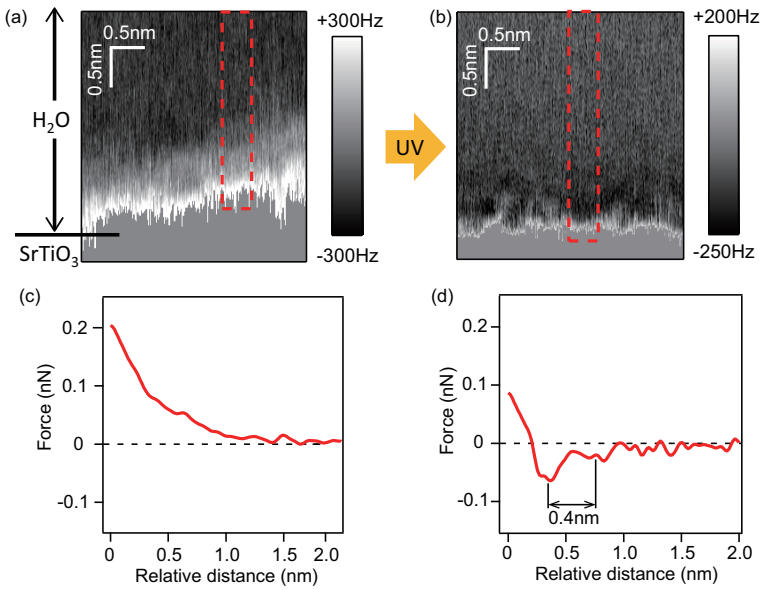

Figure 3.5: (a) FM-AFM Δf distribution observed in a zx cross-sectional scan on a weakly hydrophilic ($\sqrt{13}\times\sqrt{13}$)-$SrTiO_3$(001) surface in a 50 mM KCl aqueous solution. (b) Δf distribution observed on the same sample as in (a) after UV light irradiation. (c) and (d) Averaged force-distance curves calculated from the Δf-distance curves in the region marked with red dotted lines in (a) and in (b), respectively.

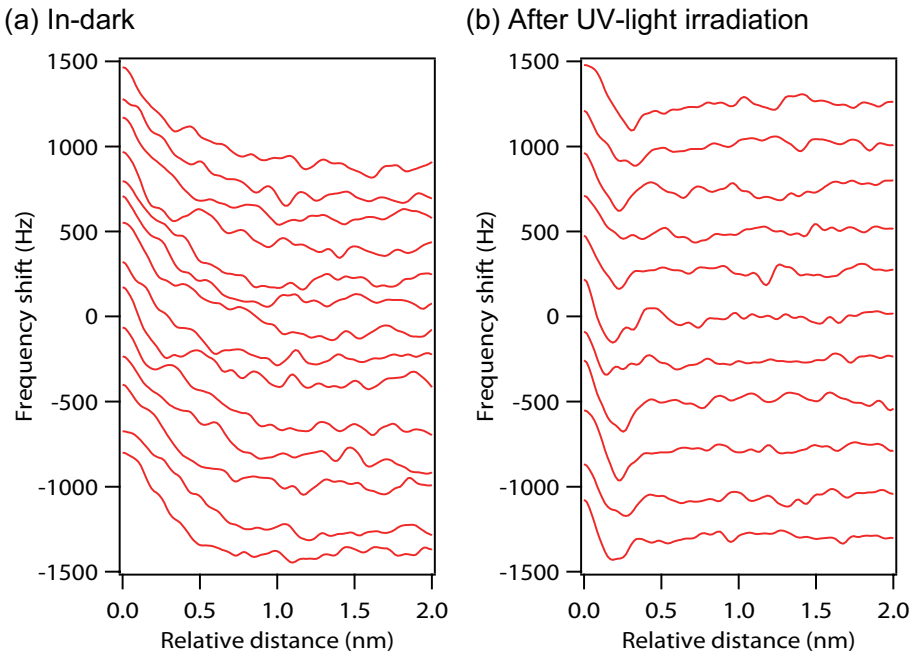

Figure 3.6: Several Δf-distance curves observed on a ($\sqrt{13} \times \sqrt{13}$)-$SrTiO_3$(001) surface (a) in dark and (b) after UV light irradiation. The data were taken from the Δf distribution mapping in Figs. 3.5(a) and (b).

The hydration structure on $SrTiO_3$ was simulated by DFT-MD and classical-MD. The DFT-MD and MD simulations were done with the CP2K [154] and LAMMPS [155, 156] codes, respectively.

In classical-MD simulations, pair potentials for each atomic pair are assumed empirically. The parameters used in the simulations are summarized in Fig. 3.7. The parameters for the interactions in bulk $SrTiO_3$ and the interface between $SrTiO_3$ and H_2O were obtained from Ref. 157. The ionic charges of Sr, Ti, and O was modified slightly to neutralize the $(\sqrt{13} \times \sqrt{13})$-$SrTiO_3(001)$ slab model. The TIP3P model [158] was adopted for the interaction in bulk H_2O. This is one of the 3-site models commonly used for MD simulations. The O-H bond distance and the H-O-H bond angle of a H_2O molecule are 0.9572 Å and 104.52° in the TIP3P model, which exactly reproduces the actual experimental values of 0.9572 Å and 104.52°, respectively. For each atomic pair, a pair potential includes coulomb and van der Waals interactions. In these simulations, the van der Waals interaction between cations were not taken into account. The van der Waals interactions in the bulk of $SrTiO_3$ were approximated with the Buckingham potential $U(r) = A\exp(-r/r) - B/r^6$ and the ones between $SrTiO_3$ and water were described by a Lennard-Jones potential $U(r) = 4\epsilon[(\sigma/r)^{12} - (\sigma/r)^6]$.

Fig. 3.8 shows snapshots of a unit cell of the water and $(\sqrt{13} \times \sqrt{13})$-$SrTiO_3(100)$ interface, simulated by DFT-MD and classical-MD. In the DFT-MD simulation, the unit cell was constructed with a $(\sqrt{13} \times \sqrt{13})$-terminated $SrTiO_3$ slab with $\sim$ 1 nm thickness and $\sim$ 1 nm bulk water between two slabs. In the classical-MD simulation, the unit cell was constructed with a $(\sqrt{13} \times \sqrt{13})$-terminated $SrTiO_3$ slab with $\sim$ 3 nm thickness and $\sim$ 14 nm bulk water between two slabs. In both simulations, the unit cells were connected assuming 3-dimensional periodic boundary conditions. The DFT-MD simulation was run for 5 ps with a time step of 0.5 fs in an NVT ensemble at 300 K. PBE-D3 was used for exchange and correlation functions. On the other hand, the classical-MD simulation was run for 0.5 ns with a time step 1 fs in an NPT ensemble at 310 K under 0 atm.

It was found by DFT-MD simulations that water molecules molecularly adsorb on a $(\sqrt{13} \times \sqrt{13})$-$SrTiO_3$ surface. Although water dissociation was observed on TiO_2-terminated and SrO-terminated $SrTiO_3(001)$ surfaces, the dissociation rate was much lower on the $(\sqrt{13} \times \sqrt{13})$ surface, consistent with the high chemical stability of the $(\sqrt{13} \times \sqrt{13})$ structure. The results are consistent with the experimental results that the surface atomic structure is stable even in water, as confirmed by RHEED and AFM. The stability was also confirmed by classical-MD simulations. The atomic structure of $(\sqrt{13} \times \sqrt{13})$ remained intact through the 0.5 ns simulation, as shown in Fig. 3.9. The $(\sqrt{13} \times \sqrt{13})$ structure after 0.5 ns relaxation was nearly identical to the ideal structure, though the surface TiO_x layer had a small displacement.

(a)

Atom	Mass (amu)	Charge (e)
Sr	87.6210	1.760
Ti	47.8671	2.400
O	15.9994	-1.350
O_W	15.9994	-0.834
H_W	1.0080	0.417

(b)

Atomic pair	A (kcal/mol)	ρ (Å)	C (Å^6 kcal/mol)	ε (Å^{12} kJ/mol)	σ (Å^9 kJ/mol)
Sr-Sr	-	-	-	-	-
Sr-Ti	130687.880	0.29	124.43871	-	-
Sr-O	50629.837	0.30	599.26435	-	-
Ti-O	158710.470	0.22	207.31824	-	-
Ti-Ti	-	-	-	-	-
O-O	40305.7230	0.30	1248.92520	-	-
Sr-O_W	-	-	-	0.00500	4.35000
Ti-O_W	-	-	-	0.00500	3.47500
O-O_W	-	-	-	1.23671	2.98543
Sr-H_W	-	-	-	-	-
Ti-H_W	-	-	-	-	-
O-H_W	-	-	-	0.010000	2.600000
O_W-O_W	-	-	-	0.152100	3.150574
O_W-H_W	-	-	-	0.083646	1.775294
H_W-H_W	-	-	-	0.046000	0.400014

Figure 3.7: (a) Atomic mass and charge of each atom. (b) Parameters used for describing each pair potential between two atoms for Sr, Ti , and O of a $SrTiO_3$ slab and H (H_w and O_w of water. Buckingham potential $U(r) = A\exp(-r/r) - B/r^6$, Lennard-Jones potential $U(r) = 4\epsilon[(\sigma/r)^{12} - (\sigma/r)^6]$).

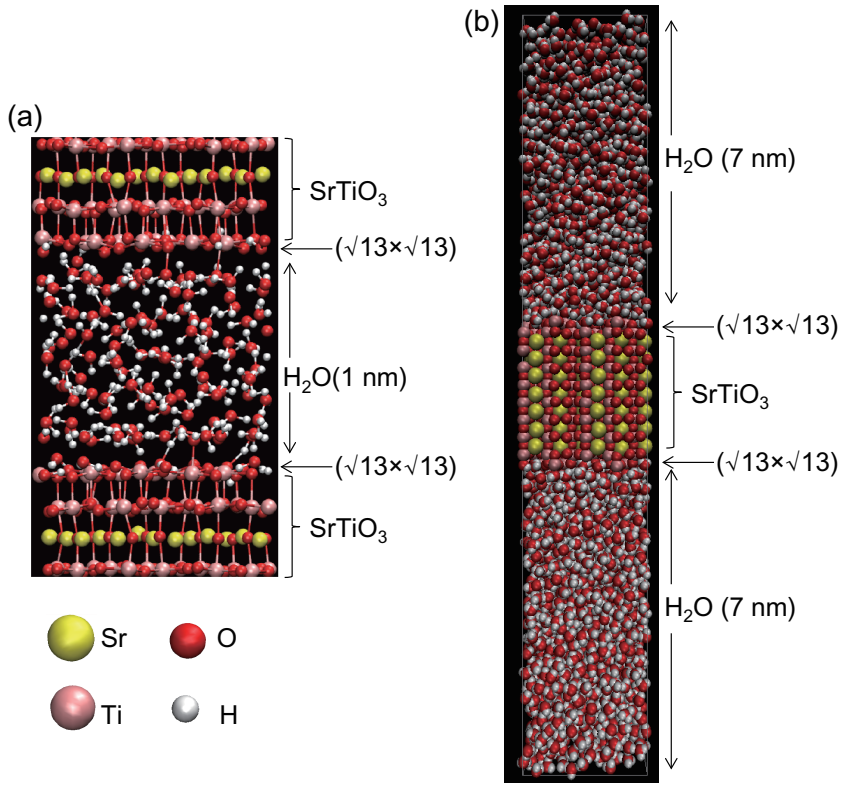

Figure 3.8: Snapshots of a unit cell of water and ($\sqrt{13} \times \sqrt{13}$)-$SrTiO_3$(100) interface simulated by (a) DFT-MD and (b) classical-MD. Yellow, pink, red, and white balls are Sr,Ti, O, and H, respectively.

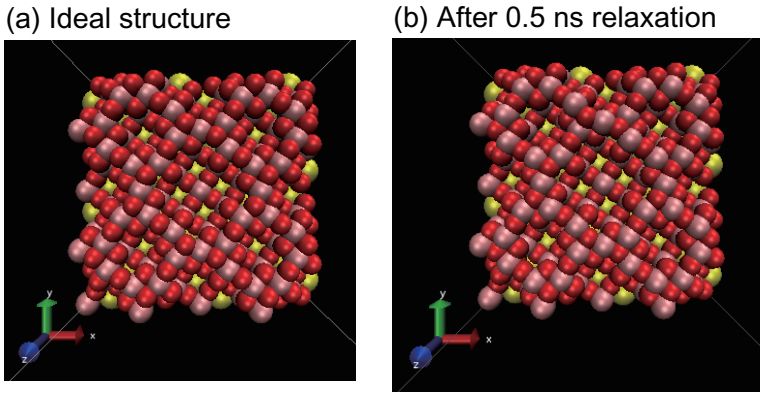

Figure 3.9: Snapshots of (a) an ideal ($\sqrt{13} \times \sqrt{13}$)-terminated $SrTiO_3$(001) surface without relaxation and (b) ($\sqrt{13} \times \sqrt{13}$) surface in a simulation of the water interface after a 0.5 ns simulation. Water molecules are removed in (b) to see the surface structure.

Fig. 3.10 shows the time-averaged particle density profiles of Sr, Ti, and O of $SrTiO_3$ and hydrogen (H_w) and oxygen (O_w) of H_2O at water/($\sqrt{13} \times \sqrt{13}$)-$SrTiO_3$(100) interface, together with water density profiles, simulated by DFT-MD and classical-MD simulations. Although the classical-MD simulation excluded dissociation, the water density profiles of both simulations were quite similar. This suggests that water molecules adsorb on ($\sqrt{13} \times \sqrt{13}$)-$SrTiO_3$(100) without dissociation. In both simulations, two water layers were observed with a 0.26 nm spacing. The distance was consistent with the hydration layer distance observed by FM-AFM. It should be noted that the $SrTiO_3$ surface was always superhydrophilic, independent of the volume of water in both DFT-MD and classical-MD simulations, which indicates that the $SrTiO_3$ surface is intrinsically superhydrophilic. Still, the effects of UV light irradiation and surface contamination on the hydration structure have not been investigated so far.

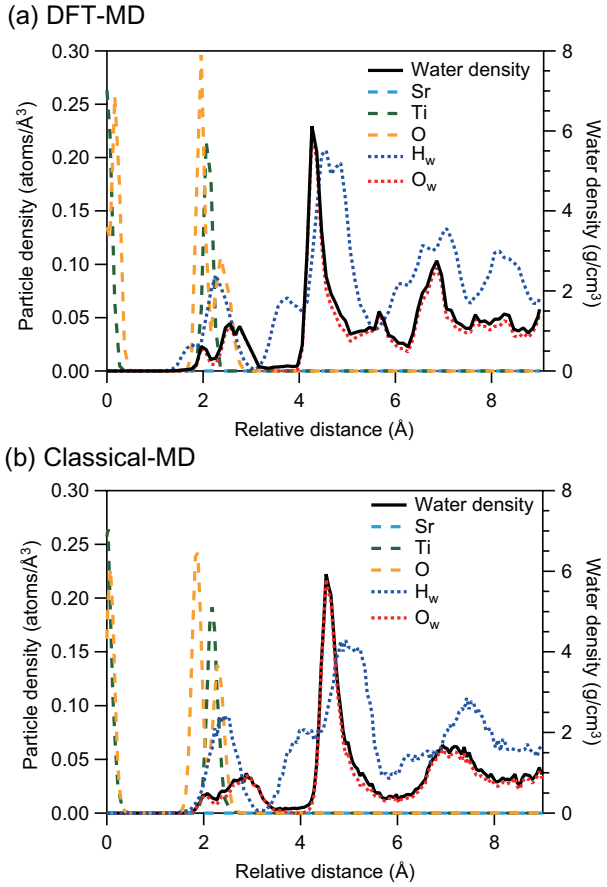

Figure 3.10: Time-averaged particle density profiles of Sr, Ti, and O of $SrTiO_3$ and hydrogen (H_w) and oxygen (O_w) of H_2O at water/($\sqrt{13} \times \sqrt{13}$)-$SrTiO_3$(100) interface, together with water density profiles, simulated by (a) DFT-MD and (b) classical MD.

3.3 Intrinsic superhydrophilicity of oxide surfaces

To understand the changes that occur at the water / photocatalyst interface under light illumination and to determine the mechanism of photo-induced superhydrophilicity, it is indispensable to measure the intrinsic hydrophilicity of photocatalyst surfaces, especially for Ti-oxide surfaces. Based on the experimental RHEED and AFM results, and the theoretical MD simulations, the atomic structure of the ($\sqrt{13} \times \sqrt{13}$)-$SrTiO_3$ surface was found to be quite stable, even in water. In this study, ($\sqrt{13} \times \sqrt{13}$)-$SrTiO_3$ surface was therefore selected as a model photocatalyst surface to investigate the water/Ti-oxide interface.

Measuring the intrinsic hydrophilicity of a solid surface is difficult because surface wettability is determined by the water contact angle. An ideal clean surface, however, is usually prepared in a vacuum chamber without air or water exposure. This complication led to a long-standing controversy over the intrinsic hydrophilicity of Au surface until 1980 or even later [159]. Since the water contact angle is often measured in atmosphere, the water contact angle was not reproducible among experimenters because the Au surface in such a measurement is always contaminated by ubiquitous carbonous species in air. T. Smith finally concluded that the Au surface is intrinsically superhydrophilic [159]. He carefully studied the surface contamination by Auger electron spectroscopy and measured the water contact angle on the Au surface within a few minutes of air exposure. A clean Au surface showed a water contact angle of $\sim 0^\circ$. If Au surface was exposed to air for more than 10 min, the surface became hydrophobic. However, almost all reports on the hydrophilicity of photocatalyst surfaces ignore the effect of surface contamination when measuring the water contact angle.

Therefore, the intrinsic hydrophilicity of solid surfaces has to be investigated while carefully considering the existence of surface contamination. The water contact angle on ($\sqrt{13} \times \sqrt{13}$)-$SrTiO_3$ surface was measured after different surface treatments. The results are summarized in Fig. 3.11. For the water contact angle measurements, a 2 μl water droplet (the systematic error was less than 0.030 μl) was dropped on a sample surface with a micropipette (M & S Instruments Inc., P2). The water contact angle on the sample (A) was measured within 1 min of air exposure after preparing a ($\sqrt{13} \times \sqrt{13}$) reconstructed surface in a vacuum chamber. The temperature of the sample surface may affect the surface wettability due to variations in surface tension of water with temperature. Thus, all samples were cooled to room temperature before measuring the water contact angle by keeping the sample in the vacuum chamber for over 12 hours. Sample (A) showed a water contact angle of $< 4^\circ$. When the water contact angle is less than 4°, the contact angle is determined by the volume of the water droplet due to the small size of the sample. At very low contact angles the water droplet spreads to the sample edges and the angle is determined by the water volume, not purely by water / solid interaction strength. Hence, in this study, surfaces with water contact angles below 4° were considered to be superhydrophilic. However, sample (A) might not be an ideal ($\sqrt{13} \times \sqrt{13}$) surface and

may have had a certain amount of oxygen vacancies and excessive Sr-species on the surface, since the sample was prepared by annealing at ~ 1000°C and 10^{-5}Torr of oxygen. Sample (B) was otherwise identical to (A), but the crystal was kept in air for over 1 day. The water contact angle on (B) was ~ 30°, which indicates that the air exposure destroyed the superhydrophilic state. Air exposure contaminates a solid surfaces with carbonous species, so sample (B) might have been coated with carbon-related contamination. To check the effect of oxygen vacancies on the hydrophilicity of a $SrTiO_3$ surface, as-prepared ($\sqrt{13} \times \sqrt{13}$)-$SrTiO_3$ surfaces were post-annealed at 600°C and 10^{-1}Torr for 1 hour (sample (C)). The annealing conditions of 600°C and 10^{-1}Torr for 1 hour was optimized to remove oxygen vacancies as much as possible without degrading the atomic structure of the ($\sqrt{13} \times \sqrt{13}$)-$SrTiO_3$ surface. Sample (C) also showed superhydrophilicity but subsequent air exposure again destroyed the superhydrophilic state of sample (C). Image (D) has the sample (C) after having been exposed to air for 10 min, which resulted in a water contact angle increase to ~ 20°. Even a 10 min air exposure was thus sufficient for deteriorating the superhydrophilicity, as was the case for the Au surface [159].

Annealing of $SrTiO_3$ in reducing conditions tends to cause Sr segregation to the crystal surface. Segregated Sr may thus co-exist with the double-layer Ti surface reconstruction on the ($\sqrt{13} \times \sqrt{13}$)-$SrTiO_3$ and affect the water contact angle. It has been reported that hot water can remove surface Sr-species from $SrTiO_3$ [160]. Any Sr residue that may have been on the surface of sample (A) was therefore removed by a hot water soaking (> 60°C), obtaining sample (E). The surface of sample (E) was still highly hydrophilic, meaning that the ($\sqrt{13} \times \sqrt{13}$)-$SrTiO_3$ surface is superhydrophilic regardless of the existence of Sr species. Similarly to sample (D), the superhydrophilicity of sample (E) was destroyed by air exposure, as shown by image (F). By annealing sample (F) at 600°C and 10^{-1}Torr for 1 hour (sample (G)), the surface carbonous contamination and oxygen vacancies were removed to the extent possible without triggering segregation [161]. Sample (G) was the cleanest ($\sqrt{13} \times \sqrt{13}$)-$SrTiO_3$ surface, having minimal Sr-related residues, carbonous contamination, and oxygen vacancies. Sample (G) showed superhydrophilicity, but after a 10 min air exposure the hydrophilicity decreased, as shown in image (H). The conclusion from the experiments was that all samples exposed to air for more than about 10 min were weakly hydrophilic and clean samples just after unloading from the vacuum chamber showed superhydrophilicity. The results clearly shows that air exposure is the dominant effect for degrading the superhydrophilicity of ($\sqrt{13} \times \sqrt{13}$)-$SrTiO_3$ surfaces.

It should be noted that $SrTiO_3$ is intrinsically superhydrophilic independent on surface reconstruction, crystal plane, or Nb-doping level. $SrTiO_3$ substrates were annealed at 600°C and 10^{-1}Torr for 1 hour in order to remove carbonous contamination from the surface. Before measuring the water contact angle, the samples were cooled to room temperature by keeping them in a vacuum chamber for over 12 hours. A 2 μl water droplet was dropped on the sample surface less than 1 min after air exposure. Fig. 3.12 shows the water droplets on $SrTiO_3$ (110) and (111) surfaces, together with the AFM corresponding topography images. Independent of the

crystal plane, $SrTiO_3$ became superhydrophilic after surface cleaning. The effect of Nb doping on surface hydrophilicity was also investigated (Fig. 3.13). However, all $SrTiO_3$ substrates showed superhydrophilicity after surface cleaning.

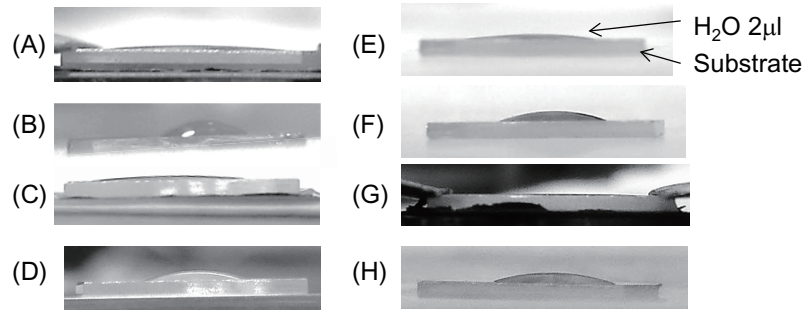

Sample	Treatment	θ (°)	Plausible residues
(A)	Exposed to air for <1 min	<4	Sr, V_o
(B)	Exposed to air for 1 day	~30	Sr, V_o, C
(C)	Annealed at 600 °C, $P(O_2)=10^{-1}$Torr for 1 h, and exposed to air for <1 min	<4	Sr
(D)	After removing water on (C) by N_2-flow, exposed to air for 10 min	~20	Sr, C
(E)	Etched in hot water (~60 °C) for 10 min, and dipped in water for cooling to r.t.	<4	V_o
(F)	After removing water on (E) by N_2-flow, exposed to air for 10 min	~20	V_o, C
(G)	After (E), annealed at 600 °C, $P(O_2)=10^{-1}$ Torr for 1 h, and exposed to air for <1 min	<4	(clean)
(H)	After removing water on (G) by N_2-flow, exposed to air for 10 min	~20	C

Figure 3.11: Photographs of a 2 μl water droplet on ($\sqrt{13} \times \sqrt{13}$)-$SrTiO_3$ surface prepared in different procedures. Treatments, contact angles, and plausible surface residues are listed in the table. Sr and C represent the surface residues of Sr- and carbon- related compounds, respectively. V_O represents the existence of a certain amount of oxygen vacancies.

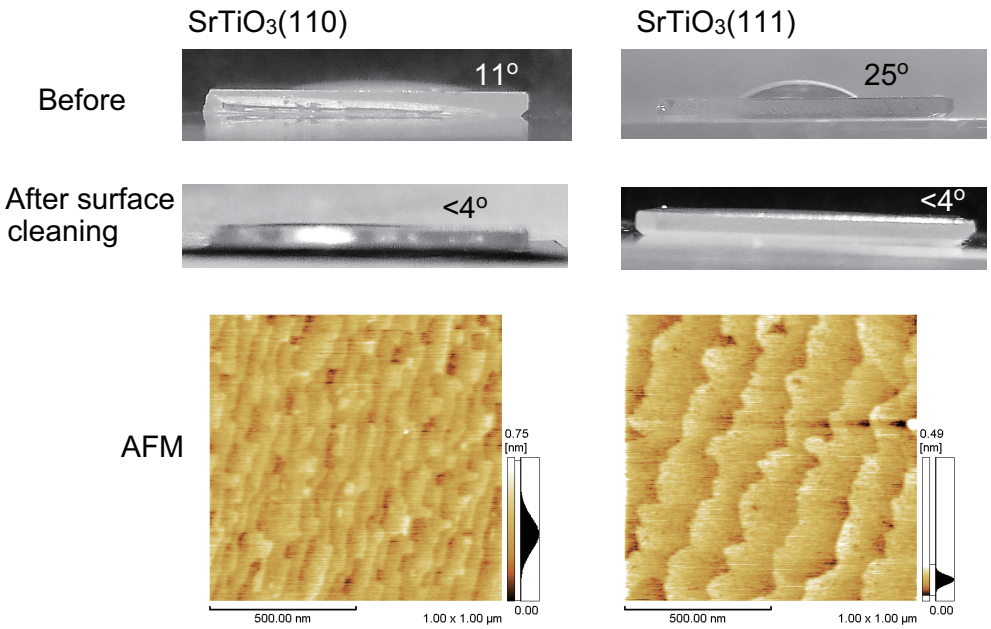

Figure 3.12: Images showing a water droplet (2 μl) on $SrTiO_3$ (110) and (111), before and after surface cleaning, measured at 20°C and RH~ 50%. The AFM images showed step-and-terrace morphologies for both surfaces.

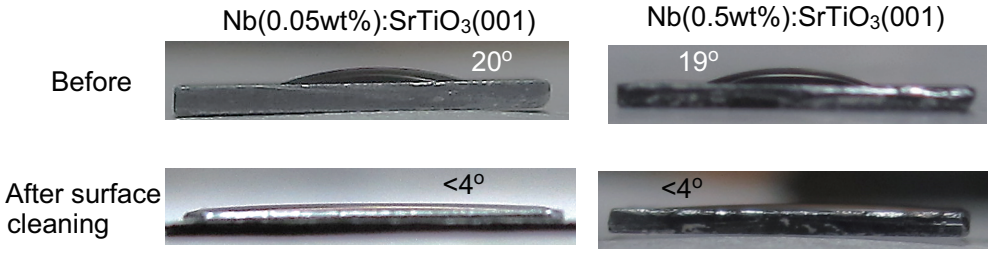

Figure 3.13: Images showing a water droplet (2 μl) on Nb:$SrTiO_3$ (001) with doping levels of 0.05 and 0.5 wt%, before and after surface cleaning at 20°C and RH~ 50%.

The water contact angle was also measured in N_2 atmosphere using a glove bag directly attached to a loading chamber of the PLD chamber in order to remove the effects from oxygen and carbonous species that come from air-exposure on the water contact angle of clean surfaces. Fig. 3.14 is a photograph of the glove bag used in this study. The glove bag is a simple and convenient way to prevent contamination from air-exposure [162]. The water contact angle on clean surfaces was always $< 4°$, suggesting that these oxide surfaces are intrinsically superhydrophilic without UV light irradiation and the presence of oxygen.

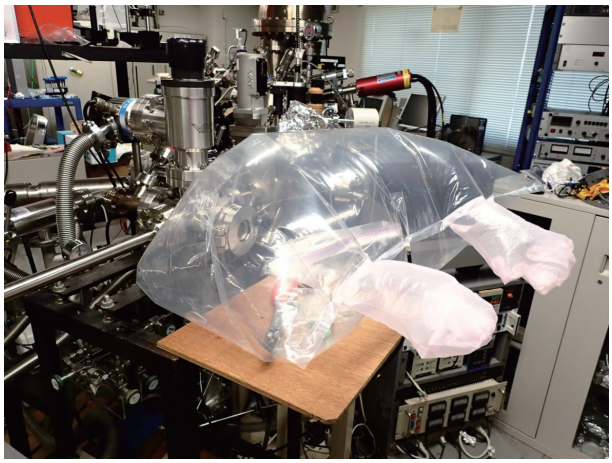

Figure 3.14: Glove bag attached to the vacuum chamber. The bag was filled with pure N_2 gas.

The water contact angle was measured for other oxide surfaces as well. Fig. 3.15 shows water contact angles for step-and-terrace TiO_2(110), Al_2O_3(0001), $NdGaO_3$(001), and LSAT(001) surfaces. The water contact angles of untreated surfaces showed strong variability among samples, ranging from 20° on TiO_2 to 92° on $NdGaO_3$(001). After surface cleaning, the water contact angle became less than 4° for all sample surfaces. Surface cleaning was done by annealing substrates at 600°C, 10^{-1} Torr of oxygen pressure for 1 hour. Under these conditions, surface carbonous species were removed while the step-and-terrace surface morphology was not changed. In addition, the fact that the color of the LSAT substrate turned brownish indicated that the density of oxygen vacancies was decreased by this treatment. For comparison LSAT substrates also become brownish by annealing at 600°C in air in an electric furnace, but do not change color when annealed at 600°C, 10^{-6}Torr. The results show that these oxide surfaces are also intrinsically superhydrophilic. However, the superhydrophilicity was destroyed by ~10 min air exposure.

The water contact angles of a polycrystalline anatase TiO_2 film and single crystal rutile TiO_2(110) surfaces without UV light irradiation have been reported in several papers [39, 41, 142, 163–166]. The reported water contact angle values show large variations as summarized in Fig. 3.16. The water contact angle is often measured in the ambient atmosphere, which causes

variations of the observed water contact angles and leads to poor experimental reproducibility. Even when measurements are done in a vacuum chamber filled with a well-defined atmosphere, surface contamination may still affect the measurements [41]. However, the quick contact angle measurement used in this study gives very strong evidence that a clean rutile TiO_2(110) surface is indeed superhydrophilic with a water contact angle smaller than 4°.

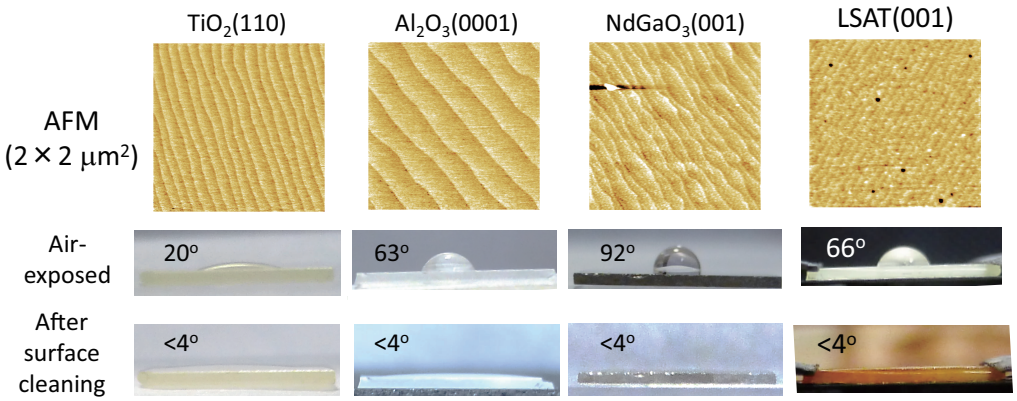

Figure 3.15: AFM topographies (2×2 μm^2) of TiO_2(110), Al_2O_3(0001), $NdGaO_3$(001), and LSAT(001). Photographs of a 2 μl water droplet on each surface before and after surface cleaning. Water contact angles on the clean surfaces were measured within 1 min of the start of air exposure. Surface cleaning was done by annealing the substrates at 600°C, 10^{-1} Torr of oxygen for 1 hour.

Sample	Water	C.A. (º)	Reference
polycrystalline film on glass anatase sol-gel at 500ºC	~2 μl	43~49	N.Sakai *et al.*, *Langmuir* 14, 5918 (1998).
polycrystalline film on glass anatase sol-gel at 500ºC	~2 μl	35~62	T.Watanabe *et al.*, *Thin Solid Films* 351, 260 (1999).
polycrystalline film on glass anatase sol-gel at 500ºC	~2 μl	20~25	N.Sakai *et al.*, *J. Electrochem. Soc.* 148, E395 (2001).
polycrystalline film on glass anatase sol-gel at 500ºC	~2 μl	15~40	N.Sakai *et al.*, *JPCB* 107, 1028 (2003).
Single crystal (rutile(110))	~2 μl	53~90	T.Watanabe *et al.*, *Thin Solid Films* 351, 260 (1999).
Single crystal (rutile(110))	~2 μl	65~74	R.Wang *et al.*, *JPCB* 103, 2188 (1999).
Single crystal (rutile(110)(1x1))	unknown	20~32	T.Zubkov *et al.*, *JPCB* 109, 15454 (2005).
Single crystal (rutile(110))	2 μl	~30	K.Takahashi *et al.*, *JPCC* 113, 20322 (2009).
Single crystal (rutile(110))	2 μl	<4	This work

Figure 3.16: Table of water contact angles on a polycrystalline anatase TiO_2 film and single crystal rutile TiO_2 surfaces without UV exposure, reported in Refs. 39, 41, 142, 163–166. In this work, a clean TiO_2(110) surface showed a water contact angle of less than 4° without UV light irradiation.

The physical model of the water contact angle (θ) is based on Young's equation

$$\gamma_S = \gamma_{SL} + \gamma_L \cos\theta, \tag{3.1}$$

where γ_S, γ_L, and γ_{SL} are the surface energies of solid and liquid, and the interfacial energy at solid/liquid interface, respectively. The equation was derived by considering an equilibrium of surface tensions of solid and liquid, and the interfacial tension of the solid/liquid interface. The unit of surface energy is J/m^2, which is equivalent to N/m, used for surface tension. Thus, the equilibrium of surface tensions is equivalent to a thermodynamic equilibrium of surface energies. The thermodynamic equilibrium of surface energies can also be formulated by the Girifalco-Good equation as

$$\gamma_{SL} = \gamma_S + \gamma_L - 2\phi\sqrt{\gamma_S\gamma_L}, \tag{3.2}$$

where ϕ is defined as the interaction parameter at the interface. ϕ is empirically known to be in the range from 0.5 to 1.1 [167]. From Eqs. 3.1 and 3.2, θ can be expressed as

$$\cos\theta = 2\phi\sqrt{\gamma_S/\gamma_L} - 1. \tag{3.3}$$

The surface energy of water, $\gamma(H_2O)$, is 72.8 mJ/m^2 at 20°C [168]. Fig. 3.17 shows the variation of water contact angle as a function of surface energy of the solid surface and the interaction parameter calculated from Eq. 3.3 at 20°C. As shown in Fig. 3.18, polar molecules generally have small interface energies at the water interface and thus have large interaction parameters. Since oxides have more strongly ionic character than organic compounds, water/oxide interfaces should have large interaction parameters, close to 1. According to Fig. 3.17, oxide surfaces that have a surface energy larger than 200 mJ/m^2 should, in principle, show very small water contact angles of $\sim 0°$.

Surface energies of various materials have been determined from experiments or estimated based on theoretical calculations [169–176]. Some of the data is listed in Fig. 3.19. In general, oxide surfaces have very large surface energies of hundreds of mJ/m^2. Therefore, following the physical model of water contact angle, oxide surfaces should be intrinsically superhydrophilic. This fact is consistent with the experimental results obtained in this work, showing intrinsic superhydrophilicity on various types of clean oxide surfaces.

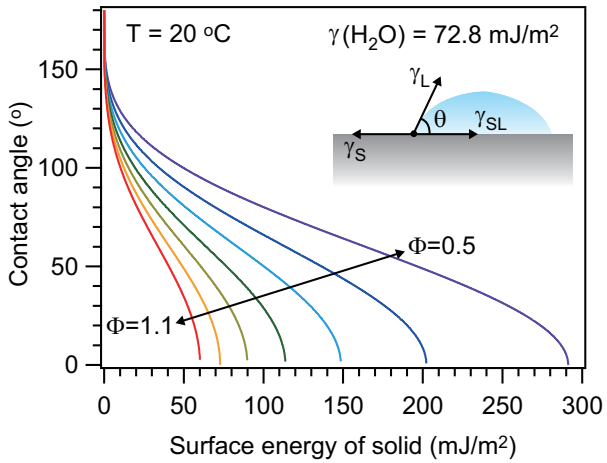

Figure 3.17: Water contact angle (θ) on an ideal flat surface dependent on the surface energy of the solid and the interaction parameter (ϕ), calculated from Eq. 3.3 at 20°C. The surface energy of water, $\gamma(H_2O)$, was assumed to be 72.8 mJ/m^2 at 20°C [168]. The inset shows an illustration of a water droplet on a surface with contact angle where force vectors of surface tensions of solid (γ_S), liquid (γ_L), and interface tension (γ_{SL}) are described.

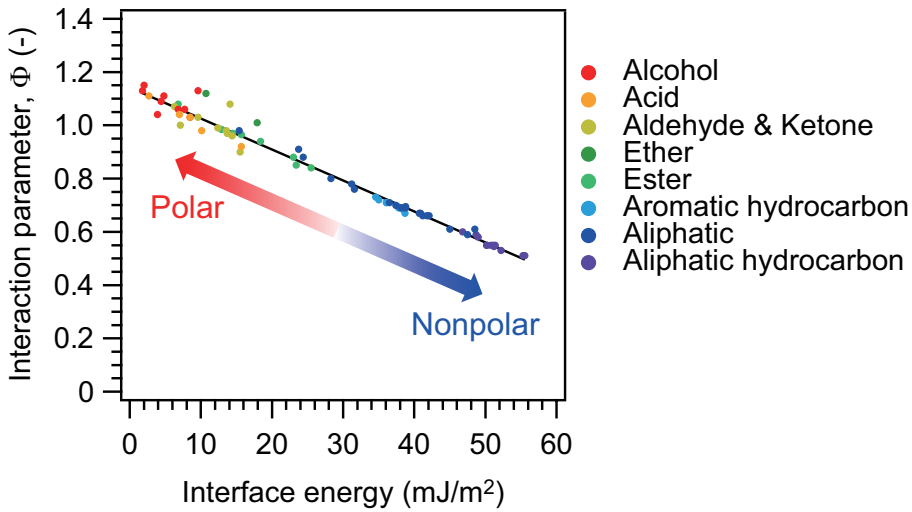

Figure 3.18: Interaction parameters between water and various types of organic compounds as a function of interface energy at 20°. In general, polar molecules have small interface energies at the water interface and thus have large interaction parameters. The data were obtained from Ref. 167.

Material	Face	γ_S (mJ/m^2)	Material	Face	γ_S (mJ/m^2)
TiO_2(rutile)	(110)	1780	α-Fe_2O_3	(0001)	1530
	(011)	1850		(10-10)	2360
	(100)	2080	MgO	(100)	1070
	(poly)	1910	CaO	(100)	800
TiO_2(anatase)	(011)	1400	SrO	(100)	650
	(001)	1280	LiF	(100)	563
	(poly)	1320	NaCl	(100)	280
$SrTiO_3$	$(100)_{SrO}$	1100-1400	Au	(100)	918-1710
	$(100)_{TiO_2}$	890-1450	Pt	(100)	1650-2480
	$(110)_{SrTiO}$	3100	$CaCO_3$(calcite)	(10-11)	190
	$(110)_{O_2}$	2200	Diamond	(111)	5650
α-Al_2O_3	(0001)	2030	Graphite	(0001)	119
	(10-10)	2230	$C_{20}F_{42}$	$(100)_{CF_3}$	7

Figure 3.19: List of surface energies for various types of materials. The data was picked from Refs. 169–176.

It should be noted that in the case that the solid surface is not flat and has a considerable surface roughness, the Young equation has to be revised and the water contact angle is expressed by Wenzel mode or Cassie mode (Fig. 3.20). If the surface roughness is not that large, the water contact angle is expressed by the Wenzel mode. In the Wenzel mode model, the area at the water/solid interface is multiplied by the roughness ratio (r). The Young equation is in this case revised as

$$\cos\theta = r\cos\theta_0, \tag{3.4}$$

where θ is the observed contact angle and θ_0 is the ideal contact angle on a flat surface. Here, because $r > 1$, hydrophilic surfaces have θ smaller than θ_0, while hydrophobic surface have θ larger than θ_0, which means that hydrophilicity is overestimated. When roughness is larger than a certain level and the air stays at the hollows at the liquid/solid interface, the contact angle is described by the Cassie model as

$$\cos\theta = f\cos\theta_0 + f - 1, \tag{3.5}$$

where f is the fraction of the solid surface area ($f < 1$). The threshold surface roughness that marks a transition from the Wenzel to Cassie modes is $r \sim 1.7$ [177]. Thus, in order to evaluate the intrinsic hydrophilicity of solid surfaces, the solid surface should be atomically flat. For this reason, I used step-and-terrace surfaces for evaluating the intrinsic hydrophilicity of oxide surfaces.

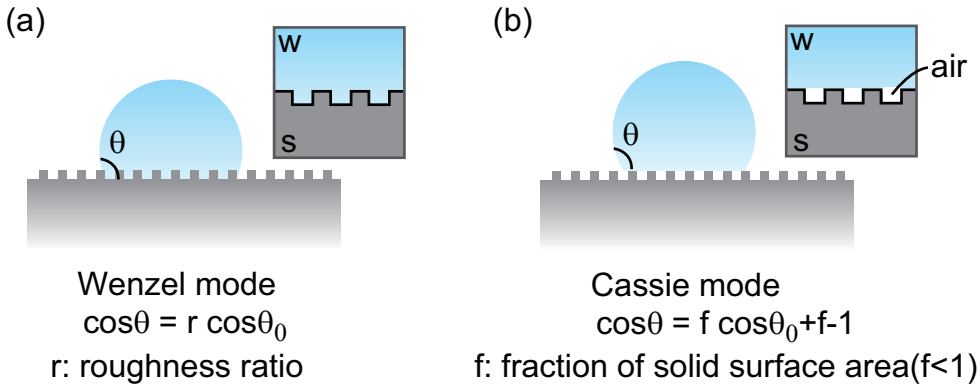

Figure 3.20: Water contact angle following (a) Wenzel and (b) Cassie modes. W and S represent water and solid.

3.4 Understanding the mechanism of photo-induced superhydrophilicity

Since the original discovery of photo-induced superhydrophilicity of TiO_2 [38], the phenomenon has been extensively studied from various viewpoints [178,179]. However, the true mechanism of photo-induced superhydrophilicity is still controversial. So far, there are two main models, including the surface reconstruction model [39] and the contamination model [40, 41]. A combined model has also been proposed [144]. The most difficult problem that prevents reliable mechanism studies is the difficulty of distinguishing between the effects of photocatalytic decomposition of carbonous contaminants and photo-induced surface roughening on photo-induced hydrophilicity changes. Both occur simultaneously on oxide surfaces under UV light irradiation. Most published works report the hydrophilicity measured in ambient conditions where surfaces are usually contaminated by ubiquitous carbonous contaminants present in air and the effect of air exposure is typically not reported. Yates, Jr. *etal*. carefully measured water contact angles in a controlled atmosphere using a vacuum chamber, but they still did not observe superhydrophilicity of TiO_2 without UV light irradiation [41]. They concluded that even a fractional monolayer of contaminants reduces the intrinsic superhydrophilicity of TiO_2. In a word, the intrinsic hydrophilicity of a TiO_2 surface has not been carefully evaluated so far, in my view. The evaluation of intrinsic hydrophilicity of Ti-oxides is indispensable for determining the true mechanism of photo-induced superhydrophilicity.

Hence, in my study, I prepared nearly ideal atomically flat Ti-oxide surfaces, especially the $(\sqrt{13} \times \sqrt{13})$-R33.7° $SrTiO_3(001)$ surface, and evaluated the water contact angle on the bare surfaces. After surface cleaning in a vacuum chamber by annealing the sample at 600°C, 10^{-1}Torr, the oxide surfaces showed superhydrophilicity with almost 0° water contact angle. Based on a physical model of the water contact angle, it was recognized as a reasonable result that such a highly energetic surface with surface energy of several hundred mJ/m^2 shows ~0° water contact angle. The hydrophilicity is clearly affected far more by surface contamination than any surface morphology changes of the reconstructed structure. Any surface roughening that may occur under UV light irradiation has a much smaller effect on the interaction between TiO_2 and water and thus the effect on the water contact angle is small. I conclude that the true mechanism of photo-induced superhydrophilicity is the contamination model.

In fact, there has been no clear direct experimental evidences to prove the surface reconstruction model. Conversely, there are many experimental results that are incompatible with the surface reconstruction model. If a metastable surface state really is produced through a chemical reactions on a TiO_2 surface by UV light irradiation, the surface state should be observable by surface scientific analysis techniques, such as scanning probe microscopy and/or spectroscopy. Careful analysis has concluded that there is no significant changes on TiO_2 surface induced by UV light irradiation in vibrational spectra [40,41,139–142], in ambient pressure

XPS measurements [141], and in TPD spectra [143]. The time constant of the reverse reaction of the degradation of photo-induced superhydrophilicity in dark has large variation from a few tens of minutes [166] to over a month [179]. Considering the experimental results that the superhydrophilicity of TiO_2 surface is easily destroyed by ultrasonic agitation [163] and by surface rubbing [180], the metastable superhydrophilic surface state should not be stable enough to survive for more than a day. Moreover, if the metastable surface state was produced by chemical reactions to form new surface hydroxyl groups on the TiO_2 surface, weak mechanical stimuli like ultrasonic washing and surface rubbing should not affect the metastable state. The contamination model is thus the most plausible mechanism explaining all previous experimental reports.

There has been a long-standing controversy over whether $SrTiO_3$ shows photo-induced superhydrophilicity like TiO_2. Miyauchi *etal*. studied the photo-induced hydrophilicity change of various types of oxide materials, and reported that $SrTiO_3$ (polycrystalline film) is one example of photocatalysts that decompose organic compounds but do not show superhydrophilicity [181, 182]. Based on these results, they suggested that the mechanism of photo-induced superhydrophilicity is not completely explained by the contamination model. In contrast, Katayama *etal*. [108] and Katsumata *etal*. [183] have reported that single crystal $SrTiO_3$ shows photo-induced superhydrophilicity. Katayama *etal*. [108] reported that the photo-induced superhydrophilicity is affected by the atomic composition of the surface, and that TiO_2-terminated $SrTiO_3(001)$ shows photo-induced superhydrophilicity, whereas SrO-terminated $SrTiO_3(001)$ does not. Katayama *etal*. [108] observed the photo-induced superhydrophilicity of single crystal $SrTiO_3(001)$, (110) and (111) surfaces, concluding that $SrTiO_3$ shows photo-induced superhydrophilicity independent of the crystal planes. These experiments were done at room temperature in the ambient atmosphere. In my experiments, I confirmed that the superhydrophilicity of $SrTiO_3$ is intrinsic, it is independent of the surface plane and the surface Sr coverage. All experimental results can be understood by considering the formation of $SrCO_3$ on a $SrTiO_3$ surface by air exposure. $SrTiO_3$ exposed to air commonly has $SrCO_3$ on the surface [184], due to a reaction between SrO in $SrTiO_3$ and CO_2 in air. Since $CaCO_3$ has lower surface energy of 190 mJ/m^2 (Fig. 3.19), $SrCO_3$ should also have a surface energy that is smaller than $CaCO_3$ due to the large ionic radius of Sr^{2+} compared to Ca^{2+}. The intrinsic superhydrophilicity of $SrTiO_3$ is usually hidden in the atmosphere by the interferences from surface contamination, including carbonous compounds and Sr-related residues like $SrCO_3$ and $Sr(OH)_2$. Photocatalytic oxidation of $SrTiO_3$ under UV light irradiation can decompose carbonous contamination but does not remove $SrCO_3$. By photocatalytic decomposition of carbonous contaminants, the surface hydrophilicity is increased to a certain level but superhydrophilic conditions are not reached due to the remaining presence of $SrCO_3$. Although Miyauchi *etal*. [181, 182] concluded that $SrTiO_3$ did not show superhydrophilicity, the weak hydrophilicity of $SrTiO_3$ can be explained by the interference from $SrCO_3$ covering the polycrystalline $SrTiO_3$ surface, in my opinion. The

reason why a SrO-terminated $SrTiO_3$ surface did not show photo-induced superhydrophilicity can be explained by the low activity of photocatalytic organic decomposition [185], but also explained by the presence of $SrCO_3$. Therefore, the effect of surface $SrCO_3$ should be taken into account when studying the hydrophilicity of $SrTiO_3$.

Finally I discuss the superhydrophilic domains on TiO_2 surface proposed by Wang *etal*. [38,186]. Besides the discovery of the phenomenon of photo-induced superhydrophilicity they reported that superhydrophilic domains appear on a TiO_2(110) surface after UV irradiation [38,186]. They observed by friction force microscopy (FFM) $\sim$ 50 nm domains oriented along the [001] direction and suggested that the amphiphilic TiO_2 was caused by the coexistence of hydrophilic and oleophilic domains induced by UV light irradiation. They studied oleophilicity by measuring contact angles of glycerol trioreate andhexadecane. The formation of the domains might be related to the formation of oxygen vacancies and Ti^{3+} on TiO_2 surface, they proposed [38,186]. Later, they additionally reported with AFM images that the domains were formed by annealing TiO_2 at 300°C in air and by argon ion sputtering as well as by UV light irradiation [187].

However, no other group has reproduced the formation of superhydrophilic domains. An attempt was therefore made to observe superhydrophilic domains of TiO_2(110) surface by FFM after preparing a superhydrophilic TiO_2 surface by UV irradiation ($\lambda = 365 \pm 10$ nm, 1.15 mW/cm^2, 1 hour), but FFM showed no signs of superhydrophilic domains reported in Ref. 166, as shown in Fig. 3.21. In my opinion, the superhydrophilic domains observed by Wang *etal*. were artifacts caused by surface contamination. Also, it should be noted that according to Eq. 3.3, it is natural that organic compounds like glycerol trioreate and hexadecane, due to the smaller surface tension than water, show smaller contact angles than water. A superhydrophilic surface is therefore naturally highly amphiphilic. My experiments, performed on well-defined step-and-terrace surfaces showed no signs of superhydrophilic domain formation. It is thus highly likely that the formation of superhydrophilic domains on TiO_2 surfaces, as reported by Wang *etal*. does not occur on clean TiO_2 surfaces.

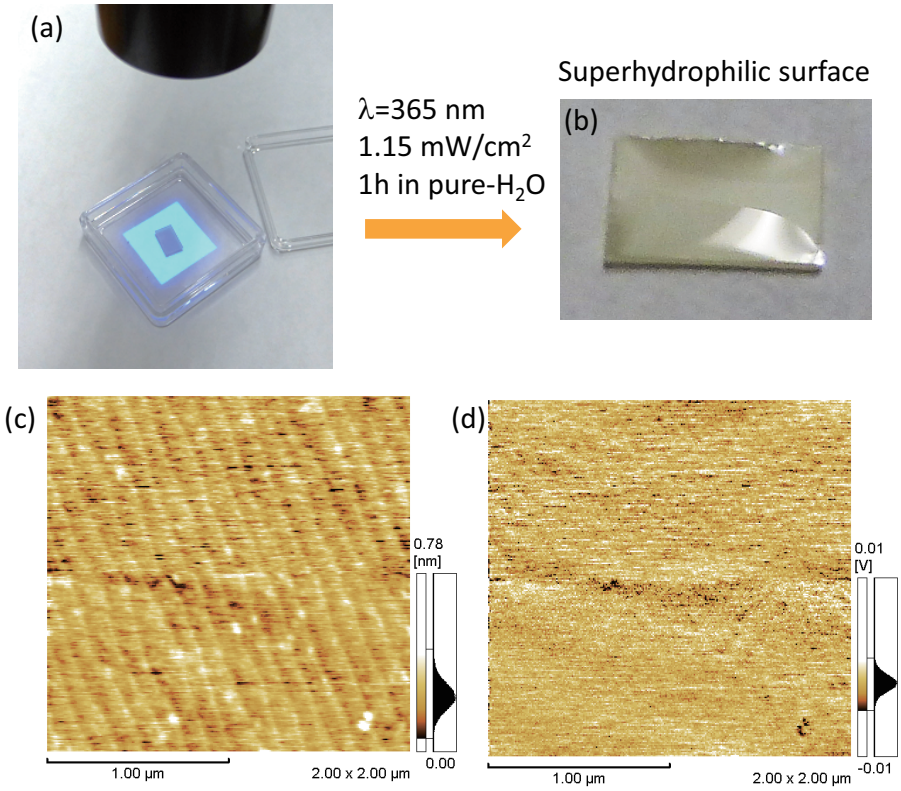

Figure 3.21: (a) Image showing a rutile TiO_2(110) substrate in pure water under UV light irradiation. (b) A rutile TiO_2(110) substrate after UV irradiation ($\lambda = 365 \pm 10$ nm, 1.15 mW/cm^2, 1 hour) in pure water, showing that the surface became superhydrophilic. (c) AFM and (d) FFM (2×2 μm^2) of the sample shown in (b) after removing water from the surface by N_2 blow drying. The measurements were done at 20°C, RH>70%.

3.5 Conclusion

Intrinsic hydrophilicity of oxide surfaces was investigated to clarify the true mechanism of photo-induced superhydrophilicity of Ti-oxide photocatalysts. In this study, ($\sqrt{13}\times\sqrt{13}$)-$SrTiO_3$ (001) was used as an ideal model photocatalyst surface. The ($\sqrt{13}\times\sqrt{13}$)-$SrTiO_3$ (001) surface has been recognized as environmentally the most stable $SrTiO_3$ surface due to an extra TiO_x layer on the TiO_2-terminated $SrTiO_3$(001) surface [151]. I found that the surface is stable even in water, which adsorbs molecularly on this surface. The stability of the atomic structure was also supported by theoretical simulations. This surface showed superhydrophilicity whenever the surface was cleaned by annealing a crystal in an oxygen atmosphere to remove carbonous contamination. The results showed that the Ti-oxide surfaces are intrinsically superhydrophilic, suggesting that the mechanism of photo-induced superhydrophilicity can be fully explained by a contamination model. Superhydrophilicity was obtained just by the removal of carbonous contamination without the need for light irradiation. Intrinsic superhydrophilicity was also confirmed on other oxide surfaces, TiO_2, Al_2O_3, $NdGaO_3$, and LSAT. Based on a physical model of the contact angle of a water droplet on a solid surface, ionic surfaces having a large surface energy (> 200 mJ/m^2) should be intrinsically superhydrophilic. Since oxide surfaces have large surface energies, it is natural that clean surfaces are intrinsically superhydrophilic. The results also suggested that a fundamental study of surface wettability should not be done in the ambient atmosphere. Surface wettability is very sensitive to air exposure, as previously reported in the study of intrinsic surface hydrophilicity of Au surfaces [159]. Based on previous reports, the surface reconstruction model has been contradicted by careful surface analyses using scanning probe microscopy and spectroscopy. Direct observation of a photoinduced reconstructed metastable surface state has not been successful so far. The formation of superhydrophilic domains observed by Wang *etal*. [38, 186] on TiO_2 appears to be unreproducible and was probably caused by surface contamination. Therefore, I conclude that the true mechanism of the photo-induced superhydrophilicity is surface contamination, as originally proposed by Yates Jr. *etal*. [41] and Anpo *etal*. [40].

Chapter 4

Photoelectrochemical activity and electronic structure of doped $SrTiO_3$

The relationship between the electronic structure and the photoelectrochemical activity of doped $SrTiO_3$ is discussed in this section. In general, the photoelectrochemical and photocatalytic properties of doped semiconductors are known to be strongly dependent on the dopant species.

In my work, Rh- and Ir-doped $SrTiO_3$ were the main subjects for study. Rh-doped $SrTiO_3$ was already known to be an effective hydrogen-evolution photocatalyst, but the electronic structure had not been studied in detail. Ir doping was selected due the similarity of the electronic structures of Ir:$SrTiO_3$ and Rh:$SrTiO_3$, except for a systematic shift of Ir-related in-gap states to a slightly higher energy. The valence of Rh and Ir dopants in $SrTiO_3$ was successfully controlled by optimizing the film growth temperature and the ambient oxygen pressure. The electronic structure, especially the dopant-related in-gap state positons relative to the valence and conduction band edges, was investigated by several forms of X-ray spectroscopy, including XPS, XAS, and XES. The experimentally determined density of states of Rh- and Ir-doped $SrTiO_3$ was compared with first-principles calculations and the results were found to be consistent. All experimental spectral features could thus be identified and assigned. The effect of the dopant species, film thickness, and carrier concentration on the photoelectrochemical activity was investigated by conventional three-electrode electrochemical measurements under light irradiation. The differences in the photoelectrochemical activity of Rh- and Ir-doped $SrTiO_3$ was discussed from the viewpoint of general semiconductor physics, specifically the generation and recombination of photocarriers in doped or defect-rich semiconductors. The most important parameter affecting the photoelectrochemical activity of doped $SrTiO_3$ was found to be the photocarrier diffusivity. Excited carrier diffusivity is affected by the density of trap states and the carrier lifetime, which is determined by the impurity level positions within the gap. The work shows that there is a trade-off between increasing light absorption and a reduction of the photocarrier diffusion length in doped $SrTiO_3$. The relationship between these two critical

parameters can be understood at least qualitatively.

4.1 Introduction

Doping in wide-gap oxide semiconductors has been studied as one possible strategy for tuning the bandgap to create stable and visible-light-driven photocatalysts [11]. Doping generally forms impurity levels within the band gap region. If such impurity levels are close to the valence band top or the conduction band minimum, the effective energy gap required for the photocarrier generation can be reduced. TiO_2 doped with N^{3-} [188] and co-doped with Rh^{3+}/Sb^{5+} [54], Cr^{3+}/Sb^{5+} [189], or Ni^{2+}/M^{5+}(M = Nb, Ta) [52] have been reported to be photocatalytically active. For $SrTiO_3$, doping with Rh^{3+} [59], Ir [59], and Cr^{3+} [190–195] has been studied. Various co-doping schemes have been explored to control the charge compensation, such as Rh^{3+}/Sb^{5+} [198–200], Cr^{3+}/M^{5+}(M = Sb, Nb, Ta) [66, 189, 196], Cr^{3+}/La^{3+} [197], and Ni^{2+}/M^{5+}(M = Nb, Ta) [52]. Among these materials, Rh:$SrTiO_3$ in particular has attracted attention due to its high hydrogen evolution [59] activity under visible light irradiation and also its apparent *p*-type character [92]. The Rh valence is known to be an important factor in determining the photoelectrochemical activity of Rh:$SrTiO_3$; Rh^{3+}:$SrTiO_3$ is photocatalytically active while Rh^{4+}:$SrTiO_3$ is not active for the hydrogen evolution reaction [59]. In fact, Rh:$SrTiO_3$ is a rather rare case, where an oxide material can be used as a visible-light-driven photocatalyst for the hydrogen evolution reaction in Z-scheme systems [201–204].

In this study, my focus was on clarifying the difference in the photocatalytic activities of Rh^{4+}- and Rh^{3+}-doped $SrTiO_3$. In addition, to understand the role of the Rh dopant in the relatively high photocatalytic activity of Rh:$SrTiO_3$, a comparative study of Ir:$SrTiO_3$ was also undertaken. Powder samples and epitaxial thin films of Rh- and Ir-doped $SrTiO_3$ were prepared to investigate the detailed photoelectrochemical properties and the electronic structure. The valence of Rh and Ir was successfully controlled by optimizing the oxygen pressure during film growth. The electronic structure, particularly the impurity levels near the band gap edges of $SrTiO_3$, was elucidated by X-ray spectroscopy and supported by first-principles band structure calculations.

4.2 Sample Fabrication of Metal-Doped $SrTiO_3$

4.2.1 M:$SrTiO_3$ (M = Rh, Ir) powders

Doped powder samples of M:$SrTiO_3$ (M = Rh, Ir) were synthesized by standard bulk ceramic techniques [59,92] by using $SrCO_3$ (Wako Pure Chemical; > 95.0%, treated in air at 300°C for 2 h before use), TiO_2 (Wako Pure Chemical; > 99.0%), Rh_2O_3 (Wako Pure Chemical; > 98.0%), and IrO_2 (Soekawa Chemical; > 97.0%) as source materials. The powders were mixed with a small amount of methanol in a ratio according to the composition of $SrTi_{1-x}M_xO_3$, and pre-calcined in air at 900°C for 1 hour, followed by calcining in air at 1100°C for 10 hours in an alumina crucible.

The sintered powders were pelletized in a molding press at 10 ~ 20 MPa and calcined again at 1200°C for 12 hours. The pellets were used as ablation targets for thin film growth and for the measurement of bulk electronic spectra by XAS and XES. The color of Rh:$SrTiO_3$ depends on Rh valence, Rh^{4+}:$SrTiO_3$ is purple, while Rh^{3+}:$SrTiO_{3-\delta}$ is yellow. The yellow-colored reduced Rh:$SrTiO_{3-\delta}$ samples were prepared by annealing the purple Rh^{4+}:$SrTiO_3$ powder in flowing H_2 gas at a pressure of 10^5 Pa and 300°C for 2 hours.

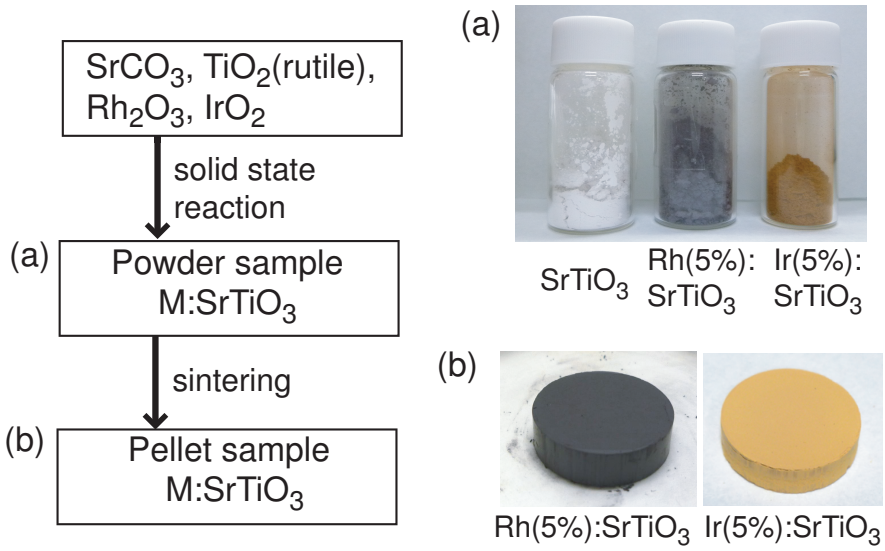

Figure 4.1: Flowchart showing the powder and pellet sample fabrication.

The pelletized samples were confirmed by XRD to contain a single phase. Typical diffraction patterns are shown in Fig. 4.2 and Fig. 4.3.

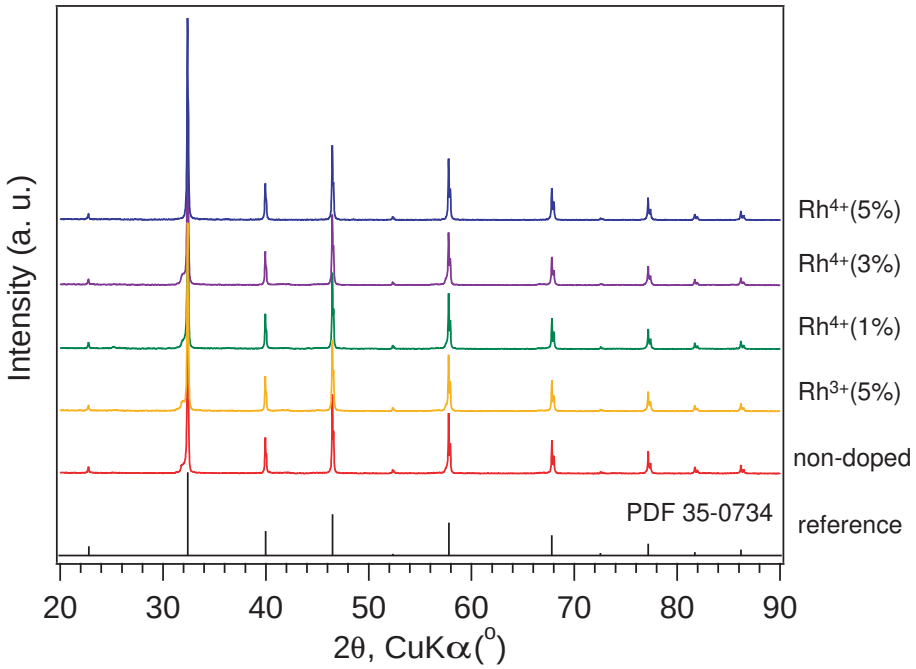

Figure 4.2: XRD patterns of powder Rh:$SrTiO_3$ samples. From the top to the bottom, Rh^{4+}(5, 3, 1%):$SrTiO_3$, Rh^{3+}(5%):$SrTiO_3$, and non-doped $SrTiO_3$, together with reference $SrTiO_3$ data.

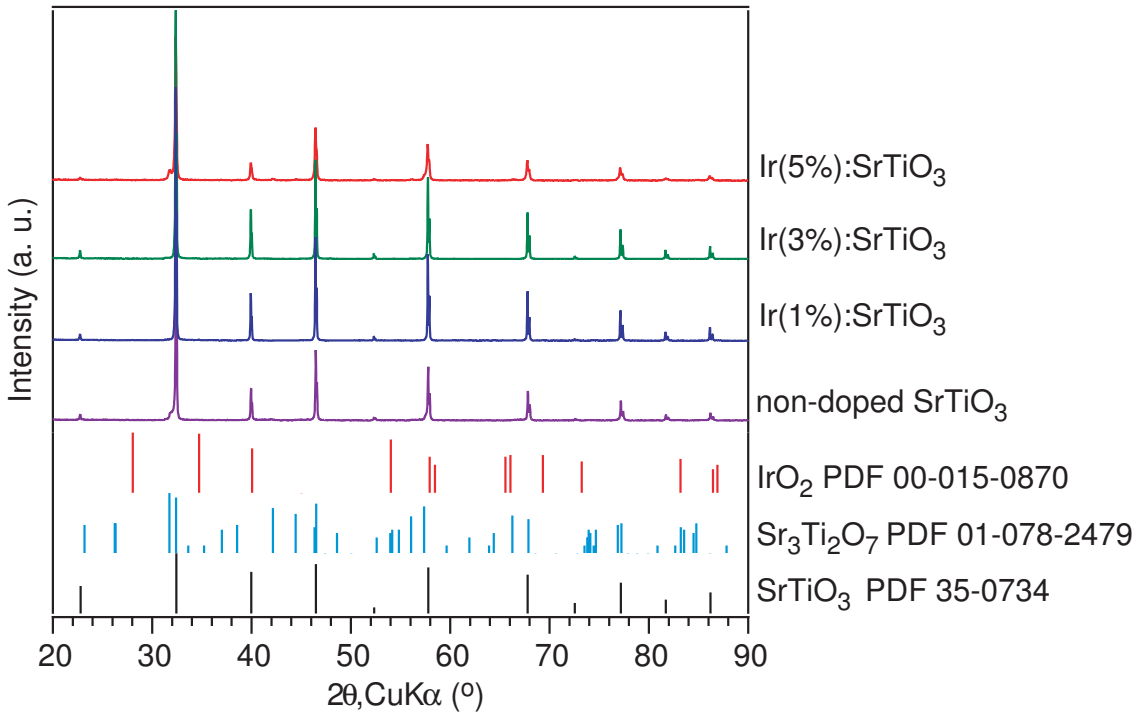

Figure 4.3: XRD patterns of powder Ir:$SrTiO_3$ samples. From the top to the bottom, Ir^{4+}(5, 3, 1%):$SrTiO_3$ and non-doped $SrTiO_3$, together with reference data of IrO_2, $Sr_3Ti_2O_7$, and $SrTiO_3$.

4.2.2 M:$SrTiO_3$ (M = Rh, Ir) epitaxial thin films

To achieve high-quality epitaxial thin film growth by PLD, many parameters such as the substrate surface treatment, growth temperature, oxygen pressure, and laser fluence needed to be optimized. The most important factor for epitaxial growth is the lattice matching between the film and the substrate. To obtain the best possible crystallinity in the thin film samples, the doped *M*:$SrTiO_3$ films were grown homoepitaxially on $SrTiO_3$ (001) substrates from Shinkosha. There are several substrate options for different sample types. Most of the growth characterization was done on non-doped insulating $SrTiO_3$ substrates. When metallic back electrodes and Ohmic contacts with *n*-type films was required, metallic Nb(0.05wt%):$SrTiO_3$ (001) substrates were used. The substrates are usually single-side polished with a matte back side. For optical absorption spectroscopy, transparent double-side polished nondoped substrates were used. Although the film and substrate materials were the same, the thin film bandgap was always narrower than the substrate due to the Rh and Ir doping. It was thus possible to measure accurate absorption spectra, even though the films were grown on $SrTiO_3$ substrates. The only exception was the dynamic THz absorption experiment, which requires a substrate that is transparent to the THz radiation. The samples used for optical transient absorption measurements were therefore grown on LSAT ($(LaAlO_3)_{0.3}(SrAl_0.5Ta_0.5O_3)_{0.7}$) substrates.

The substrates were pre-annealed in the deposition chamber just before film deposition for every sample (Fig. 4.4). The pre-annealing treatment removed most of the surface contamination and yielded a uniform step and terrace structure on the substrate surface. The pre-annealing was done in 10^{-5} Torr oxygen at 1000°C, and lasted for 10 minutes. AFM images showed that the step-and-terrace structure was obviously clean and that the step edges were equidistant and nearly straight (Fig. 4.4 (ii)).

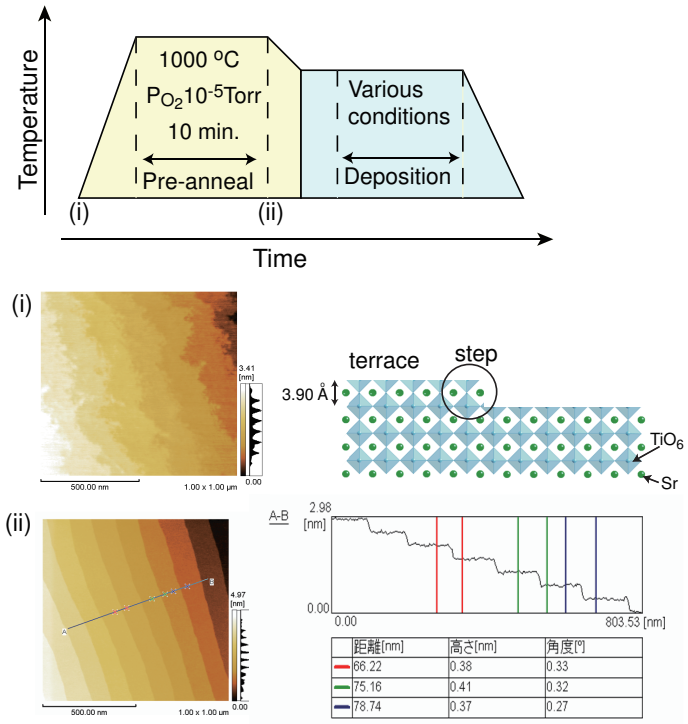

Figure 4.4: Deposition conditions of M:$SrTiO_3$ (M = Rh, Ir)/$SrTiO_3$ thin films and AFM images of a nondoped $SrTiO_3$ substrate surfaces (i) before and (ii) after the pre-annealing treatment. A clean step-and-terrace surface can be seen on the pre-annealed $SrTiO_3$ substrate. The step height is ~ 3.90 Å, corresponding to the unit cell height of $SrTiO_3$ (3.905 Å).

Pulsed laser deposition has several unique features that make it suitable for oxide thin film growth. In particular, precursor adatoms ae delivered from the target to the substrate surface in short, microsecond-scale pulses, followed by a long relaxation interval on the order of a second. For oxide films, this means that the crystal formation and oxidation processes can be separated in time. When the ablation plume hits the substrate surface, adatoms have high energy and can rapidly move on the substrate surface over long distances, forming a high-quality crystal structure. The oxidation process occurs during the interval between ablation pulses over a much longer time period. This means that the average oxygen pressure can be kept low, at around 10^{-6} to 10^{-1} Torr, while almost complete oxidation can be achieved if the laser pulse rate is kept low enough. PLD thus offers an interesting combination of thermodynamic parameters (temperature, oxygen pressure) and kinetics (pulse interval, fluence). Two important parameters, crystallinity (related to the growth rate) and oxygen stoichiometry can be independently controlled. For the growth of M(5 at%):$SrTiO_3$ films, a KrF excimer laser was used at a fluence of ~ 1 J/cm^2 and a repetition rate of 2 Hz. The valence of either Rh or Ir dopants was controlled by tuning the ambient oxygen pressure.

For Rh:$SrTiO_3$, the Rh dopant valence affects the film color, which makes is easy to distinguish visually the valence difference between films grown at different oxygen pressures. The quite obvious film color change can be seen in Fig. 4.5, which shows the optical absorption spectra of valence-controlled Rh:$SrTiO_3$ bulk samples and thin films, together with photographs of three samples grown at 700°C. Reference absorption data is shown for a non-doped $SrTiO_3$ powder sample as well. The three thin film samples were grown at 10^{-1} Torr (fully oxidized, purple), 10^{-3} Torr (brown, mixed valence), 10^{-6} Torr (yellow, reduced). The purple sample corresponds to pure Rh^{4+}:$SrTiO_3$ and the yellow film contains predominantly Rh^{3+}:$SrTiO_3$. The absorption data for the powder samples were calculated by the Kubelka-Munk method from diffuse reflectance spectra. A absorption edge at 380 nm corresponds to the 3.2 eV band gap of nondoped $SrTiO_3$ [91]. The 580 nm peak is due to in-gap states related to Rh^{4+} while the absorption increase below 420 nm occurs for both Rh^{4+} and Rh^{3+} dopants [59].

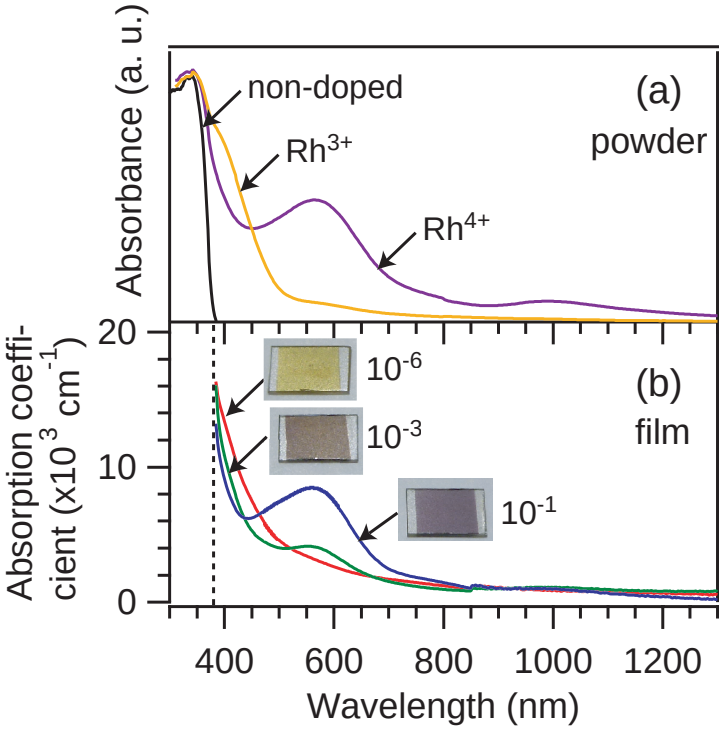

Figure 4.5: (a) Absorption spectra of Rh(1%):$SrTiO_3$ and $SrTiO_3$ powders calculated from diffuse reflectance spectra. (b) Absorption spectra of Rh(5%):$SrTiO_3$ films grown at three different oxygen pressures at 700°C, together with sample images showing a systematic film color change from purple (10^{-1} Torr) to yellow (10^{-6} Torr).

The easiest method for determining the Rh valence state in a thin film sample is to measure the Rh3*d* core level binding energy by XPS and compare the value to known reference compounds. The XPS core level profiles in Fig. 4.6 show that the Rh valence in the films changed systematically with the film growth oxygen pressure. A comparison of the Rh $3d_{5/2}$ peak positions shows that films grown under the most oxidizing conditions, at an oxygen pressure of 10^{-1} Torr, stabilized the highest rhodium valence state (A). Based on literature references, the binding energy of 310 eV can be assigned to the Rh^{4+} state [205]. A gradual reduction of Rh was observed for lower growth pressures, with a distinct shoulder appearing at the lower binding energy side in films grown at 10^{-3} Torr (B). Dopant reduction to metallic rhodium was seen in films grown at 10^{-6} Torr (C). The appearance of the metallic state seems to be limited to the surface of the film, since the probing depth of the XPS measurements at 1060 eV is only about 2 nm, and X-ray absorption near edge structure (XANES) analysis clearly indicated that Rh is in the Rh^{3+} state in the yellow sample grown at 10^{-6} Torr. Fig. 4.7 shows Rh K-edge XANES spectra of a Rh_2O_3 powder and two Rh(5%):$SrTiO_3$ film samples grown at 10^{-6} and 10^{-1} Torr. The film sample grown at 10^{-1} Torr showed a chemical shift to higher photon energy side compared to the Rh^{3+} film, indicating that the purple sample has higher oxidation number than +3. This is consistent with the XPS result that indicated that the purple sample contains Rh^{4+}.

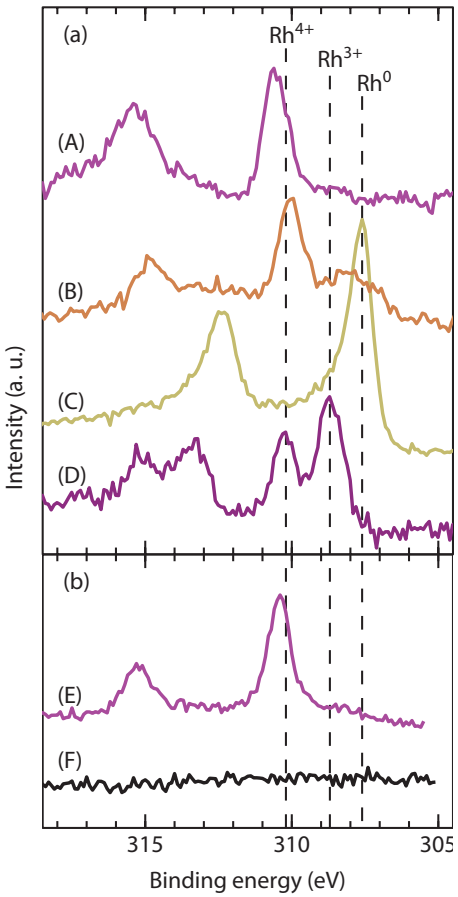

Figure 4.6: X-ray photoelectron spectra of Rh(5%):$SrTiO_3$ films deposited at (A) 700°C, 10^{-1} Torr, (B) 700°C, 10^{-3} Torr, and (C) 700°C, 10^{-6} Torr. (D) Film (A) annealed at 700°C, 10^{-6} Torr for 2 h. Rh loss can be seen by comparing spectra of samples grown at (E) 1100°C, 10^{-1} Torr, and (F) 1100°C, 10^{-6} Torr. (A), (D) were measured at $h\nu$ = 445 eV, all other spectra at $h\nu$ = 1060 eV. The Rh $3d_{5/2}$ peak reference positions for simple Rh oxides, shown at the top of the figure, were taken from Refs. [205–207]. The binding energies were referenced to the Ti $2p_{3/2}$ core-level peak at 459.1 eV [208].

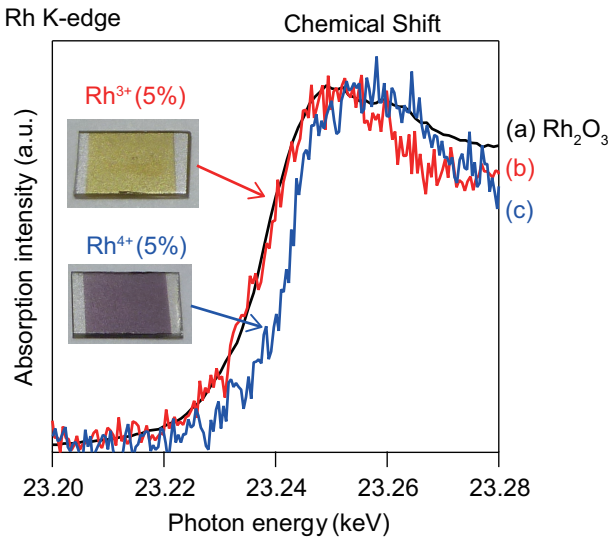

Figure 4.7: XANES spectra of (a) Rh_2O_3 powder and film samples deposited at 700° C under (b) 10^{-6} and (c) 10^{-1} Torr.

All films discussed so far were grown at a fixed 700°C temperature. From the point of view of thermodynamics, both oxygen pressure and temperature should be considered when attempting to control the valence of a dopant. However, at the highest oxygen pressure of 10^{-1} Torr, the effect of temperature is negligible, as shown by a comparison of spectrum (A) with spectrum (E), which corresponds to a film grown at 1100°C and the same 10^{-1} Torr oxygen pressure. In contrast, Rh reduction occurs when a film is annealed at low pressure (E) and a near-complete loss due to evaporation occurs when a film is grown at high temperature and low oxygen pressure (F).

The Rh loss from a film grown at 1100°C and 10^{-6} Torr (F) occurs due to the low stability of the trivalent Rh oxide. The vapor pressures of various possible oxide species occurring on a film surface are compared in Fig. 4.8 [209, 210]. Although pure Rh metal has comparable stability with SrO and TiO_2, nonstoichiometric Rh oxides are volatile. Out of the possible RhO_x species that may exist on the film surface, such as Rh_2O, RhO, Rh_2O_3, and RhO_2 [212], thermodynamic data is available only for RhO_2 and Rh_2O_3 [209, 210]. According to the reference data Rh_2O_3 would be expected to decompose under typical film growth temperature and oxygen pressure, forming volatile Rh oxides or metallic Rh [212]. Since the vapor pressure of Rh metal is extremely low, the surface Rh content is governed by a kinetic balance between the film growth rate and the evaporation of RhO_2 [213]. The growth of high-quality Rh^{3+}:$SrTiO_3$ films is thus mainly complicated by Rh depletion from the film surfaces. As spectrum (F) in Fig. 4.6 shows, complete Rh depletion occurs at 1100°C. The only option is to lower the growth temperature, which may reduce the crystallinity of the film. Based on the vapor pressure data in Fig. 4.8, increasing the

growth pressure to 10^{-1} Torr can effectively suppress the Rh loss even at the highest growth temperature of 1100°C.

The core level shifts observed in films grown at low temperature but different oxygen pressures indicate that the Rh dopant valence is governed by the oxygen stoichiometry. For nondoped $SrTiO_{3-\delta}$, each oxygen vacancy would release up to two delocalized electrons that would occupy Ti 3*d* orbitals [214]. While stoichiometric nondoped $SrTiO_3$ is a wide-gap insulator, the delocalized carriers associated with oxygen vacancies turn the material into a semiconductor and lead to a bluish hue due to the free carrier absorption in the red and near-infrared parts of the optical spectrum. However, no conductivity is measurable in Rh-doped oxygen-deficient $SrTiO_3$ films, which means that the additional electrons are responsible for the Rh valence change and the additional carriers are localized at the Rh sites. Due to the low diffusivity of oxygen vacancies in Rh:$SrTiO_3$ films, vacuum annealing is not effective at changing the color of a relatively thick film sample.

However, reduction of a thin surface layer is possible and the associated reduction of the dopant to Rh^{3+} is clearly visible after vacuum annealing a Rh^{4+}:$SrTiO_3$ sample, as shown by a comparison of spectra (A) and (D) in Fig. 4.6. Spectrum (A) corresponds to a film grown at 700°C and 10^{-1} Torr, showing a pure Rh^{4+} state. Annealing in the XPS chamber at 700°C and 10^{-6} Torr for 2 h resulted in spectrum (D), which clearly shows two components that can be assigned to Rh^{4+} and Rh^{3+}, based on literature references [205–207].

Based on the XPS analysis, most doped samples were grown at 700°C to avoid Rh evaporation. The oxygen pressure was set at either 10^{-6} Torr or 10^{-1} Torr to control the Rh valence between 3+ and 4+ states.

The growth of Ir:$SrTiO_3$ suffers from similar volatility problems because several Ir oxides are volatile at high temperature [209]. A comparison of vapor pressures of several Rh and Ir oxides are compared in Fig. 4.8. The strategy for preventing Ir depletion from a film is similar to the Rh-doped films. The growth temperature was fixed at 700°C, which reduced the Ir loss and the same 10^{-1} Torr and 10^{-6} Torr oxygen pressures were used for Ir valence control. Using the same growth temperature and pressures for both Rh- and Ir-doped films had the additional benefit of making it easier to compare the performance of the films, since the crystallinity of all films should be quite similar.

In situ film growth monitoring by RHEED showed stable specular intensity oscillations as shown in Fig. 4.9, indicating that the films grew in the layer-by-layer mode and maintained a flat surface. In layer-by-layer growth, each RHEED intensity oscillation correspond to the growth of a single unit cell layer. A record of RHEEd oscillations can thus be used to count the number of deposited unit cells. After growth, a clean step-and-terrace surface morphology was observed by AFM (Fig. 4.9 (c) and (d)).

Initial visual observation of the color change from yellow to brown for films grown at 10^{-1} Torr and 10^{-6} Torr suggested that the valence control of the Ir dopant was achieved. Images

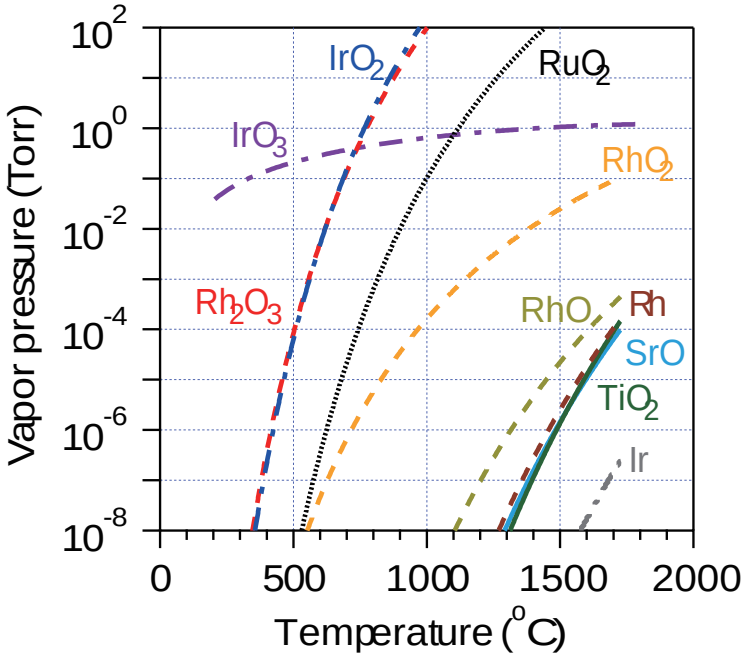

Figure 4.8: Vapor pressure of Rh, RhO, Rh_2O_3, RhO_2, RuO_2, Ir, IrO_2, IrO_3 SrO, and TiO_2 [209–211]. Oxides of Rh, Ru and Ir are significantly more volatile under typical deposition conditions than TiO_2 or SrO.

of Ir(5%):$SrTiO_3$ film samples and the corresponding optical absorption spectra are shown in Fig. 4.10, together with reference data for Ir(1%):$SrTiO_3$ and non-doped $SrTiO_3$ powders. The spectral shape of yellow Ir:$SrTiO_3$ is consistent with that of the Ir:$SrTiO_3$ powder.

XPS was used to prove that the film color change is indeed due to a change of the Ir valence. The yellow sample grown at 10^{-5} Torr contained only Ir^{4+} dopants, while the brown sample grown at 10^{-6} Torr was dominated by Ir^{3+} (Fig. 4.11). According to published reference data, the binding energy of the Ir4$f_{7/2}$ peak is 62.3-63.0 eV Ir^{4+} and 61.6-62.0 eV for Ir^{3+} [215, 216]. The unusual asymmetric core-electron line shapes in the metallic oxide IrO_2 is thought be due to many-body screening response of the 5*d* conduction electrons [220], although the other possibility is that the IrO_2 sample has a certain amount of other Ir oxidation states [221].

To measure the electrochemical response of thin film photocatalysts, the semiconductor photoelectrodes require at least modest sample conductivity or an Ohmic bottom electrode. It is therefore important to ensure that a Schottky barrier does not form at the interface between the semiconductor film and a metal electrode.

The motivation for studying Rh:$SrTiO_3$ was the relatively hydrogen evolution efficiency of the material. It was already known that Rh:$SrTiO_3$ works as a photocathode and shows cathodic photocurrent under visible light. Since electrons are extracted from a photocathode

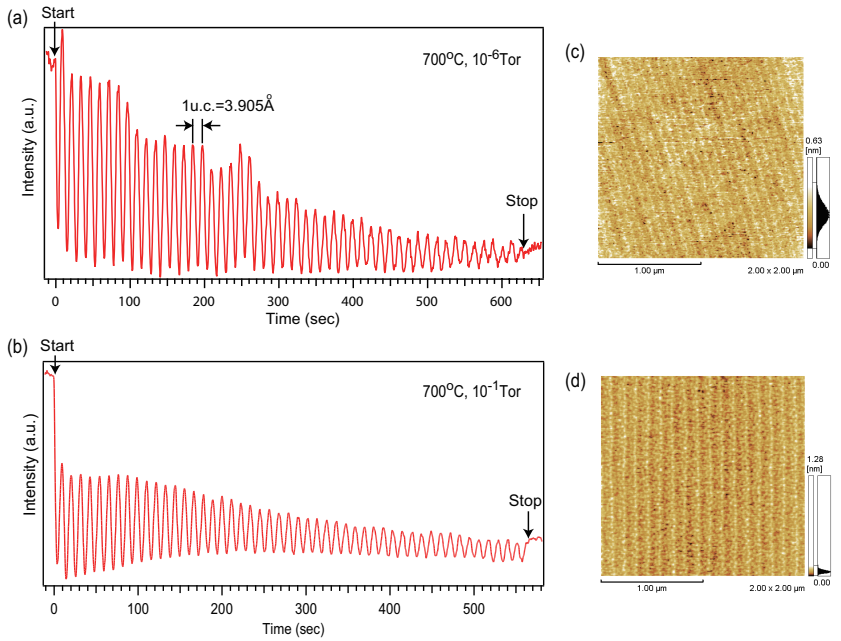

Figure 4.9: Typical RHEED intensity oscillations observed during Ir:$SrTiO_3$ thin film growth on $SrTiO_3$ (001) substrates at 700°C at (a) 10^{-6} Torr and (b) 10^{-1} Torr, together with the corresponding post-deposition AFM images ($2\times2\mu m^2$). One RHEED intensity oscillation corresponds to the growth of a single Ir:$SrTiO_3$ unit cell layer. The film thickness was 20 nm for both samples. The KrF laser fluence was $\sim$ 1 J/cm^2.

surface, it can be assumed that an electron depletion layer forms at a Rh:$SrTiO_3$ film surface when it is immersed in water and the material behaves as a *p*-type semiconductor [92]. Intrinsic $SrTiO_3$, however, is a well-known *n*-type semiconductor. To avoid Schottky barriers, a low work function metal, such as aluminum, is commonly used to obtain Ohmic contacts with *n*-type $SrTiO_3$, while a high work function metal, e.g., gold, would be used for *p*-type oxide semiconductors. Al/Rh:$SrTiO_3$ and Au/Rh:$SrTiO_3$ junctions were therefore prepared to determine from the current-voltage (I-V) characteristics if the contacts are Ohmic or not.

The I-V characteristics of various film and metal combinations are shown in Fig. 4.12. It is clear that the Au/Rh^{4+}:$SrTiO_3$ junction is fully Ohmic with a linear I-V plot. However, a Schottky-like behavior is seen for the Al/Rh^{4+}:$SrTiO_3$ junction. considering the work functions of Al and Au, which are 4.1-4.3 eV and 5.1-5.4 eV, respectively [222], the I-V characteristics indicate that the Fermi level of Rh^{4+}:$SrTiO_3$ is over $\sim$ 1 eV deeper than that of non-doped $SrTiO_3$. Rh^{4+}:$SrTiO_3$ may thus indeed have a *p*-type character, as suggested by the photocathode behavior. On the other hand, Rh^{3+}:$SrTiO_3$ formed an Ohmic contact with both Al and Au electrodes (Fig 4.12 (c) and (d)), which means that the Fermi level of Rh^{3+}:$SrTiO_3$ is higher, located roughly midway

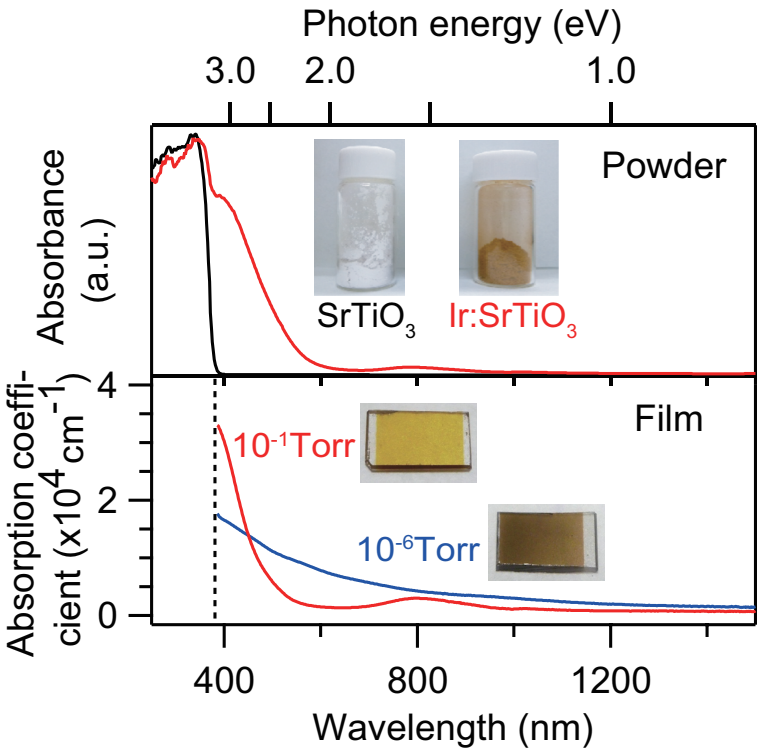

Figure 4.10: (a) Absorption spectra of Ir(1%):$SrTiO_3$ and $SrTiO_3$ powders calculated from diffuse reflectance spectra. (b) Absorption spectra of Ir(5%):$SrTiO_3$ films grown at 700°C at 10^{-1} Torr and 10^{-6} Torr, together with representative thin film sample images showing a systematic film color change from brown to yellow.

between those of Rh^{4+}:$SrTiO_3$ and intrinsic $SrTiO_3$. It is quite unusual for a semiconductor to form an Ohmic contact with metals that differ in work functions by about 1 eV (Au and Al), but one possibility suggested by the XPS results is that metallic Rh exists on the surface of the Rh^{3+}:$SrTiO_3$ films.

Metal contact electrodes on the edge of a thin film can be used in electrochemical measurements if the film has reasonably high conductivity. However, for the Rh- and Ir-doped films, the conductivity can be quite low, especially in dark conditions when no photocarriers are present. It may thus be necessary to use a metallic back electrode, in which case the current path length would be determined by the film thickness (nm scale), rather than the lateral dimensions (mm scale). While it is easy to change the material of a metallic contact electrode on the film surface, the choice of a bottom electrode material is more difficult. The observation that Au forms an Ohmic contact with both Rh^{4+}:$SrTiO_3$ and Rh^{3+}:$SrTiO_3$ suggested that the bottom electrode should have a high work function, close to that of gold. However, there are no suitable substrate materials that would be metallic and have a work function of ~ 5 eV. Due to this, Sr_2RuO_4 was

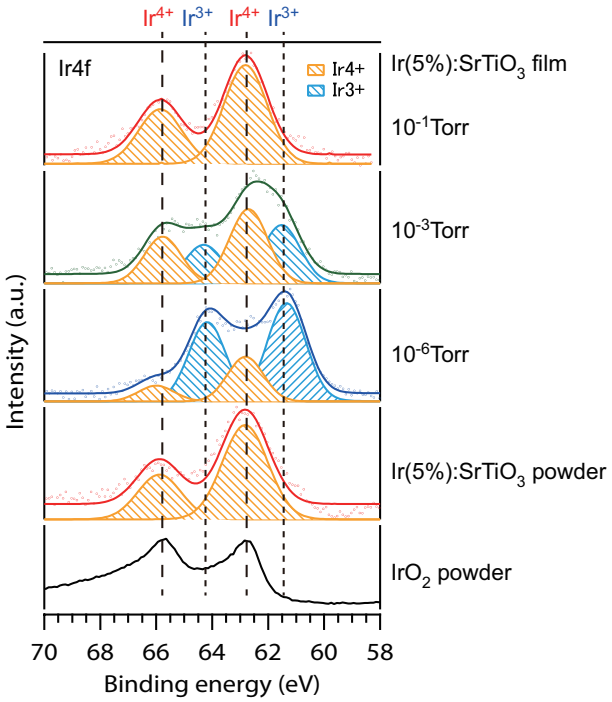

Figure 4.11: Ir4f core level XPS spectra of Ir(5%):$SrTiO_3$ films deposited at various oxygen pressure at 700°C, Ir(5%):$SrTiO_3$, and IrO_2 powders. All spectra were measured with a Mg K_α $h\nu$ = 1253.6 eV x-ray source. The $Ir4f_{7/2}$ peak reference positions for Ir^{4+} and Ir^{3+}, shown at the top of the figure, were taken from Refs. [215, 216]. The binding energies were referenced to the C1*s* core-level peak at 284.8 eV [217–219].

selected as the bottom electrode layer. It has a work function of ~ 5.2 eV, it is lattice matched with $SrTiO_3$, and thermally stable.

The Sr_2RuO_4 films were grown at 900°C at an oxygen pressure of 10^{-1} Torr with a KrF excimer laser operating at 2 Hz and a fluence of 1.1 J/cm^2. A $SrRuO_3$ target was used for the deposition. The electrode layers were atomically flat with a step-and-terrace surface, and the correct *c*-axis oriented crystal structure as shown in Fig. 4.13(a,b). The XRD fringe pattern fitting for the Sr_2RuO_4 (006) diffraction peak gave a film thickness estimate of 25 ML = 16 nm, as expected. Reciprocal space mapping (Fig. 4.14) showed that the in-plane lattice constant of the Sr_2RuO_4 film was the same as that of the $SrTiO_3$ substrate, meaning that the Sr_2RuO_4 film was epitaxially grown on $SrTiO_3$.

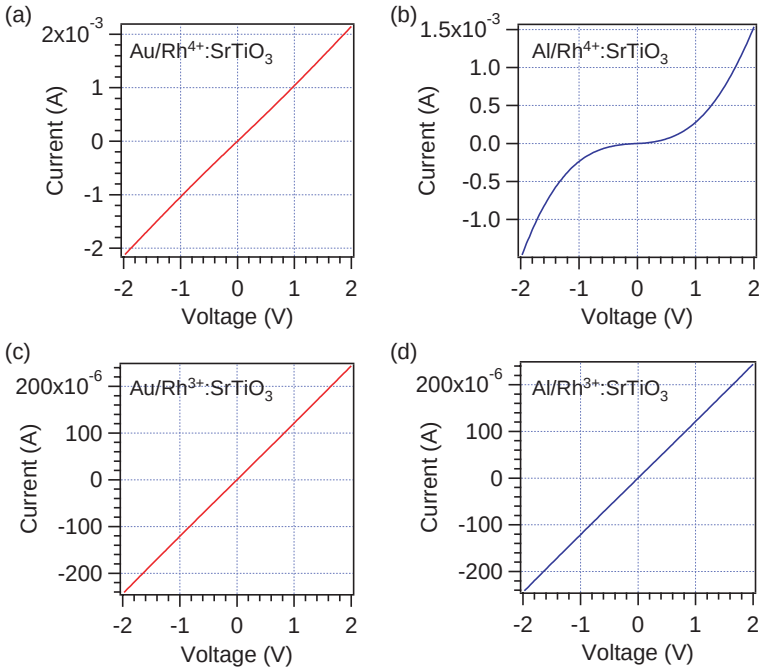

Figure 4.12: Current-Voltage curves of (a) Au/Rh^{4+}:$SrTiO_3$, (b) Al/Rh^{4+}:$SrTiO_3$, (c) Au/Rh^{3+}:$SrTiO_3$, and (d) Al/Rh^{3+}:$SrTiO_3$ junctions. The Rh:$SrTiO_3$ film thickness was 100 nm in all cases.

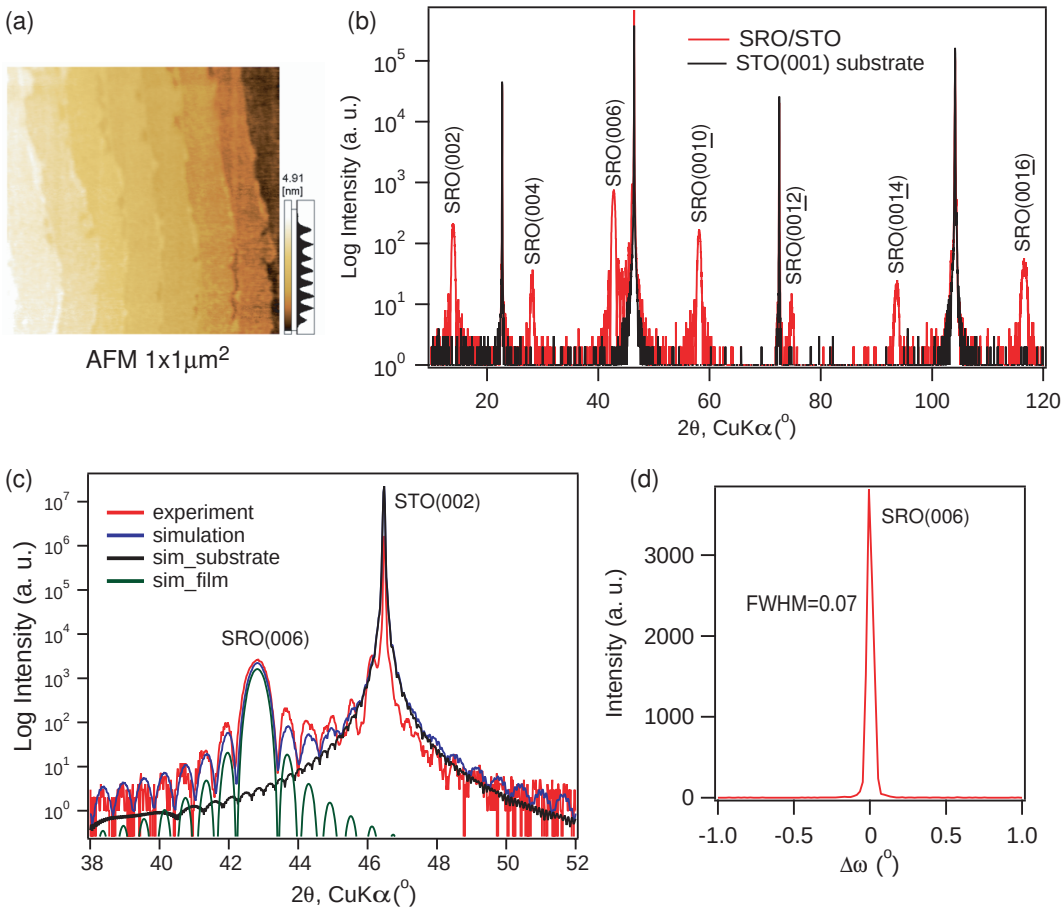

Figure 4.13: (a) AFM image and (b) XRD patterns of Sr_2RuO_4 (25 ML) on $SrTiO_3$. (c) Narrow scan around the Sr_2RuO_4 (006) peak compared with simulated profiles for the assumed structure of 25 ML Sr_2RuO_4 on $SrTiO_3$. (d) Rocking curve of the Sr_2RuO_4 (006) peak.

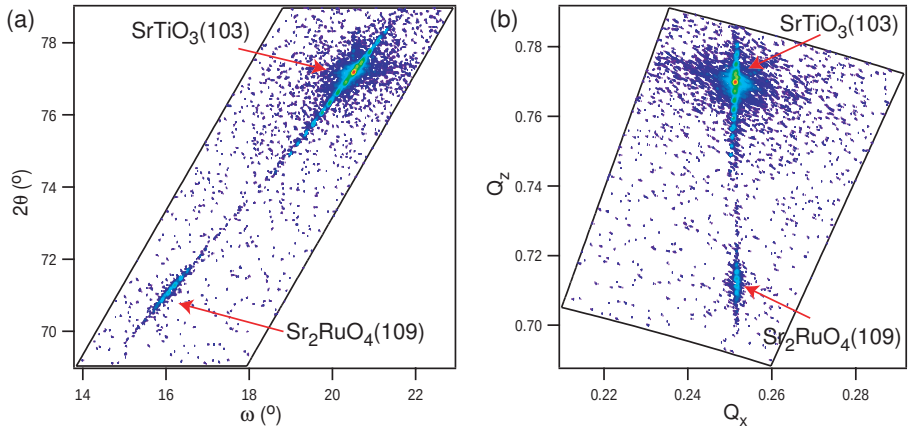

Figure 4.14: Reciprocal space mapping of Sr_2RuO_4(25ML)/$SrTiO_3$ (001). (a) $2\theta - \omega$ plot and (b) $Q_x - Q_z$ plot, showing that the in-plane lattice constant of the Sr_2RuO_4 film grew coherently on the $SrTiO_3$ substrate.

RHEED intensity oscillations were clearly observed during the growth of the electrode layer and during subsequent Rh:$SrTiO_3$ deposition on the Sr_2RuO_4 layer, as shown in Fig. 4.15. AFM (Fig. 4.16) showed a clean step-and-terrace surface morphology for the final photocatalyst film surface. Electrical contact with the Sr_2RuO_4 film was made with silver paste (Fujikurakasei; D-550) at the edge of the sample as shown in Fig. 2.12.

Obtaining Ohmic contacts with the Ir:$SrTiO_3$ films proved to be much easier than for Rh:$SrTiO_3$. As shown by the linear I-V plots in Fig. 4.17, Ohmic contact formed with aluminum for both Ir^{4+} and Ir^{3+} dopant states. This indicates that the Fermi level of Ir:$SrTiO_3$ is closer to that of nondoped $SrTiO_3$ and there is no need for a specific metallic back electrode layer. Instead conducting Nb:$SrTiO_3$ (work function: $\sim$ 4.2 eV [237]) substrates can be used directly for preparing Ir:$SrTiO_3$ film samples for photoelectrochemical characterization.

In conclusion, the optimal growth conditions for both Rh- and Ir-doped $SrTiO_3$ films were similar, except that for Ir:$SrTiO_3$ films could be grown directly on commercially available metallic Nb(0.5wt%):$SrTiO_3$ (001) substrates, while for Rh:$SrTiO_3$ a Sr_2RuO_4 electrode needed to be inserted between a nondoped substrate and the film. The conductivity of Nb:$SrTiO_3$ substrates depends on the Nb doping level. Although the best metallic character can be obtained with heavily-doped Nb(0.5wt%):$SrTiO_3$ substrates, the surface flatness is much better for Nb(0.05wt%):$SrTiO_3$ crystals. The 0.05 wt% doping level was therefore chosen for the metallic substrates. The resistivity and the carrier density of Nb(0.05wt%):$SrTiO_3$ are $7 \sim 10 \times 10^{-2}$ Ωcm and $1 \sim 2 \times 10^{19}$ cm^{-3}, while those of Nb(0.5wt%):$SrTiO_3$ are $3 \sim 7 \times 10^{-3}$ Ωcm and $1 \sim 2 \times 10^{20}$ cm^{-3} [238]. An InGa alloy, consisting of In (Nilaco; 4N) 1g and Ga (Nilaco; 6N) 3g was used for making contacts with the Nb:$SrTiO_3$ substrates.

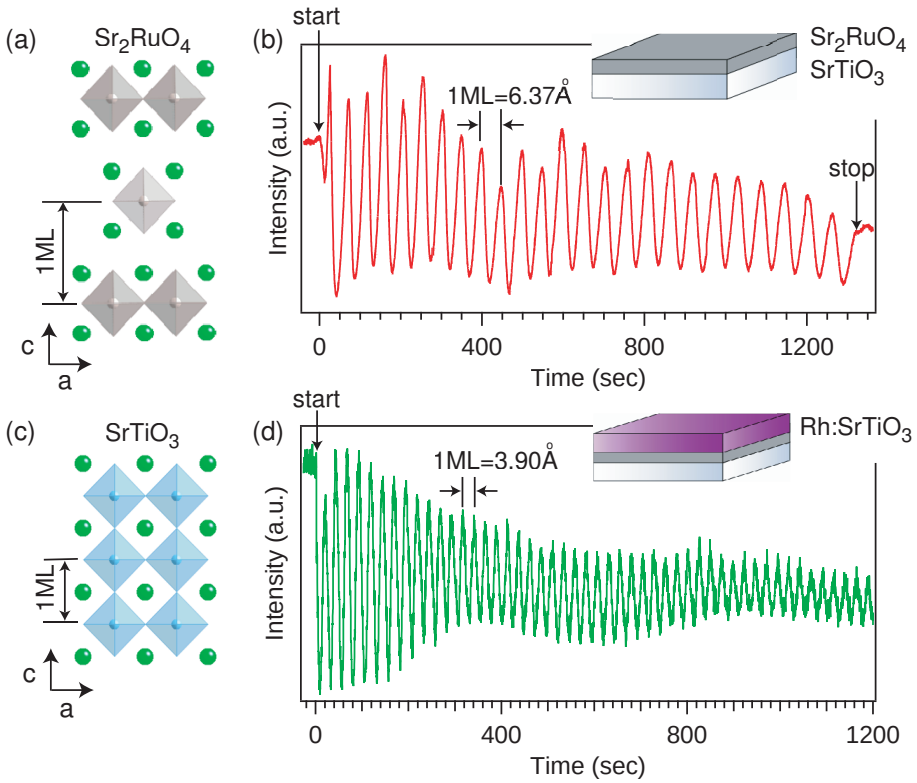

Figure 4.15: The crystal structures of (a) Sr_2RuO_4 and (c) $SrTiO_3$. RHEED oscillations during (b) $SrRuO_3$ and (d) Rh(5%):$SrTiO_3$ deposition.

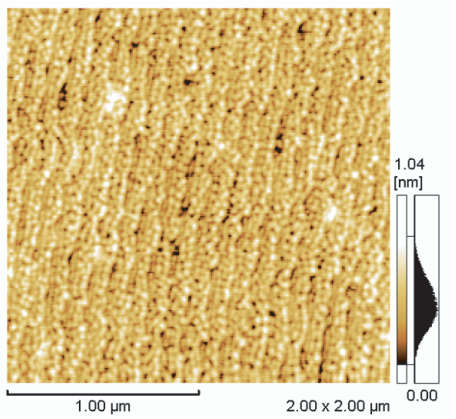

Figure 4.16: AFM image (2×2 μm^2) of Rh(5%):$SrTiO_3$(20nm)/Sr_2RuO_4(16nm)/$SrTiO_3$.

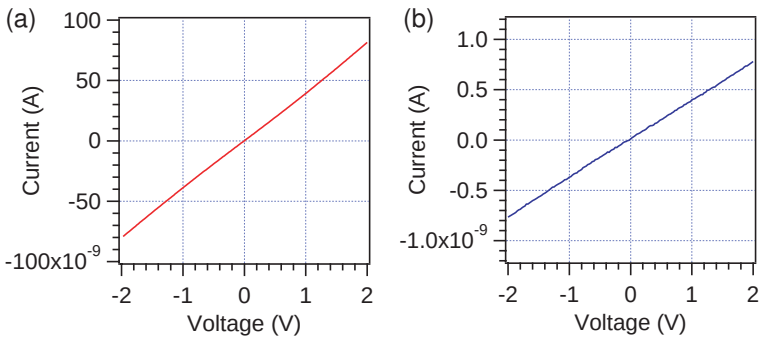

Figure 4.17: Current-Voltage curves of (a) Al/Ir^{4+}:$SrTiO_3$, (b) Al/Ir^{3+}:$SrTiO_3$ junctions. The Ir:$SrTiO_3$ film thickness was 200 nm.

4.3 Electronic structure of metal-doped $SrTiO_3$

Photocatalytic reactions on a semiconductor surface are initiated by nonequilibrium photocarriers generated in the semiconductor by light irradiation. The photoexcited electrons quickly relax to the conduction band minimum (CBM) and holes to the valence band maximum (VBM). The photocarriers are generated throughout the thickness of the photocatalyst film due to the low absorption coefficient and large absorption length of visible light in a doped semiconductor. The carriers generated in the bulk of the semiconductor need to be transported to the surface to participate in the electrochemical reactions at the liquid interface. The driving force for the migration of carriers to the film surface is an electric field associated with the formation of a depletion or accumulation layers at the solid - liquid interface. For nominally *p*-type materials with a deep Fermi level, an accumulation layer usually forms at the surface, forcing photogenerated electrons to the surface. Electrons at the CBM are responsible for cathodic reactions, i.e., hydrogen generation in the water splitting reaction. for *n*-type semiconductors, the surface is usually depleted and photogenerated holes migrate to the surface, driving anodic reactions, such as oxygen evolution from water.

The photocarrier generation and migration are thus affected by the position of the conduction and valence band edges, and presence of in-gap states due to defects, dopants, and surface states. The electronic structure needs to be considered when evaluating the efficiency of carrier generation, lifetime, migration to the surface, and the role in chemical reactions at the surface for a particular material.

In this study, the electronic structure, especially the impurity level positions of Rh- and Ir-doped $SrTiO_3$ were studied by X-ray spectroscopy and first-principles calculations.

4.3.1 Electronic structure of Rh:$SrTiO_3$

Powder samples of $SrRh_xTi_{1-x}O_3$ with x = 0, 0.01, 0.03, and 0.05 were synthesized by conventional solid-state reaction. The powders were pelletized at 10 MPa and calcined at 1200°C for 12 h, yielding purple Rh^{4+}:$SrTiO_3$ samples. Reduced Rh^{3+}:$SrTiO_3$ pellets were obtained by annealing a purple Rh^{4+} pellet in flowing H_2 gas at atmospheric pressure and 300°C for 2 h. Photographs of the pellet samples are shown in Fig. 4.18. The samples were confirmed to be single phase by x-ray diffraction (Fig. 4.2)

The Rh valence was confirmed by XPS, measured with JPS-9010MC (JEOL) and a Mg K_α laboratory X-ray source. The binding energies were referenced to the Ti $2p_{3/2}$ peak position. Deconvolution of the Rh core level peak profiles showed that the purple Rh:$SrTiO_3$ contained only Rh^{4+}, while the yellow Rh:$SrTiO_3$ sample consisted of a mixture of 90.4% of Rh^{3+} and 9.6% of Rh^{4+}. Although the yellow Rh:$SrTiO_3$ pellet contained ~10% of Rh^{4+}, the 0.05at% of Rh^{4+} in $SrTiO_3$ is negligible from the point of view of XAS/XES analysis used in this study.

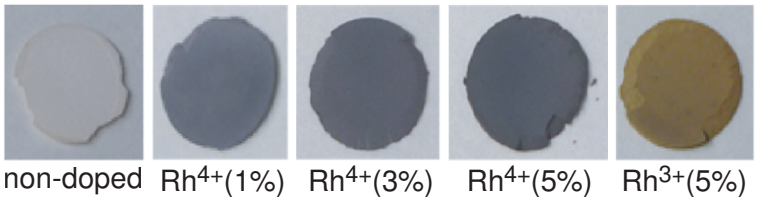

Figure 4.18: Pellet samples used for electronic structure measurements. From the left: Rh^{4+}(x at%):$SrTiO_3$ (x = 0, 1, 3, 5) and Rh^{3+}(5 at%):$SrTiO_3$.

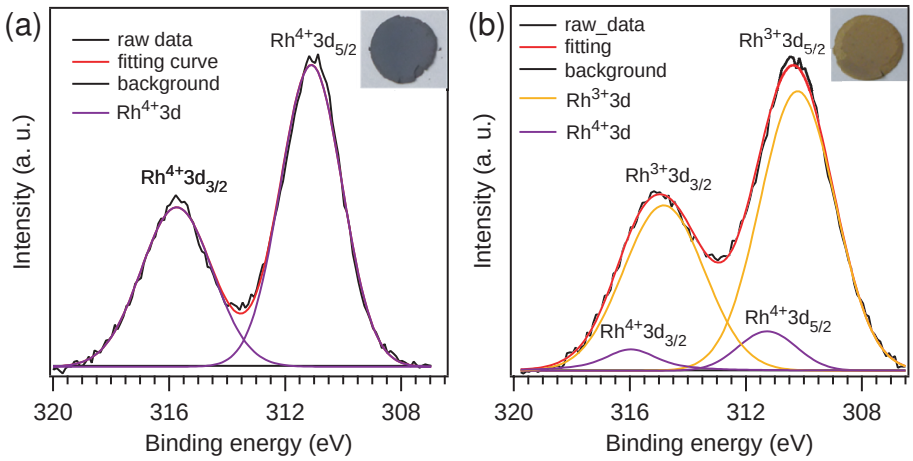

Figure 4.19: XPS spectra of Rh3d core levels for (a) purple and (b) yellow Rh:$SrTiO_3$ pellet samples. The same samples were used for the XAS/XES experiments. The purple Rh:$SrTiO_3$ has only Rh^{4+}, while yellow Rh:$SrTiO_3$ has 90.4% of Rh^{3+} and 9.6% of Rh^{4+}. The binding energy was referenced to Ti2$p_{3/2}$ = 459.1 eV. The powder samples were attached on carbon tape to reduce charging during the XPS measurement.

The spin states of $4d$ electrons in Rh:$SrTiO_3$ were determined by electron spin resonance (ESR). The ESR spectra for purple and yellow Rh:$SrTiO_3$ pellets in Fig. 4.20 were measured at a microwave frequency of 9.4 GHz, at 77 K in vacuum [97].

Since the spectrum of the yellow Rh^{3+}:$SrTiO_3$ sample shows no peaks in the ESR spectrum, it is possible to conlcude that the spin number is zero and there are no unpaired electrons. For a $4d^6$ electron configuration of Rh^{3+}, the lack of unpaired electrons means that the dopant ion is in the low-spin state corresponding to a $4d^6_{t2g}$ configuration (Fig. 4.20 (b)).

Assuming that the Rh atoms are substituting at the octahedral Ti site, possible spin configurations for Rh^{4+} are $t^5_{2g}e^0_g$ (low-spin) and $t^3_{2g}e^2_g$ (high-spin). Since Rh^{4+}:$SrTiO_3$ showed only a single peak in the ESR spectrum, indicating that there is one unpaired electron in the material, it is impossible to say from the ESR data whether the ion is in a low- or high-spin state However, the low-spin state is more common for $4d$ and $5d$ ions octahedrally coordinated by O^{2-} anions due to the large crystal field splitting [239]. For example, $Rh^{4+/3+}$ possesses the low-spin configuration in $La_{1-x}M_xRhO_3$ (M=Ca, Sr, and Ba) compounds [240]. The assumption that Rh^{4+} also has a low-spin configuration in Rh:$SrTiO_3$ is therefore reasonable.

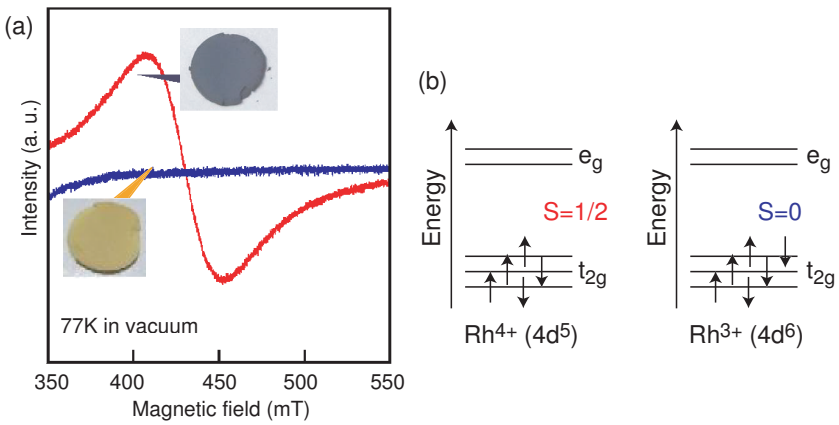

Figure 4.20: (a) ESR spectra of purple and yellow Rh(1at%):$SrTiO_3$ measured at 9.4 GHz and 77 K in vacuum [97], indicating that the yellow Rh:$SrTiO_3$ does not have unpaired electrons, while the purple Rh:$SrTiO_3$ does. This result supports the the electronic structure assignments of low-spin Rh^{4+} $4dt^5_{2g}$ ((b) left) and low-spin Rh^{3+} $4dt^6_{2g}$ ((b) right).

Approximate estimates for the locations of dopant-related in-gap levels in Rh:$SrTiO_3$ can be made based on UV-Vis-NIR absorption spectra calculated from diffuse reflection spectra with the Kubelka-Munk method. Absorption spectra for the purple and yellow Rh:$SrTiO_3$ samples are shown in Fig. 4.21, together with schematic energy level diagrams. The absorption edge at 380 nm corresponds to the band gap excitation of nondoped $SrTiO_3$ (E_g = 3.2 eV). The absorption peak at 580 nm corresponds to excitations from the O2p valence band (VB) to an unoccupied Rh^{4+} acceptor level (Fig. 4.21 (b)), while the 430 nm shoulder is due to carrier excitations from occupied Rh-related states at the top of the valence band to the conduction band. A weak $d - d$ transition (state A to B) can be observed at around 1000 nm [59, 92, 241].

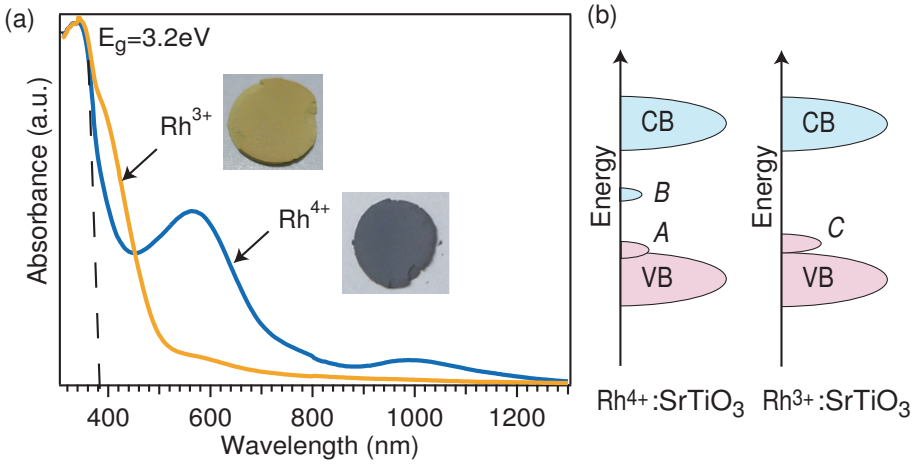

Figure 4.21: (a) UV-Vis-NIR absorption spectra and (b) schematic illustration of the electronic structures of Rh^{4+}:$SrTiO_3$ and Rh^{3+}:$SrTiO_3$. The Rh doping level was 1 at%. States A and C are assumed to be occupied Rh donor levels, while state B is an unoccupied acceptor level.

The unoccupied states of Rh:$SrTiO_3$ was studied by O1s XAS. The spectra for nondoped $SrTiO_3$, Rh^{3+}:$SrTiO_3$, and Rh^{4+}:$SrTiO_3$ with several doping levels are compared in Fig. 4.22. Following the dipole selection rules, these spectra probe transitions from an O1s core level to an unoccupied O2p state that is hybridized with Ti3d or Rh4d states. The main peak at around 531 eV corresponds to the conduction band that is composed mainly of Ti3d states hybridized with the O2p states [242, 243]. An unoccupied in-gap state can be seen at ~ 1.5 eV below the CB edge in the Rh^{4+} samples. The intensity of the peak follows the doping level. No in-gap absorption peaks were found in the spectra of Rh^{3+}(5at%):$SrTiO_3$ and nondoped $SrTiO_3$ samples. The in-gap 528.2 eV peak can thus be assigned to an unoccupied Rh^{4+} acceptor level, in accordance with the schematic energy level diagram inferred from the optical absorption spectra [59, 92, 241]. However, unlike Sc:$SrTiO_3$, there was no peak corresponding to holes created at the VB maximum [242, 243].

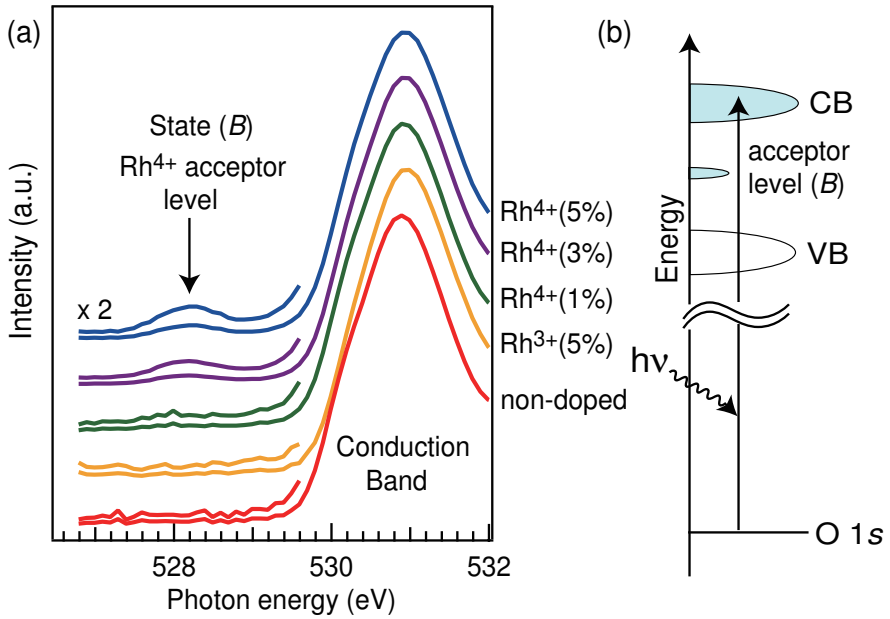

Figure 4.22: (a) O1*s* X-ray absorption spectra of Rh^{4+}(*x* at%):$SrTiO_3$ (*x* = 0, 1, 3, 5) and Rh^{3+}(5 at%):$SrTiO_3$. (b) Energy level diagram for the transitions probed by the O1*s* XAS measurement.

The occupied valence band and in-gap states were probed by XES. Fig. 4.23 shows O1*s* XES spectra measured at an excitation energy of 530.9 eV. The main peaks at 523.5 and 526 eV belong to the $SrTiO_3$ valence band and correspond to transitions from bonding and nonbonding O2*p* states to the O1*s* core level [244]. The feature at 530.9 eV is due to elastically scattered excitation X-rays. The interesting part of the spectrum is the fluorescence intensity shoulder between 527 to 528.3 eV. The intensity of this fetaure increases systematically with the Rh content and is due to $Rh^{4+/3+}$ dopant t_{2g} photocarrier donor levels. A spectral weight shift to higher emission energy by $\sim$ 0.5 eV is evident for the reduced Rh^{3+}:$SrTiO_3$ sample. The Rh donor levels close to the VB maximum of $SrTiO_3$ can also be seen as a shoulder close to the band gap excitation energy in the UV-vis-NIR absorption spectra of the $Rh^{4+/3+}$:$SrTiO_3$ samples in Fig. 4.21.

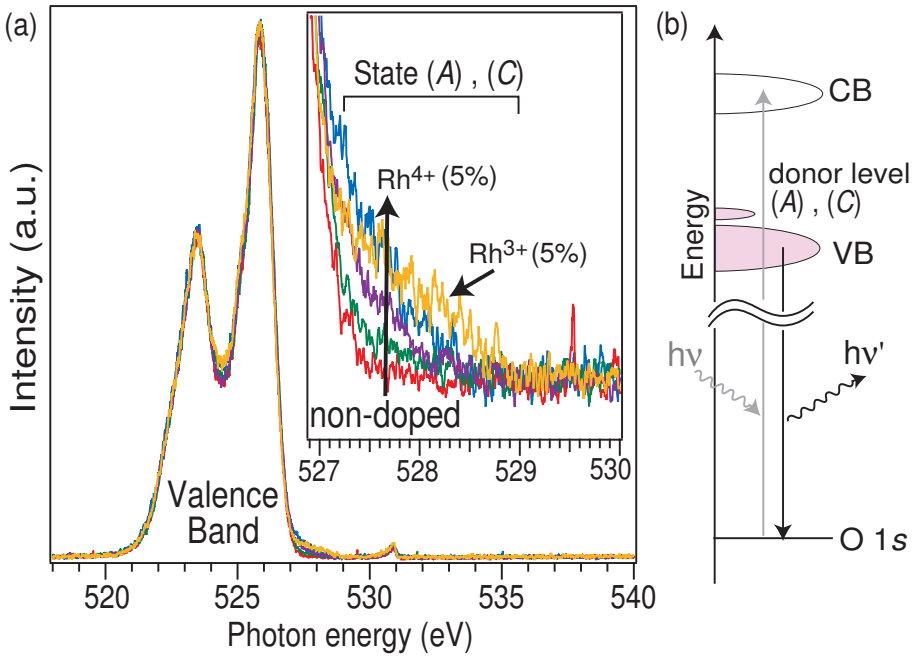

Figure 4.23: (a) O1*s* x-ray emission spectra of Rh^{4+}(*x* at%):$SrTiO_3$ (*x* = 0, 1, 3, 5), Rh^{3+}(5 at%):$SrTiO_3$, and non-doped $SrTiO_3$, taken at an x-ray energy of 530.9 eV. The inset shows an expansion of the top of the valence band. (b) Schematic view of the transitions involved in O1*s* XES.

The existence of an unoccupied Rh^{4+} mid-gap photocarrier acceptor level at 1.5 eV below the conduction band bottom indicates that the Fermi level of Rh^{4+}:$SrTiO_3$ is deeper than the mid-gap level position and, thus, that Rh:$SrTiO_3$ may have *p*-type character. It is important to note that the Fermi level position for nondoped $SrTiO_3$ is within ~ 300 meV of the conduction band bottom, and a Fermi level shift by more than 1.5 eV in $SrTiO_3$ is quite extraordinary.

Fermi level shifts are generally observable in XPS by a systematic shift of all core level peaks by an equal amount. A Fermi level shift between $SrTiO_3$ and Rh:$SrTiO_3$ should thus be observable as a systematic shift of O1*s*, Ti2*p*, Sr3*d*, and Sr3*p* core level binding energies. Fig. 4.24 shows the XPS results for $SrTiO_3$ and $Rh^{4+/3+}$:$SrTiO_3$ powder samples. As expected, systematic peak shifts were observed for all core levels. The Fermi level shifts relative to non-doped $SrTiO_3$ were calculated from the Ti2*p*, yielding 0.8 eV for Rh^{3+}:$SrTiO_3$ and 2.0 eV for Rh^{4+}:$SrTiO_3$. However, these binding energy shifts may include systematic errors due to sample charging, because of the insulating nature of $SrTiO_3$.

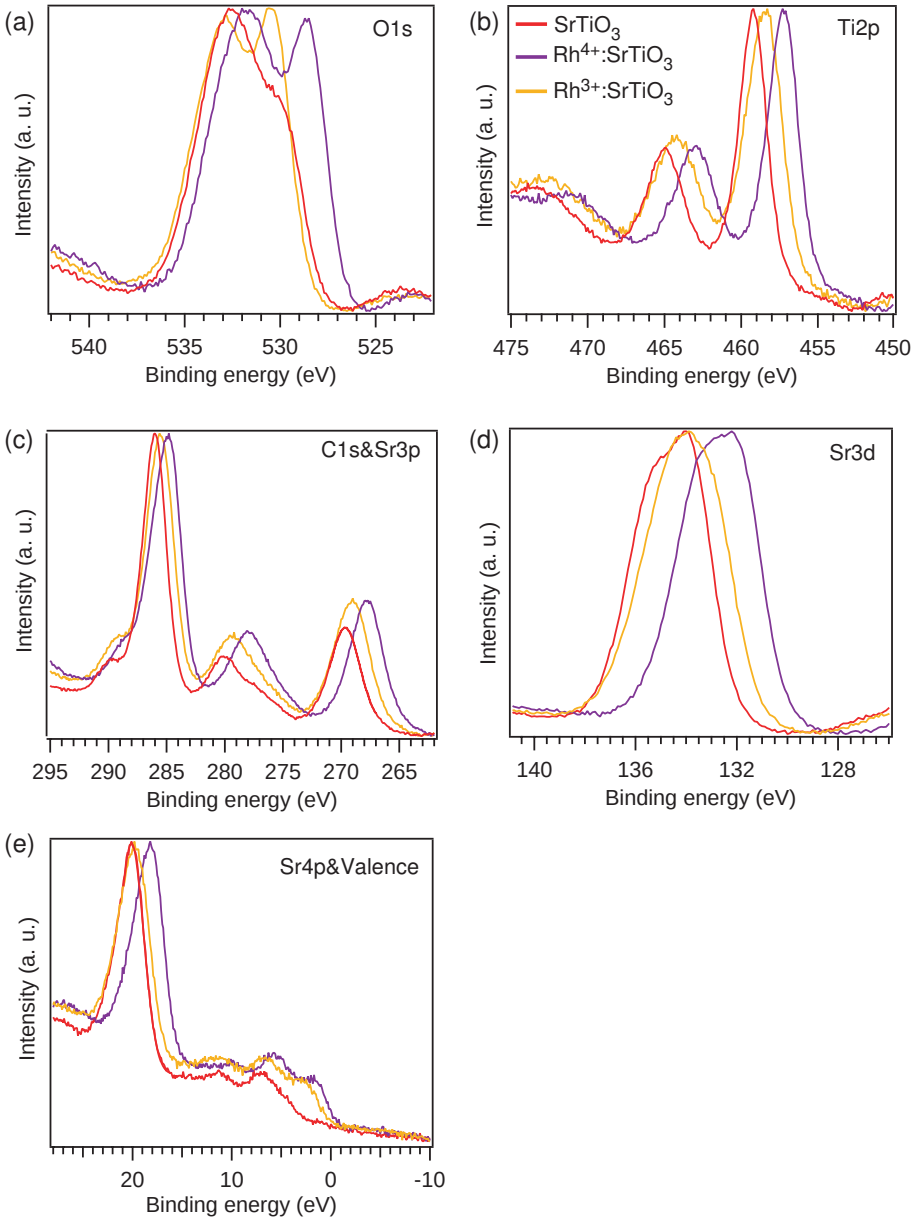

Figure 4.24: XPS spectra of (a) O2*p*, (b) Ti2*p*, (c) C1*s* and Sr3*p*, (d) Sr3*d*, and (e) Sr4*p* and valence. Red, purple, and yellow lines correspond to non-doped $SrTiO_3$, Rh^{4+}:$SrTiO_3$, and Rh^{3+}:$SrTiO_3$, respectively. The binding energy was referenced to Au4$f_{7/2}$ = 84.0 eV.

The assignment of spectral features observed in optical absorption and X-ray spectra was based on first-principles density of states (DOS) calculations done with the VASP code [245,246]. The calculations were done by Prof. K. Akagi at Tohoku University. A $3 \times 3 \times 3$ $SrTiO_3$ unit cell was used with one of the Ti^{4+} sites substituted with a Rh^{4+} ion, corresponding to a doping level of 3.70at% (Fig. 4.25 (a)). The Rh^{3+}:$SrTiO_3$ system was modeled by injecting an excess electron with the same amount of uniform background counter charge. As shown in Fig. 4.25 (b), the added electron was localized in the vicinity of the Rh site.

The PAW method [247,248] was used for effective atomic potentials and the cutoff energy of the plane wave basis set was 300 eV. A $2 \times 2 \times 2$ Monkhorst-Pack k-point mesh [249] was used. Gaussian smearing was applied with a width of 0.2 eV. The lattice constant was set to the experimental value of 3.905 Å [250]. Structure optimization was done using the HSE06 functional until the maximum force became less than 0.03 eV/Å. The obtained structures were almost the same for pure $SrTiO_3$, Rh^{4+}:$SrTiO_3$, and Rh^{3+}:$SrTiO_3$ within a margin of 0.02 Å. The DOS data were calculated based on these optimized structures.

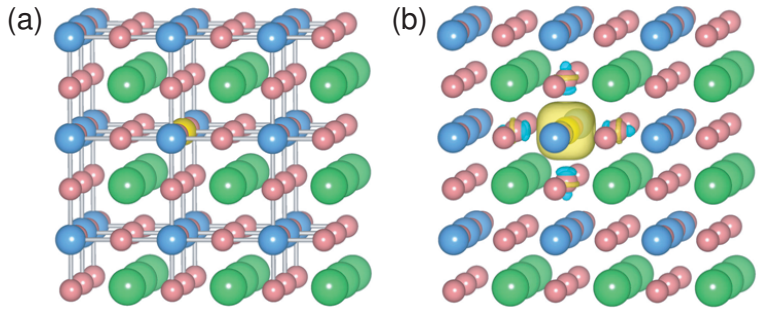

Figure 4.25: (a) The $3 \times 3 \times 3$ $SrTiO_3$ unit cell showing Sr (green), Ti (blue), O (red), and Rh (yellow). (b) The charge difference distribution, $d\rho(r)$, of the Rh:$SrTiO_3$ system, with $d\rho(r) = \rho(r; N+1) - \rho(r; N)$, where N and $N+1$ are the number of electrons in the cell. The yellow and blue isosurfaces mark regions with increased and decreased electron density, respectively. The isovalue is ±0.01 e/Å^3, and the amount of charge inside this isosurface is -1.04 e.

The hybrid HSE06 functional [252] was used in the simulation. A GGA/PBE96 [251] functional was also tested, but it was found to underestimate the band-gap width (ca. 1.5 eV for $SrTiO_3$) and failed to describe the gap states. The hybrid HSE06 functional accurately reproduced the band-gap width (ca. 3.0 eV for $SrTiO_3$) and successfully described both the in-gap and mid-gap states (Figs .4.26 and 4.27).

The main advantage of the HSE06 functional is that it includes the Hartree-Fock exchange interactions in the calculation. The fact that only the HSE calculation reproduces a Rh^{4+} mid-gap acceptor level implies that the Hartree-Fock exchange interaction induces the mid-gap acceptor level in Rh^{4+}:$SrTiO_3$. The Hartree-Fock exchange interaction affects the energy level positions between up- and down-spin states in the case that there is unequal number of up- and down-spin electrons in the material. Thus, $Rh^{3+}(4d^6, S = 0)$ produces up- and down-spin states at the same energy levels, unlike $Rh^{4+}(4d^5, S = 1/2)$. Also, the higher-spin states of the $Rh^{4+/3+}$:$SrTiO_3$ system were less stable than the low-spin state, consistent with the experimental results (Fig. 4.20).

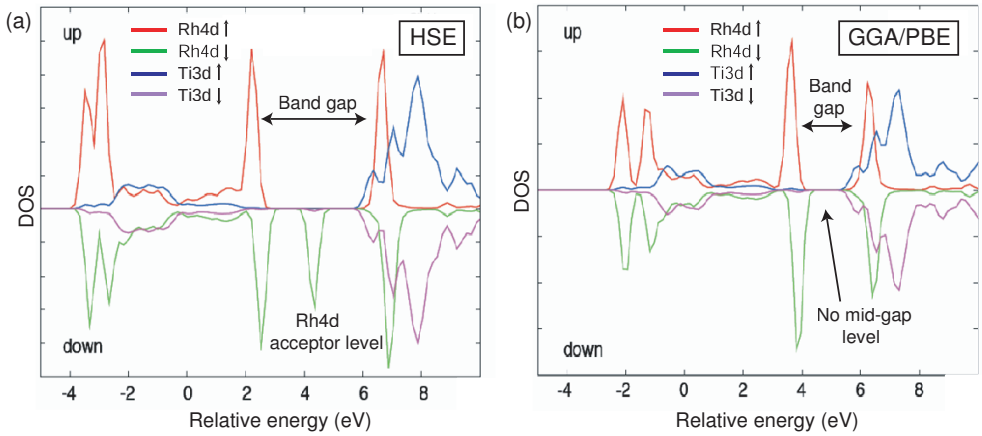

Figure 4.26: PDOS of Ti3*d* and Rh4*d* for Rh^{4+}:(3.7at%):$SrTiO_3$ obtained by first-principles calculations using (a) the HSE06 functional and (b) the GGA/PBE96 functional. Up and down spin states are shown as blue and purple lines for Ti3*d*, and red and green lines for Rh4*d*. The Rh4*d* PDOS is shown on an expanded scale to emphasize the energy level positions. Up and down spin states are distinguished in this system due to the existence of an unpaired electron at the Rh^{4+} site.

The calculated DOS for $Rh^{4+/3+}$(3.7at%):$SrTiO_3$ and non-doped $SrTiO_3$ are shown in Fig. 4.28 (a) with an expanded view (×10) in Fig. 4.28 (b), highlighting the partial density of states (PDOS) of Rh. The PDOS plots for Ti, Sr, and O, together with the calculated Fermi level positions, are also shown for each case. The calculation shows that two in-gap features related to the Rh4*d* orbitals exist for isovalent Rh^{4+} substitution at the Ti^{4+} site in $SrTiO_3$, with peaks appearing close

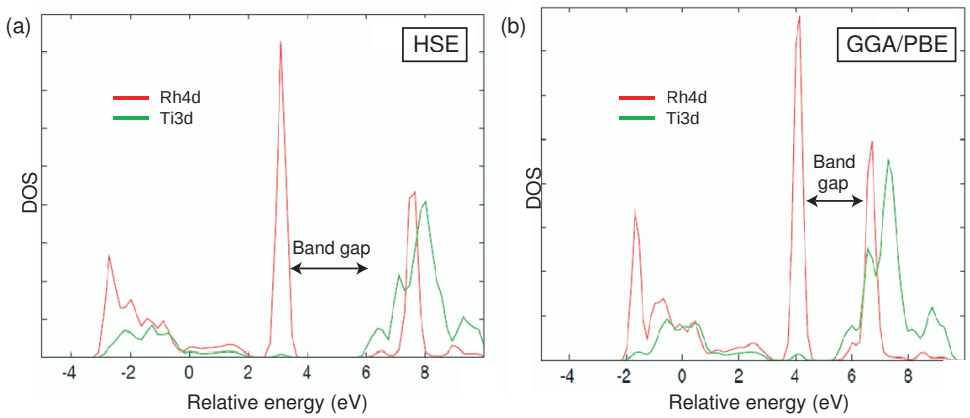

Figure 4.27: PDOS of Ti3*d* and Rh4*d* for Rh^{3+}:(3.7at%):$SrTiO_3$ obtained by first-principles calculations using (a) the HSE06 functional and (b) the GGA/PBE96 functional. The Ti3*d* and Rh4*d* states are shown with green and red lines, respectively. The PDOS of Rh4d is expanded to emphasize the energy level positions. Up and down spin states are not distinguished in this system, since both up and down spin states are located at the same energy positions due to the absence of any magnetic anisotropy in this system.

to the VB maximum and at approximately the mid-gap position, labeled *A* and *B*, respectively. For Rh^{3+}, only a single in-gap level was found close to the VB maximum, labeled *C* in Fig. 4.28 (b). The calculation shows that the Fermi level shifts by ~0.7 eV between Rh^{4+}:$SrTiO_3$ and Rh^{3+}:$SrTiO_3$.

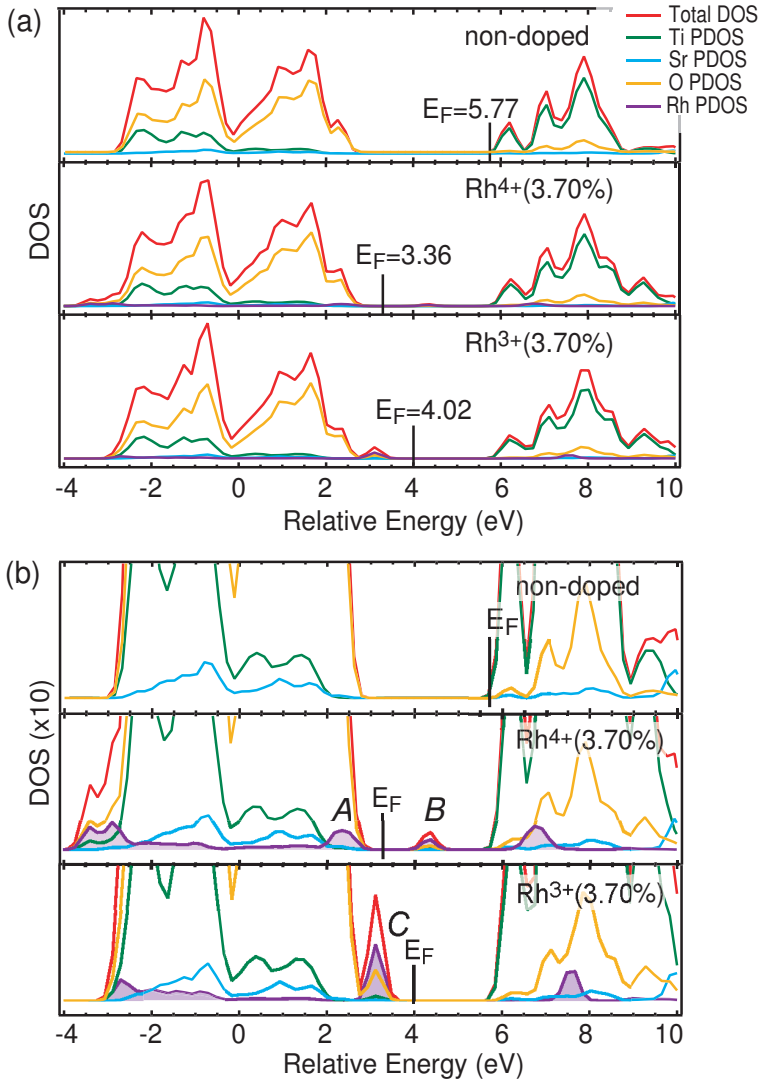

Figure 4.28: Density of states obtained by first-principles calculations for non-doped $SrTiO_3$ and $Rh^{4+/3+}$ (3.7at%):$SrTiO_3$. The total DOS and PDOS are shown for each sample. (b) An expanded view (×10) of the data with highlights marking the Rh-related PDOS. The Rh^{4+} donor and acceptor levels are marked with *A* and *B*, respectively. The Rh^{3+} donor level is marked with *C*. The calculated Fermi level positions are marked with E_F.

The charge density isosurfaces corresponding to the states labeled *A*, *B*, and *C* are shown in Fig. 4.29. It is obvious that lobes surrounding the Rh atom for these states spread into the directions between the O atoms, indicating that the states are derived from the Rh4*d* t_{2g} orbitals. The Rh PDOS peaks in the conduction band region, at a relative energy of 6.5 eV for the Rh^{4+} sample and 7.5 eV for the Rh^{3+} sample, are derived from Rh4*d* e_g orbitals. The mid-gap level *B* is an unoccupied down-spin state. This state is destabilized by the short-range Hartree-Fock exchange interaction in the HSE06 functional due to the existence of an unpaired electron at the Rh^{4+} (d^5) site; the Rh^{3+} (d^6) sample does not have an unpaired electron and thus no mid-gap state. The calculated molecular energy diagrams for Rh^{4+} and Rh^{3+} dopants are summarized in Fig. 4.30.

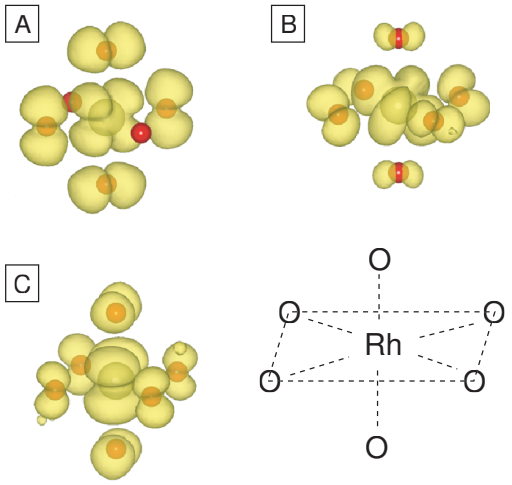

Figure 4.29: Charge density isosurfaces (yellow) of the states labeled *A*, *B*, and *C* at the relative energies of 2.17, 4.24, and 2.93 eV, respectively, in Fig. 4.28(b) and an illustration of the octahedrally-coordinated oxygen ligands surrounding a Rh atom.

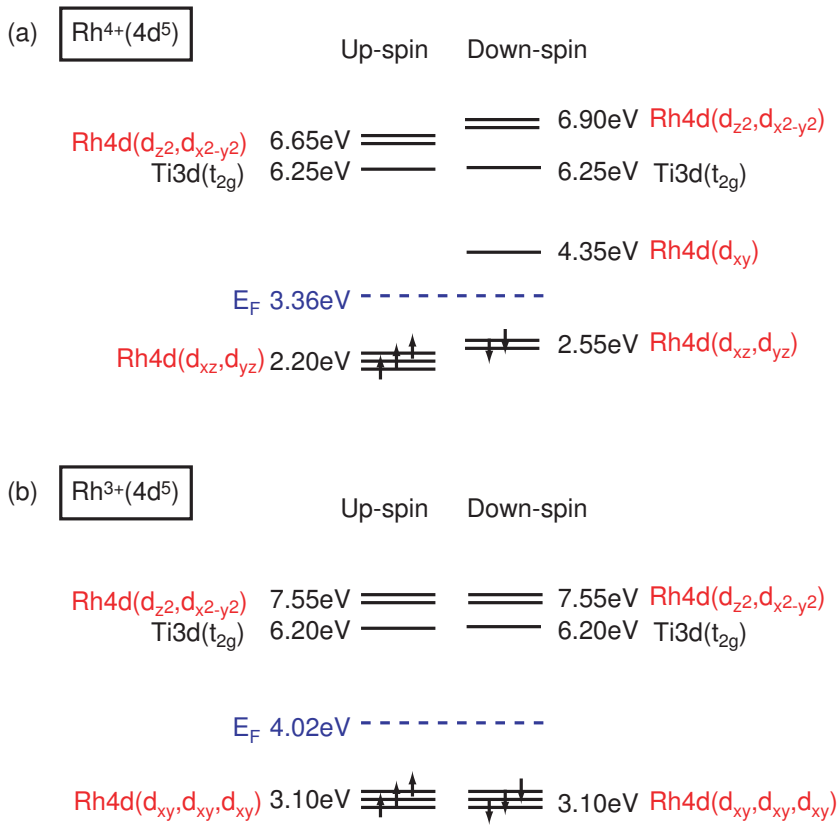

Figure 4.30: Molecular energy diagram for Rh^{4+} and Rh^{3+} dopants in Rh(3.7%):$SrTiO_3$.

Based on the simulations, all observed spectral features can be assigned to Rh-related in-gap states. The mid-gap state *B* in Fig. 4.28 is above the Fermi level and therefore unoccupied. Experimentally, this state appears in the X-ray absorption spectra of Rh^{4+}:$SrTiO_3$ in Fig. 4.22 at 528.2 eV. The fact that the state is predicted to be unoccupied by the calculation and only observable in Rh^{4+}:$SrTiO_3$ XAS, adds credibility to the conclusion that the Rh^{4+} dopant transforms $SrTiO_3$ into a *p*-type material with a very deep Fermi level. The *A* and *C* peaks partly overlap with the valence band top, and can therefore only be seen by XES as a small shoulder at around 528 eV in Fig. 4.23. The sin 0.5 eV spectral weight shift between the 5at% Rh^{4+}- and Rh^{3+}-doped samples in Fig. 4.23 matches the calculated shift of the Rh^{3+} donor level in Fig. 4.28 (b). Regardless of the Rh valence, the calculated Fermi levels remain deep in the $SrTiO_3$ band gap, indicating that both Rh^{4+}- and Rh^{3+}-doped $SrTiO_3$ have a *p*-type character and a large downward band bending may be expected at the Rh:$SrTiO_3$ surface in contact with water, explaining the observed high-efficiency H_2 evolution reaction for this material [59, 92, 241].

4.3.2 Electronic structure of Ir:$SrTiO_3$

The analysis of Ir 5*d* impurity level positions in the band gap region of $SrTiO_3$ was similar to the Rh case —simulation results from first-principles calculations were compared with high-resolution XPS data. The calculated total and partial density of states (PDOS) of Ir for $Ir^{4+/3+}$(3.7 at%):$SrTiO_3$ and nondoped $SrTiO_3$ are shown in Fig. 4.31. The vertical scale for $Ir^{4+/3+}$:$SrTiO_3$ has been multiplied by 10. The Fermi level positions are marked by E_F in the plots. The calculation shows that two in-gap features related to the Ir 5*d* orbitals exist for Ir^{4+} substituting at the Ti^{4+} site in $SrTiO_3$, with peaks appearing ~ 0.5 eV higher than the top of the VB and ~ 0.8 eV below the bottom of the CB, labeled *A* and *B*, respectively. For Ir^{3+}, only a single in-gap level was found in the mid-gap region, ~ 1.2 eV higher than the top of VB, labeled *C*.

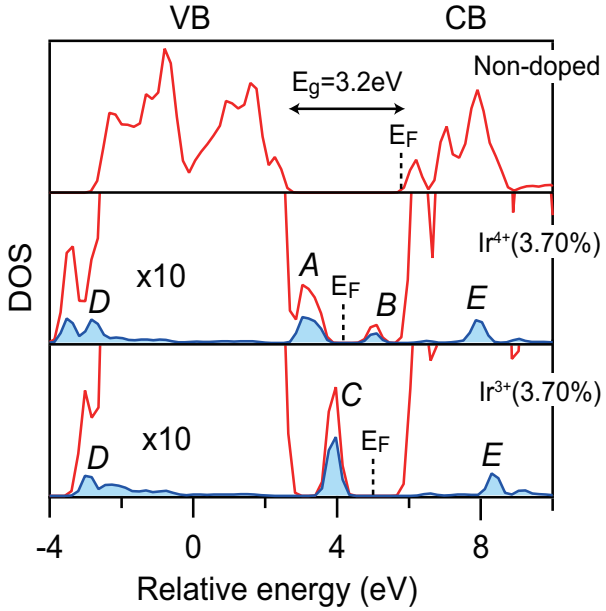

Figure 4.31: Density of states calculated for nondoped $SrTiO_3$ and $Ir^{4+/3+}$(3.70 %):$SrTiO_3$. The total DOS (red line) and PDOS of Ir (blue line) are shown for each sample. The vertical scale for $Ir^{4+/3+}$(3.70 %):$SrTiO_3$ is multiplied by 10. The Ir^{4+} donor and acceptor levels are marked with *A* and *B*, respectively. The Ir^{3+} donor level is marked with *C*. *D* and *E* are Ir 5*d* states hybridizing with the O 2*p* valence band and with the conduction band, respectively. E_F marks the calculated Fermi level positions.

It should be noted that all of these impurity levels are derived from Ir 5*d* t_{2g} states and that state *B* is induced by the short-range Hartree-Fock exchange interaction in the HSE06 functional due to the existence of an unpaired electron at the Ir^{4+} (d^5) site. The peaks marked by *D* and *E* are Ir 5*d* states overlapping with the lower-energy O 2*p* valence band states and with the conduction band, respectively. Simulations using the GGA/PBE functional, which does not

consider the exchange interaction, produced only a single impurity level in the gap region for Ir^{4+}-doped $SrTiO_3$ as well as Rh^{4+}-doped $SrTiO_3$. Fig. 4.32 shows the comparison of the simulated DOS of Ir^{4+}(3.70 %):$SrTiO_3$ calculated with the HSE06 and the GGA/PBE functional.

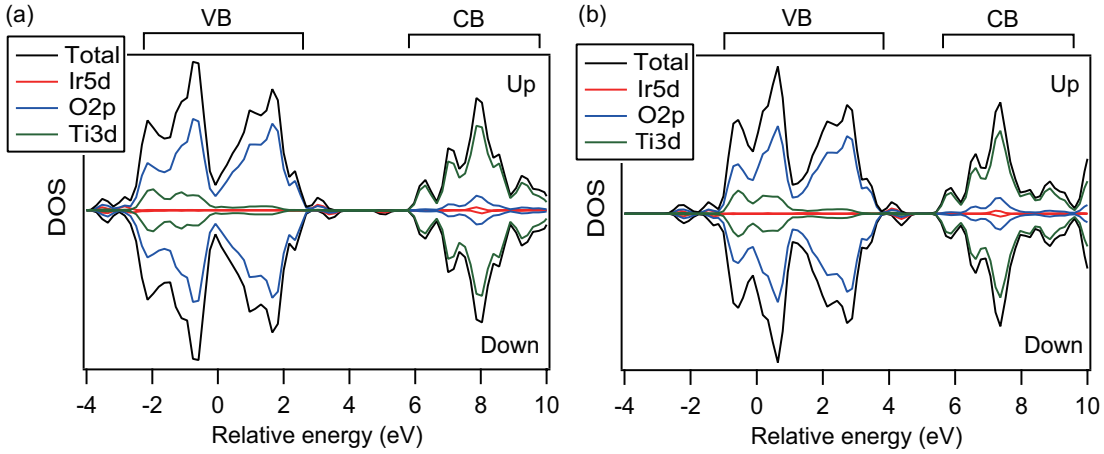

Figure 4.32: Total DOS (black) and PDOS of Ir 5*d* (red), O 2*p* (blue), and Ti 3*d* (green) for Ir^{4+}:(3.7 at%):$SrTiO_3$ obtained by first-principles calculations using (a) the HSE06 functional and (b) the GGA/PBE96 functional. Up and down spin states are shown in the upper and lower parts of the figures, respectively. Up and down spin states are distinguished in this system due to the existence of an unpaired electron at the Ir^{4+} site.

Fig. 4.33 shows high-resolution valence band X-ray photoelectron spectra of Ir(5%):$SrTiO_3$ films deposited at 700°C and either 10^{-1} or 10^{-6} Torr of oxygen, measured at photon energies $h\nu$ = 600, 1000, and 1400 eV using a synchrotron light source. The binding energy was referenced to the Au Fermi edge. The main components observed in the valence band region are attributed to bonding (O 2*p* - σ) and nonbonding O 2*p* (O 2*p* - π) orbitals at ~ 6 and ~ 4 eV binding energies, respectively [254].

The contribution of Ir states to the valence band spectra cannot be easily seen due to an overlap with the dominant oxygen 2*p* states. However, the photoexcitation cross section Ir/O ratio increases with the incident photon energy (Fig. 4.34). A comparison of valence band spectra taken at photon energies of 600, 1000, and 1400 eV can thus be used to separate the Ir contribution from the O 2*p* states. The difference spectra, calculated by subtracting the $h\nu$ = 600 eV spectrum from the $h\nu$ = 1000 eV and $h\nu$ = 1400 eV spectra show two peaks at binding energies of ~ 8 eV and ~ 2 eV. The peak observed at the top of the valence band at ~ 2 eV is assigned to the Ir 5*d* orbitals (states *A* and *C* in Fig. 4.31), while the peak at the bottom of the valence band at ~ 8 eV corresponds to O 2*p* - σ orbitals hybridizing with Ir 5*d* states (state *D* in Fig. 4.31).

The Ir 5*d* spectral components close to the top of the valence band, within the gap of the

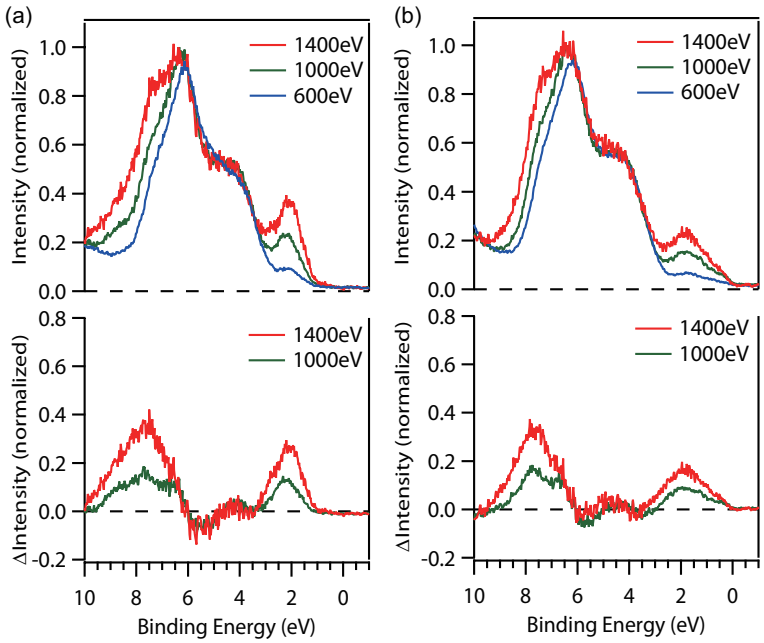

Figure 4.33: Synchrotron X-ray photoelectron spectra of the valence band of Ir(5%):$SrTiO_3$ films deposited at (a) 700°C, 10^{-1} Torr (Ir^{4+}:$SrTiO_3$) and (b) 700°C, 10^{-6} Torr ($Ir^{4+/3+}$:$SrTiO_3$). The photon energy was either 600, 1000, or 1400 eV. An increase of the Ir related spectral components can be seen in the difference spectra measured at higher photon energies (lower panels); the intensity increase is visualized by subtracting the $h\nu$ = 600 eV data from the spectra taken at $h\nu$ = 1000 and 1400 eV.

$SrTiO_3$ host material, were deconvoluted to show the Ir^{4+} 5*d*, Ir^{3+} 5*d*, Ir metal 5*d*, and O 2*p* - π components, as shown in Fig. 4.35. Ir^{3+} creates a shallower donor level than Ir^{4+}. The binding energy positions of Ir^{4+} 5*d* and Ir^{3+} 5*d* peaks are at 2.24 and 1.74 eV, respectively. The Ir metal contribution was calculated by including a thermally broadened Fermi-Dirac function, because the valence band spectrum of Ir metal is nearly flat in the 0 to 6 eV binding energy range [255]. Exposure of the film surface to an intense synchrotron X-ray beam in ultrahigh vacuum resulted in moderate radiation damage, partially reducing Ir^{4+} to Ir^{3+}, and Ir^{3+} to metallic Ir (Fig. 4.36). Thus, the spectrum of the film deposited at 10^{-1} Torr has both Ir^{4+} and Ir^{3+} components in Fig. 4.35, while only Ir4+ was observed with a laboratory X-ray source. Furthermore, the film deposited at 10^{-6} Torr has three components, corresponding to Ir^{4+}, Ir^{3+}, and metallic Ir. At the bottom of the VB, at relative energies of -2 to -4 eV in Fig. 4.31 (state *D*), Ir 5*d* and O 2*p* PDOS components overlap for both Ir^{4+}- and Ir^{3+}-doped samples, which corresponds to the increase of spectral intensity in the 7 to 9 eV binding energy range in Fig. 4.35.

The Ir 5*d* in-gap impurity levels and the O 2*p* - σ (O-Ir) lower valence band states simulated by first-principles calculations are consistent with the experimental results obtained from UV-

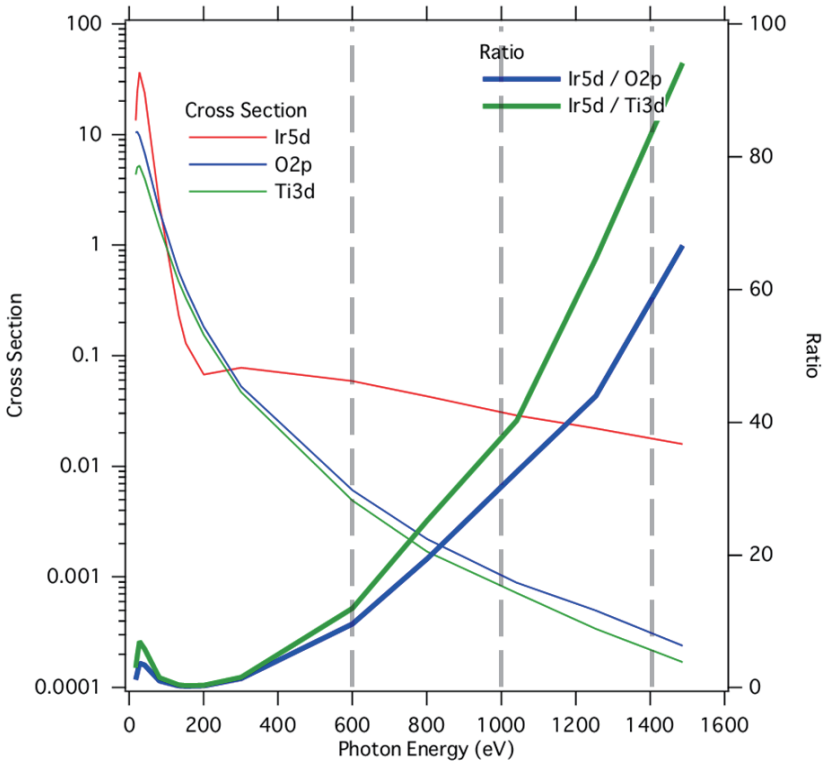

Figure 4.34: Atomic subshell photoionization cross sections for Ir 5*d*, O 2*p*, and Ti 3*d* electrons as a function of the incident X-ray photon energy.

vis-NIR absorption spectra and XPS measurements.

It is interesting to compare the electronic structure of Ir:$SrTiO_3$ with that of Rh:$SrTiO_3$. The impurity level positions of Ir:$SrTiO_3$ are similar to those of $Rh^{4+/3+}$:$SrTiO_3$, and the difference between Rh and Ir doping is only seen as a shift of Ir impurity levels by $\sim$ 0.5 eV higher than those of Rh in $SrTiO_3$. Rh and Ir are in the same group in the periodic table, but being a 5*d* element, the Ir impurity levels are systematically $\sim$ 0.5 eV higher than those of Rh 4*d* in the $SrTiO_3$ parent compound.

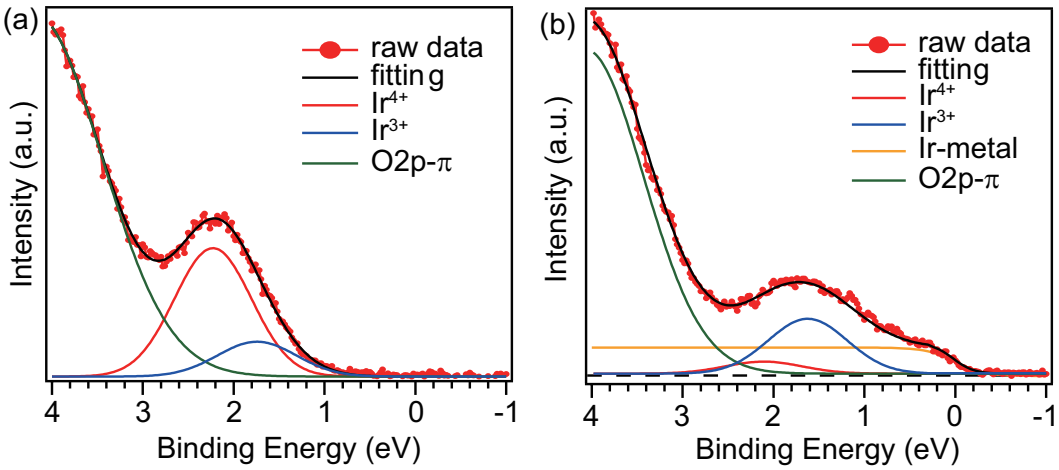

Figure 4.35: Synchrotron X-ray photoelectron spectra of the valence band of Ir(5%):$SrTiO_3$ films deposited at (a) 700°C, 10^{-1} Torr and (b) 700°C, 10^{-6} Torr. The photon energy was 1000 eV. Each raw spectrum (dotted line) is deconvoluted to Ir^{4+} 5*d* (red), Ir^{3+} 5*d* (blue), Ir metal 5*d* (orange), and O 2*p* - π (green) components. The fitting curve is shown in black.

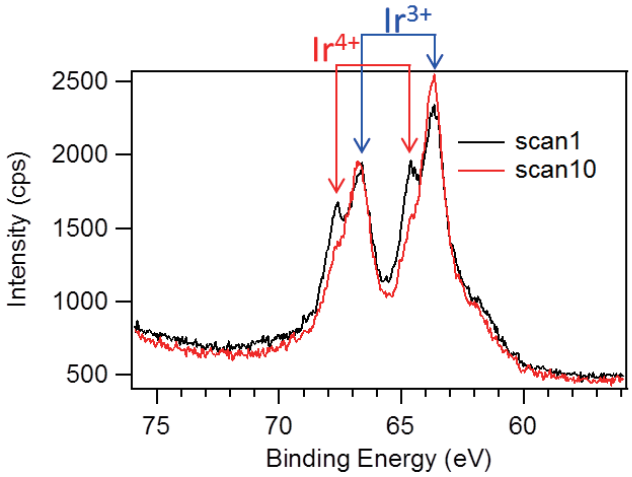

Figure 4.36: The first and 10th scan of the Ir 4*f* core level photoelectron spectra for a film sample deposited at 700°C and 10^{-1} Torr. The scans were taken continuously at the same sample position, with each scan lasting 1.5 min. The photon energy was 600 eV.

4.4 Photoelectrochemical properties of metal-doped $SrTiO_3$

The photoelectrochemical properties of Rh- and Ir-doped $SrTiO_3$ were compared with those of nondoped $SrTiO_3$ and with known *n*-type Nb:$SrTiO_3$. The Nb^{5+} doping generates free carriers in $SrTiO_3$, leading to metallic conductivity. Nb-doped single crystals can thus be used as a convenient method for studying the effect of carrier density on the photoelectrochemical behavior of $SrTiO_3$. Non-doped and Nb-doped $SrTiO_3$ (001) substrates (Shinkosha, thickness 0.5 mm) shown in Fig. 4.37(a) were annealed at 1000°C at an oxygen pressure of 10^{-5} Torr to obtain a uniform step-and-terrace surface morphology. AFM images of the annealed substrate surfaces are shown in Fig. 4.37. Since a non-doped $SrTiO_3$ substrate has too high resistivity to measure its photoelectrochemical properties, a non-doped 100-nm-thick $SrTiO_3$ film sample was grown on a conductive Nb(1.0 at%):$SrTiO_3$ (001) substrate. Due to the shorter current path, a nondoped $SrTiO_3$ film can be used in electrochemical measurements. The $SrTiO_3$ film was grown by PLD at 1200°C in at a base pressure of 10^{-7} Torr. A KrF excimer laser was used to ablate a single crystal $SrTiO_3$ target at a fluence of ~ 1 J/cm^2 and a repetition rate of 2 Hz. $SrTiO_3$ grows in step flow mode at this growth temperature, which is essential for obtaining a highly crystalline epitaxial thin film and to prevent the formation of Sr vacancies [265]. To remove the oxygen vacancies created during the film deposition, the film sample was subsequently annealed at 900°C at an oxygen pressure of 10^{-2} Torr for 1 hour. The preparation conditions were based on the growth optimization done by Kozuka *etal*. [265]. The film sample also had an atomically flat surface with a step-and-terrace surface morphology (Fig. 4.37(f)).

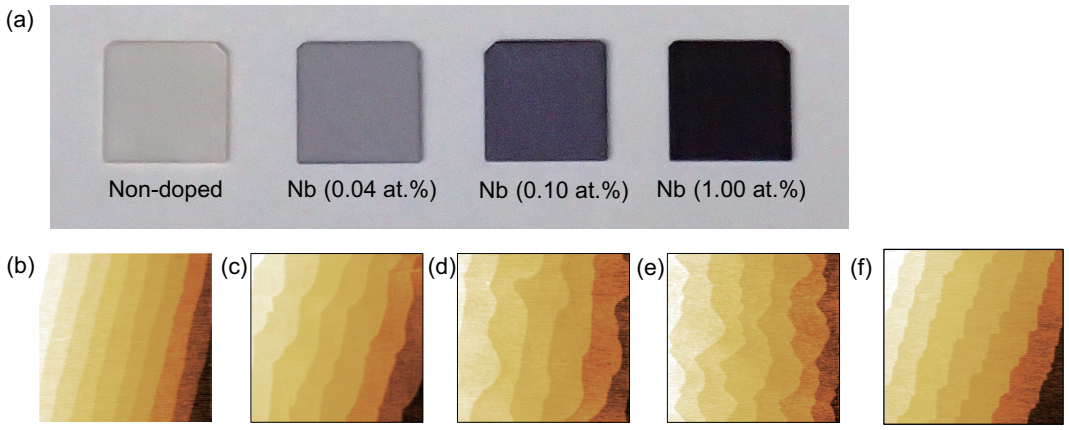

Figure 4.37: (a) A image of non-doped and Nb-doped $SrTiO_3$ (001) substrates. AFM images of (b) non-doped $SrTiO_3$ and Nb:$SrTiO_3$ (001) substrates with the Nb doping levels of (c) 0.04, (d) 0.10, and (e) 1.00 at%. (f) AFM image of a 100 nm non-doped $SrTiO_3$ film deposited on Nb(0.1 at%):$SrTiO_3$ (001) substrate.

The flat band potential (U_{fb}) and the carrier density (n_{MS}) were evaluated by Mott-Schottky

analysis in a $HClO_4$ aqueous solution (pH=1.0) (Fig. 4.38). The permittivity of $SrTiO_3$ is known to be affected by an electric field, resulting in non-linear Mott-Schottky plots [266,267,269–271]. The relative permittivity of $SrTiO_3$ was assumed to follow the electric field as reported by Suzuki *etal*. [266]

$$\epsilon_r(E) = b/\sqrt{a + E^2}, \tag{4.1}$$

where $a = 1.64 \times 10^{15}$ (V^2/m^2) and $b = 1.42 \times 10^{10}$ (V/m) at room temperature. The conventional Mott-Schottky equation can be rewritten as

$$\frac{1}{C^2} = \frac{2\sqrt{a}}{b\epsilon_0 e N_D}(U - U_{fb}) + \frac{1}{b^2\epsilon_0^2}(U - U_{fb})^2, \tag{4.2}$$

where C, U, and N_D are the differential capacitance formed in the semiconductor at the semiconductor / water interface, electrode potential, and carrier density, respectively. The constants e, ϵ_0, k, and T are the elementary charge, vacuum permittivity, the Boltzmann constant, and temperature, respectively. The Schottky barrier potential $V(x)$ and relative permittivity $\epsilon_r(x)$ are analytically determined as a function of the distance from the water interface x as

$$V(x) = \frac{b\epsilon_0\sqrt{a}}{eN_D}\left\{\cosh[\frac{eN_D}{b\epsilon_0}(W - x)] - 1\right\} + V, \tag{4.3}$$

$$\epsilon_r(x) = b/\sqrt{a}\cosh[\frac{eN_D}{b\epsilon_0}(W - x)], \tag{4.4}$$

and

$$W = \frac{b\epsilon_0}{eN_D}\cosh^{-1}[1 + \frac{eN_D}{\sqrt{a}b\epsilon_0}(U - U_{fb})]. \tag{4.5}$$

The obtained flat band potential and carrier densities are summarized in Fig. 4.38, together with the carrier density (n_{Hall}) and electron mobility (μ_e) calculated from van der Pauw Hall effect measurements. The resistivity (ρ), and photocarrier lifetime (τ) were calculated as explained in Ref.268. The photocarrier lifetime is dependent on the carrier density and can be expressed as

$$\tau = \frac{1}{2A + CN_D^2} \tag{4.6}$$

where $A = 1.7 \times 10^7$ s^{-1}, $C = 1.3 \times 10^{32}$ cm^6/s [268].

The cyclic-voltammetry curves of a 100 nm non-doped $SrTiO_3$ film on Nb(0.1 at%):$SrTiO_3$ (001), and Nb(x at%):$SrTiO_3$ single crystals with x = 0, 0.04, 0.10, and 1.00, measured in a $HClO_4$ aqueous solution (pH=1.0) under UV-light irradiation (1 kW Xe lamp) are shown in Fig. 4.39. Clearly, the photocurrent density increased with decreasing carrier density of $SrTiO_3$. The photocurrent density at 1.23 V vs. RHE (J_{ph}), width of space charge region (W_{SC}), and conductivity (σ) as a function of carrier density (n) of $SrTiO_3$(001) are summarized in Fig. 4.40.

Since a non-doped $SrTiO_3$ substrate (thickness 0.5 mm) has a large resistance, the current density is suppressed by the large Ohmic losses in the sample and no photocurrent was observed. Increasing the carrier density by Nb doping increases the conductivity, but it also reduces the width of the space charge region near the water interface ($\sim$ 14 nm in Nb(1.0 at%):$SrTiO_3$), where efficient photoexcited electron-hole pair separation occurs. The effect of Nb doping on the photoelectrochemical properties observed here is consistent with previous reports [272]. The trade-off between sample conductivity and space charge width limits the efficiency of a photoelectrochemical cell as well as the efficiency of a solar cell [31]. A nondoped $SrTiO_3$ film deposited on a conductive Nb(0.1 at%):$SrTiO_3$ therefore showed the largest photocurrent density. The film sample possesses both a large space charge layer width near the water interface and sufficient conductivity due to the much shorter current path.

IPCE measured at 1.23 V vs. RHE also clearly showed that a sample with low carrier density has higher photon-to-current conversion efficiency, independent on wavelength, while a non-doped $SrTiO_3$ substrate showed no photocurrent due to its high resistance (Fig. 4.41). IPCE in the ultraviolet part of the spectrum, at wavelengths below 320 nm was over 70% for the low-carrier-density samples. The behavior can be quantitatively understood by a mismatch between the light absorption length and the space charge layer thickness at the water interface. The penetrating light intensity and the internal potential as a function of distance from the water interface are plotted in Fig. 4.42. Photocarriers generated in the space charge region can migrate from the bulk to the surface, driven by the internal electric field, whereas photocarriers generated in deeper flat band region in the bulk of the semiconductor cannot contribute to the photoelectrochemical reaction. The incident light should thus be absorbed within the space charge region to achieve the highest possible energy conversion efficiency. At 1.23 V vs. RHE, surface recombination is negligible and the photocurrent density can be approximated with Gärtner's model [273]

$$J_{ph} = eJ_{ab}\left[1 - \frac{\exp(-\alpha W_{SC})}{1 + \alpha L_{min}}\right], \tag{4.7}$$

where J_{ab}, α, and L_{min} are the light absorption photon flux, light absorption coefficient, and the diffusion length of minority carriers, respectively.

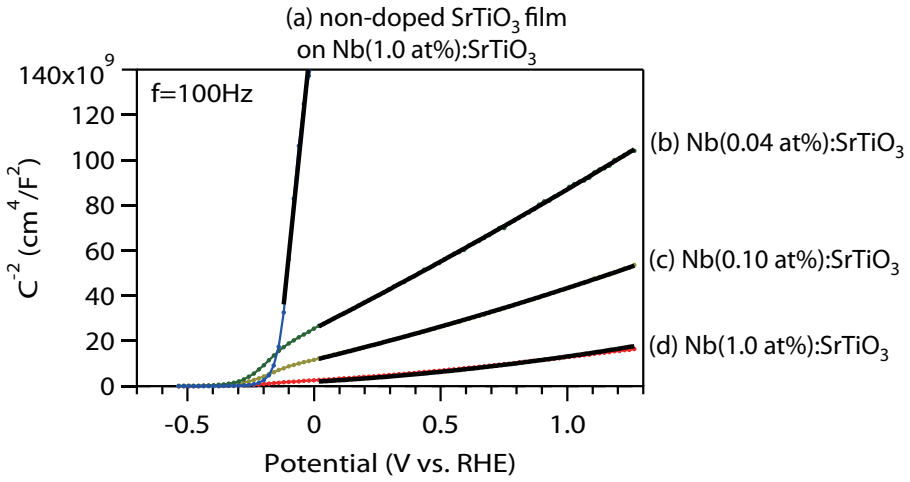

	Nb (at.%)	U_{fb} (V vs. RHE)	n_{MS} (cm^{-3})	n_{Hall} (cm^{-3})	μ_e ($cm^2/V\,s$)	ρ (Ω cm)	τ (ns)
(a)	-	-	4.0×10^{17}	-	-	-	29
(b)	0.04	-0.46	5.1×10^{18}	5.07×10^{18}	6.37	0.194	29
(c)	0.10	-0.46	1.2×10^{19}	1.33×10^{19}	6.42	0.0724	28
(d)	1.00	-0.46	1.5×10^{20}	1.65×10^{20}	7.06	0.00861	3

Figure 4.38: Mott-Schottky plots of (a) 100 nm non-doped $SrTiO_3$ film deposited on Nb(0.1 at%):$SrTiO_3$ (001) and Nb:$SrTiO_3$ (001) substrates with Nb doping levels of (b) 0.04, (c) 0.10, and (d) 1.00 at%, respectively. The black lines are the fitting curves. Light source: 1 kW Xe-lamp. Electrolyte: 0.1 M $HClO_4$ aq. Frequency: 100 Hz. The flat band potential (U_{fb}), carrier density estimated from the Mott-Schottky plot (n_{MS}), carrier density (n_{Hall}), and electron mobility (μ_e) evaluated by Hall measurement, resistivity (ρ), and photocarrier lifetime (τ) estimated by the equation reported in Ref.268 are summarized in the table.

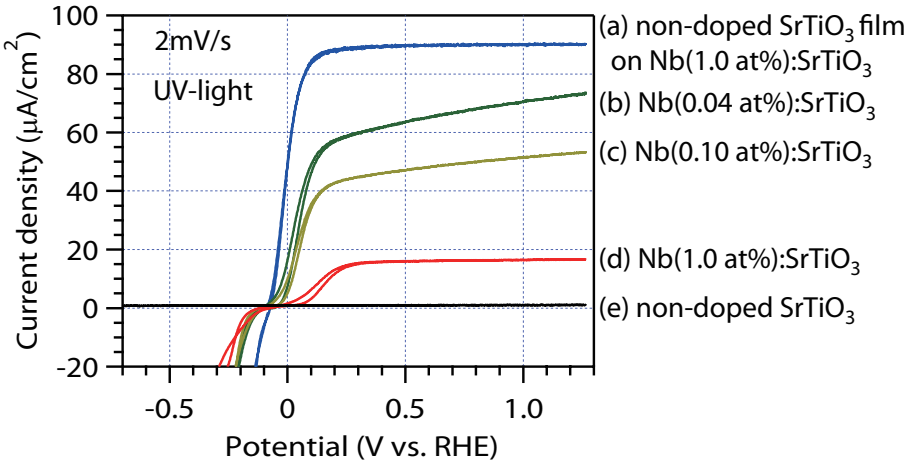

Figure 4.39: Cyclic-voltammetry curves of (a) 100 nm non-doped $SrTiO_3$ film deposited on Nb(0.1 at%):$SrTiO_3$ (001) substrate, and Nb:$SrTiO_3$(001) single crystals with Nb doping levels of (b) 0.04, (c) 0.10, (d) 1.00, (e) 0.00 at%. The measurement used $HClO_4$ aqueous solution electrolyte (pH=1.0), 2 mV/s sweep rate, and a 1 kW Xe lamp light source.

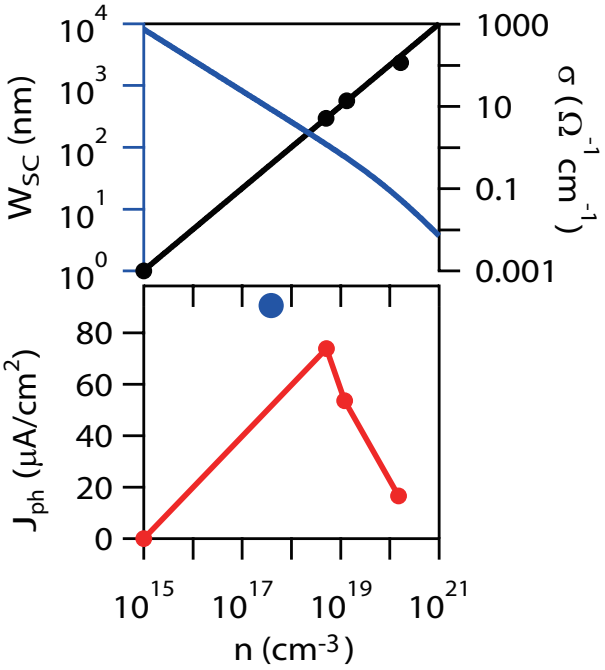

Figure 4.40: Photocurrent density at 1.23 V vs. RHE (J_{ph}), width of space charge region (W_{SC}), and conductivity (σ) as a function of carrier density (n) of $SrTiO_3$(001) photoelectrodes. Photocurrent density at 1.23 V vs. RHE of a 100 nm non-doped $SrTiO_3$ film deposited on Nb(0.1 at%):$SrTiO_3$ (001) is marked with a blue circle.

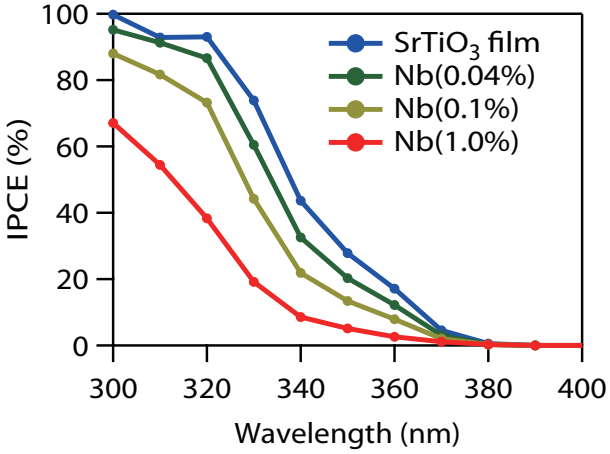

Figure 4.41: IPCE measured at 1.23 V vs. RHE of a 100-nm-thick non-doped $SrTiO_3$ film deposited on a Nb(0.1 at%):$SrTiO_3$(001) substrate and Nb(0.04, 0.10, 1.0 at%):$SrTiO_3$(001) single crystals.

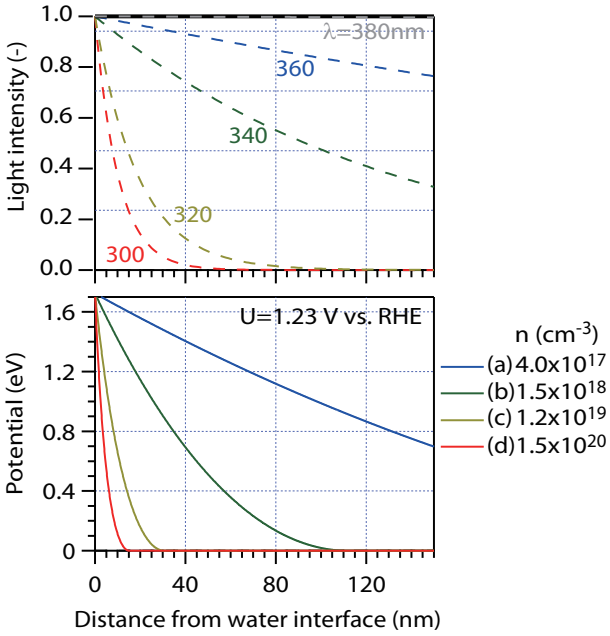

Figure 4.42: Penetrating light intensity and electric potential in a $SrTiO_3$ as a function of the distance from the water interface. The penetrating light intensity is plotted for several different wavelengths (λ), while the electric potential under a 1.23 V vs. RHE bias is plotted for various carrier densities in $SrTiO_3$.

The role of dopants in modifying the photoelectrochemical properties of $SrTiO_3$ was studied by preparing a series of M:$SrTiO_3$(M = Rh, Ir) thin films by PLD and measuring the cyclic voltammetry response under visible light irradiation. Particular attention was paid to determining the effects of the dopant valence, and the film thickness.

The valence of the Rh and Ir dopants was controlled by choosing either oxidizing or reducing conditions for the film growth process. The M^{4+} state was stabilized in films deposited at 10^{-1} Torr, while a predominantly M^{3+} state was obtained by depositing films at 10^{-6} Torr of oxygen. For Rh doping, it is known that the dopant valence plays an important role in determining the photocatalytic activity in the H_2 evolution reaction [59]. Fig. 4.43 shows cyclic voltammetry curves of Rh(5at%):$SrTiO_3$ samples, measured under chopped visible light from a 300 W Xe lamp, filtered with an L42-filter (420-800 nm passband). The Rh valence and the film thickness were systematically varied. A cathodic electrochemical response was observed in all samples, which means that hydrogen gas was generated at the electrode surface. Since the hydrogen evolution reaction is driven by electrons transferred from the semiconductor to water, it is evident that an accumulation layer with downward band bending occurs at the water interface of Rh:$SrTiO_3$ films and Rh:$SrTiO_3$ can thus be considered to have a p-type electronic character, as has been reported in literature for bulk samples [92].

An important photoelectrochemical parameter is the onset potential, i.e., the threshold bias at which the light-induced electrochemical response appears. The cyclic voltammetry scans in Fig. 4.43(a,c) show that there is an onset potential shift of $\sim$ 0.6 V between the Rh^{4+}:$SrTiO_3$ and Rh^{3+}:$SrTiO_3$ film samples. Another observation that can be made from the voltammetry data is that the response of the Rh^{4+}:$SrTiO_3$ film is hysteretic, i.e., the measured current density depends on the bias sweep direction, marked by arrows in Fig. 4.43(c). In general, hysteresis in a cyclic voltammetry loop indicates that the Rh valence changes with applied bias, but it remain unclear why such behavior was not observed for samples that contain a mixture of Rh^{4+} and Rh^{3+} valence states (Figs. 4.43(b,e)). The most likely reason for the reduced photocurrent density of mixed-valent $Rh^{4+/3+}$:$SrTiO_3$ samples in Figs. 4.43(b) compared to Rh^{3+} (a) and Rh^{4+} samples (c) is the increase of recombination rate due to a higher density of crystal defects.

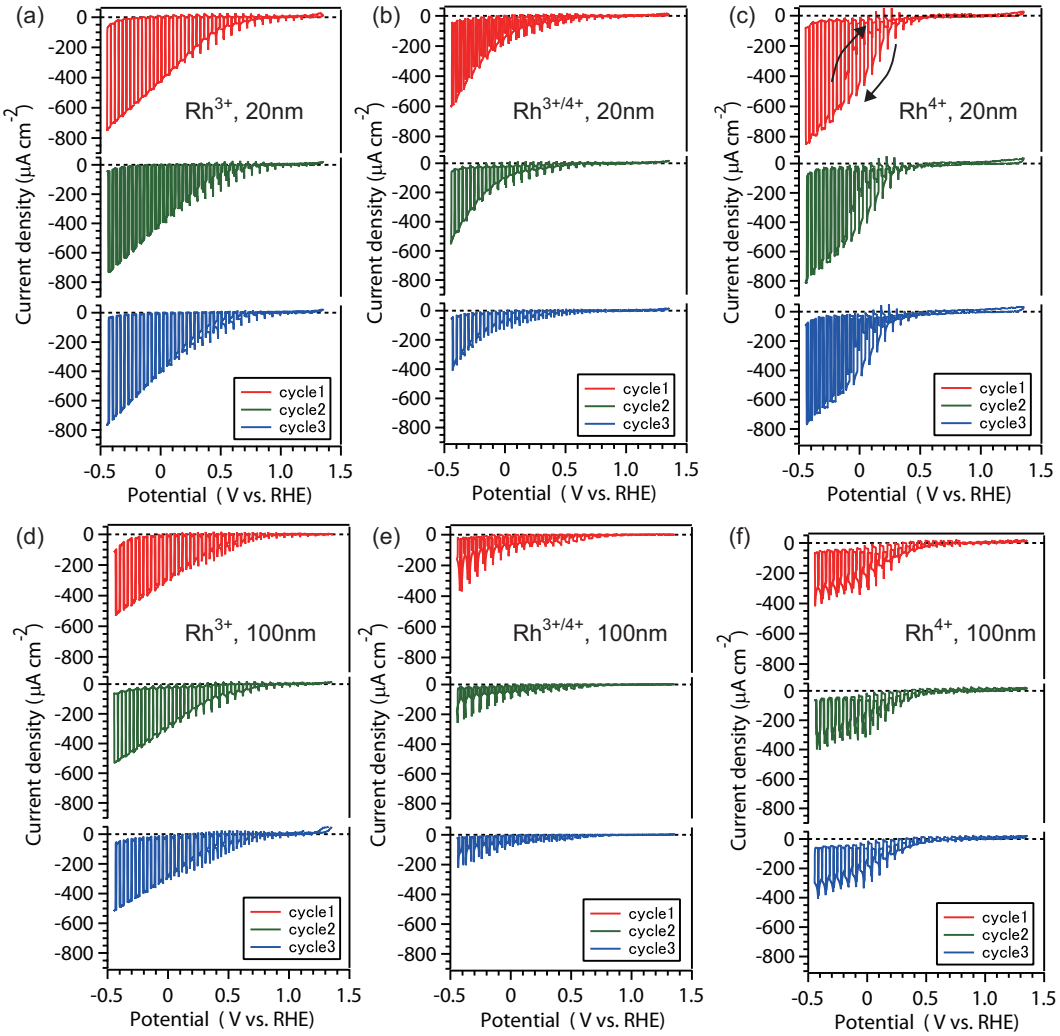

Figure 4.43: Cyclic-voltammetry curves of Rh(5at%):$SrTiO_3$ showing the Rh valence dependence of the photocurrent. Each sample was measured over 3 cycles to confirm its stability. The Rh valence and thickness were (a) Rh^{3+}, 20 nm, (b) $Rh^{3+/4+}$, 20 nm, (c) Rh^{4+}, 20 nm, (d) Rh^{3+}, 100 nm, (e) $Rh^{3+/4+}$, 100 nm, and (f) Rh^{4+}, 100 nm. Arrows in (c) mark the direction of the potential sweep. Light source: chopped 300 W Xe lamp with L42-filter (420-800 nm). Electrolyte: 0.1 M K_2SO_4 aq. (pH=6.0). Sweep rate: 20 mV/s.

Long-term stability is an important characteristic for water splitting phptocatalysts from an application point of view, but even for a model system it is necessary to determine if any non-reversible surface photocorrosion reactions are occurring under light irradiation and applied bias. The short-term stability of the film surfaces was evaluated by repeating the cyclic voltammetry measurements - three sweep cycles were typically measured for each sample. Only the Rh^{3+} sample reproduced the same photocurrent density (-750 μA/cm^2 at -0.45 V vs RHE for three consecutive cycles. The $Rh^{3+/4+}$ and Rh^{4+} samples showed a gradual decrease, dropping from an initial -600 μA/cm^2 during the first cycle to -400 μA/cm^2 in the third cycle for the $Rh^{3+/4+}$ sample, and from -850 μA/cm^2 to -750 μA/cm^2 at the -0.45 V point vs RHE over three cycles. The highest photocurrent density was consistently observed for the Rh^{3+} samples, regardless of the film thickness or cycle number, which shows that Rh^{3+}:$SrTiO_3$ has the highest photoelectrochemical activity and that the 3+ state is the most stable dopant valence in the H_2 evolution reaction from water. this conclusion is similar to the results obtained for Rh:$SrTiO_3$ powder samples [59].

Although the general behavior of the thin films is similar to bulk powder samples, the current density measured in thin films is nearly an order of magnitude higher than for powder sample photoelectrodes [92]. There can be several reasons for the improved efficiency, with improved crystallinity and better thickness control being the most likely reasons. The photoelectrochemical efficiency of a photocatalyst depends on several physical parameters related to carrier generation, recombination, and transport. The thickness of the band bending region with a strong internal electric field that is needed to separate photogenerated electrons and holes is an important parameter that can be directly probed in thin films by varying systematically the film thickness. A general observation from the data in Fig. 4.43 is that thinner samples (20 nm) tend to show larger photocurrent densities than thicker samples (100 nm), regardless of the Rh valence.

The carrier density and the flat-band potential were determined from Mott-Schottky plot, measured at several frequencies. As shown in Fig. 4.44, the electrochemical cell capacitance was frequency dependent, probably due to inhomogeneity in the samples or leakage currents, but for each frequency, the C^{-2} decrease was a linear function of the potential with a positive bias axis intercept. The presence of downward band bending at the water interface and the *p*-type character of Rh:$SrTiO_3$ was thus confirmed for both Rh^{4+} and Rh^{3+} samples. The measured flat-band potential was nearly independent of the measurement frequency equal to 1.75 and 1.65 V for Rh^{4+}:$SrTiO_3$ and Rh^{3+}:$SrTiO_3$, respectively.

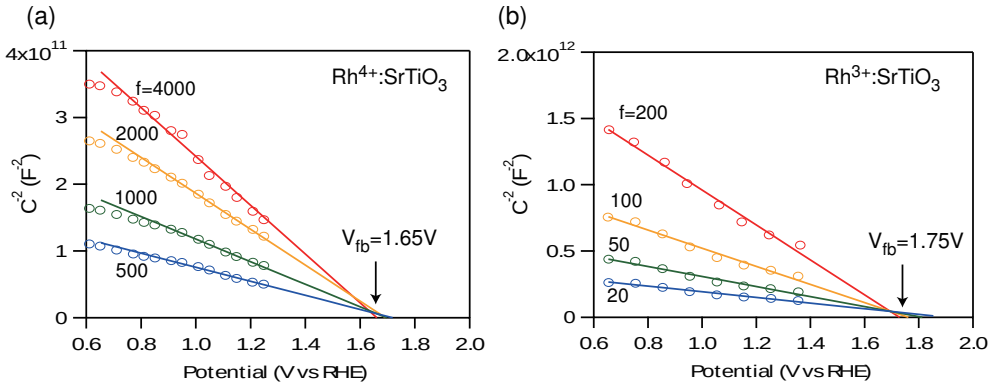

Figure 4.44: Mott-Schottky plots of (a) Rh^{4+}(5 at%) and (b) Rh^{3+}(5at%) doped $SrTiO_3$. Measurements were done at several frequencies from 20 to 4000 Hz for. The film thickness was 20 nm. Electrolyte: 0.1 M K_2SO_4 aq. (pH=6.0).

The effect of the film thickness on the photocurrent density was investigated in detail because it is possible to directly measure the thickness of the surface accumulation layer at the photocatalyst surface. The film thickness was determined by counting the number of RHEED specular intensity oscillations during the film deposition. Fig. 4.45 shows cyclic voltammetry loops for 300, 100 and 20 nm-thick Rh^{3+}:$SrTiO_3$ films under chopped visible-light irradiation. It is clear that although the onset potential didn't change, the photocurrent density systematically decreased for thicker films. This result was initially puzzling, since thicker films should absorb significantly more light.

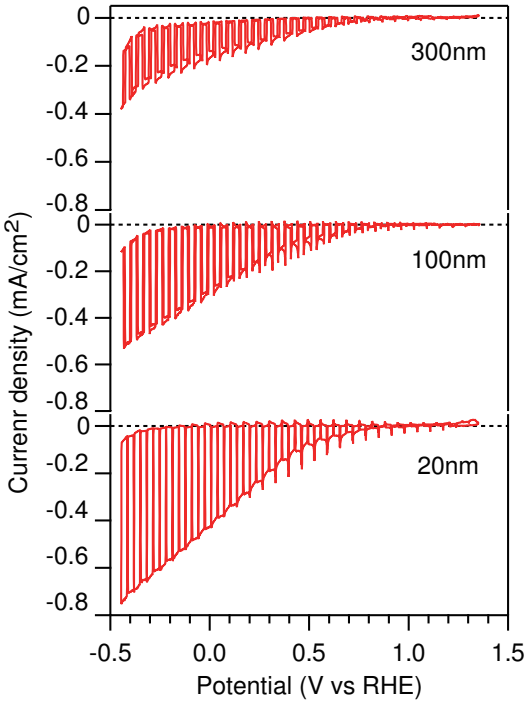

Figure 4.45: Cyclic-voltammetry curves of Rh^{3+}:$SrTiO_3$. The film thickness was, from top to bottom, 300, 100, and 20 nm. Light source was a 300 W Xe lamp with L42-filter (420-800 nm). Electrolyte : 0.1 M K_2SO_4 aq. (pH=6.0). Sweep rate: 20 mV/s.

The film thickness dependence of the photocurrent density is shown with a red line in Fig. 4.46(a). The optimum thickness was 20 $\sim$ 30 nm, with both thinner and thicker samples showing lower photocurrent densities. The film thickness is not always discussed in the study of photoelectrochemical cells, but the results clearly indicate that the film thickness is a critically important factors for optimizing the photoelectrochemical performance. The physics behind the film thickness dependence of the photocurrent in solar cells is similar to the case of photocatalysts and a quantitative analysis is available for solar cells [274]. The film thickness dependence was analyzed with the help of a model illustrated in Fig. 4.46(b), which assumes that the electric potential in a Rh^{3+}:$SrTiO_3$ film is linear. The model is analogous to what is commonly used for analyzing the solar cell performance [275]. The fitting curve was obtained from an equation expressing the external quantum efficiency of a solar cell as reported in Ref.275. Although the current density under 300 W Xe lamp ($\lambda > 420$ nm) illumination is not completely proportional to the IPCE, the current density and the IPCE should show a similar film thickness dependence. The best fitting curve was obtained with a photocarrier lifetime of $\tau = 7$ ps, mobility $\mu = 0.5$ cm^2/Vs, and light absorption coefficient of $\alpha = 10^4$ cm^{-1}.

In general, the film thickness effect on the photocurrent can be understood in terms of light absorption and charge transport efficiency. A photoelectrode can absorb more photons when the film is made thicker, but the photocarrier transport efficiency is suppressed. Clearly, the charge transport efficiency is the most significant factor in the case of a Rh^{3+}:$SrTiO_3$ photoelectrode. The critical parameters that determine the carrier transport efficiency are the mobility and the photocarrier lifetime. The strategy to enhance the photoelectrochemical efficiency of a semiconductor photoelectrode is thus to increase the carrier mobility and to prolong the photocarrier lifetime. That is generally achieved by increasing the crystallinity of the semiconductor material, similarly to the solar cell technology. Transition metal doped photocatalyst materials, e.g. M:$SrTiO_3$, generally suffer from a fundamental difficulty of low carrier mobility and short photocarrier lifetime, that can be easily seen as a broad band dispersion and the fact that the transition metal dopant works as a recombination center in semiconductor materials. Moreover, doped materials generally have a relatively small light absorption coefficient. These points need to be considered when developing new photoelectrode materials based on the strategy of transition metal doping in host oxides.

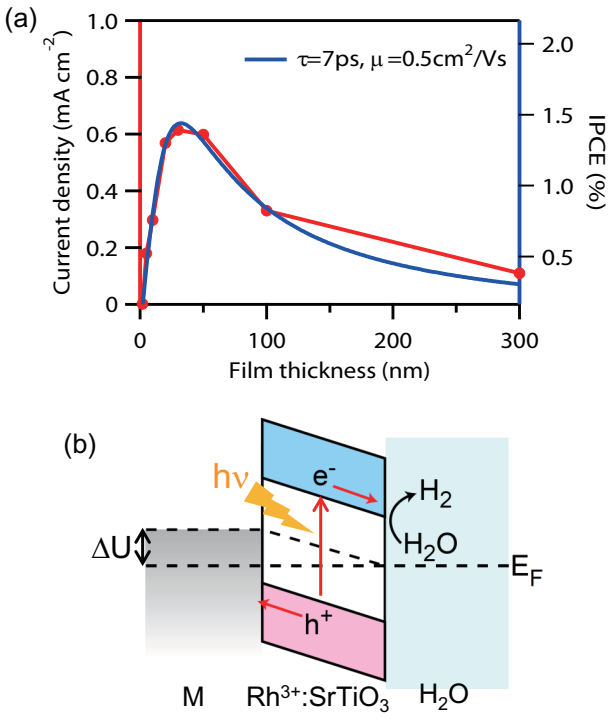

Figure 4.46: (a) Photocurrent density of Rh^{3+}:$SrTiO_3$ at -0.25 V vs RHE as a function of film thickness, measured under 300 W Xe lamp (> 420 nm) illumination. Simulation parameters; photocarrier lifetime 7 ps, mobility 0.5 cm^2/Vs, light absorption coefficient 4×10^4 cm^{-1}. (b) Schematic band diagram of a Rh^{3+}:$SrTiO_3$ photoelectrode facing water with an applied electrode potential ΔU relative to the Fermi level. M is a bottom electrode of a Rh:$SrTiO_3$ film.

Although the electronic structures of Rh- and Ir-doped $SrTiO_3$ were found to be qualitatively similar according to the first-principles simulations, the position of the Fermi level was predicted to be higher in the band gap. Current-voltage characteristics also showed that Ir:$SrTiO_3$ forms an Ohmic contact with Nb:$SrTiO_3$ and with Al metal. Indeed, the cyclic voltammetry data in Fig. 4.47 shows an anodic photoelectrochemical response for Ir:$SrTiO_3$. The voltammetry curves compare the performance of Ir^{4+}- and Ir^{3+}-doped $SrTiO_3$ films (20 nm) deposited on Nb(0.05wt%):$SrTiO_3$ (001) substrates. The measured current density scales with the Ir doping level within the 1 at% to 5 at% doping range. Nb(0.05wt%):$SrTiO_3$ was used for the bottom electrode since I-V characteristics showed an Ohmic contact for the Ir:$SrTiO_3$ / Nb:$SrTiO_3$ interfaces and the substrate itself doesn't show any photoresponse in the visible part of the spectrum. The film thickness was set at 20 nm because this was found to be the optimal thickness for the Rh-doped films and the desire was to prepare a comparable set of Ir-doped film samples.

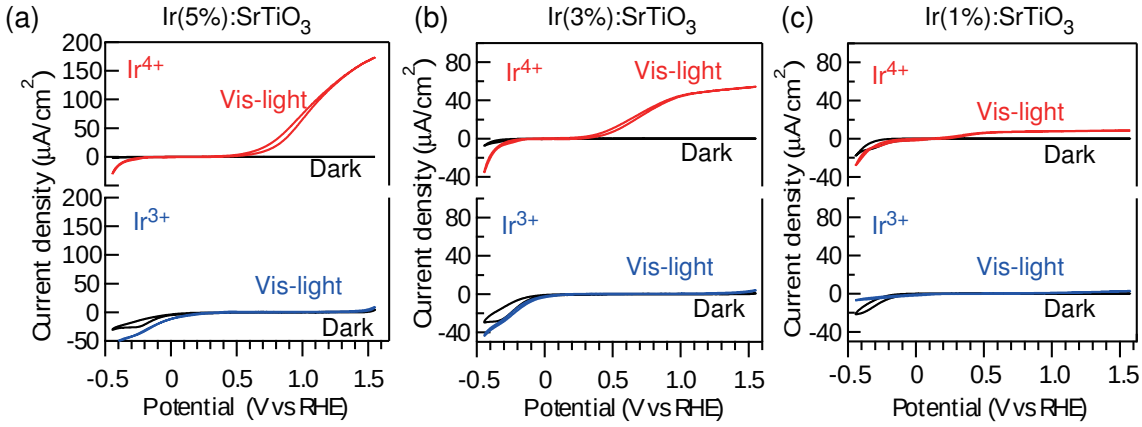

Figure 4.47: Cyclic voltammetry curves of Ir^{4+} and Ir^{3+} doped $SrTiO_3$ films (20 nm) on Nb(0.05 wt%):$SrTiO_3$ (001) substrates. The Ir doping levels were (a) 5 at%, (b) 3 at%, and (c) 1 at%. Light source: chopped 300 W Xe lamp with an L42-filter (420-800 nm). Electrolyte: 0.1 M K_2SO_4 aqueous solution. Sweep rate: 20 mV/sec.

The photoelectrochemical response was anodic for all Ir^{4+}:$SrTiO_3$ films, showing a photocurrent at the positive side of the bias scale. The observed current polarity corresponding to an O_2 evolution reaction under visible light irradiation. The onset potential was 0.5 V for Ir 5%, -0.4 V for Ir 3%, and -0.3 V for the Ir 1% sample, indicating that the Fermi level was not pinned, but decreased with increasing doping levels. Another major difference between the Rh and Ir dopings is that there was no detectable response from the Ir^{3+}:$SrTiO_3$ films while Rh^{3+}:$SrTiO_3$ showed a strong photoresponse. The stabilization of the Ir^{3+} state was done by depositing a film at low oxygen pressure, which means that the charge balance in the crystal is maintained as in $SrTi^{4+}_{1-x}Ir^{3+}_{x}O_{3-x/2}$, which corresponds to electron doping of bulk of $SrTiO_3$. Despite the apparent electron doping, the I-V characteristics showed a resistance that was nearly two orders of magnitude higher for Ir^{3+}:$SrTiO_3$ than for isovalent Ir^{4+}:$SrTiO_3$ doping (Fig. 4.17). As with Rh:$SrTiO_3$, the additional electrons appear to be strongly localized at the Ir^{3+} impurity sites, which also means that the photocarrier recombination rate is very high. The excited photocarriers thus recombine before migrating from the bulk of the Ir:$SrTiO_3$ film to the surface, quenching the photoelectrochemical reaction response. Ir^{3+}:$SrTiO_3$ is thus not an effective photocatalyst.

Fig. 4.47 shows a systematic increase of the photocurrent density for higher Ir doping levels. Since the film thickness was fixed at 20 nm, the photocurrent increase is due to an increase of the light absorption coefficient as a function of the doping level. To probe the photocarrier migration rate and depth independently of the number of absorbed photons, a set of films was prepared such that the total number of absorption photons would be approximately the same regardless of the doping level. The absorption tuning was done by scaling the sample thickness, 20 nm for a Ir 5% sample, 33 nm for Ir 3%, 100 nm for the Ir 1% film. The cyclic voltammetry data is shown in Fig. 4.48. This data set shows that if the light absorption rate is compensated for, the apparent photocurrent density increase in the 33 nm-thick Ir(3%):$SrTiO_3$ sample over a 20-nm film disappears, and the 20 nm-thick Ir(5%):$SrTiO_3$ sample clearly shows the largest photocurrent.

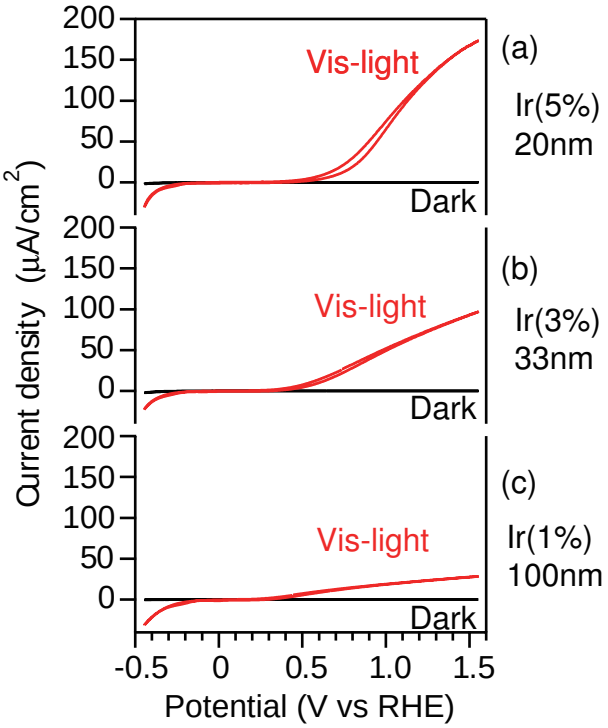

Figure 4.48: Cyclic voltammetry curves of Ir^{4+}:$SrTiO_3$ films. The Ir doping levels and film thickness were (a) 5 %, 20 nm (b) 3 %, 33 nm and (c) 1 %, 100 nm, which means that each sample had the same amount of Ir in the film and thus the total light absorption intensity is the same for all three samples. Light source: chopped 300 W Xe lamp with an L42-filter (420-800 nm). Electrolyte: 0.1 M K_2SO_4 aq.(pH=6.0). Sweep rate: 20 mV/s.

The incident photon-to-current conversion efficiency (IPCE) of Ir^{4+}(5%):$SrTiO_3$ (20 nm) and Ir^{3+}(5%):$SrTiO_3$ (20 nm), measured at 1.55 V vs RHE is shown in Fig. 4.49. The absorption coefficients of $Ir^{4+/3+}$:$SrTiO_3$ and non-doped $SrTiO_3$ are also shown for comparison. The plot shows that the onset of the electrochemical response overlaps with the absorption edge of Ir^{4+}:$SrTiO_3$, which means that the anodic photocurrent can be attributed to a band gap transition from the Ir^{4+} donor level to the conduction band. The Ir^{3+}:$SrTiO_3$ IPCE plot is flat, as the photoresponse under visible-light irradiation was nearly zero.

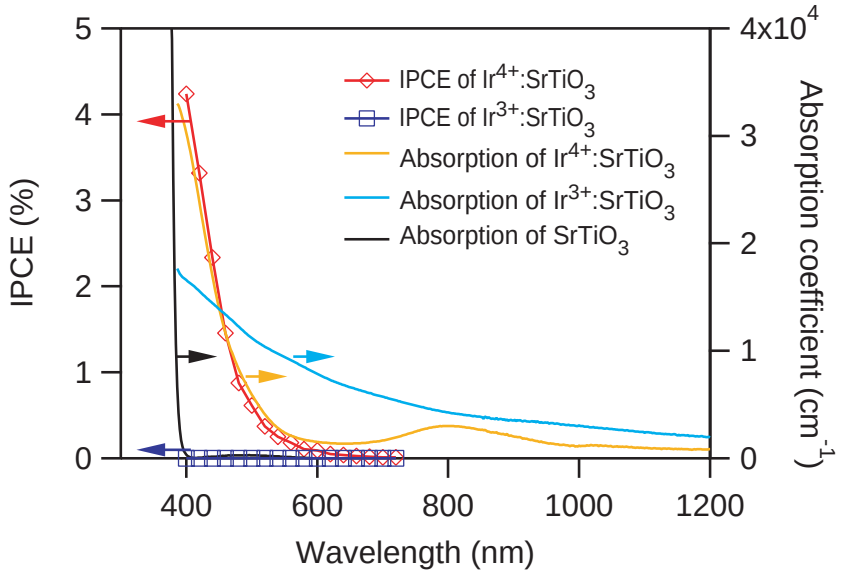

Figure 4.49: IPCE of $Ir^{4+/3+}$(5 %):$SrTiO_3$ (20 nm), together with the absorption coefficient of $Ir^{4+/3+}$:$SrTiO_3$ and non-doped $SrTiO_3$. The IPCE was measured at 1.55 V vs RHE under monochromatic light. Light source; 100 W Xe-lamp with band-pass filters. Electrolyte: 0.1 M K_2SO_4 aq.(pH = 6.0).

4.5 Effect of impurity level positions on photoelectrochemical activity

Chemical doping in semiconductors affects several material properties, such as the surface morphology, grain size, the density of lattice defects, the lattice constant, light absorption, charge density, carrier mobility, photocarrier lifetime, surface states, etc. Not surprisingly, the photoelectrochemical activity is strongly dependent on the dopant species, as was seen for Rh- and Ir-doped $SrTiO_3$. However, details of the doping effects are often ignored beyond a simple comparison of absorption spectra. Here, I would like to discuss the photoelectrochemical activity from the viewpoint of the electronic structure and, in particular, look at the effect that the impurity level positions have on photogenerated carrier dynamics.

In most photocatalytic materials, the activity is determined by the ratio of all photogenerated carriers that can be consumed in electrochemical reactions at the surface. In practice, most of the photocarriers recombine in the bulk or at the surface of a semiconductor photocatalysts before reacting with water. Fig. 4.50 illustrates four types of recombination processes. Bulk recombination occurs in three different processes; band-to-band, trap-assisted, and Auger recombination, while surface recombination occurs through surface states.

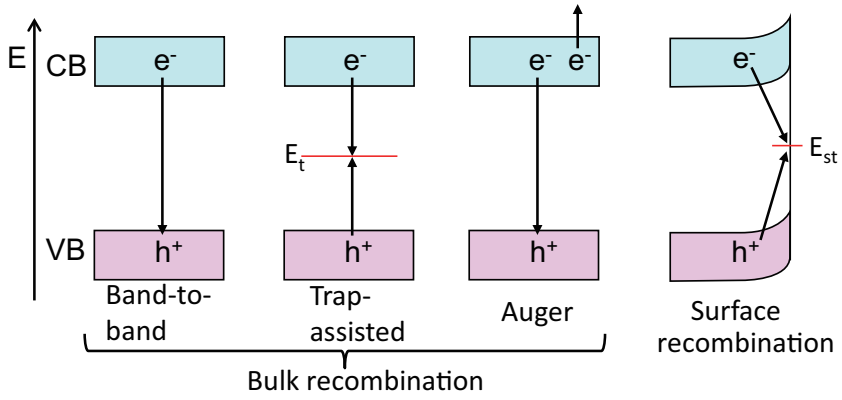

Figure 4.50: Recombination processes. Bulk recombination occurs in band-to-band, trap-assisted, and Auger recombination processes. Surface recombination occurs through the surface states.

The band-to-band recombination probability can be expressed as

$$U_{b-b} = b(np - n_i^2), \tag{4.8}$$

where b is a coefficient, n, p, and n_i are the electron, hole, and intrinsic carrier densities,

respectively. The trap-assisted recombination rate is given by

$$U_{trap} = \frac{np - n_i^2}{n + p + 2n_i \cosh[(E_t - E_i)/kT]} N_t \sigma v_{th}, \tag{4.9}$$

where E_t and E_i are the trap state and intrinsic Fermi level energies, and N_t, σ, and v_{th} are the density of the trap states, carrier capture cross section, and thermal velocity of electrons, respectively. The capture cross sections are assumed to be the same for electrons and holes. Auger recombination can be calculated from

$$U_{Auger} = \Gamma_n n(np - n_i^2) + \Gamma_p p(np - n_i^2), \tag{4.10}$$

where Γ_n and Γ_p are coefficients for the Auger recombination for electrons and holes. The surface-state-assisted recombination is given by

$$U_{surface} = \frac{np - n_i^2}{n + p + 2n_i \cosh[(E_s t - E_i)/kT]} N_s t \sigma v_{th}, \tag{4.11}$$

where $E_s t$ and $N_s t$ are the energy and density of the surface trap states. Thus, the recombination probabilities are affected by the energy positions, the density of trap states, and by the Fermi level position.

Photocarrier lifetime also depends on the impurity level and Fermi level positions, following an equation reported by W. Shockley *etal*. [256]:

$$\tau = \tau_{p0} \times \frac{n_0 + n_1}{n_0 + p_0} + \tau_{n0} \times \frac{p_0 + p_1}{n_0 + p_0} \tag{4.12}$$

$$n_0 = N_C \exp((E_F - E_C)/k_B T) \tag{4.13}$$

$$p_0 = N_V \exp((E_V - E_F)/k_B T) \tag{4.14}$$

$$n_1 = N_C \exp((E_t - E_C)/k_B T) \tag{4.15}$$

$$p_1 = N_V \exp((E_V - E_t)/k_B T) \tag{4.16}$$

$$n_i^2 = n_0 p_0 = n_1 p_1, \tag{4.17}$$

where τ_{p0} and τ_{n0} are the lifetimes of photoholes and photoelectrons in an intrinsic semiconductor. The photocarrier lifetime is plotted as a function of the impurity level and Fermi level positions in Fig. 4.51, assuming that $\tau_{p0} = \tau_{n0}$. Thus, the impurity level and Fermi level positions affect logarithmically the photocarrier lifetime. In order to suppress photocarrier recombination, the Fermi level should be near the center of the band gap whereas the impurity levels should not be near the center of the band gap.

The photocarrier lifetime of Rh:$SrTiO_3$ was measured by transient absorption spectroscopy. Free electrons in a semiconductors show a characteristic optical Drude response due to intraband transitions in THz region (0.1-10 THz, ~10 meV) [257]. Since the time resolution of ~1

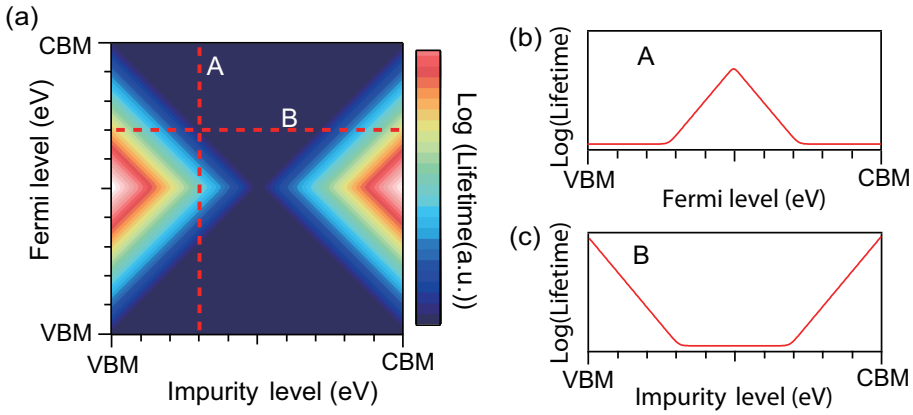

Figure 4.51: (a) The dependence of the photocarrier lifetime in a semiconductor on the impurity level and Fermi level positions, assuming $\tau_{p0} = \tau_{n0}$. Cross-sectional views along (b) A and (c) B lines marked in (a).

ps can be achieved, the THz frequency region is suitable for the observation of ultrafast photocarrier dynamics in semiconductors [258]. The ps-ns dynamics of photo-excited carriers were investigated by ultraviolet-pump THz-probe transient absorption spectroscopy. Non-doped and Rh-doped $SrTiO_3$ epitaxial thin films deposited on LSAT substrates were used for this study, since $SrTiO_3$ shows strong absorption in the THz region. Absorption in LSAT is negligible, making this a more suitable substrate material for THz-absorption measurements. Fig. 4.52 shows the transient absorption dynamics of 0.5-2.5 THz radiation for non-doped $SrTiO_3$, Rh^{3+}(5 %):$SrTiO_3$, and Rh^{4+}(5 %):$SrTiO_3$. The optical density change (ΔOD) was measured at the peak of the THz waveform by scanning the pump-probe pulse delay time. After the initial rapid photocarrier generation by a fs laser pulse at the 0 ps mark, ΔOD increased rapidly for all samples. However, the amplitude and the decay time clearly depend on the valence of the Rh dopant. Two decay processes with a lifetime of 2 ps and 10 ps can be discerned for the dynamics in Rh^{3+}:$SrTiO_3$. ΔOD at 0 ps is close to that of non-doped $SrTiO_3$ which means that most of the photo-excited electrons rapidly populate the Ti 3*d* conduction band minimum, transferring the excess optical energy to phonons.

In contrast, the ΔOD signal dropped to zero just 1 ps after laser irradiation for Rh^{4+}:$SrTiO_3$. The result of least square fitting by an exponential decay, considering the finite time resolution (~1 ps) suggests that the initial ΔOD=0.008, and the lifetime is 0.46 ps, indicating that electron trapping or recombination process becomes very fast (¡1 ps) in Rh^{4+}:$SrTiO_3$. The results are consistent with the general tendency of photocarrier lifetime dependence on the impurity level positions as discussed in Fig. 4.51. Since Rh^{4+} creates an unoccupied impurity level at the mid-gap position, the photocarrier lifetime is much shorter than for non-doped $SrTiO_3$ or for Rh^{3+}-doped $SrTiO_3$. The ΔOD signal in non-doped $SrTiO_3$ decreases to one third of the initial

value at 30 ps. Previous studies on the photoluminescence of non-doped $SrTiO_3$ single crystal substrates gave a carrier recombination lifetime to be 60 ns [259, 260]. One possible reason for the shorter lifetime of electrons at the conduction band minimum is electron trapping at oxygen vacancy levels (V_O). The non-doped $SrTiO_3$ thin film was deposited at a growth temperature of 700°C and an oxygen pressure of 10^{-6} Torr. The low oxygen pressure induces a moderately high V_O density [261]. The other reason may be electron trapping by lattice defects levels derived from the lattice mismatch between $SrTiO_3$(a = 3.905Å) thin films and the LSAT (a = 0.3868Å) substrate.

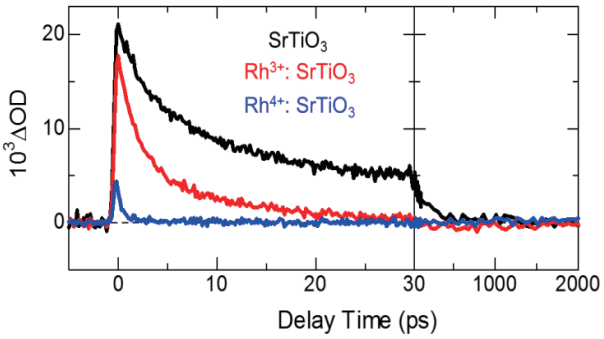

Figure 4.52: Transient THz (~ 10 meV) absorption dynamics of Rh:$SrTiO_3$ thin films. Excitation was at 4.65 eV and 27.8 J/m^2 (0.062 photon/Ti site). Non-doped $SrTiO_3$ (black), Rh^{3+}(5 %):$SrTiO_3$ (red), Rh^{4+}(5 %):$SrTiO_3$ (blue). Film thickness was 100 nm. Substrate is LSAT(001).

Fig. 4.53 shows time evolution of the near-infrared (NIR) transient absorption in non-doped $SrTiO_3$ substrate and Rh-doped $SrTiO_3$ thin films deposited on $SrTiO_3$(001) substrates. Photo-induced absorption was observed at 1.58 eV with a decay time of ~ 30 ns in the non-doped $SrTiO_3$ substrate. This decay time agrees well with the electron-hole recombination time of ~ 60 ns inferred from a photoluminescence study [259, 260]. Fig. 4.53(b) shows the transient absorption dynamics of Rh^{3+}:$SrTiO_3$. Since the thickness of the film (400 nm) is much larger than the penetration depth of the pump light (L = 25 nm), direct photoexcitation of the substrate can be ignored. After photoexcitation, ΔOD increased for both 1.26 eV and 1.58 eV probe energies. The decay time is ~ 0.7 μs, which is much longer than for the $SrTiO_3$ substrate. The decay time difference indicates that the ΔOD increase in Rh^{3+}:$SrTiO_3$ is not due to thermal effects, but due to photoexcited carriers. The photogenerated electrons thus appear to be trapped at mid-gap states within ~ 0.7 μs, since the THz transient absorption data showed no free carriers on this time scale. The energy of the trap levels from the conduction band minimum must be less than 1.26 eV, because photoinduced absorption was observed at a 1.26 eV probe energy as well. The absorption can thus be ascribed to transitions from in-gap trap levels to the conduction band. A candidate for an electron trap in Rh^{3+}:$SrTiO_3$ is the oxygen vacancy. Since Rh^{3+} substitutes at

the Ti^{4+} site, oxygen vacancies should also form to compensate the charge balance and satisfy charge neutrality. The expected number of oxygen vacancy should be half of the number of Rh^{3+} ions. Experimental and theoretical studies showed that the V_O energy is ~ 0.3 eV below the conduction band minimum [262–264], and the electrons excited by the NIR-probe light can thus be assigned to trapped electrons at V_O sites. Fig. 4.53(c) shows the near-infrared ΔOD dynamics of Rh^{4+}:$SrTiO_3$. The ΔOD behavior is quite different, with photoinduced absorption appearing at 1.58 eV and photoinduced bleching at 1.26 eV. The decay time of the signals was 0.27 μs for both cases, suggesting that the same in-gap states are involved in both cases. This result indicates that the photogenerated electrons fall into mid-gap levels, and recombine with holes in ~ 0.27 μs. Rh^{4+}:$SrTiO_3$ has a mid-gap unoccupied impurity level and an occupied impurity level close to the valence band maximum. The probe photon energy of 1.26 eV corresponds to the transition from the occupied impurity level just above the valence band top to the unoccupied mid-gap impurity level, while 1.58 eV is the resonant energy for a transition from the unoccupied mid-gap states to the conduction band minimum. As the occupation number of the mid-gap states increases by photocarrier trapping, the probability of optical transitions to the mid-gap states (~ 1.2 eV) decreases. In contrast, optical transition from these states (~ 1.5 eV) appear since electrons become available at the normally unoccupied mid-gap state. Since both signals decay by recombination of electrons and holes, the photoinduced absorption and bleaching signals have the same delay time.

Fig. 4.54 shows a schematic illustration of the photocarrier dynamics of Rh^{4+}:$SrTiO_3$ and Rh^{3+}:$SrTiO_3$. In Rh^{4+}:$SrTiO_3$, photogenerated electrons in the conduction band are trapped by the mid-gap impurity state within 1 ps, followed by recombination of the trapped electrons with holes within 1 μs. Due to the short lifetime of electrons in the conduction band, most carriers are trapped at deep trap levels ~ 1.5 eV below the conduction band bottom before reaching the surface catalytic sites, resulting in the low photocatalytic activity of Rh^{4+}:$SrTiO_3$. In contrast, for Rh^{3+}:$SrTiO_3$, the photoexcited electrons in the conduction band are trapped at shallow trap levels formed by V_O (~ 0.3 eV below the conduction band) with a lifetime of ~ 10 ps. The photocarriers trapped at the shallow trap levels remain mobile due to a thermal trap-and-release conduction process and still contribute to photoelectrochemical reactions, albeit the mobility is low. Therefore, Rh^{3+}:$SrTiO_3$ shows higher photocatalytic activity than Rh^{4+}:$SrTiO_3$.

The photocarrier mobility is strongly affected by the impurity level position in the band gap while the number of excited carriers reaching the surface is also a function of the photocarrier lifetime. In doped semiconductors with significant disorder, as in Rh:$SrTiO_3$, carrier transport in the dopant-related bands occurs by variable-range hopping. The hopping probability between two states at a spatial separation R and an activation energy E_a can be expressed as

$$p \propto \exp(-2R/\alpha - E_a/kT), \tag{4.18}$$

where α is the localization length, k is the Boltzmann constant, and T is the temperature. If

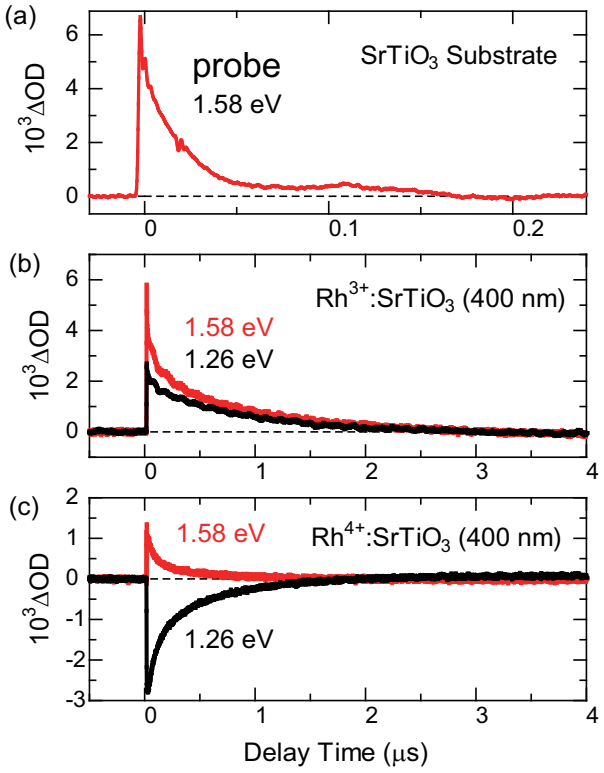

Figure 4.53: Transient near infrared (1.26 and 1.58 eV) absorption of (a) $SrTiO_3$(001) substrate, (b) Rh^{3+}(5 %):$SrTiO_3$ (400 nm) film, and (c) Rh^{4+}(5 %):$SrTiO_3$ (400 nm) film. The excitation energy was 4.65 eV at a fluence of 29.7 J/m^2.

$SrTiO_3$ has an unoccupied photocarrier acceptor level at an energy ΔE below the conduction band minimum as shown in Fig. 4.55(a), the photogenerated electrons trapped at the acceptor level can migrate with a hopping probability proportional to $\exp(-\Delta E/kT)$, assuming that the activation energy for the variable-range hopping is proportional to ΔE. If ΔE is too large, carriers cannot migrate from the bulk to the surface as illustrated in Fig. 4.55(c). The hopping mobility is proportional to the hopping probability

$$\mu \propto p \propto \exp(-\Delta E/kT). \tag{4.19}$$

Thus, the mobility decreases exponentially with an increase of ΔE. As is clearly seen in Fig. 4.56, even a ΔE of a few hundred meV would strongly suppress the carrier mobility. In case $SrTiO_3$ has a photocarrier donor level at ΔE from the valence band maximum (Fig. 4.55(b)), the hopping mobility should also be proportional to $\exp(-\Delta E/kT)$.

Impurity levels in semiconductors generally work as trap sites for photocarriers, shortening the photocarrier lifetime and reducing the photocarrier mobility, even though the light

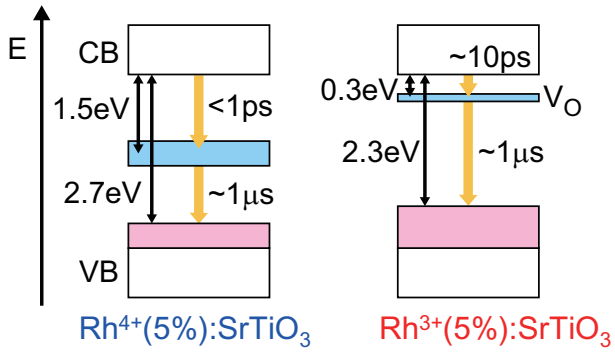

Figure 4.54: Diagram of photocarrier recombination processes in Rh^{3+}:$SrTiO_3$ and Rh^{4+}:$SrTiO_3$. The photocarrier relaxation time for each step was estimated by transient absorption measurements.

absorption intensity under sunlight is improved by the formation of the impurity levels in the band gap. The photocatalytic activity is thus strongly dependent on the impurity level positions. The qualitative tendency of the photocatalytic activity of doped $SrTiO_3$ as a function of impurity level positions is shown in Fig. 4.57(b). The efficiency of the doped semiconductor photocatalysts is thus limited to a certain level due to an unavoidable trade-off between the light absorption strength and the photocarrier diffusivity.

So far, almost all possible dopant elements in TiO_2 and $SrTiO_3$ have been tested as agents for increasing the visible light photoresponse of the parent compounds. The impurity levels induced by doping in $SrTiO_3$ are summarized in Fig. 4.58. To compile the data in this figure, many theoretical and experimental papers were referenced for determining the energy level positions [52, 55–57, 59, 65, 66, 276–340]. The general tendency of the impurity level positions corresponds to the electronegativity of the dopants [276]. Following the scenario of the trade-off between light absorption and photocarrier diffusivity as a function of impurity level positions, only a few elements can be considered as suitable dopants for $SrTiO_3$, namely Rh^{3+} and Cr^{3+}. These dopants form occupied impurity levels at the top of the valence band of $SrTiO_3$.

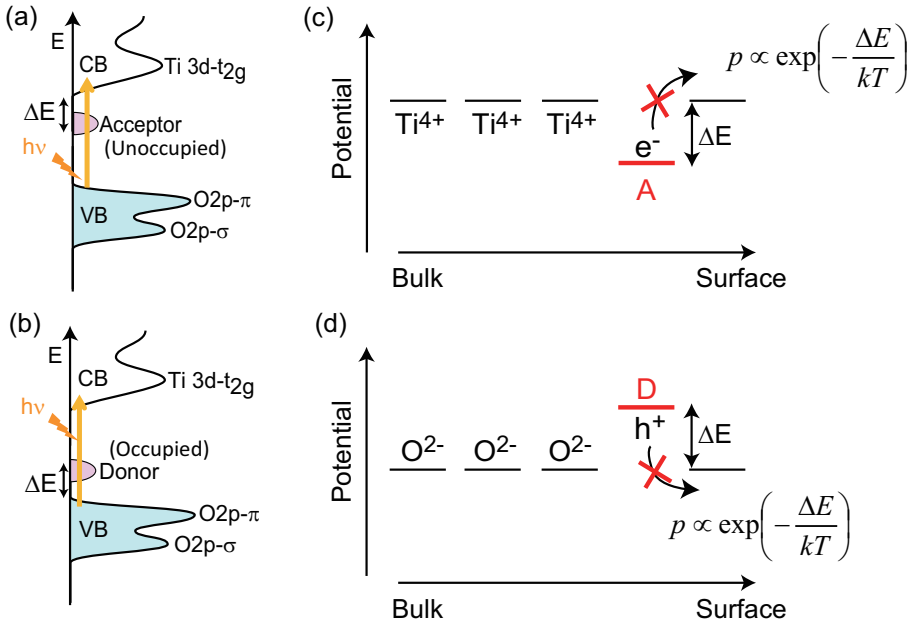

Figure 4.55: Schematic illustrations showing that impurity levels suppress photocarrier migration. Photoexcitation process of $SrTiO_3$ having (a) photocarrier acceptor and (b) donor levels. Energy level diagrams showing (c) photoelectron transports in the conduction band formed of Ti d orbitals and (d) photohole transport in the valence band formed of O $2p$ orbitals.

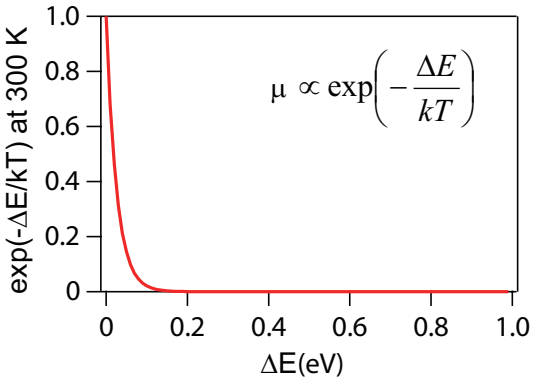

Figure 4.56: Behavior of the $\exp(-\Delta E/kT)$ function at 300 K as a function of ΔE, showing that ΔE of even a few hundreds of meV strongly suppresses the hopping mobility.

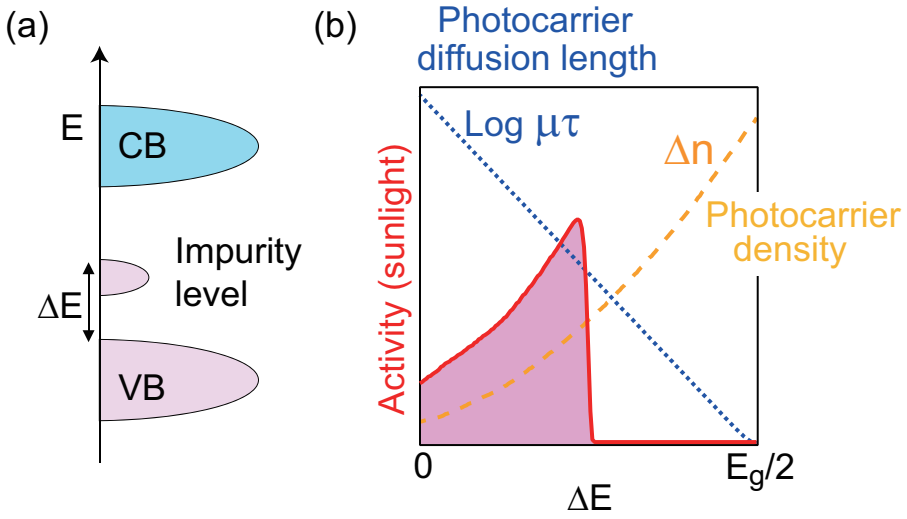

Figure 4.57: (a) Schematic band diagram of doped semiconductors. (b) Schematic diagram qualitatively showing the dopant level position effect on photoelectrochemical activity of a doped semiconductor photocatalysts under sunlight. Photocarrier diffusion length logarithmically decreases as the energy separation of the impurity level from the band gap edge increase, while the photocarrier density (light absorption intensity) increases.

Figure 4.58: Periodic table showing the impurity level positions induced by doping in the band gap region of $SrTiO_3$. The energy positions are compiled from literature, based on published experimental results and theoretical calculations [52, 55–57, 59, 65, 66, 276–340].

The discussion can be extended to other types of semiconductor photocatalysts. Here, as one example, I discuss the reason for the low photoelectrochemical activity of double perovskite oxides. A double perovskite has a crystal structure in which two elements fill the *B*-sites in the perovskite structure (Fig. 4.59(a)). In ABO_3 perovskite materials like $SrTiO_3$, the valence band is formed from O2*p* orbitals while the conduction band is formed of the unoccupied orbitals of *B*. So, if we assume $A_2BB'O_6$ to have an electronic structure shown in Fig. 4.59(b), by following the rigid-band model, the density of states of the conduction band bottom is smaller than for $AB'O_3$. The small density of states at the conduction band bottom suppresses the photocatalytic reduction reaction and also the migration of the photoelectrons in the conduction band. The photocarriers are scattered by the multiple B-site ions (Fig. 4.59(c)). The photocatalytic activity of $A_2BB'O_6$ is thus expected to be lower than for $AB'O_3$.

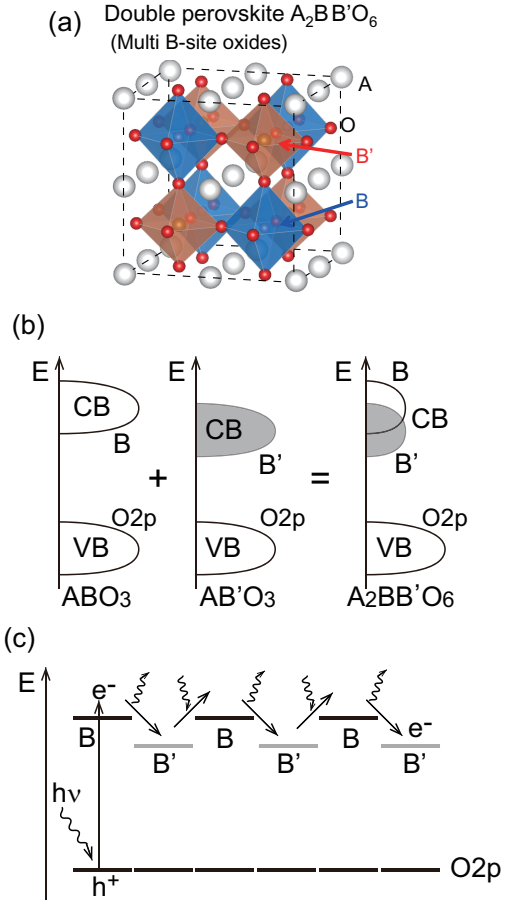

Figure 4.59: (a) Crystal structure of double perovskite oxides ($A_2BB'O_6$). (b) Electronic structure of double perovskite oxides, approximated by a linear combination of two perovskites (ABO_3 and $AB'O_3$), assuming a rigid band model. (c) Energy diagram showing that photoelectrons are strongly scattered in the conduction band of a double perovskite.

4.6 Conclusion

The electronic structure and the photoelectrochemical activity of Rh- and Ir-doped $SrTiO_3$ were investigated. The electronic structure of Rh- and Ir-doped $SrTiO_3$ was investigated experimentally by several forms of X-ray spectroscopy and by theoretical density of states calculations. The impurity level positions were determined and assigned. The photoelectrochemical properties of non-doped and Rh- and Ir-doped $SrTiO_3$ were investigated by conventional photoelectrochemical analysis. The carrier density dependence of the photoelectrochemical activity of Nb:$SrTiO_3$ clearly showed the importance of the matching the light absorption and photocarrier diffusion distances. The photoelectrochemical activity was strongly dependent on the dopant species (element, valence, and concentration). The dopant dependence of the photoelectrochemical activity was qualitatively understood from the viewpoint of the electronic structure. The impurity levels affect not only the light absorption intensity but also the photocarrier diffusion. Even though the light absorption intensity under sunlight is improved by the formation of the impurity levels in the band gap, the photocarrier diffusion length (the product of lifetime and mobility) becomes shorter by the formation of the impurity levels, especially by the impurity levels near the center of the band gap, because the impurity levels work as trap states and promote photocarrier recombination. The photocarrier lifetime of Rh-doped $SrTiO_3$ was investigated by pump-probe transient absorption spectroscopy, showing that the photocarrier lifetime was actually strongly dependent on the dopant species. Suitable dopant elements for $SrTiO_3$ are thus limited to Rh^{3+} and Cr^{3+}, elements that form occupied impurity levels at the top of the valence band of $SrTiO_3$.

However, the film thickness dependence of the photoelectrochemical activity of R^{3+}:$SrTiO_3$ indicated that the short photocarrier diffusion length is the most severe issue in doped $SrTiO_3$ photocatalysts. Therefore, the efficiency of the doped semiconductor photocatalysts is limited to a certain maximum level and will always suffer from a trade-off between the light absorption and the photocarrier diffusion rates.

Chapter 5

Photoelectrochemical activity enhanced by self-assembled metal nanopillars

The analysis of the photoelectrochemical activity of doped $SrTiO_3$ indicated that the limiting factor for the energy conversion efficiency is the low photocarrier mobility. This is a critical problem that needs to be overcome to construct practical efficient photoelectrodes. Considering the results of the photocarrier dynamics measurements, it is clear that the rapid carrier trapping and recombination leads to a serious mismatch between the very short photocarrier diffusion length and the large light absorption length of doped $SrTiO_3$.

In this chapter, I propose a new nanostructure design concept to enhance the photoelectrochemical activity of an oxide photoelectrode by working around the diffusion and absorption length mismatch problem. Implanting metal nanopillars in a semiconductor photoelectrode creates a nanoscale composite material where the photocarrier transport length can be made shorter to match the low carrier diffusivity. The charge separation efficiency is further improved in the oxide-metal composite material due to the formation of 3-dimensional Schottky junction space charge regions around the metal nanopillars. The formation of epitaxial metal nanopillars in an oxide thin film was successfully achieved by inducing phase separation during thin film growth. The growth dynamics of metal nanopillar structures and the enhancement of the photoelectrochemical activity are discussed. In particular, Ir-doped $SrTiO_3$ with embedded Ir metal nanopillars showed good operational stability in a water oxidation reaction and achieved over 80% utilization of photogenerated carriers under visible light in the 400 to 600 nm wavelength range.

5.1 Introduction

The photocurrent density can be described by the following equation,

$$J_{ph} = eJ_{ab} \times \eta_{ct} \times \eta_{sr}, \tag{5.1}$$

where e is the elementary charge and J_{ab}, η_{ct}, and η_{sr} are the absorbed photon flux, and the carrier transport and the surface reaction efficiencies, respectively. There are three main strategies for improving the photoelectrochemical activity of an electrode. The first is to select a semiconductor that has a large visible light absorption coefficient, i.e., a suitable band gap to absorb sunlight. The second strategy is to decorate the photoelectrode surface with an efficient electrocatalyst for the water splitting reaction, reducing the overpotential that is needed for the electrochemical reaction to occur. The third approach is to modify the morphology of the semiconductor. In the case of a film photoelectrode, only the depleted region near the water interface has a sufficient internal electric field to drive photogenerated charge to the water interface. Only a thin surface layer can therefore contribute to the photoelectrochemical reaction. In contrast, by controlling the morphology and forming nanowires, nanotubes or other 3-dimensional structures, it is possible to achieve a large specific surface area and also a large volume fraction of the semiconductor electrode filled with space charge regions. The photoelectrochemical efficiency can be improved by a combination of all these strategies as illustrated in Fig. 5.1.

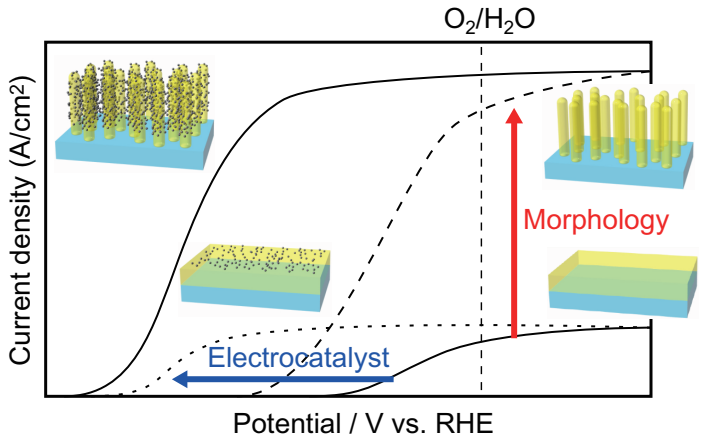

Figure 5.1: Strategy for improving a photoanode performance with representative photocurrent vs. potential curves showing the expected effects of morphology control. The line marked with O_2/H_2O corresponds to the redox potential of water oxidation.

The study of doped $SrTiO_3$ indicated that the most critical problem in this family of materials is the low efficiency of photocarrier transport from the bulk semiconductor to the photoelectrode

surface due the short intrinsic photocarrier diffusion length. Nanoscale material design of photoelectrodes is an effective method for improving photocarrier transport. Morphology control in the form of nanowires [341] or nanotubes [342], and the use of composite materials that combine a semiconductor with a metal [343] or a different semiconductor [344] have been shown to improve the photocarrier extraction efficiency from the bulk to the surface either by decreasing the charge transport distance or by creating additional internal electric field regions.

I demonstrate here a new nanoscale design concept, based on the utilization of self-assembled nanopillar structures (Fig. 5.2(a)) for improving the separation of photogenerated carriers. The major advantage of this structure is the mechanical stability compared to other nanostructures that are exposed on the surface of a photoelectrode, such as nanowires (Fig. 5.2(b)) and nanotubes. If a metal with an appropriate work function is embedded in the form of nanopillars, Schottky junctions form at the interface between the pillar and the semiconductor matrix, and band bending in the depletion region around each nanopillar promotes photocarrier separation and transport from the bulk semiconductor to the metal pillar and to the surface. My interest is in developing a nanocomposite material combining an n-type oxide semiconductor matrix with embedded three-dimensional noble metal electrodes. Since noble metals have high work functions, a Schottky barrier forms in an *n*-type oxide semiconductor in the vicinity of a metal pillar (Fig. 5.2(c)). The electric field in the Schottky depletion region helps to separate the photogenerated electrons from holes, effectively reducing recombination losses. Since the depletion region extends along the length of the pillar, through the thickness of the thin film, it is possible to increase the film thickness to absorb more sunlight, while still maintaining efficient carrier extraction to the surface. Even for thick semiconductor layers, the volume fraction that is effective in photogenerating charge can thus be kept high. Once the charge is generated in the bulk of the semiconductor, the carriers that migrate to the metal pillar can quickly reach the liquid interface. The nanopillars thus work as nanoscale embedded electrodes for charge extraction. The use of a noble metal as the nanopillar material has the additional advantage of noble metals being efficient electrocatalysts. The charge that is transported to the electrode surface via the metal pillars can thus participate directly in the oxygen evolution reaction on the metal surface.

During steady-state operation of a photoelectrode, a conduction path must be provided for both photogenerated holes and electrons. In case of an *n*-type semiconductor, the back electrode of a film can be a heavily-doped *n*-type conductor, such as Nb:$SrTiO_3$. If such a design is used, the noble metal nanopillars that extend through the thickness of the electrode, form a Schottky junction at the bottom substrate interface as well. This design thus insulates the metal nanopillar electrically from the substrate, forcing the collected charge to the liquid interface, rather than creating an electrical short circuit between the biased liquid interface and the back electrode. The improvement of photoelectrochemical activity has been demonstrated with coated nanowires (Fig. 5.2(b)). The improvement is due to the large surface area of a nanowire brush and the

short charge extraction distance along the radial direction of each nanowire. Nanowires can therefore, at least in principle, math the light absorption length (along the length of the wire) with the charge transport length (along the radius of the wire). However, operational longevity of a photoelectrode must also be considered. Exposed nanowires are mechanically far less robust than embedded metal pillars inside a bulk semiconductor and require costly multi-step fabrication procedures. In contrast, the embedded nanopillar composites form spontaneously in a single thin film growth process by adjusting the growth rate, substrate temperature, and the oxygen pressure. The synthesis process is much simpler, while providing a mechanically robust nanoscale electrode geometry.

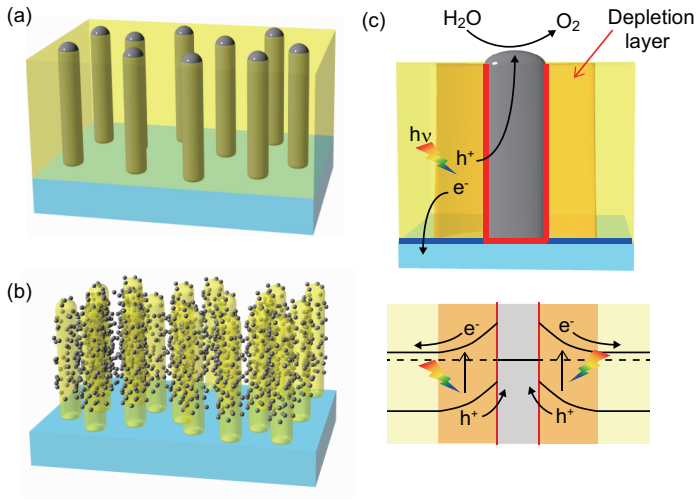

Figure 5.2: (a) Schematic illustration of embedded metal nanopillars in a semiconductor film. (b) Schematic illustration of semiconductor nanowires coated with electrocatalyst nanoparticles. (c) Schematic illustration of a tubular 3-dimensional Schottky junction formed around a metal nanopillar and a qualitative band structure diagram. Red lines mark Schottky barriers, blue lines mark Ohmic interfaces.

5.2 Fabrication of self-assembled metal nanopillars in an oxide thin film

Here, I show that spontaneous noble metal segregation in an oxide perovskite matrix can be used in a simple single-step film deposition process to grow metal-oxide nanocomposites consisting of noble metal nanopillars in a semiconducting oxide matrix.

Spontaneous nanoscale phase separation is not a new discovery. For example, segregation of ferromagnetic CoPtCr grains in a CrO_x [345] or SiO_x [346] matrix has been suggested as a way to create patterned magnetic recording media. In such designs, the embedded functional nanoparticles are randomly distributed in the matrix, while the matrix material itself only functions as a spacer, without having a functional role in the magnetic recording process.

In other designs, both the matrix and the embedded nanostructures work together to obtain the desired functional behavior. The coupling can be electronic or elastic, as in a composite consisting of self-organized ferromagnetic $CoFe_2O_4$ nanopillars in a ferroelectric $BaTiO_3$ matrix leads, where strain coupling between the magnetostrictive nanopillars and the matrix leads to strain-mediated multiferroic behavior [347]. A similar idea has been used for efficient solar energy harvesting in organic solar cells by combining *n*- and *p*-type semiconductors in a 3-dimensional bicontinuous network of internal donor-acceptor heterojunctions [348].

Segregation of pure metals in oxides has also been observed. Reports exist for the segregation of Fe [349], Co [350], Cu [351], AgCo [352], Pb [353] and several noble metals such as Rh, Pd, Pt, and Au [354, 355].

Phase separation can lead to the formation of many types of nanostructures. For photoelectrode designs, the interest is in forming vertical pillar-shaped structures, as explained earlier. Self-assembled nanopillar formation has been observed for various combinations of materials. Metal nanopillars in an oxide matrix have been reported for Fe [345, 346], $LaSrFeO_4$ [349], Co nanopillars in YSZ [350], AgCo nanopillars in TiO_2 [352], and Cu nanopillars in $SrTiO_3$ [351]. Besides simple metals, nanopillar formation has also been reported for several oxide systems. For example, MgO nanopillars in $La_{0.7}Ca_{0.3}MnO_3$ thin film have been fabricated by PLD [356]. Later, $CoFe_2O_4$ nanopillars in $BaTiO_3$ [347], $BaMO_3$(M = Zr, Sn, Hf) nanopillars in $YBa_2Cu_3O_{7-x}$ [357, 358], ZnO nanopillars in $La_{0.7}Sr_{0.3}MnO_3$ [359], Sm_2O_3 nanopillars in $BiFeO_3$ [359], $CoFe_2O_4$ nanopillars in $Bi_5Ti_5FeO_15$ [360] have been demonstrated. The fabrications and the functionalities of the vertically oriented oxide composites have been reviewed in ref.361, 362. The formation mechanism and he growth dynamics has been simulated by Monte Carlo simulations [363]. Vertical nanocomposite fabrication in a single film deposition process has also been reported for organic materials and the structure has been utilized in bulk-heterojunction organic solar cells [364, 365].

Generally, spontaneous phase separation during thin film growth induces the formation of the self-assembled nanostructures, often in the form of isolated nanoparticles. If the phase

separation occurs during the initial growth phase or during the film nucleation, nanopillars can form. The growth of nanopillars is governed by a balance between thermodynamic phase separation and the kinetics of thin film growth. Fig. 5.3 illustrates the growth process of self-assembled metal nanopillars in a thin film matrix. When a two-phase mixture that tends to separate thermodynamically is deposited on a substrate, spontaneous phase separation induces a nucleation of nanoparticles at the initial stage of the film growth (Fig. 5.3(c)). The metal segregates continuously on the metal surface during the film growth, so that the metal grows vertically in the film matrix, forming a vertically oriented self-assembled nanopillar structure (Fig. 5.3(f)). The diameter of a single nanopillar is dependent on the film deposition rate, the composition ratio of two-phase mixture, the temperature, and the oxygen pressure during growth.

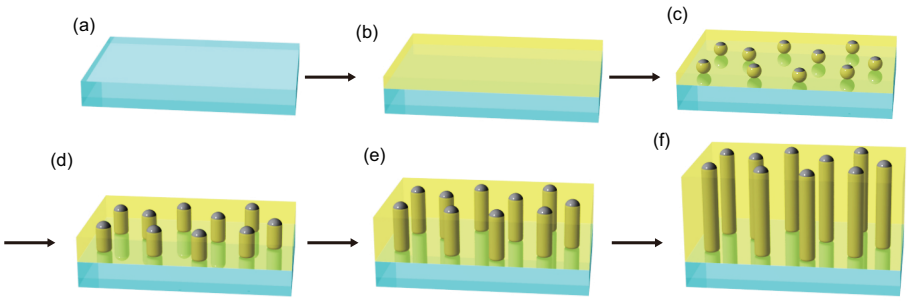

Figure 5.3: Illustrations showing the growth process of self-assembled metal nanopillar in a thin film matrix. (a) Substrate. (b) Thin film deposited on a substrate. If phase separation occurs during thin film growth, metal nanoparticles appear in the initial nucleation layer (c). Continuous phase separation during thin film deposition leads to the growth of metal nanoparticles in the out-of-plane direction (d), and finally nanopillar structures are spontaneously formed (e, f). The substrate, thin film, and metal are blue, yellow, and gray, respectively.

In this study, the formation of noble metal nanopillars in a $SrTiO_3$ matrix was studied in a single film deposition process using PLD. Since the separation of a pure metal phase from $SrTiO_3$ is an essential requirement for making metal nanopillars in $SrTiO_3$, the formation enthalpy of binary oxides and the bond dissociation energy are useful indicators as selection guidelines for considering which elements are good candidates for forming metal nanopillars in a $SrTiO_3$ matrix. Fig. 5.4 shows the standard formation enthalpy of binary AO_x oxides. The data was obtained from Ref.366 and divided by 1 mol of A atoms. Elements that have a large negative formation enthalpy tend to be easily oxidized, whereas elements with a small formation enthalpy tend to be resistant to oxidation. There is a periodicity in the plot, showing that elements in groups 3,4,5,13, and 14 have large negative formation enthalpy in binary oxides, and elements in groups 10,11,17, and 18 tend to have small enthalpies. Both TiO_2 and SrO have

large negative formation enthalpies of < 500 kJ/mol, indicating that Ti and Sr do not usually exist as pure metals in the atmosphere. In contrast, Au, Ag, Pt, and other noble metals have small formation enthalpies for binary oxides, and can be much more stable as pure metals.

Difference of bond dissociation energies between *A*-*A* and *A*-O bonds indicates how easily elements react with oxygen to form oxides. Fig. 5.5(a) shows the difference of bond dissociation energies between *A*-*A* and *A*-O bonds. This plot also shows a more or less similar periodicity with the standard formation enthalpy of binary oxides. The bond dissociation energy was taken from Ref. 367. My purpose in fabricating metal nanopillars in $SrTiO_3$ is to create Schottky junctions around each nanopillar for enhancing the electron-hole separation and charge collection efficiency in doped $SrTiO_3$. The metal elements that tend to be oxidation resistant compared to $SrTiO_3$ and have large work functions are suitable for this purpose. The difference of bond dissociation energies between *A*-*A* and *A*-O bonds as a function of the work function of metals is plotted in Fig. 5.5(b). Thus, Ir, Rh, Pd, Au, and Pt were selected and examined as candidates for fabricating metal nanopillars in $SrTiO_3$. These metals have the *fcc* structure with lattice constants of ~ 4 Å. The lattice constants are a = 3.8394 Å for Ir, a = 3.71559 Å for Rh, a = 3.8898 Å for Pd, a = 4.07864 Å for Au, and a = 4.39231 Å for Pt, whereas $SrTiO_3$ has a cubic perovskite structure with a lattice constant of a = 3.905 Å. Since all these metals have small lattice mismatch with $SrTiO_3$, they can be epitaxially grown on $SrTiO_3$.

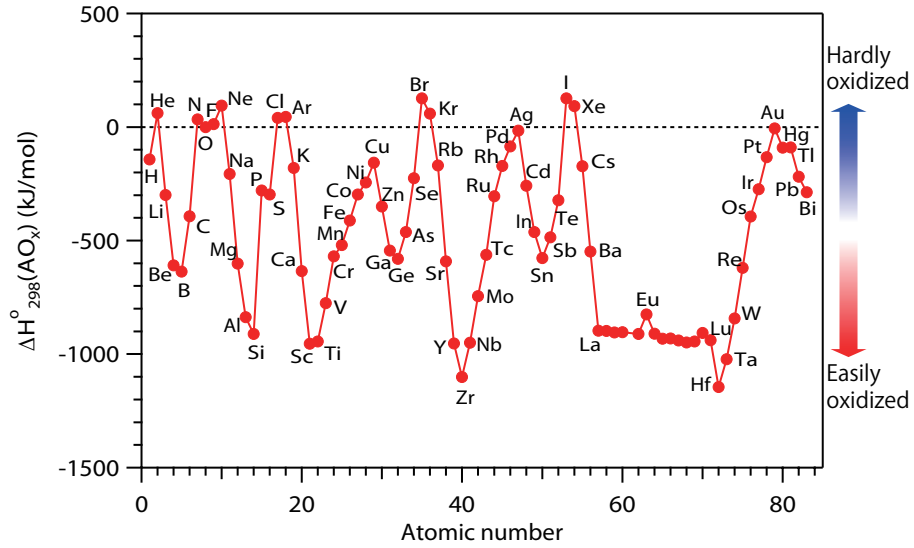

Figure 5.4: The standard formation enthalpy of binary oxides AO_x. The data was obtained from Ref.366 and divided by 1 mol of *A* atoms.

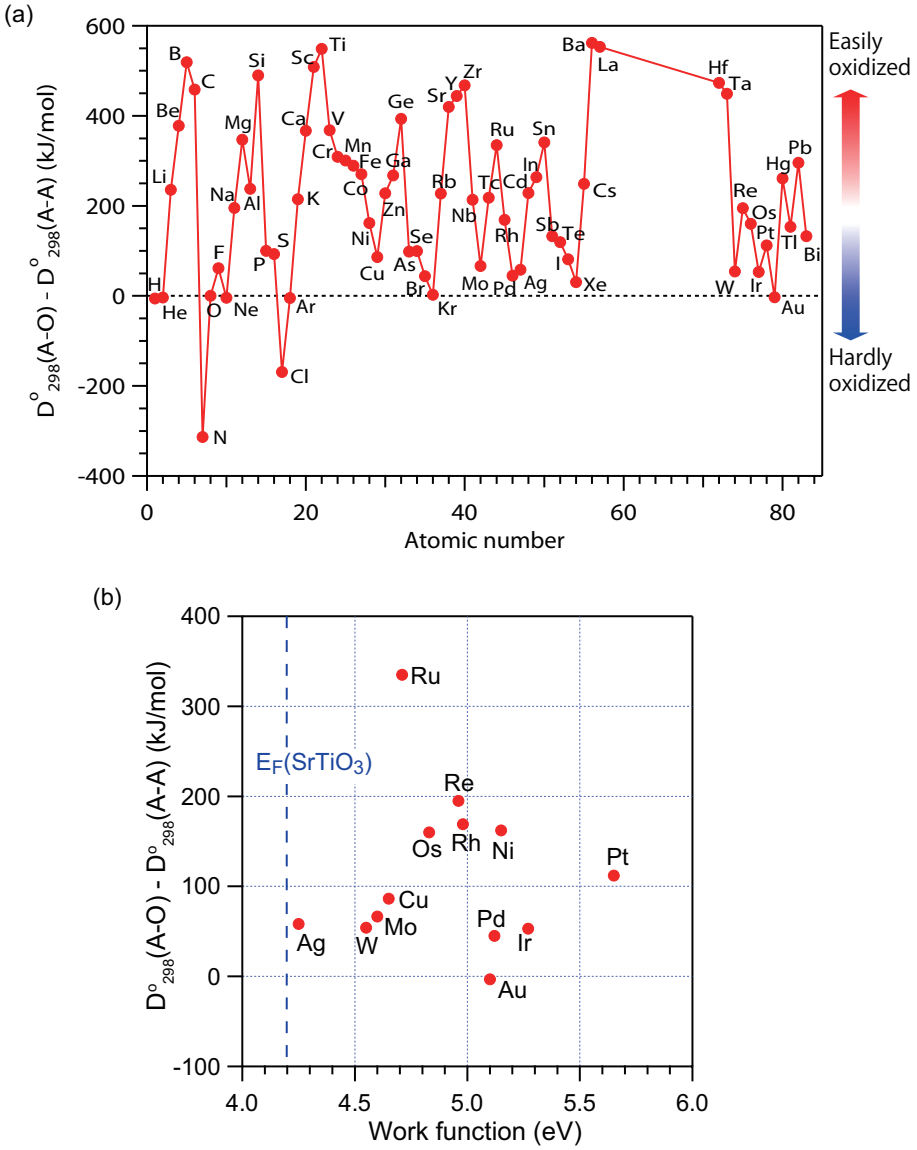

Figure 5.5: (a) Difference of bond dissociation energies between *A*-*A* and *A*-O bonds. (b) Difference of bond dissociation energies between *A*-*A* and *A*-O bonds as a function of the work function of metals. The bond dissociation energy and the work function were taken from Ref. 367 and Ref. 222, respectively. The work function of $SrTiO_3$ is reported to be 4.2 eV. [223]

Spontaneous phase separation during thin film growth induces a formation of self- assembled nanopillar structure. Here, noble metal segregation from $SrTiO_3$ matrix was demonstrated by PLD and the dynamics of metal segregation dependent on the film growth conditions (temperature, oxygen pressure, growth rate, and metal/$SrTiO_3$ composition) was investigated.

$SrTi_{0.95}M_{0.05}O_3$ (M(5%):$SrTiO_3$) (M = Ir, Rh, Pd, Pt, and Au) targets were used for PLD deposition to examine the formation of metal nanopillars of Ir, Rh, Pd, Pt, and Au metals in $SrTiO_3$. The targets were prepared by conventional solid state synthesis using $SrCO_3$(Wako, 99.99%), TiO_2(rutile)(Wako, 99.99 %), IrO_2(Wako, > 99.7%), Rh_2O_3(Wako; > 98.0%), PdO(Wako; 99.9 %), Au_2O_3(Wako; 99.9%), and PtO_2(Wako; 99.95%). Fig. 5.5 shows the images of the M:$SrTiO_3$ targets. $SrTiO_3$ has a 3.2 eV band gap, does not absorb visible light and therefore has no color. However, the M:$SrTiO_3$ targets have color, except for Au:$SrTiO_3$. This indicates that Ir, Rh, Pd, and Pt dope $SrTiO_3$ and created impurity levels in the band gap of $SrTiO_3$. The fact that Au:$SrTiO_3$ was white indicated that Au did not work as a dopant and probably dispersed n th form of segregated metal particles in the target.

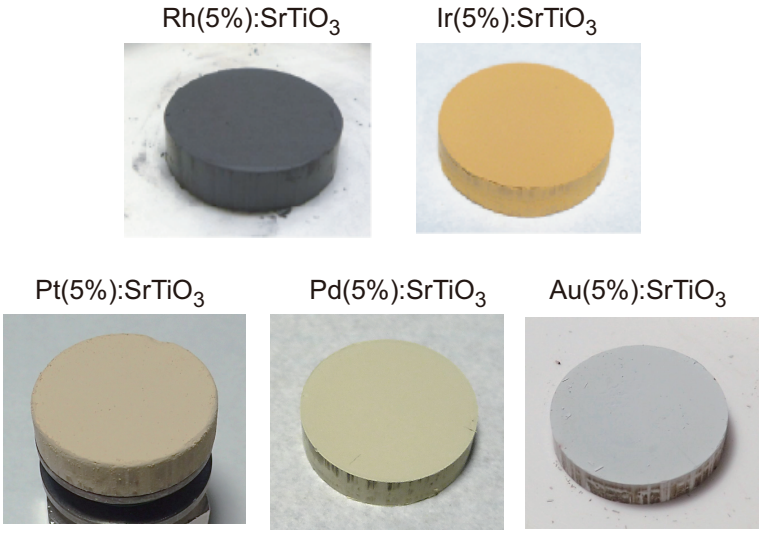

Figure 5.6: Images of M(5%):$SrTiO_3$ (M = Ir, Rh, Pd, Au, and Pt) targets.

Ir(5%):$SrTiO_3$ films were deposited on $SrTiO_3$ (001) substrates at various substrate temperature and oxygen pressure by PLD. Deposition conditions of Ir(5%):$SrTiO_3$ films are marked with red circles in Fig. 5.7, together with vapor pressure plots of binary oxides and Ir metal [209,368] and the Ir Ellingham curve [369]. Ir metal segregation was found by AFM in films grown at around 700°C, 10^{-3} Torr of oxygen at an ablation pulse rate of 2 Hz. Increasing the temperature to 1100°C caused a loss of Ir from the film due to the volatility of nonstoichiometric Ir oxides. No metal clustering was observed at 500°C or lower, Ir was incorporated in the $SrTiO_3$ lattice instead. The metal segregation is quite sensitive to the oxygen pressure. At both high

(10^{-1} Torr) and low (10^{-6} Torr) oxygen pressures, Ir metal segregation was not observed and clear step-and-terrace film surfaces were obtained. Under the optimum conditions at 700°C and 10^{-3} Torr, ~ 60% of Ir substituted at the Ti site of the $SrTiO_3$ host material as Ir^{4+} and the remaining 40% segregated as pure Ir metal in nanopillars.

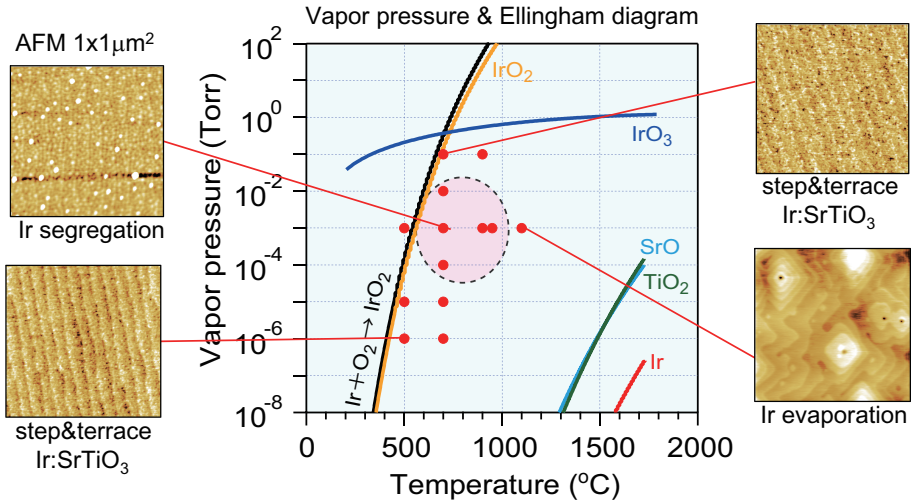

Figure 5.7: Deposition window of Ir(5%):$SrTiO_3$ films (red circles) together with vapor pressure plots of binary oxides and Ir metal [209,368]. The black line marks the Ir Ellingham curve [369]. Ir metal nanopillars formed in the region encircled with the dotted line. The AFM imaging area was 1×1 μm^2.

The Ir segregation can be monitored by in-situ RHEED during thin film growth. Fig. 5.8 shows typical RHEED patterns before and after Ir(5%):$SrTiO_3$ film deposition at 700°C, 10^{-3} Torr, together with the time evolution of the RHEED specular spot intensity during film deposition. After film deposition, a spotty RHEED pattern appeared. Such a spot pattern is typically caused by transmission-mode electron diffraction form 3-dimensional islands. Since the segregated metal formed a clear bump on the $SrTiO_3$ surface as shown by AFM, a mixed pattern of Ir metal transmission spots overlapped with the $SrTiO_3$(001) surface diffraction of spots on Laue circles and vertical streaks. This behavior indicates that Ir metal diffused very rapidly on the $SrTiO_3$ surface and formed liquid-like droplets at the initial nucleation stage. RHEED showed a transmission spot pattern from the time when the first or the second unit cell of $SrTiO_3$ layer was grown, indicating that Ir metal segregation started at a very early stage of the film growth. The time evolution of RHEED intensity diffracted from the $SrTiO_3$ film surface showed intensity oscillations, which can be clearly seen between 0 and 150 sec marks in Fig. 5.8(c). This oscillation corresponds to layer-by-layer growth of the $SrTiO_3$ matrix.

The film thickness dependence of Ir metal segregation is summarized in Fig. 5.9. The AFM images show that Ir metal precipitates appears from the initial stage of the film growth. The

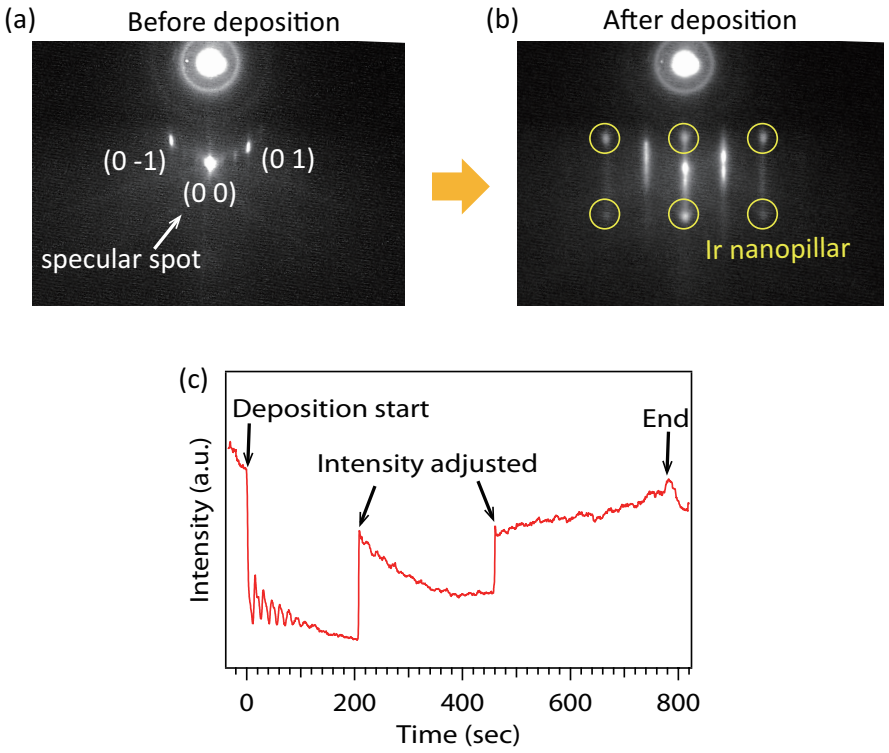

Figure 5.8: Typical RHEED patterns of a $SrTiO_3$(001) substrate (a) before and (b) after Ir(5%):$SrTiO_3$ deposition at 700°C, 10^{-3} Torr. From the initial stage of the film deposition, a transmission spot pattern (marked with yellow circles) was observed in addition to the diffraction from the flat $SrTiO_3$(001) surface. (c) Time evolution of the specular RHEED intensity during film deposition.

Ir metal particles were clearly observed even on a film with 1 or 2 ML thickness. The surface coverage of the Ir metal was almost constant, independent of the film thickness. The size of the Ir metal precipitates grew gradually as the film thickness increased, whereas the number density of the precipitates decreased. Especially when the film thickness became larger than ~ 100 nm, the diameter of the Ir precipitates on the surface became much wider. This may indicate that the growth mode of the metal nanopillars changed when the film thickness increased over ~ 100 nm.

The effect of the film growth rate on Ir metal segregation is illustrated in Fig. 5.10. Ir(5%):$SrTiO_3$ films with 20 nm thickness were deposited at 700°C, 10^{-3} Torr. The growth rate was controlled by changing the repetition rate of the KrF excimer laser. The laser fluence was ~ 1 J/cm^2. The size and coverage of Ir metal precipitates was clearly dependent on the growth rate. When the film was deposited at a fast growth rate, the Ir metal precipitates became smaller. On the other hand, the film deposited at slow rate had much larger precipitates. In this case,

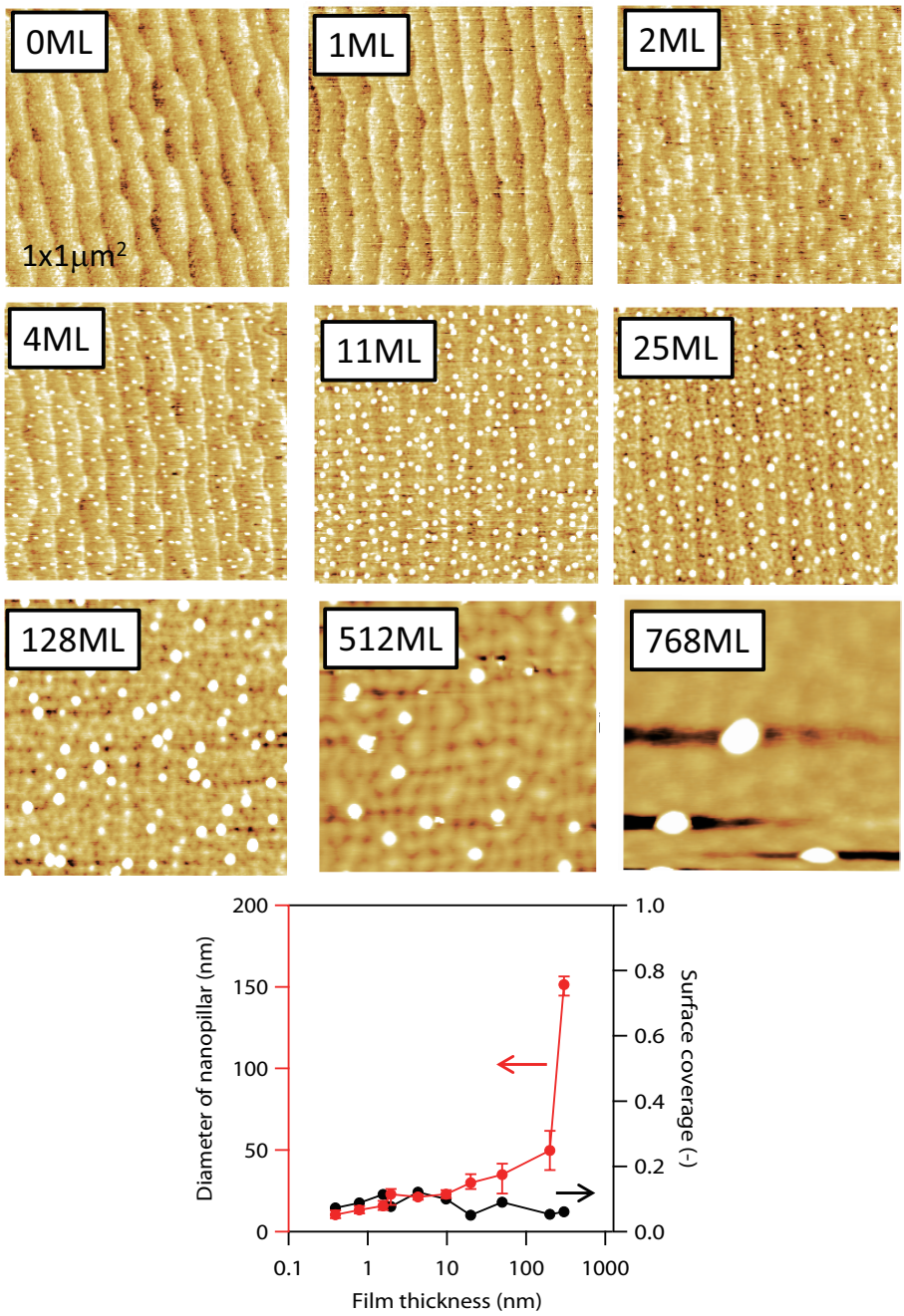

Figure 5.9: AFM images ($1 \times 1\ \mu m^2$) of Ir(5%):$SrTiO_3$ deposited at 700°C, 10^{-3} Torr, with different film thickness of 0 ~ 768 ML (300 nm). A summary of the thickness dependence of the diameter and the surface coverage of the Ir metal precipitates is shown in the plot.

small Ir metal nanoparticles might be dispersed in the film. Therefore, the size of the Ir metal precipitates appears to be determined by the time between deposition pulses, during which the Ir metal atoms can migrate on the surface, similar to a nanoparticle ripening process. However, at the slowest growth rate of 312 sec/nm, Ir metal precipitates no longer formed and a non-doped film was obtained. This could be understood by the evaporation of Ir metal due to the slow deposition rate. The results indicate that the size of the segregated Ir metal nanostructures is controlled by the surface relaxation time between deposition pulses, while the slowest growth limit is set by the evaporative loss of Ir from the surface. Metal nanopillars must thus be grown at a suitable deposition rate to obtain the desired nanopillar diameter.

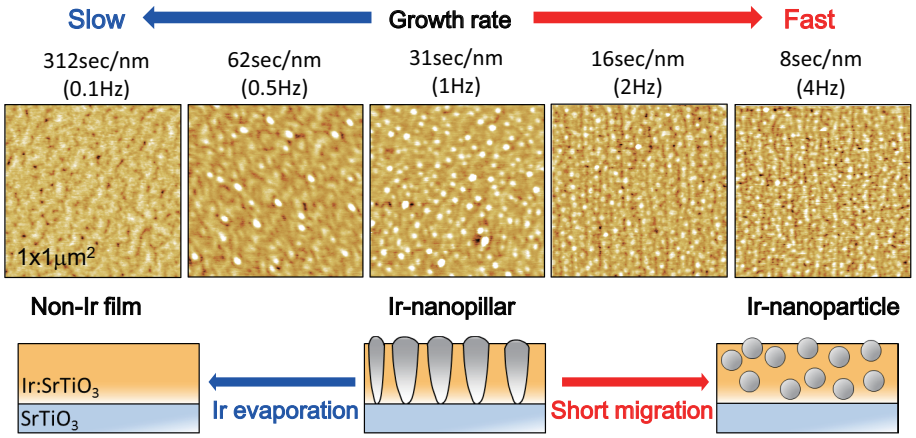

Figure 5.10: AFM images (1×1 μm^2) of Ir(5%):$SrTiO_3$ (thickness 20 nm) grown at 700°C, 10^{-3} Torr at different growth rates. The growth rate was controlled by changing the repetition rate of the KrF excimer laser.

The growth dynamics of Ir metal precipitates in the process of $SrTi_{1-x}Ir_xO_3$ deposition by PLD, discussed above, are summarized in Fig. 5.11. The tendencies of Ir metal nanopillar growth could be understood to be governed by a balance between surface migration and evaporation of Ir during growth. At high temperature, Ir evaporation is dominant and precipitates disappear from the surface. At low temperature, Ir migration length becomes too short for macroscopic segregation to occur. The oxygen pressure dependence indicates that Ir evaporates from the surface at low background oxygen pressure, while the surface migration of Ir is suppressed at high oxygen pressure, stabilizing an oxide phase. Hence, there is a optimum temperature and oxygen pressure for Ir metal nanopillar growth in $SrTiO_3$, at 700°C and 10^{-3} Torr. The deposition rate was also an important factor that determines the Ir metal nanopillar size. At fast deposition rates, the interval between deposition pulses is insufficient for Ir to migrate on the surface and coalesce into larger precipitates. Instead, at high laser pulse rates small precipitates were dispersed in the film. If the growth rate is too slow, Ir may be lost from the

surface due to slow evaporation and metal segregation can no longer occur. These tendencies are basically similar to the growth dynamics of oxide nanopillar composites [363], although the evaporation effects must be considered in the case of metal nanopillars.

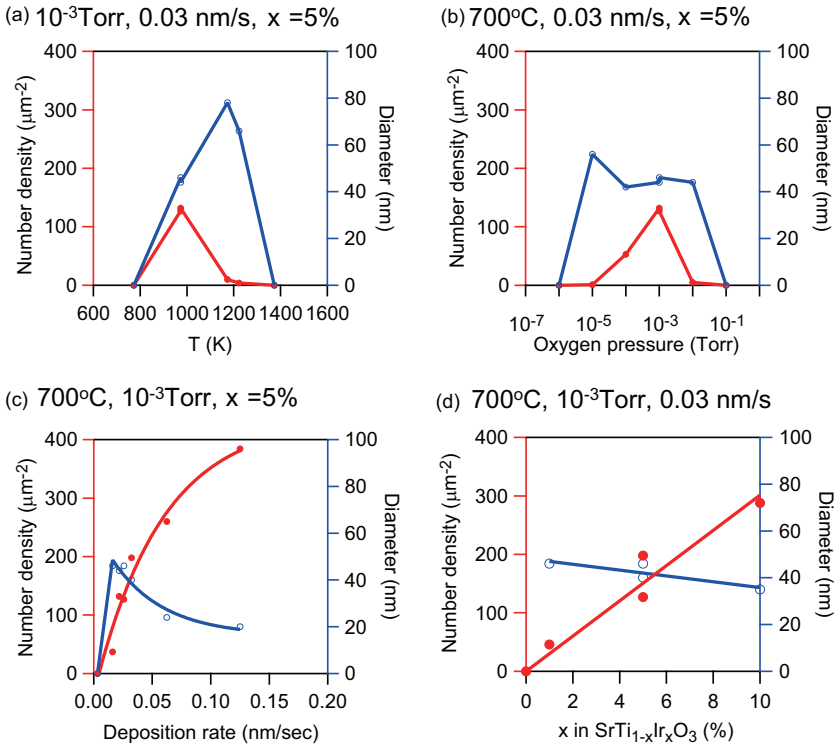

Figure 5.11: Growth dynamics of Ir metal precipitates in the process of $SrTi_{1-x}Ir_xO_3$ deposition by PLD. The number density and diameter of Ir metal precipitates are plotted as a function of growth temperature, oxygen pressure, deposition rate, and Ir content in $SrTiO_3$. (a) Temperature dependence investigated at 10^{-3} Torr, 0.03 nm/s, x = 5%. (b) Oxygen pressure dependence investigated at 700°C, 0.03 nm/s, x = 5%. (c) Deposition rate dependence investigated at 700°C, 10^{-3} Torr, x = 5%. (d) Ir content dependence investigated at 700°C, 10^{-3} Torr, 0.03 nm/s.

XRD revealed that the nanopillars consisted of Ir metal with the bulk fcc structure and had a cube-on-cube epitaxial relationship with the $SrTiO_3$ matrix. Fig. 5.13 shows XRD $\omega - 2\theta$ scan profiles of an Ir:$SrTiO_3$ film (thickness 300 nm) deposited on a $SrTiO_3$(001) substrate at 700°C, 10^{-3} Torr overlapped with the data of a bare $SrTiO_3$(001) substrate, together with the expected bulk peak positions of Ir metal. The (002) and (004) peaks of Ir metal were observed in addition to the diffraction peaks from $SrTiO_3$ film and the substrate, meaning that Ir was epitaxially grown in $SrTiO_3$. The peak positions of Ir metal were slightly shifted from the peak positions of the reference data, showing that the Ir lattice was distorted. That is most likely due to epitaxial strain between $SrTiO_3$ (a = 3.905 Å) and Ir (a = 3.839 Å), where the lattice mismatch is 1.7%.

Fig. 5.13(a) shows a pole figure measured at $2\theta = 40.673°$, corresponding to the diffraction angle of the Ir (111) plane. The four peaks at $\phi = 45$, 135, 225, and 315° are assigned to diffraction from (111), $(1\bar{1}1)$, $(\bar{1}11)$, and $(\bar{1}\bar{1}1)$ of Ir metal. This proves that Ir metal was epitaxially grown on $SrTiO_3$ (001) with cube-on-cube alignment.

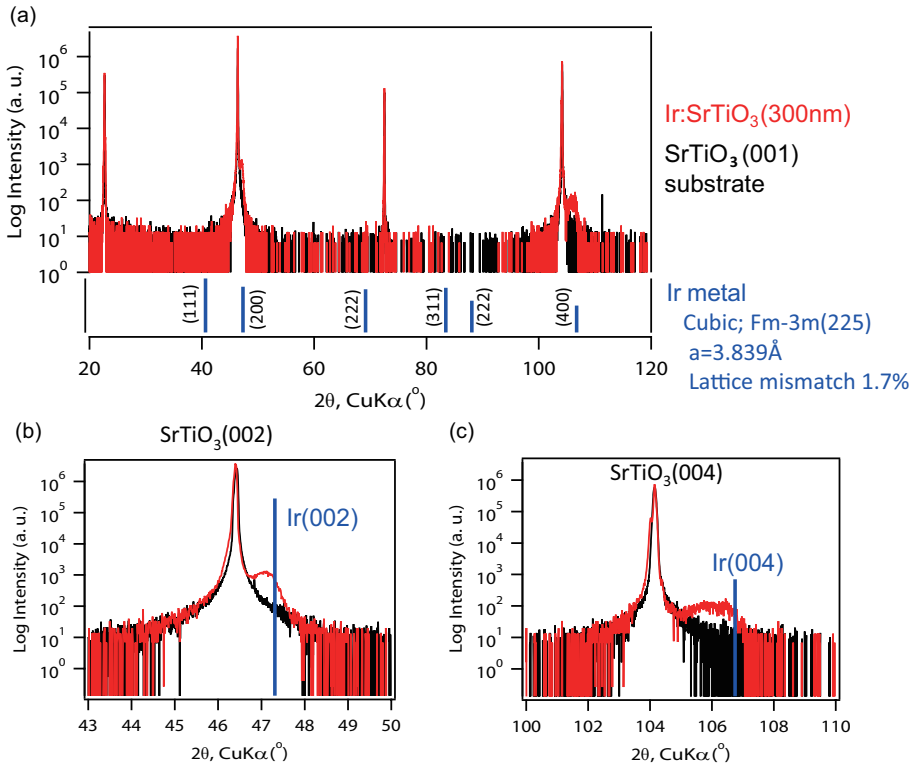

Figure 5.12: XRD $\omega - 2\theta$ scans of Ir:$SrTiO_3$ film (thickness 300 nm) deposited on a $SrTiO_3$(001) substrate at 700°C, 10^{-3} Torr, overlapped with the data of a bare $SrTiO_3$(001) substrate, together with peak positions of Ir metal. (a) A wide image, and narrow scaled images around (b) $SrTiO_3$(002) and (c) $SrTiO_3$(004).

The atomic-scale structure of Ir nanopillars was analyzed by high-angle annular dark field scanning transmission electron microscopy (HAADF-STEM). The pillar structure was observed by HAADF-STEM in a Ir:$SrTiO_3$ film (thickness 20 nm) deposited on a $SrTiO_3$(001) substrate at 700°C, 10^{-3} Torr (Fig. 5.14). Since the HAADF-STEM contrast is proportional to the atomic weight, heavier elements are shown brighter in the images. The bright dots in the plan-view image thus correspond to segregated Ir. The areal density of the bright spots in the STEM image is comparable to the density of surface precipitation features seen in AFM images. While AFM images could not be used to determine if the observed Ir precipitates remain only on the film surface or extend into the film, the cross-section STEM image clearly shows that the Ir metal pillars extend to the substrate interface. The in-plane and out-of-plane STEM images give direct

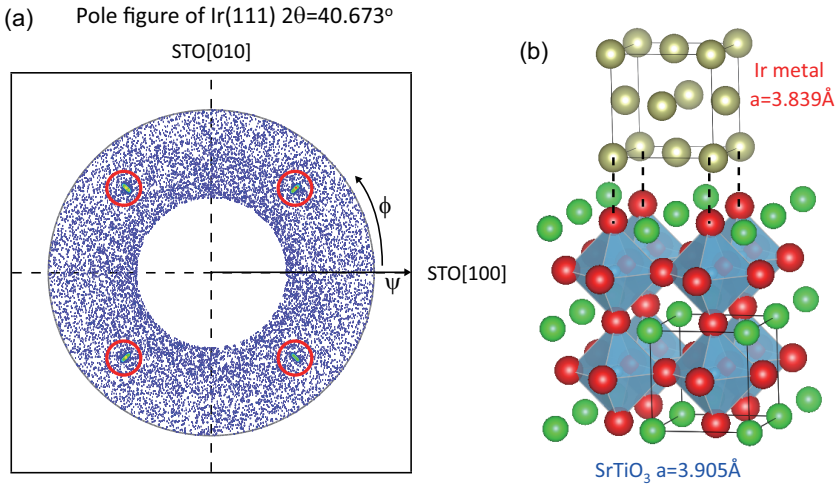

Figure 5.13: (a) Pole figure at $2\theta = 40.673°$ corresponding to Ir(111). The diffraction peaks from Ir metal (111) are marked with red circles. (b) Schematic illustration showing the epitaxial relationship between Ir and $SrTiO_3$. The XRD analysis indicated that Ir was grown in $SrTiO_3$ with a cube-on-cube geometry.

proof that there is indeed an epitaxial relationship between the fcc metal lattice in the Ir pillars and the $SrTiO_3$ lattice, as was inferred from the X-ray diffraction pole figures.

Interestingly, the STEM images show that the crystal quality of an Ir:$SrTiO_3$ film deposited at 700°C, 10^{-3} Torr was exceptionally high. The film lattice is nearly indistinguishable from the $SrTiO_3$ substrate lattice in Figs. 5.14(c) and (d). It appears that the Ir nanopillars may function as defect getter sites due to the high surface mobility of Ir metal. For comparison, even homoepitaxial $SrTiO_3$ films grown at 700°C include many point defects induced by cation non-stoichiometry, as can be seen in typical STEM images of homoepitaxial $SrTiO_3$ films [113, 114]. The role of the Ir metal may thus be similar to a flux for $SrTiO_3$ growth [370], as indicated by the formation of ~ 5 unit-cell-high $SrTiO_3$ cones around the Ir nanopillars.

Since Ir metal has a very high work function of 5.3 ~ 5.8 eV [222] and $SrTiO_3$ is an *n*-type semiconductor with a work function of 4.2 ~ 4.3 eV [223], a Schottky junction forms at the pillar interface with the $SrTiO_3$ matrix. The formation of a depletion layer around the metal nanopillars increases the volume fraction of the film where strong internal electric fields enhance photocarrier separation. The transport characteristics of the embedded nanopillars can be measured with local-probe transport analysis of the with a conducting AFM tip (Fig. 5.15(a)). The current-mode AFM images showed that the Ir nanopillars form a Schottky junction with the conducting Nb:$SrTiO_3$ substrate (Fig. 5.15(b)). The built-in potential was ~ 1.5 V, which is consistent with the work function difference between Ir metal and the Nb:$SrTiO_3$ substrate. Figs. 5.15(c) and (d) show AFM topography and simultaneously acquired current mapping

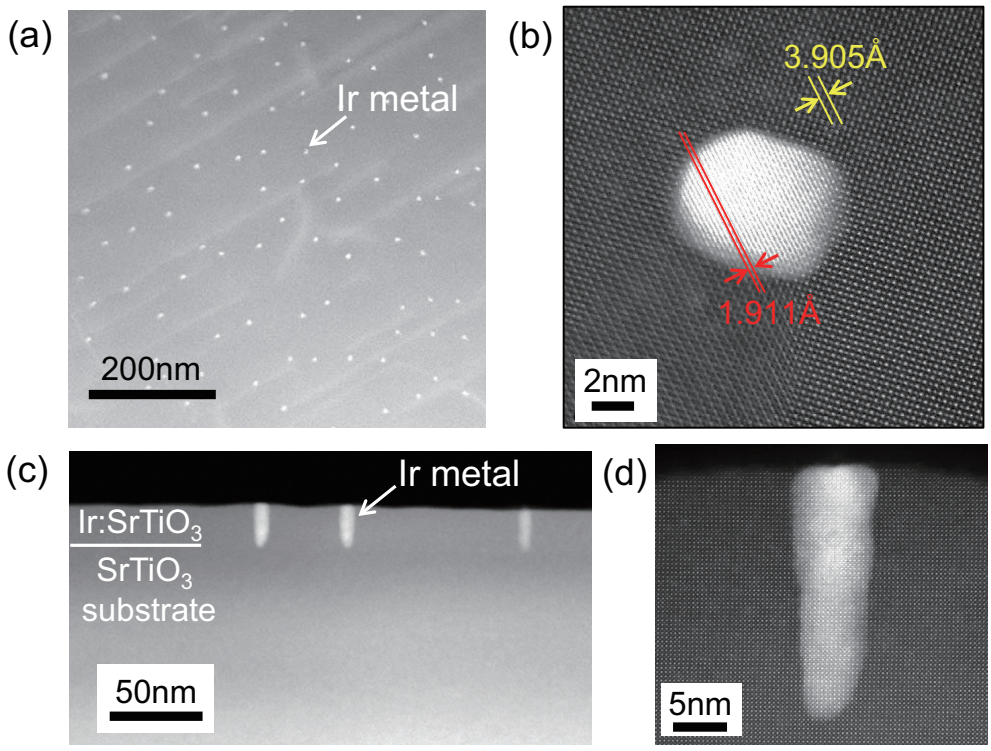

Figure 5.14: (a) Plan-view HAADF-STEM image of an Ir(5%):$SrTiO_3$ (20 nm) film deposited at 700°C, 10^{-3} Torr. The bright dots correspond to the Ir metal pillars. (b) A plan view image of a single pillar shows that the Ir metal lattice is epitaxially matched with the $SrTiO_3$ crystal lattice. The lattice parameters are 3.905 Å for $SrTiO_3$ and 1.911 Å for the Ir metal. The Ir atom spacing corresponds to half of the lattice constant of fcc Ir metal (a = 3.839 Å). (c) and (d), Wide and narrow cross-section HAADF-STEM images of the same sample.

images of a Ir(5%):$SrTiO_3$ film, measured at an applied ac bias of 2.5 V. Metallic conductivity at the pillar positions exceeded the Ir:$SrTiO_3$ film conductivity by a factor of at least 10^5.

The formation of Pt, Pd, Rh, and Au nanopillars in $SrTiO_3$ was also demonstrated. Thin films of $SrTi_{0.95}M_{0.05}O_3$ (M = Pt, Pd, Rh, and Au) were deposited at various temperatures and oxygen pressures by PLD to optimize the conditions for each metal where pillar segregation occurs. The growth condition mapping results are summarized in Fig. 5.16, where the vapor pressures of binary oxides and metals, together with Ellingham curves of metals are also plotted. The deposition conditions at which metal precipitates were observed by AFM are marked with red circles, and the conditions at which metal segregations were not clear are marked with red triangles. Also, the conditions at which metal precipitates were not observed are marked with red x-marks. The corresponding AFM images for Pt, Pd, Rh, and Au are summarized below. The optimum growth conditions were dependent on the metal species; 1100°C and 10^{-6} Torr

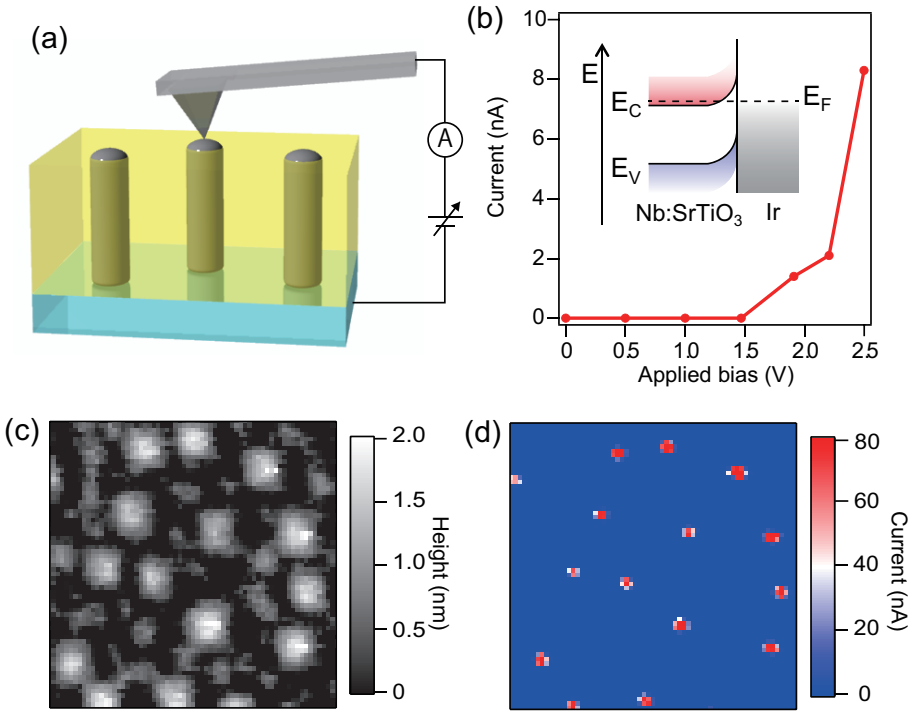

Figure 5.15: Local-probe conductivity analysis of a nanopillar composite film. (a) Schematic illustration of the current mapping measurement. (b) Current-voltage curve measured on a single Ir metal nanopillar. The inset illustrates the band diagram of the Schottky junction between an Ir pillar and the Nb(0.1%):$SrTiO_3$ substrate. (c) Topographic AFM image (250*times*250 nm^2) of an Ir(5%):$SrTiO_3$ nanopillar film. (d) Current mapping obtained at an applied bias of 2.5 V, simultaneously acquired with (c).

for Pt, 700°C and 10^{-6} Torr for Pd, 900°C and 10^{-3} Torr for Rh, and 700°C and 10^{-6} Torr for Au. In general, metal segregation from M:$SrTiO_3$ occurs at high temperature and low oxygen pressure, but when the temperature is close to the vapor pressure of a metal (or metal oxide) the metals evaporate from the film surface. There is thus an optimum range of temperature and oxygen pressure for each metal where metal precipitates can form. If the migration rate of a metal on the film surface is low, the metals doped the $SrTiO_3$ host matrix or possibly form nanoscale metal clusters. In contrast, if the thermal diffusion rate of a metal is too high, e.g., due to the use of lower oxygen pressure, the metals evaporate from the film. For all metals studied here, intermediate condition were found, where the metals segregate and are stabilized as metal nanopillars. Therefore, a suitable balance between thermodynamic phase separation and kinetic thin film growth is necessary for preparing nanopillar composite thin films.

Since Pt-O interaction is stronger than Ir-O, Pd-O, and Au-O, as seen in Fig. 5.5(a), Pt might have a very short diffusion length on a oxide surface compared to Ir, Pd, and Au. The optimum

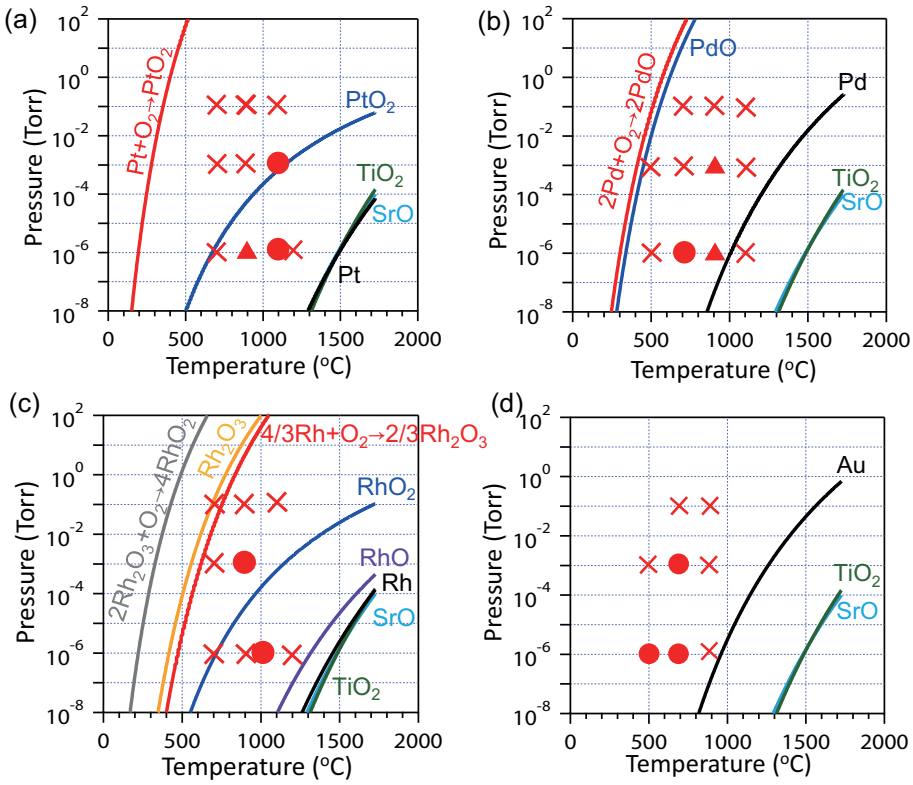

Figure 5.16: Growth condition of (a) Pt, (b) Pd, (c) Rh, and (d) Au nanopillars in $SrTiO_3$. Vapor pressures and Ellingham curves of related binary oxides and metals are plotted in each panel. Red circles indicate the deposition conditions at which metal nanopillars are clearly formed. Red triangles indicates the deposition conditions at which segregation can be observed but pillars were not formed, while red crosses mark conditions at which metal segregation did not occur.

growth temperature to form Pt nanopillars was 1100°C, which is much higher than the optimal values for Ir, Pd, and Au. An AFM image of a Pt:$SrTiO_3$ film deposited at 900°C, 10^{-6} Torr showed holes on the surface, indicating that the segregated Pt metal particles suppressed the growth of a homogeneous $SrTiO_3$ film and that the Pt metal surface migration rate was not sufficient to form nanopillars at 900°C. At low temperature, under 700°C, the surface diffusion rate was not sufficient to induce Pt metal segregation. The surface morphology of Pt(5%):$SrTiO_3$ grown at 900 ~ 1100°C, 10^{-1} Torr had a regular step-and-terrace surface morphology, indicating that at these conditions, Pt was stabilized as a dopant in $SrTiO_3$.

AFM images give us information only about the surface morphology, and even if precipitates are observed on the surface, there is no guarantee that metal nanopillars actually form in the film. STEM observation is necessary to prove that the segregated metals actually form the

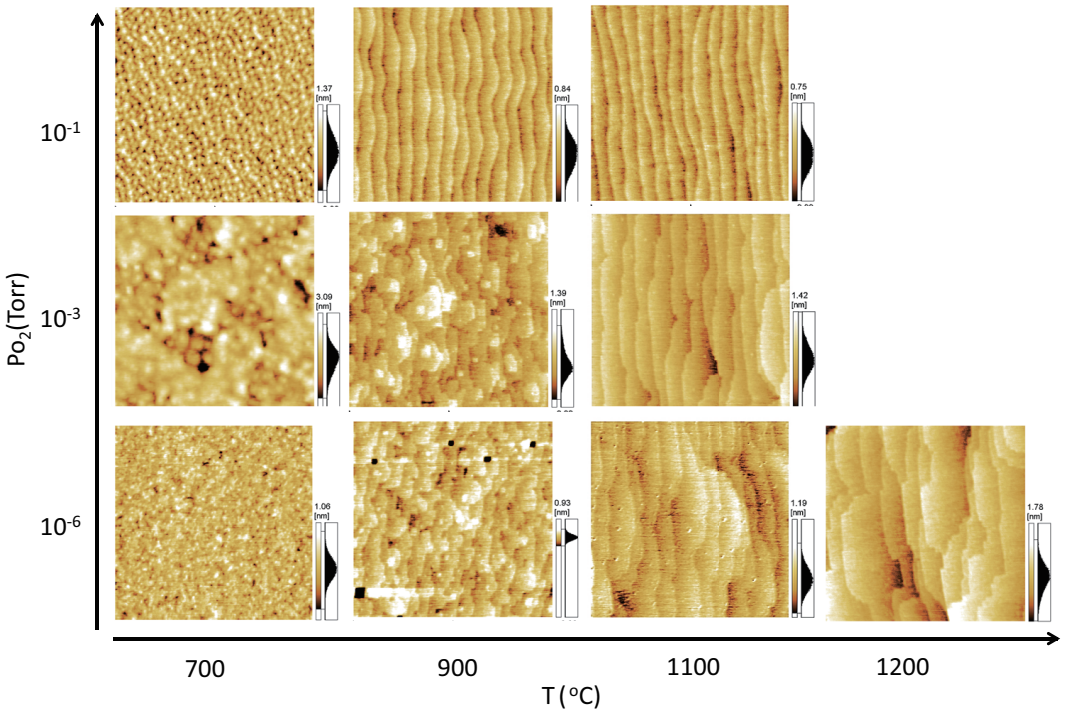

Figure 5.17: AFM images (1×1 μm^2) of Pt(5%):$SrTiO_3$ films deposited at various temperatures and oxygen pressures. The laser fluence was $\sim$ 1 J/cm^2 and the repetition rate 2 Hz. The film thickness was 20 nm.

desired nanopillar shapes. STEM images revealed that Pt formed epitaxial nanopillars in $SrTiO_3$ in a similar way as Ir, shown in Fig. 5.18. The STEM images (Fig. 5.18(b)) also revealed that unlike Ir, the Pt metal nanopillars were nearly covered by $SrTiO_3$ on the film surface. It is known that strong metal-support interaction (SMSI) often induces encapsulation of noble metals with oxides under reducing condition, driven by the formation of oxygen vacancies in the oxide support [371,372]. The 1100°C, 10^{-6} Torr growth conditions are sufficiently reducing to generate oxygen vacancies in $SrTiO_3$ [373], which appears to be the reason why $SrTiO_3$ covers the Pt metal nanopillars at the film surface. Despite that, however, the large atomic diffusion rate at 1100°C induced the formation of Pt nanopillars and the growth of very high crystallinity $SrTiO_3$. The Pt nanopillars were strongly faceted and grew straight in the out-of-plane direction with clear crystal facets on the both top and bottom of the nanopillars (Fig. 5.18(b) and (c)).

The optimum conditions for Pd nanopillar growth was 700°C, 10^{-6} Torr, but the growth window was slightly wider than for Pt or Ir. In fact, Pd metal segregation from $SrTiO_3$ was found in the AFM images of Pd(5%):$SrTiO_3$ films deposited at 700°C, $10^{-6} \sim 10^{-3}$ Torr. At 1100°C, 10^{-1} Torr, grains were observed in AFM images. However, these grains may have been Pd (or PdO) nanoparticles, rather than nanopillars, because the step-and-terrace structure of $SrTiO_3$

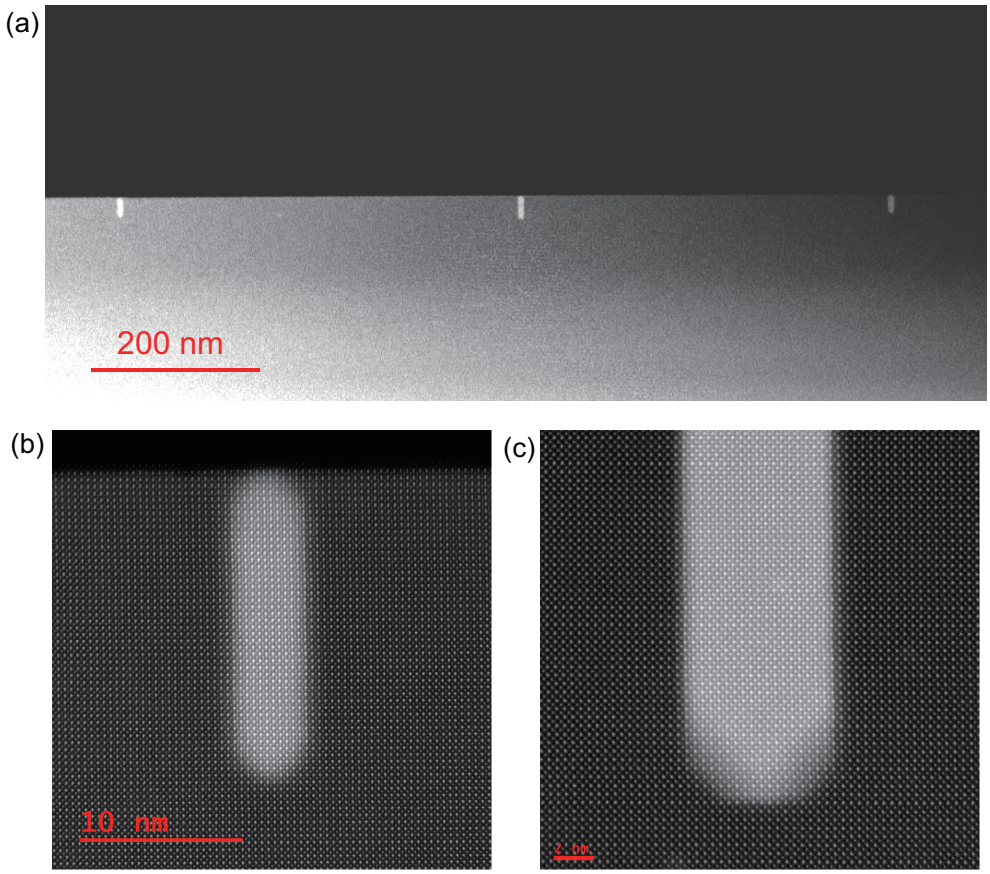

Figure 5.18: Cross-sectional HAADF-STEM images of Pt(5%):$SrTiO_3$ thin film (thickness 20 nm) grown at 1100°C, 10^{-6} Torr. (a) A wide scale image and (b) and (c) magnified images.

was no longer observed. At 1100°C and low oxygen pressure, below 10^{-3} Torr, Pd evaporated from the films. Fig. 5.20 shows cross-sectional STEM images of a 20 nm-thick Pd(5%):$SrTiO_3$ film on $SrTiO_3$(001), deposited at 700°C, 10^{-6} Torr. The faceting behavior is different for Pd, causing the Pd nanopillars grown at 700°C to favor the (110) facets and therefore warping along the length. The lattice constant of Pd(fcc) is a = 3.8898 Å, which means that the mismatch with $SrTiO_3$ (a = 3.905 Å) is just 0.4%. The lack of strain in the metal lattice may be the reason why Pd does not prefer the (001) growth direction.

Rh nanopillars were fabricated by the deposition of Rh(5%):$SrTiO_3$ at 900°C, 10^{-3} Torr or 1000°C, 10^{-6} Torr. Rh loss due to evaporation occurred at temperatures higher than 1100°C, and Rh-doped $SrTiO_3$ was obtained at temperatures of 700°C and lower. STEM images (Fig.5.22) showed that the Rh nanopillars were narrow near the film/substrate interface and increased in diameter up to a film thickness of ~ 10 nm. Beyond this film thickness, the nanopillar diameter became uniform. Rh is a noble metal and shows SMSI, similar to Pt [371], but at least the Rh

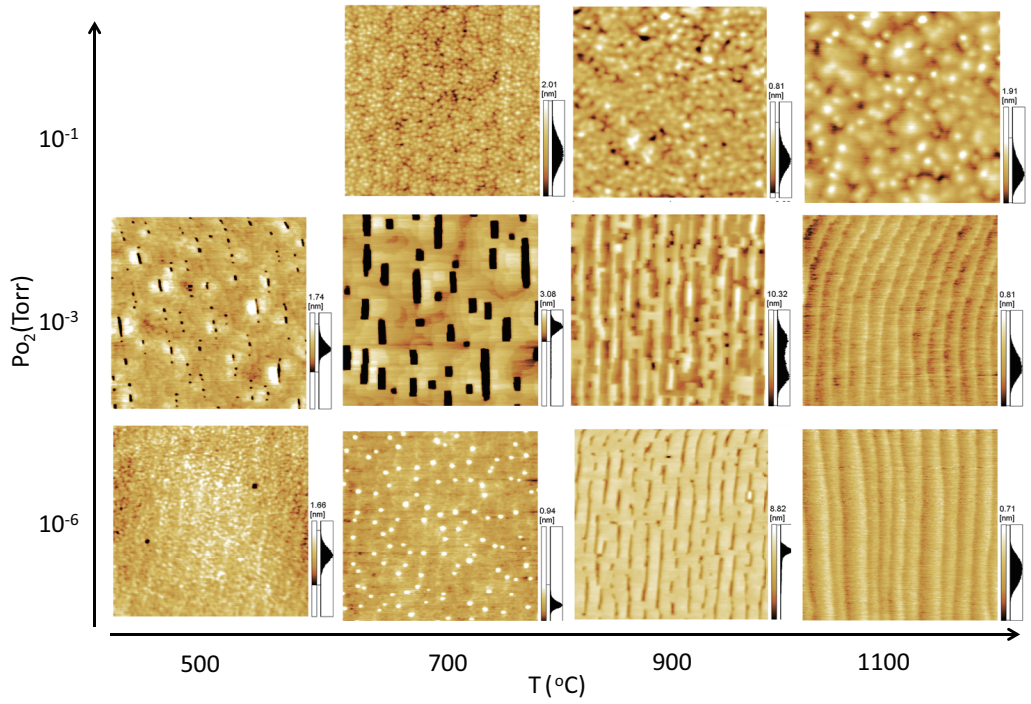

Figure 5.19: AFM images (1×1 μm^2) of Pd(5%):$SrTiO_3$ films deposited at various temperatures and oxygen pressures. The laser fluence and repetition rate were $\sim$ 1 J/cm^2 and 2 Hz, respectively. The film thickness was 20 nm.

nanopillars grown at 900°C, 10^{-3} Torr were not covered with $SrTiO_3$ as can be seen in Fig. 5.22(c).

Gold has a higher vapor pressure than any of the other metals studied, and it is not possible to dope gold in $SrTiO_3$. Therefore, segregation of metallic Au is more likely happen than for other elements. As with other noble metals, Au nanopillars were obtained at 700°C and even at 500°C and 10^{-6} Torr. The threshold temperature for metal evaporation is also lower than for any of the other noble metals, at $\sim$ 900°C. Although the nanopillar formation was not verified by STEM, the observation of AFM images and RHEED patterns suggests that Au nanopillars did grow in $SrTiO_3$.

The metal nanopillars grew continuously from the film/substrate interface to the thin film surface. However, STEM revealed that the growth mode of metal nanopillars, in some cases, changes during thin film growth. Fig. 5.24 shows cross-sectional and plan-view HAADF-STEM images of a 300-nm-thick sample of Ir:$SrTiO_3$, revealing that the growth of small Ir metal nanopillars stopped at a film thickness of a few tens of nm and subsequently the pillar growth mode changed to a smaller number of much larger Ir pillars. The change in the pillar structure always appears to be accompanied by the formation of $\sim$ 100 nm diameter spherical Ir metal inclusions. The large Ir pillars also had an epitaxial matching with $SrTiO_3$, with Ir (110) as the

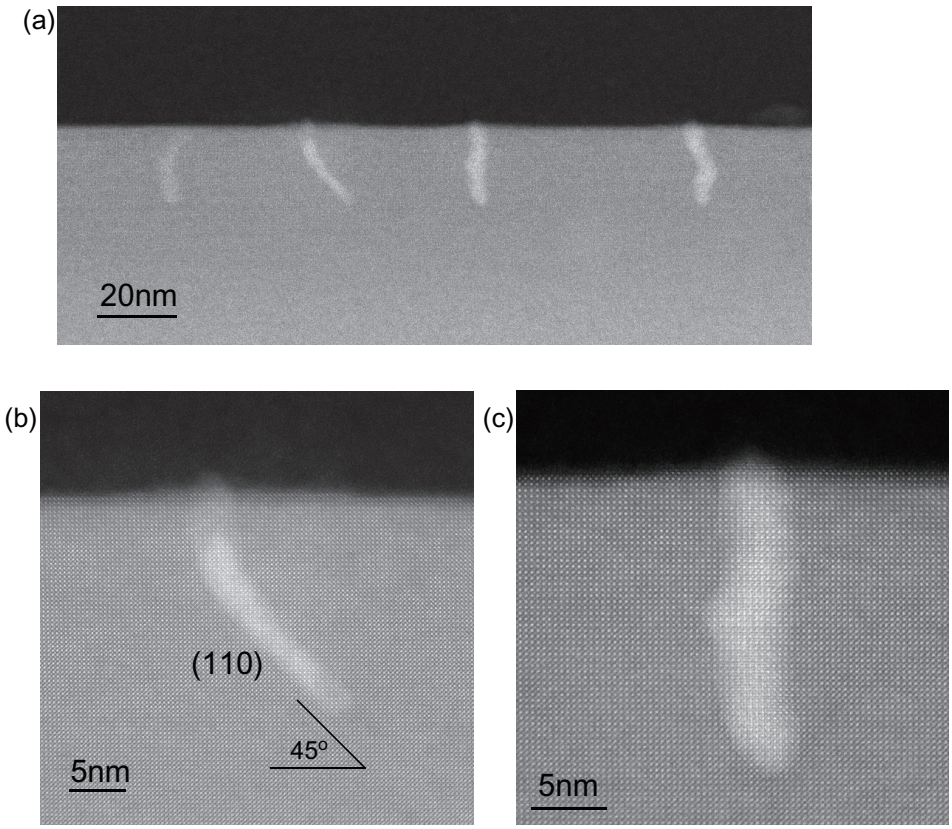

Figure 5.20: Cross-sectional HAADF-STEM images of Pd(5%):$SrTiO_3$ thin films (thickness 20 nm) grown at 700°C, 10^{-6} Torr. (a) A wide scale image and (b) and (c) magnified images.

dominant facet appearing in plan-view images. Not all pillars grew vertically through the film, some Ir pillars were found to have grown in the lateral direction in the $SrTiO_3$ film (Fig. 5.24(b)). The growth dynamics these larger pillars is still unclear. The effect was only observed for Ir pillars and may be related not only to a change of thermodynamic conditions on the film surface but may also be related to a difference in the composition of the PLD plume as the target surface is gradually consumed by the ablation laser.

Somewhat different pillar morphology change was seen for Pt. In the case of Pt (Fig. 5.25), the nanopillars were homogeneous up to 100 nm from the film/substrate interface, but above $\sim$ 100 nm, many disconnected metal nanopillars appeared. All the Pt nanopillars were grown straight in the out-of-plane direction, but the Pt nanopillars had various lengths. The lateral pillar size was homogeneous, at $\sim$ 10 nm, unlike the case of Ir pillars shown in Fig. 5.24. The detailed growth dynamics of metal nanopillar structures have not been fully understood, and further investigation is needed to obtain better control over the length, diameter, and areal density of metal pillars. However, the pillar structures obtained here are sufficient for exploring

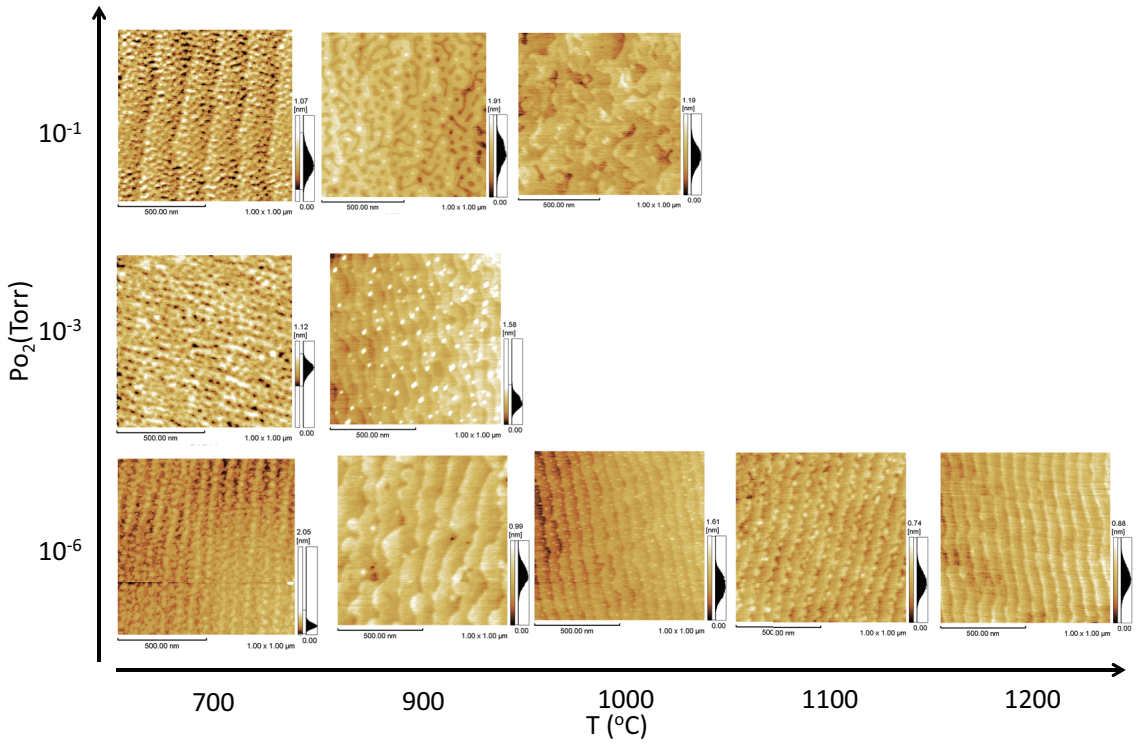

Figure 5.21: AFM images (1×1 μm^2) of Rh(5%):$SrTiO_3$ deposited at various temperatures and oxygen pressures. The laser fluence and repetition rate were $\sim$ 1 J/cm^2 and 2 Hz, respectively. The film thickness was 20 $\sim$ 50 nm.

novel photoelectrode structures based on embedded nanopillar composite materials.

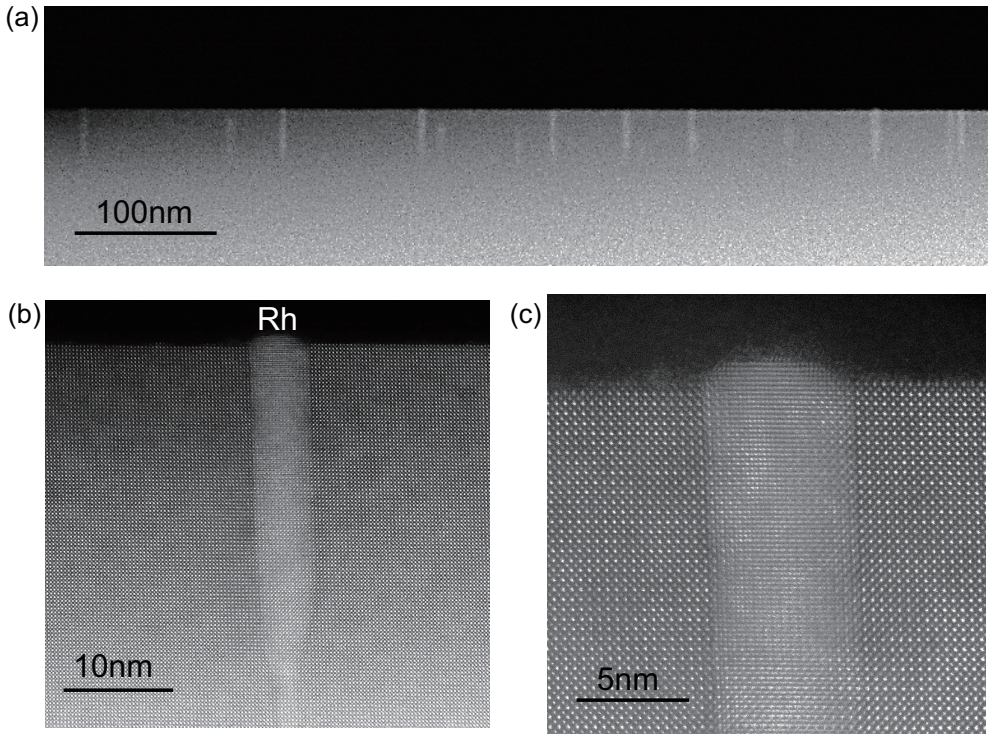

Figure 5.22: Cross-sectional HAADF-STEM images of Rh(5%):$SrTiO_3$ thin films (thickness 50 nm) grown at 700°C, 10^{-6} Torr. (a) A wide scale image and (b) and (c) magnified images.

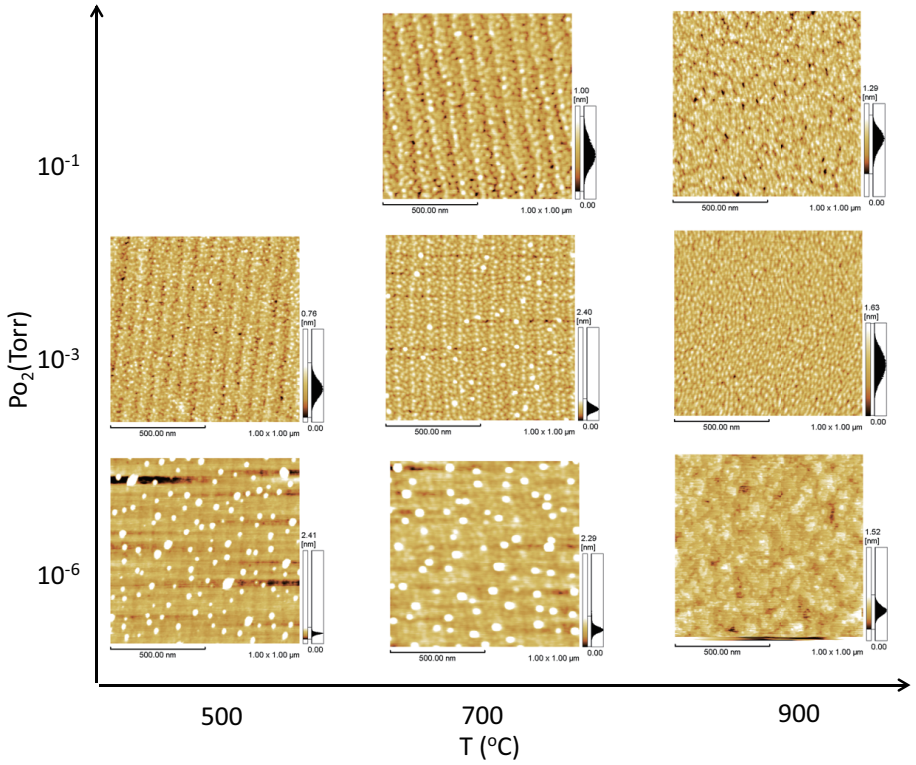

Figure 5.23: AFM images (1×1 μm^2) of Au(5%):$SrTiO_3$ deposited at various temperatures and oxygen pressures. The laser fluence and repetition rate were ~1 J/cm^2 and 2 Hz. The film thickness was 20 nm.

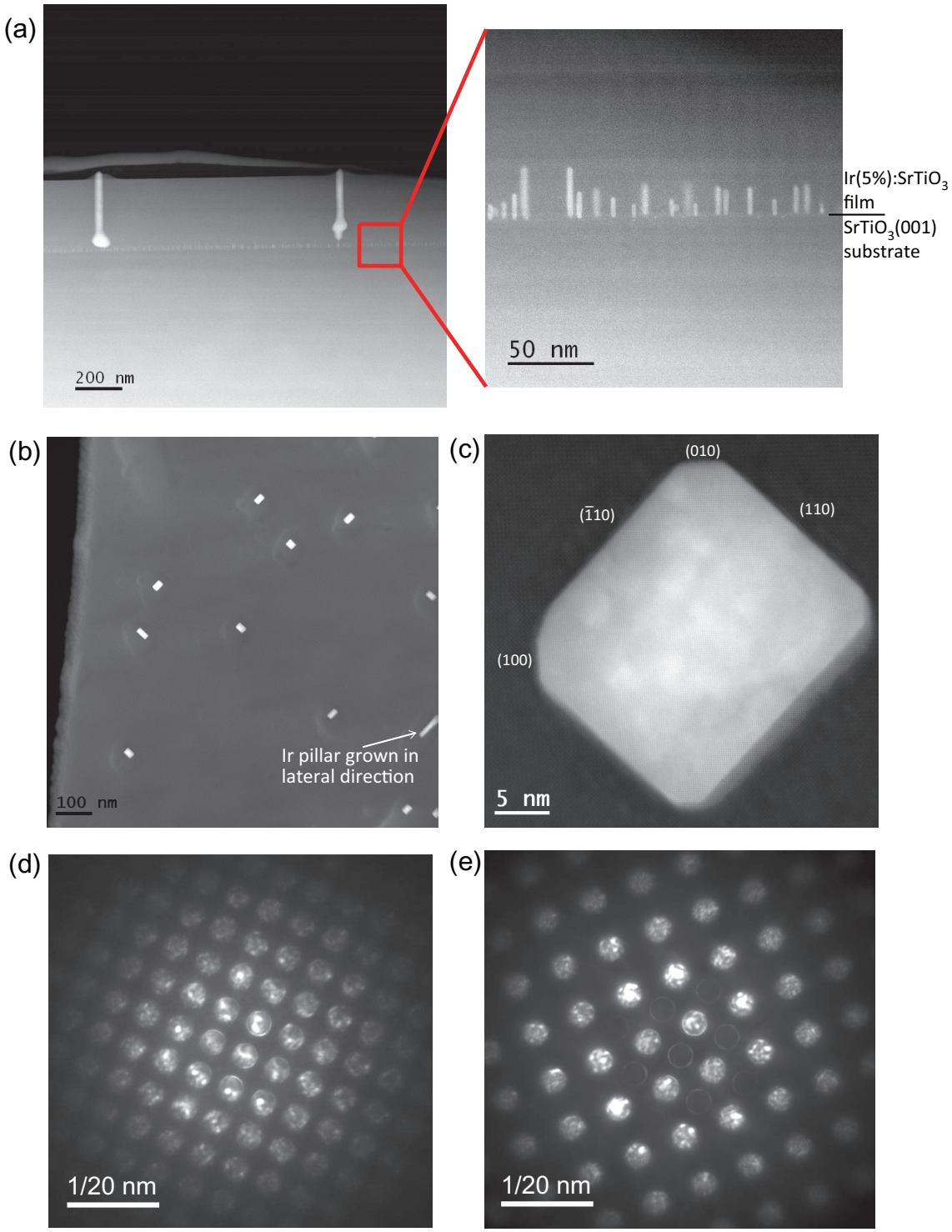

Figure 5.24: (a) Cross-sectional STEM images of 300 nm Ir(5%):$SrTiO_3$ grown at 700°C, 10^{-3} Torr. (left) A full scale image and (right) a magnified image at the film/substrate interface. (b) and (c) Plan-view STEM images of the same sample as in (a). (d) and (e) Electron diffraction patterns acquired at $SrTiO_3$ film and Ir pillar parts, respectively.

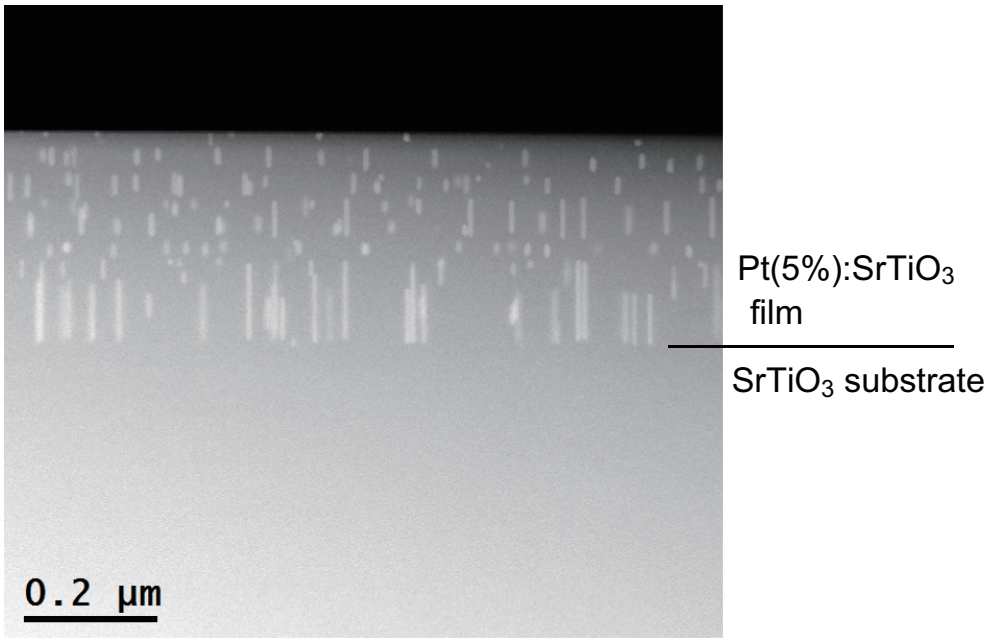

Figure 5.25: STEM image of Pt(5%):$SrTiO_3$.

5.3 Photoelectrochemical activity of Ir:$SrTiO_3$ enhanced by metal nanopillars

Epitaxial metal nanopillar composite M:$SrTiO_3$ (M = Ir, Pt, Pd, Rh, Au) thin films were fabricated in a single-step PLD process from polycrystalline $SrTi_{1-x}M_xO_3$ (x = 1, 3, 5, 10%) ablation targets. Among the samples, Ir:$SrTiO_3$ with embedded metal nanopillars showed the highest photoelectrochemical activity under visible light irradiation. Since M:$SrTiO_3$ (M = Pt, Pd, Au) do not absorb visible-light, these samples did not show any clear improvement in the photoelectrochemical activity. Rh:$SrTiO_3$ shows photoelectrochemical water reduction under visible-light but it has a *p*-type character with $E_F \sim 1.5$ eV below the conduction band minimum, which means that Rh metal does not form a Schottky junction with Rh:$SrTiO_3$. Hence, the implantation of Rh nanopillars did not improve the photoelectrochemical activity of Rh:$SrTiO_3$. Therefore, this study focused on the investigation of the photoelectrochemical activity of *n*-type Ir:$SrTiO_3$, enhanced by the presence of self-assembled Ir nanopillars.

Fig. 5.26 shows the current-potential curves of Ir(3 or 5%):$SrTiO_3$ thin films and an Ir(5%):$SrTiO_3$ film sample that contains embedded Ir nanopillars. The measurements were done under visible light irradiation. The Ir(3 or 5%):$SrTiO_3$ films were grown at 700°C, 10^{-1} Torr, whereas the nanopillar composite Ir(5%):$SrTiO_3$ film was grown at 700°C, 10^{-3} Torr. The film thickness was 20 nm for all samples. The composite Ir(5%):$SrTiO_3$ film with nanopillars showed the largest photocurrent in a water oxidation reaction under visible light irradiation. The sharp increase of the photocurrent density shows that photocarrier recombination was effectively suppressed by the implantation of Ir nanopillars. The photocurrent density at 1.6 V vs. RHE was 6 times larger than that of an equivalent homogeneous Ir(5%):$SrTiO_3$ thin film. According to optical absorption measurements of the Ir^{4+} impurity levels, $\sim$ 60% of Ir substituted at the Ti site of $SrTiO_3$ in the Ir(5%):$SrTiO_3$ nanopillar film, while $\sim$ 40% of Ir segregated in the metal nanopillars. The effective Ir^{4+} doping level in the Ir:$SrTiO_3$ film was thus $\sim$ 3%. The current-potential curve of an Ir(3%):$SrTiO_3$ epitaxial thin film is therefore also shown in Fig. 5.26 to obtain a reference with the same effective Ir doping level. Compared to the Ir(3%):$SrTiO_3$ epitaxial thin film, the metal nanopillar composite Ir(5%):$SrTiO_3$ film showed 20 times larger photocurrent density at 1.6 V vs. RHE. However, the onset potential for the photoelectrochemical water oxidation reaction on the nanopillar composite sample surface was more positive than for a homogeneous epitaxial Ir:$SrTiO_3$ thin film without the nanopillars. Ir doping in $SrTiO_3$ lowers the Fermi level of $SrTiO_3$ by forming an unoccupied impurity level in the band gap, which is why Ir:$SrTiO_3$ shows a positive shift of the onset potential from the value of non-doped $SrTiO_3$. Thus, the onset potential of Ir(5%)-doped sample was more positive than that of the Ir(3%)-doped sample. Ir is known to be an efficient electrocatalyst for the water oxidation reaction [45]. However, since $SrTiO_3$ has a deep valence band composed of O2p orbitals at $\sim$ 3 V vs. RHE, $SrTiO_3$ has a strong intrinsic photo-oxidation activity, similar to TiO_2. Thus, the onset potential

of the Ir nanopillar sample was more positive than those of $SrTiO_3$ and Ir:$SrTiO_3$.

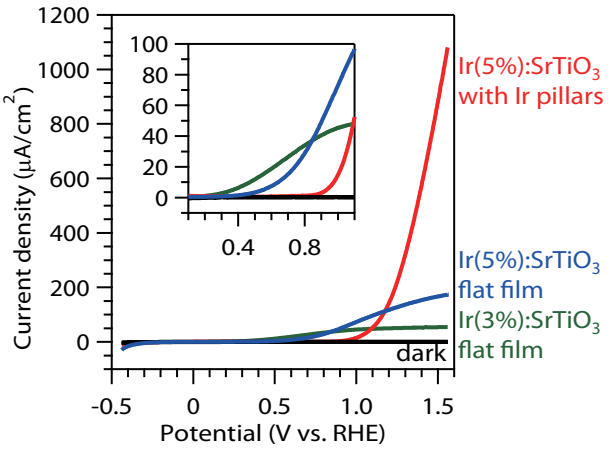

Figure 5.26: Current-potential curves of Ir(5%):$SrTiO_3$ (red) with and (blue) without self-assembled Ir nanopillars, measured under visible light irradiation, compared with (green) a homogeneous Ir(3%):$SrTiO_3$ film. The black lines show the dark current. Inset shows the difference in the onset potentials. The film thickness was 20 nm. Measurements done in a 0.1 M K_2SO_4 aq. solution under visible $\lambda > 420$ nm light illumination from a 300 W Xe lamp.

The photocurrent density of Ir:$SrTiO_3$ with self-assembled Ir nanopillars increased with the Ir doping levels (Fig. 5.27). In this study, Ir(10%):$SrTiO_3$ showed the highest photocurrent density. The enhancement of the photocurrent density can be attributed to more efficient charge transport from bulk Ir:$SrTiO_3$ to the water interface, accelerated by the Schottky junctions surrounding the Ir nanopillars and the increase of the light absorption intensity due to the Ir^{4+} impurity levels in the band gap.

The Ir:$SrTiO_3$ films with embedded Ir nanopillars showed a strong photocurrent response under visible light irradiation. However, chronoamperometry indicated a stability problem with the nanopillar samples. Fig. 5.28(a) shows a chronoamperometry measurement result of a Ir(5%):$SrTiO_3$ film grown at 700°C and 10^{-3} Torr, measured at 1.56 V vs. RHE under light irradiation. A K_2SO_4 aq. (pH = 6) electrolyte was used in the measurement. The photocurrent density gradually decreased to one third of the initial value after 12 hours, indicating that the Ir nanopillars were not stable under these reaction conditions. Cyclic-voltammetry was measured before and after the chronoamperometry (Fig. 5.28(b)), showing that the photocurrent density actually dropped after the long-term chronoamperometry. However, the fact that the onset potential did not shift and the saturated photocurrent was of the same order of magnitude indicated that the surface catalytic sites deteriorated but the semiconductor part was stable. Fig. 5.29 shows AFM images of the sample surface taken before and after the long-term chronoamperometry experiment. The images clearly show that the Ir metal nanopillars

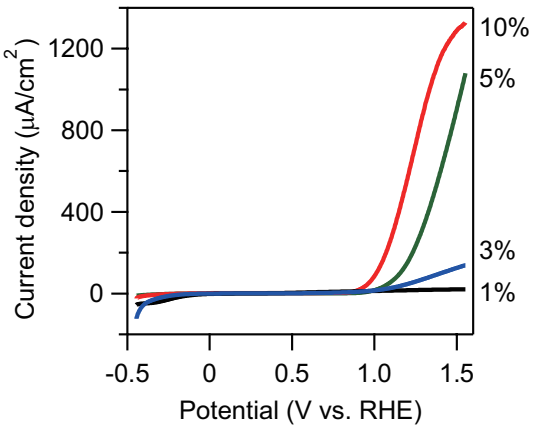

Figure 5.27: Current-potential curve of Ir:$SrTiO_3$ with Ir doping levels from 1 to 10%. All films were 20 nm thick. The light source was a 300 W Xe lamp (λ > 420 nm). Light source: 300 W Xe-lamp (λ > 420 nm). Electrolyte: 0.1 M K_2SO_4 aq. Sweep rate: 20 mV/sec.

had been etched away during the photoelectrochemical measurements, leaving deep holes in the film surface. In contrast, the step-and-terrace structure of $SrTiO_3$ film was completely stable. These results show that the photogenerated holes in the bulk of Ir:$SrTiO_3$ flowed to the It metal nanopillars and that the oxygen evolution reaction occurred at the surface of the Ir metal nanopillars.

Ir metal was etched by the photoelectrochemical anodic reaction. The etching might be related to the generation of H^+ on the Ir surface as a by-product of the water oxidation reaction. In order to prevent the Ir metal corrosion during photoelectrochemical reactions, KOH was used as an electrolyte instead of K_2SO_4. In alkaline conditions, the Ir metal surface is protected by a layer of Ir oxides or hydroxides. Fig. 5.30 shows a chronoamperometry plot of an Ir(5%):$SrTiO_3$ nanopillar film grown at 700°C, 10^{-3} Torr and measured at 1.6 V vs. RHE in KOH aq. (pH = 13) under light irradiation over a period of 24 hours. The photocurrent density was constant for 24 hours, while the photocurrent in K_2SO_4 aq. (pH = 6) gradually decreased in 12 hours. Cyclic-voltammetry curves showed almost the same photocurrent density before and after measuring the long-term chronoamperometry. The surface morphology was also stable and no signs of photocorrosion was observed after the long-term chronoamperometry experiment, as shown in Fig. 5.31. The metal nanopillar composite Ir:$SrTiO_3$ was thus stable in alkaline conditions in the photoelectrochemical water oxidation reaction.

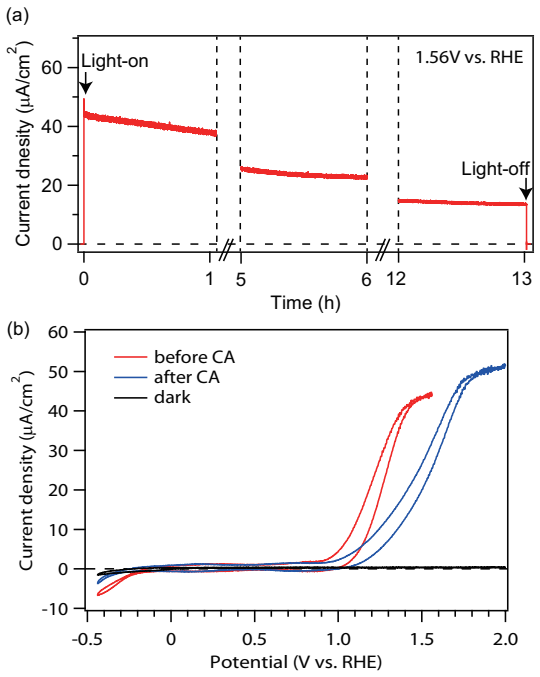

Figure 5.28: (a) Chronoamperometry of Ir(5%):$SrTiO_3$ grown at 700°C, 10^{-3} Torr, measured at 1.56 V vs. RHE under light irradiation. (b) Cyclic-voltammetry curves of the same sample, measured (a) before (red) and after (blue) the chronoamperometry experiment. The voltammetry curves were measured under visible light irradiation. The dark current (black) curves are also shown. The film thickness was 20 nm. Measured in a 0.1 M K_2SO_4 aq. (pH = 6) electrolyte. The light source was a 1 kW Xe lamp (λ > 420 nm).

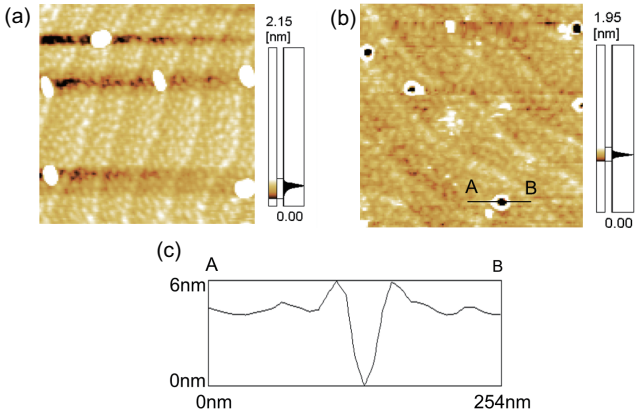

Figure 5.29: AFM images of Ir(5%):$SrTiO_3$ films grown at 700°C, 10^{-3} Torr (a) before and (b) after measuring the long-term chronoamperometry. (c) Cross-sectional height profile corresponding to the position marked with A-B in (b).

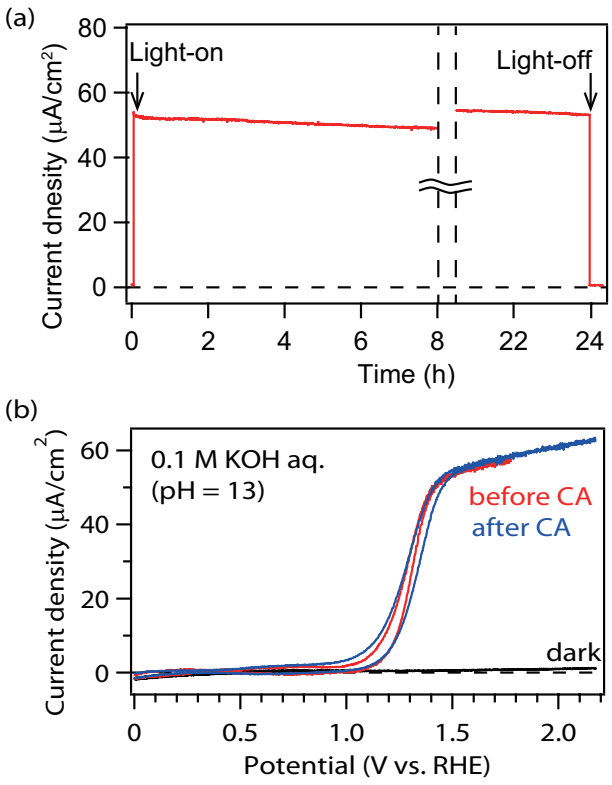

Figure 5.30: (a) Chronoamperometry of an Ir(5%):$SrTiO_3$ film grown at 700°C, 10^{-3} Torr measured at 1.6 V vs. RHE, showing that the photoelectrochemical activity was stable in an alkaline solution over a period of 1 day. (b) Cyclic-voltammetry curves of the same sample as in (a) before (red) and after (blue) the chronoamperometry measurement. Voltammetry curves were measured under light irradiation, plots also show the dark current curves (black). Film thickness 20 nm, light source was a 1 kW Xe lamp (λ > 420 nm), applied potential 1.6 V vs. RHE, solution 0.1 M KOH aq.(pH = 13.0).

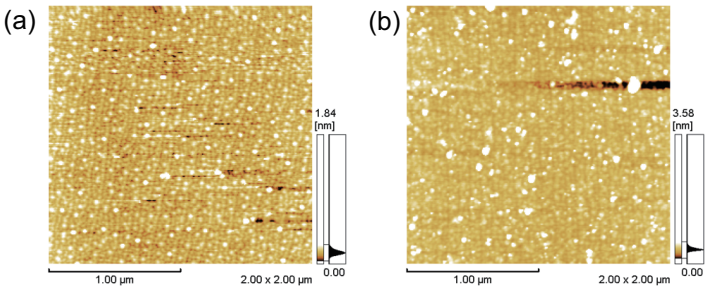

Figure 5.31: AFM images of (a) Ir(5 %):$SrTiO_3$ grown at 700°C, 10^{-3} Torr and (b) the same sample after chronoamperometry measurement for 24 hours in KOH aq. (pH 13).

The absorbed photon-to-current efficiency (APCE) and incident photon-to-current efficiency (IPCE) measured at 1.6 V vs. RHE are shown in Fig. 5.32 together with the light absorption coefficient plot. The Ir:$SrTiO_3$ films absorb visible light due to the Ir-induced impurity levels in the $SrTiO_3$ band gap. As expected, the IPCE curve followed the light absorption curve, showing that the photocurrent is derived from the photocarrier generation in Ir:$SrTiO_3$. Although the IPCE was less than 10% due to the small absorption coefficient, the maximum APCE value exceeded 80% in the 400 to 600 nm wavelength range. The results show that the photocarrier recombination was effectively suppressed by the metal nanopillars.

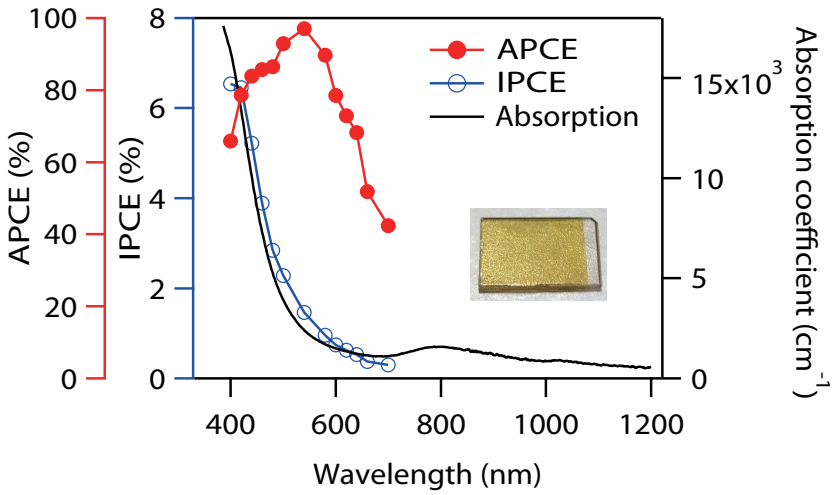

Figure 5.32: APCE and IPCE measured at 1.6 V vs. RHE, together with the light absorption coefficient plot. The inset shows a photograph of an Ir(5%):$SrTiO_3$ film deposited at 700°C, 10^{-3} Torr on a nondoped $SrTiO_3$(001) substrate. The film thickness was 20 nm, light source was a 1 kW Xe lamp with a monochromator. Measured in a 0.1 M KOH aq. (pH = 13.0) solution.

5.4 Conclusion

In this chapter, I demonstrated a novel nanostructure design concept using self-assembled metal nanopillar structures to achieve efficient photocarrier transport from a bulk semiconductor to the photoelectrode surface for accelerating the photoelectrochemical water splitting reaction. By implanting noble metal nanopillars with a large work function, Schottky junctions were created around each metal nanopillar in $SrTiO_3$. Band bending in the space charge region of the Schottky junctions improves the photocarrier transport efficiency from the bulk $SrTiO_3$ to the water interface. The self-assembled nanopillar structure was fabricated by selecting suitable elements and tuning the deposition conditions. Self-assembled epitaxial metal nanopillars of Ir, Pt, Pd, Rh, and Au were successfully fabricated in a $SrTiO_3$ thin film by a single-step PLD process using simple polycrystalline $SrTi_{1-x}M_xO_3$ (M = Ir, Pt, Pd, Rh, and Au) ablation targets. The formation mechanism of the self-assembled metal nanopillars were investigated. A suitable balance between thermodynamic phase separation and kinetic thin film growth is important for obtaining a self-assembled nanopillar structure. The balance between surface migration and evaporation of metals determined the size and density of the metal nanopillars. It should be noted that the crystal quality of $SrTiO_3$ film was also improved by the formation of metal nanopillars in $SrTiO_3$, possibly due to a flux effect of noble metals on an oxide surface. The photocarrier transport efficiency was strongly enhanced in the Schottky space charge regions while the pillars provided an efficient charge extraction path. In particular, Ir-doped $SrTiO_3$ with embedded Ir metal nanopillars showed good operational stability in a water oxidation reaction and achieved over 80% utilization of photogenerated carriers under visible light in the 400 to 600 nm wavelength range.

The embedded metal nanopillars demonstrated in this work have major advantages over other nanostructure designs: automatic formation of Schottky depletion layers in the surrounding semiconductor films, a single-step fabrication process, and a mechanically robust film structure. These factors simplify the synthesis process without compromising operational longevity. The self-assembled nanocomposites studied here may find use not only in the efficient utilization of photocarriers, but also in the development of various functional devices based on nanopillars and point contacts for spintronics, memories, multiferroic composites, and photonic crystals.

Chapter 6

Conclusion

Since the discovery of water splitting on the TiO_2 surface by Fujishima and Honda in 1972 [2], a huge number of materials and nanostructures have been proposed and tested for achieving efficient solar water splitting to produce H_2 from water utilizing solar energy. However, a photoelectrochemical solar conversion systems that has a high conversion efficiency and is stable in water against photocorrosion has not yet been developed.

The motivation of this study was to clarify some of the fundamental physical and chemical mechanisms in photocatalysts and photoelectrodes that limit the efficiency of photoelectrochemical reactions, and to propose new routes for developing an efficient solar-to-fuel conversion system. Well-defined single crystal substrates and epitaxial thin films can be used as "model photocatalysts" (or photoelectrodes) to investigate the dynamics of photoelectrochemical reactions. In this study, $SrTiO_3$ (and Nb:$SrTiO_3$) single crystal substrates and doped $SrTiO_3$ epitaxial thin films were used to clarify the mechanism of photo-induced superhydrophilicity and the relationship between the electronic structure (especially the impurity level positions) and photoelectrochemical activity. Theoretical limitations of solar energy conversion efficiency in doped $SrTiO_3$ were analyzed and proposals are presented for innovative material designs that improve the photoelectrochemical efficiency of oxide photoelectrodes without compromising long-term operational stability.

In Chapter 3, I investigated water / photocatalyst interfaces to clarify the mechanism of photo-induced superhydrophilicity. The ($\sqrt{13} \times \sqrt{13}$)-R33.7° $SrTiO_3$(001) surface was used as a model system to evaluate the intrinsic hydrophilicity of Ti-oxide surfaces. The atomic structure of the reconstructed ($\sqrt{13} \times \sqrt{13}$)-R33.7° $SrTiO_3$(001) surface was found to be stable in water. The surface showed superhydrophilicity when the it is sufficiently clean. The experimental results are consistent with the conventional physical model of the water contact angle. Oxide surfaces that have a high surface energy of a few hundred mJ/m^2 or more should be intrinsically superhydrophilic with a water contact angle approaching zero degrees even without UV light exposure. The mechanism of photo-induced superhydrophilicity can thus be fully explained

by the contamination model. The results supported the contamination model proposed by Anpo *etal*. [40] and Yates, Jr. et al. [41] rather than the surface reconstruction model proposed by Hashimoto *etal*. [39]. No clear experimental evidence was found for the existence of the types of metastable surface state proposed by Hashimoto *etal*. [39] by careful surface scientific analysis [40, 41, 139–143].

In Chapter 4, I clarified the relationship between the electronic structure and the photoelectrochemical activity of various photocatalytic model systems. Doped $SrTiO_3$ is an excellent model material for investigating the photoelectrochemical activity changes associated with the modification of the electronic structure. High-quality epitaxial thin films of doped $SrTiO_3$ with good crystal quality and step-and-terrace surface morphology were fabricated by PLD. The electronic structure of doped $SrTiO_3$, especially Rh- and Ir-doped $SrTiO_3$, were elucidated by X-ray spectroscopic analyses, while the photoelectrochemical properties were evaluated by conventional three-electrode photoelectrochemical measurements. The results clearly showed that the positions of the impurity levels in the band gap is important for determining the efficiency of photocarrier transport as well as the light absorption intensity. Based on a trade-off between photocarrier transport and light absorption, Rh^{3+} and Cr^{3+} were found to be the most suitable dopants for $SrTiO_3$ photocatalysts used under sunlight.

In Chapter 5, I proposed a new nanoscale material design to overcome the problems found in Chapter 4 and to enhance the efficiencies of photocarrier separation and electrochemical reaction for efficient photoelectrochemical water splitting. Mechanically robust photoelectrodes were formed by embedding self-assembled metal nanopillars in a semiconductor thin film, forming tubular Schottky junctions around each pillar. The photocarrier transport efficiency was strongly enhanced in the Schottky space charge regions while the pillars provided an efficient charge extraction path. The self-assembled nanopillar structure was fabricated by a single-step PLD process by inducing spontaneous phase separation during thin film growth. Ir, Pt, Pd, Rh, and Au epitaxial metal nanopillars were fabricated in $SrTiO_3$. In particular, Ir-doped $SrTiO_3$ with embedded Ir metal nanopillars showed good operational stability in a water oxidation reaction and achieved over 80% utilization of photogenerated carriers under visible light in the 400 to 600 nm wavelength range.

I believe this study contributed to the development of photocatalyst research. I wish the dream of efficient solar water splitting will come true in the near future, which would lead to sustainable energy supply development for the human society that is environment-friendly and independent of environmentally problematic fossil fuels.

Materials science is a key to open the door of the global sustainable development. Innovations in materials science are directly connected to the development of a sustainable global society.

References

[1] R. van de Krol, M. Gratzel, *Photoelectrochemical Hydrogen Production (Electronic Materials: Science & Technology)*, (*Springer-Verlag*, 2011).

[2] A. Fujishima, and K. Honda, *Nature*, **37**, 238 (1972).

[3] K.Maeda, and K. Domen, *J. Phys. Chem. Lett.*, **1**, 2655-2661 (2010).

[4] T.M. Mata, A.A. Martins, and N.S. Caetano, *Renewable and Sustainable Energy Rev.*, **14**, 217-232 (2010).

[5] W.C. Chueh, C. Falter, M. Abbott, D. Scipio, P. Fuler, S.M. Haile, and A. Steinfeld, *Science*, **330**, 1797-1801 (2010).

[6] S. Fukuzumi, *Curr. Opinion Chem. Biol.*, **25**, 18-26 (2015).

[7] Y. Yamazaki, H. Takedaa, O. Ishitani, *J. Photochem. Photobiol. C*, **25**, 106-137 (2015).

[8] J.S.Lee, *Catal. Surv. Asia*, **9**, 217 (2005).

[9] K.Maeda and K.Domen, *J. Phys. Chem. C*, **111**, 7851 (2007).

[10] F.E. Osterloh, *Chem. Mater.*, **20**, 35 (2008).

[11] A.Kudo and Y.Miseki, *Chem.Soc.Rev.*, **38**, 253 (2009).

[12] W. J.Youngblood, S.-H. A.Lee, K.Maeda, T. E.Mallouk, *Acc. Chem. Res.*, **42**, 1966 (2009).

[13] K. Maeda, *J. Photochem. Photobio. C: Photochem. Rev*, **12**, 237 (2011).

[14] R. Memming, *Semiconductor Electrochemistry*, (*WILEY-VCH*, 2001).

[15] Y.V. Pleskov, and Y.Y. Gurevich, *Semiconductor Photoelectrochemistry*, (*Plenum Publishing Co.*, 1986).

[16] A. Coehn, *Berichte Der Deutschen Chemischen Gesellschaft*, **43**, 880 (1910).

[17] S. Sato, T. Arai, T. Morikawa, K. Uemura, T. M. Suzuki, H. Tanaka, and T. Kajino, *J. Am. Chem. Soc.*, **133**, 15240 (2011).

[18] H. Gerischer, *J. Electrochem. Soc.*, **113**, 1174-1182 (1966).

[19] G.N. Schrauzer, and T.0. Guth, *J. Am. Chem. Soc.*, **99**, 7189 (1977).

[20] B. Kraeutler, and A.J. Bard, *J. Am. Chem. Soc.*, **100**, 2239 (1978).

[21] B. Kraeutler, and A.J. Bard, *J. Am. Chem. Soc.*, **100**, 5985 (1978).

[22] A.J. Bard, *J. Photochem.*, **10**, 59-75 (1978).

[23] K. Domen, S. Naito, M. Soma, T, Onishi, and K. Tamaru, *J. Chem. Soc.*, 543-544(1980).

[24] J. Lehn, J. Sauvage, R.Ziessel, *Nouv. J. Chim.*, **4**,623 (1980).

[25] J.R. Bolton, S.J. Strickler, and J.S. Connolly, *Nature*, **316**, 495 (1985).

[26] http://rredc.nrel.gov/solar/spectra/am1.5/

[27] T. Ohno, S. Saito, K. Fujihara, M. Matsumura, *Bull. Chem. Soc. Jpn.*, **69**, 3059 (1996).

[28] K. Sayama, K. Mukasa, R. Abe, Y. Abe, and H. Arakawa *J. Photochem. Photobiol. A*, **148**, 71-77 (2002).

[29] A. Iwase, Y.H. Ng, Y. Ishiguro, A. Kudo, and R. Amal, *J. Am. Chem. Soc.*, **133**, 11054-11057 (2011).

[30] Y. Sasaki, H. Nemoto, K. Saito and A. Kudo, *J. Phys. Chem. C*, **113**, 17536-17542 (2009).

[31] J.Manassen, D. Cahen, and G. Hodes, *Nature*, **263**, 97 (1976).

[32] C. Renz, *Z. anorg. Chem.*, **110**, 104 (1920).

[33] C. Renz, *Helv. Chim. Acta*, **4**, 961 (1921).

[34] A.E. Jacobsen, *Ind. Eng. Chem.*, **41**, 523 (1949).

[35] W.A. Weyl, Tormod Förland, *Ind. Eng. Chem.*, **42**, 257-263 (1950).

[36] M. Dormenti, F. Juillet, P. Meriaudeau, S.J. Teichner, and P. Vergnon, *J. Colloid and Interface Sci.*, **39**, 79-89 (1972).

[37] A. Fujishima, and T.N. Rao, and D. Tryk, *J. Photochem. Photobiol. C*, **1**, 1-21 (2000).

[38] R. Wang, K. Hashimoto, A. Fujishima, M. Chikuni, E. Kojima, A. Kitamura, M. Shimohigoshi, and T. Watanabe, *Nature*, **388**, 431 (1997).

[39] N. Sakai, A. Fujishima, T. Watanabe, and K. Hashimoto, *J. Phys. Chem. B*, **107**, 432 (1997).

[40] M. Takeuchi, K. Sakamoto, G. Martra, S. Coluccia, and M. Anpo, *J. Phys. Chem. B*, **109**, 7383 (2005).

[41] T. Zubkov, D. Stahl, T.L. Thompson, D. Panayotov, O. Diwald, and J.T. Yates, Jr. , *J. Phys. Chem. B*, **109**, 15454 (2005).

[42] N. Serpone and E. Pelizzetti, *Photocatalysis, Wiley, New York,*, (1989).

[43] J. Li, and N. Wu, *Catal. Sci. Technol.*, **5**, 1360-1384 (2015).

[44] A. Imanishi, T. Okamura, N. Ohashi, R. Nakamura, Y. Nakato, *J. Am. Chem. Soc.*, **129**, 11569 (2007).

[45] Y.W. Chen, J.D. Prange, S. Duhnen, Y. Park, M. Gunji, C.E.D. Chidsey, and P.C. McIntyre, *Nat. Mater.*, **10**, 539-544 (2011).

[46] G.S. Li, D.Q. Zhang, and J.C. Yu, *Environ. Sci. Technol.*, **43**, 7079-7085 (2009).

[47] S.E. Scaife, *Solar Energy*, **25**, 41-54 (1980).

[48] K. Sivula, F.L. Formal, and M. Grätzel, *ChemSusChem*, **4**, 432-449 (2011).

[49] S. Trasatti, *Pure & Appl. Chem.*, **56**, 955-966 (1986).

[50] R. Asahi, T. Morikawa, T. Ohwaki, K. Aoki, and Y. Taga, *Science*, **293**, 269 (2001).

[51] R. Asahi, T. Morikawa, H. Irie, and T. Ohwaki, *Chem. Rev.*, **114**, 9824-9852 (2014).

[52] R. Niishiro, H. Kato, and A. Kudo, *Phys. Chem. Chem. Phys.*, **7**, 2241 (2005).

[53] H. Kato and A. Kudo, *J. Phys. Chem. B*, **106**, 5029 (2002).

[54] R. Niishiro, R. Konta, H. Kato, W.-J. Chun, K. Asakura, and A. Kudo, *J. Phys. Chem. C*, **111**, 17420-17426 (2007).

[55] J. Wang, S. Yin, M. Komatsu, Q. Zhang, F. Saito, T. Sato, *J. Photochem. Photobiol. A*, **165**, 149-156 (2004).

[56] J. Wang, S. Yin, M. Komatsu, Q. Zhang, F. Saito, T. Sato, *Appl. Catal. B*, **52**, 11-21 (2004).

[57] W. Luo, Z. Li, X. Jiang, T. Yu, L. Liu, X. Chen, J. Yead, and Z. Zou, *Phys. Chem. Chem. Phys.*, **10**, 6717-6723 (2008).

[58] P. Reunchan, S. Ouyang, N. Umezawa, H. Xu, Y. Zhang, and J. Ye, *J. Mater. Chem. A*, **1**, 4221 (2013).

[59] R. Konta, T. Ishii, H. Kato, and A. Kudo, *J. Phys. Chem. B*, **108**, 8992 (2004).

[60] K. Furuhashi, Q. Jia, A. Kudo and H. Onishi, *J. Phys. Chem. C*, **117**, 19101 (2013).

[61] R. Niishiro, S. Tanaka and A. Kudo, *Appl. Catal. B*, **150-151**, 187 (2014).

[62] H.P. Maruska and A.K. Ghosh, *Sol. Energy Mater.*, **1**, 237 (1979).

[63] R.U.E. t'Lam, L.G.J.de Haart, A.W. Wiersma, G. Blasse, A.H.A. Tinnemans and A. Mackor, *Mater. Res. Bull.*, **16**, 1598 (1981).

[64] R. Asai, H. Nemoto, Q. Jia, K. Saito, A. Iwase, and A. Kudo, *Chem. Commun.*, **50**, 2543 (2014).

[65] D. Wang, J. Ye, T. Kako and T. Kimura, *J. Phys. Chem. B*, **110**, 15824 (2006).

[66] T. Ishii, H. Kato and A. Kudo, *J. Photochem. Photobiol. A*, **163**, 181 (2004).

[67] J.W. Liu, G. Chen, Z. H. Li and Z.G. Zhang, *J. Solid State Chem.*, **179**, 3704 (2006).

[68] A. Kudo, R. Niishiro, A. Iwase, and H. Kato, *Chem. Phys.*, **339**, 104 (2007).

[69] A.K. Shwarsctein, M.N. Huda, A. Walsh, Y. Yan, G.D. Stucky, Y.-S. Hu, M.M.A. Jassim, E.W. McFarland, *Chem. Mater.*, **22**, 510 (2010).

[70] A.K. Shwarsctein, M.N. Huda, A. Walsh, Y. Yan, G. D. Stucky,Y.-S. Hu, M.M.A. Jassim, E.W. McFarland, *J. Am. Chem. Soc.*, **134**, 5508 (2012).

[71] A.K. Shwarsctein, M.N. Huda, A. Walsh, Y. Yan, G. D. Stucky,Y.-S. Hu, M.M.A. Jassim, E.W. McFarland, *J. Am. Chem. Soc.*, **132**, 7436 (2010).

[72] A. Kudo, R. Niishiro, A. Iwase, H. Kato, *Chem. Phys.*, **339**, 104 (2007).

[73] H. Kato, K. Asakura, A. Kudo, *J. Am. Chem. Soc.*, **125**, 3082 (2003).

[74] J.M. Herrmann, J. Disdier, and P. Pichat, *Chem. Phys. Lett.*, **108**, 618-622 (1984).

[75] A. Kudo, K. Omori, and H. Kato, *J. Am. Chem. Soc.*, **121**, 11459-11467 (1999).

[76] Y. Hosogi, K. Tanabe, H. Kato, H. Kobayashi, and A. Kudo, *Chem. Lett.*, **33**, 28 (2004).

[77] Y. Hosogi, Y. Shimodaira, H. Kato, H. Kobayashi, and A. Kudo, *Chem. Mater*, **20**,1299 (2008).

[78] M. Higashi, R. Abe, K. Teramura, T. Takata, B. Ohtani, K. Domen, *Chem. Phys. Lett.*, **452**, 120-123 (2008).

[79] A. Kasahara, K. Nukumizu , G. Hitoki, T. Takata , J.N. Kondo , M. Hara, H. Kobayashi, and K. Domen, *J. Phys. Chem. A*, **106**, 6750-6753 (2002).

[80] H. Gerischer, *Photochem. Photobiol.*, **16**, 243-260 (1972).

[81] W. Ho, J.C. Yu, J. Lin, J. Yu, and P. Li, *Langmuir*, **20**, 5865-5869 (2004).

[82] H. Sakai, T. Kanda, H. Shibata, T. Ohkubo, and M. Abe, *J. Am. Chem. Soc.*, **128**, 4944-4945 (2006).

[83] E. Thimsen, F.L. Formal, M. Grätzel, and S.C. Warren, *Nano Lett.*, **11**, 35-43 (2011).

[84] B. O'Regan, and M. Grätzel, *Nature*, **353**, 737-740 (1991).

[85] Z. Zhang and J.T. Yates, Jr., *Chem. Rev.*, **112**, 5520-5551 (2012).

[86] L. Li, P. A. Salvador, and G.S. Rohrer, *Nanoscale*, **6**, 24-42 (2014).

[87] Q. Fu, and T. Wagner, *Surf. Sci. Rep.*, **62**, 431-498 (2007).

[88] Y. Lin, G. Yuan, R. Liu, S. Zou, S.W. Sheehan, and D. Wang, *Chem. Phys. Lett.*, **507**, 209-215 (2011).

[89] M.R. Gholipour, C.-T. Dinh, F. Beland, and T.-O. Do, *Nanoscale*, **7**, 8187 (2015).

[90] D. R. Coronado, G. R. Gattorno, M. E. E. Pesqueira, C. Cab, R. de Coss, and G. Oskam, *Nanotechnol.*, **19**, 145605 (2008).

[91] M.Cardona, *Phys.Rev.*, **140**, A651 (1965).

[92] K. Iwashina, *J. Am. Chem. Soc.*, **133**, 13272-13275 (2011).

[93] H. Kato, M. Hori, R. Konta, Y.Shimodaira, and A. Kudo, *Chem. Lett.*, **33**, 1348 (2004).

[94] H. Kato, Y. Sasaki, N. Shirakura, and A. Kudo, *J. Mater. Chem. A*, **1**, 12327-12333 (2013).

[95] R. Konta, 東京理科大学修士論文, (工藤研究室, (2004)).

[96] M.S.Wrighton, A.B.Ellis, P.T.Wolczanski, D.L.Morse, H.B.Abrahamsom, and D.S.Glinley, *J. Am. Chem. Soc.*, **98**, 2774 (1976).

[97] K. Iwashina, 東京理科大学修士論文, (工藤研究室, (2012)).

[98] H. Matsumoto, 東京理科大学修士論文, (工藤研究室, (2007)).

[99] S. Tanaka, 東京理科大学修士論文, (工藤研究室, (2008)).

[100] A. Fujishima, X. Zhang, and D.A. Tryk, *Surf. Sci. Rep*, **63**, 515-582 (2008).

[101] M.A. Henderson, *Surf. Sci. Rep.*, **46**, 1-308 (2002).

[102] U. Diebold, *Surf. Sci. Rep.*, **48**, 53-229 (2003).

[103] M.A. Henderson, and I. Lyubinetsky, *Shem. Rev.*, **113**, 4428-4455 (2013).

[104] S. Chen, M.G. Mason, H.J. Gysling, G.R. Paz-Pujalt, T.N. Blanton, T. Castro, K.M. Chen, C.P. Fictorie, W.L. Gladfelter, A. Franciosi, P.I. Cohen and J.F. Evans, *J. Vac. Sci. Technol. A*, **11**, 2419 (1993).

[105] M. Murakami, Y. Matsumoto, T. Makino, Y. Segawa, T. Chikyo, P. Ahmet, K. Nakajima, M. Kawasaki, and H. Koinuma, *Appl. Phys. Lett.*, **78**, 2664 (2001).

[106] W. Sugiyama, A. Yamazaki, H. Shigetani, J. Tanaka and T. Mitsuhashi, *Jpn. J. Appl. Phys.*, **36**, 7358 (1997).

[107] Y. Matsumoto, H. Koinuma, and T. Ohsawa, *J. Phys. Chem. C*, **111**, 10523-10527 (2007).

[108] M. Katayama, T. Miyakawa, T. Ohsawa, J. Kuwano, H. Koinuma, and Y.Matsumoto, *Jpn. J. Appl. Phys.*, **46**, L562 (2007).

[109] S. Takata, Y. Miura, and Y. Matsumoto, *Phys. Chem. Chem. Phys.*, **16**, 24784-24789 (2014). textitChem.Soc.Rev., **38**, 253 (2009).

[110] L.W. Martin, Y.-H. Chu, and R. Ramesh, *Mater. Sci. Eng. R*, **68**, 89 (2010).

[111] P.R. Willmott and J.R. Huber, *Rev. Mod. Phys.*, **72**, 315 (2000).

[112] T. Ohnishi, D. Komiyama, T. Koida, S. Ohashi, C. Stauter, H. Koinumaa,A. Ohtomo, M. Lippmaa, N. Nakagawa, M. Kawasaki, T. Kikuchi, and K. Omote, *Appl. Phys. Lett.*, **79**, 536(2001)

[113] T.Ohnishi, M.Lippmaa, T.Yamamoto, S.Meguro, and H.Koinuma, *Appl.Phys.Lett*, **87**, 241919 (2005).

[114] T.Ohnishi, K. Shibuya, T. Yamamoto, and M.Lippmaa, *J. Appl. Phys.*, **103**, 103703 (2008).

[115] B. Dam, J. Rector, M. F. Chang, S. Kars, D. G. de Groot, and R. Griessen, *Appl. Phys. Lett.*, **65**, 1581 (1994).

[116] T. Ohnishi, and K. Takada, *Appl. Phys. Express*, **5**, 055502 (2012).

[117] T. Ohnishi, and K. Takada, *Appl. Phys. Express*, **4**, 025501 (2011).

[118] S. Ohashi, M. Lippmaa, N. Nakagawa, H. Nagasawa, H. Koinuma, and M. Kawasaki *Rev. Sci. Instrum.*, **70**, 178 (1999).

[119] M. Lippmaa, 応用物理, **75-03**, 303 (2006).

[120] A.Ichimiya, *Reflection High Energy Electron Diffraction*, (*Cambrifge*, 2004).

[121] T.Ohnishi, and M.Lippmaa, 表面科学, **28**, 223 (2007).

[122] M. P.Seah,,and W. A. Dench, *Surf. Interf. Anal.*, **1**, 2 (1979).

[123] A. Toshima, H. Tanaka, T. Kikuchi, K. Amemiya, and Kazuhiko Mase, *J. Vac. Soc. Jpn.*, **54**, 580 (2011).

[124] K. Horiba, H. Ohguchi, H. Kumigashira, M. Oshima, K. Ono, N. Nakagawa, M. Lippmaa, M. Kawasaki, and H. Koinuma, *Rev. Sci. Instrum.*, **74**, 3406 (2003).

[125] Y. Senba, S.Yamamoto, H.Ohashi, I.Matsuda, M.Fujisawa, A.Harasawa, T.Okuda, S. Takahashi, N.Nariyama, T.Matsushita, T.Ohata, Y.Furukawa, T.Tanaka, K.Takeshita, S. Goto, H.Kitamura, A.Kakizaki, and M.Oshima, *Nucl. Instrum. Methods Phys. Res., Sect. A*, **649**, 58 (2011).

[126] Y. Harada, M. Kobayashi, H. Niwa, Y. Senba, H. Ohashi, T. Tokushima, Y. Horikawa, S. Shin, and Masaharu Oshima, *Rev. Sci. Instrum.*, **83**, 013116. (2012).

[127] K. Iwahori, S. Watanabe, M. Kawai, K. Kobayashi, H. Yamada, and K. Matsushige, *J. Appl. Phys.*, **93**, 3223. (2003).

[128] H. Kato, S. Shiraki, M. Nantoh, and M. Kawai, *Surf. Sci.*, **544**, L722. (2003).

[129] T. Fukuma, M. Kimura, K. Kobayashi, K. Matsushige, and H. Yamada, *Rev. Sci. Instrum.*, **76**, 053704 (2005).

[130] T. Fukuma, Y. Ueda, S. Yoshioka, and H. Asakawa, *Phys. Rev. Lett.*, **104**, 016101 (2010).

[131] T. Fukuma, *Sci. Technol. Adv. Mater.*, **11**, 033003 (2010).

[132] K. Kimura, S. Ido, N. Oyabu, K. Kobayashi, Y. Hirata, T. Imai, and H. Yamada, *J. Chem. Phys.*, **132**, 194705 (2010).

[133] J.E. Sader and S.P. Javis, *Appl. Phys. Lett.*, **84**, 1801 (2004).

[134] J. Torrent and V. Barron, *Encyclopedia of Surface and Colloid Science*, (*Marcel Dekker, Inc.: New York*, 2002).

[135] A. E. Morales, E. S. Mora, and U. Pal, *Revista Mexicana de Fisica*, **53**, 18 (2007).

[136] Z. Chen, H.N. Dinh, and E. Miller, *Photoelectrochemical Water Splitting Standards, Experimental Methods, and Protocols*, (*Springer*, 2013).

[137] H. Gerisher, and M. Meyer, *Z. Physik. Chem. Neue Folge*, **74**, 302-318 (1971).

[138] S. R.Morrison, and T. Freund, *J. Chem. Phys.*, **47**, 1543-1551 (1967).

[139] R. Nakamura, K. Ueda, and S. Sato, *Langmuir*, **17**, 2298-2300 (2000).

[140] K.Uosaki, T. Yano, and S. Nihonyanagi, *J. Phys. Chem. B*, **108**, 19086 (2004).

[141] R. Jribi, E. Barthel, H. Bluhm, M. Grunze, P. Koelsch, D. Verreault, and E. Sønderg ård, *J. Phys. Chem. C*, **113**, 8273 (2009).

[142] K. Takahashi and H. Yui, *J. Phys. Chem. C*, **113**, 20322 (2009).

[143] J.M.White, M.A.Henderson *etal*., *J. Phys. Chem. B*, **107**, 9029 (2003).

[144] M. Langlet, S. Permpoon, D. Riassetto, G. Berthome, E. Pernot, J.C. Joud, *J. Photochem. Photobiol. A*, **181**, 203-214 (2006).

[145] X. Yan, R. Abe,T. Ohno, M. Toyofuku, and B. Ohtani, *Thin Solid Films*, **516**, 5872-5876 (2008).

[146] A. Heller, *Acc. Chem. Res*, **28**, 503-508 (1995).

[147] A.N. Shultz et al., *Surf. Sci.*, **339**, 114 (1995).

[148] T. Kubo and H. Nozoye, *Sur. Sci.*, **542**, 177-191 (2003).

[149] D.M. Kienzle and L.D. Marks, *CrystEngComm*, **14**, 7833-7839 (2012).

[150] S. shiraki, M. Nantoh, S. Katano, and M. Kawai, *Appl. Phys. Lett.*, **96**, 231901 (2010).

[151] D.M. Kienzle, A.E. Becerra-Toledo, and L.D. Marks , *Phys. Rev. Lett.*, **106**, 176102 (2011).

[152] M. Naito and H. Sato, *Phys. C*, **229**, 1-11 (1994).

[153] R. Shimizu, K. Iwaya, T. Ohsawa, S. Shiraki, T. Hasegawa, T. Hashizume, and T. Hitosugi, *ACS Nano*, **5**, 7967-7971 (2011).

[154] https://www.cp2k.org/

[155] , *J. Comp. Phys.*, **117**, 1 (1995).

[156] http://lammps.sandia.gov/

[157] S.I. Lukyanov, A.V. Bandura, and R.A. Evarestov, *Surf. Sci.*, **611**, 10-24 (2013).

[158] W.L. Jorgensen, J. Chandrasekhar, J.D. Madura, R.W. Impey, M.L. Klein, *J. Chem. Phys*, **79**, 926-935 (1983).

[159] T. Smith, *J. Colloid Interface Sci.*, **75**, 51 (1980).

[160] D. Kobayashi, R. Hashimoto, A. Chikamatsu, H. Kumigashira, M. Oshima, T. Ohnishi, M. Lippmaa, K. Ono, M. Kawasaki and H. Koinuma, *J. Electron Spectrosc. Relat. Phenom.*, **443**, 144-147 (2005).

[161] T. Ohnishi, K.Shibuya, M. Lippmaa, D.Kobayashi, H.Kumigashira, M.Oshima, *Appl. Phys. Lett.*, **85**, 272 (2004).

[162] T. Miyagi, A. Sasahara, and M. Tomitori, *Appl. Surf. Sci.*, **349**, 904-910 (2015).

[163] N. Skai et al., *Langmuir*, **14**, 5918 (1998).

[164] T. Watanabe et al., *Thin Solid Films*, **351**, 260 (1999).

[165] N. Sakai et al., *J. Electrochem. Soc.*, **148**, E395 (2001).

[166] R. Wang et al., *J. Phys. Chem. B*, **103**, 2188 (1999).

[167] L.A. Girifalco and R.J. Good, *J. Phys. Chem.*, **61**, 904 (1957).

[168] M.A. Floriano and C.A. Angell, *J. Phys. Chem.*, **94**, 4199 (1990).

[169] H.L. Skriver and N.M.Rosengaard, *Phys. Rev. B*, **46**, 7157 (1992).

[170] S.M. Foiles, M.I.Baskes, and M.S.Daw, *Phys. Rev. B*, **33**, 7983 (1986).

[171] P.M. Oliver, G.W. Watson, E.T. Kelsey, and S.C. Parker, *J. Mater. Chem.*, **7**, 563 (1997).

[172] H. Zhang, and J.F. Banfield, *J. Mater. Chem.*, **8**, 2073-2076 (1998).

[173] W.C. Mackrodt, *Phys. Chem. Minerals*, **15**, 228 (1988).

[174] T. Sano et al., *J. Am. Ceram. Soc.*, **86**, 1933 (2003).

[175] T. Nishio et al., *Langmuir*, **15**, 4321 (1999).

[176] R.K. Mishra and G.Thomas, *J. Appl. Phys.*, **48**, 4576 (1977).

[177] R.E. Jonson,Jr.,and R.H. Dettre, *Adv. Chem. Ser.*, **43**, 112-135 (1963).

[178] L. Zhang, R. Dilert, D. Bahnemann, and M. Vormoor, *Energy Environ. Sci.*, **5**, 7491 (2012).

[179] K. Hashimoto, H. Irie, and A. Fujishima, *Jpn. J. Appl. Phys.*, **44**, 8269-8285 (2005).

[180] M.Kamei. and T.Mitsuhashi, *Surf. Sci*, **463**, L609-L612 (200).

[181] M. Miyauchi, K. Hashimoto et al., *Chem. Mater.*, **12**, 3 (2000).

[182] M. Miyauchi, K. Hashimoto et al., *Chem. Mater.*, **14**, 2812 (2002).

[183] K. Katsumata et al., *Chem. Lett.*, **42**, 618 (2013).

[184] G. Munuera, A.R. Gonzalez-Elipe, J.P. Espinos and E. Lopez-Molina, *Surf. Interface Anal.*, **15**, 693-697 (1990).

[185] Y. Matsumoto, H. Koinuma, and T. Ohsawa, *J. Phys. Chem.*, **111**, 10523-10527 (2007).

[186] R. Wang, K. Hashimoto, A. Fujishima, M. Chikuni, E. Kojima, A. Kitamura, M. Shimohigoshi, and T. Watanabe, *Adv. Mater.*, **10**, 135-138 (1998).

[187] L.Jiang, R.Wang, B. Yang, T.J. Li, D.A.Tryk, A.Fujishima, K.Hashimoto, and D.B. Zhu, *Pure Appl. Chem.*, **72**, 73-81 (2000).

[188] R. Asahi, T. Morikawa, T. Ohwaki, K. Aoki, Y. Taga, *Science*, **293**, 269 (2001).

[189] H. Kato and A. Kudo, J. Phys. Chem. B, 2002, 106, 5029-5034.

[190] H. P. Maruska and A. K. Ghosh, *Sol. Energy Mater.*, **1**, 237 (1979).

[191] R. U. E. t Lam, L. G. J. de Haart, A. W. Wiersma, G. Blasse, A. H. A. Tinnemans and A. Mackor, *Mater. Res. Bull.*, **16**, 1593 (1981).

[192] H. Kato and A. Kudo, *J. Phys. Chem. B*, **106**, 5029 (2002).

[193] D. Wang, J. Ye, T. Kako and T. Kimura, *J. Phys. Chem. B*, **110**, 15824 (2006).

[194] T. Ishii, H. Kato and A. Kudo, *J. Photochem. Photobiol. A*, **163**, 181 (2004).

[195] J. W. Liu, G. Chen, Z. H. Li and Z. G. Zhang, *J. Solid State Chem.*, **179**, 3704 (2006).

[196] K. Sayama, K. Mukasa, R. Abe, Y. Abe, and H. Arakawa, *Chem. Commun.*, **37**, 2416-2417 (2001).

[197] P. Reunchan, N. Umezawa, S. Ouyang, J. Ye, *J. Phys. Chem. Chem. Phys.*, **14**,1876-1880 (2012).

[198] K. Furuhashi, Q. Jia, A. Kudo and H. Onishi, *J. Phys. Chem. C*, **117**, 19101 (2013).

[199] R. Niishiro, S. Tanaka, and A. Kudo, *Appl. Catal. B*, **150-151**, 187 (2014).

[200] R. Asai, H. Nemoto, Q. Jia, K. Saito, A. Iwase, and A. Kudo, *Chem. Commun.*, **50**, 2543-2546 (2014).

[201] H. Kato, M. Hori, R. Konta, Y. Shimodaira, and A. Kudo, *Chem. Lett.*, **33**, 1348-1349 (2004).

[202] Y. Sasaki, A. Iwase, H. Kato, and A. Kudo, *J. Catal.*, **259**, 133-137 (2008).

[203] Y. Sasaki, H. Nemoto, K. Saito, and A. Kudo, *J. Phys. Chem. C*, **113**, 17536-17542 (2009).

[204] A. Kudo, *MRS Bull.*, **36**, 32-38 (2011).

[205] M. Zimowska, J. B. Wagner, J. Dziedzic, J. Camra, B. Borzecka-Prokop, and M. Najbar, *Chem. Phys. Lett.*, **417**, 137 (2006).

[206] Z. Weng-Sieh, R. Gronsky, and A. T. Bell, *J. Catal.*, **170**, 62 (1997).

[207] M. Peuckert, *Surf. Sci.*, **141**, 500 (1984).

[208] G. M. Vanacore, L. F. Zagonel, and N. Barrett, *Surf. Sci.*, **604**, 1674 (2010).

[209] O.Knacke, O.Kubaschewski, and K.Heselmann, *Themochemical Properties of Inorganic Substances Second Edition*, volume 2 (1991).

[210] C.B.Alcock and G.W.Hooper, *Proceedings of Royal Society of London. Series A Mathematical and Physical Science*, **254**, 551 (1960).

[211] W. E. Bell and M. Tagami ., *J. Phys. Chem.*, **67**, 2432 (1963).

[212] E. P. J. Mallens, J. H. B. J. Hoebink, and G. B. Marin, *J. Catal.*, **167**, 43 (1997).

[213] I. Barin, *Thermochemical Data of Pure Substances*, (*VCH, Weinheim*, 1998).

[214] O. N. Tufte and P. W. Chapman, *Phys. Rev.*, **155**, 796 (1967). 7

[215] S. Ardizzone, C.L. Bianchi, G. Cappelletti, M. Ionita, A. Minguzzi, S. Rondinini, and A. Vertova, *J. Electroanal. Chem.*, **589**, 160 (2006).

[216] L.A. da Silva, V.A. Alves, S.C. de Castro, J.F.C. Boodts, *Colloids and Surfaces A: Physicochem. Eng. Aspects*, **170**, 119 (2000).

[217] A. Koizumi, K. Yamauchi, and M. Sato, *J. Surf. Anal.*, **13**, 234 (2006).

[218] A. Koizumi, K. Yamauchi, M. Sato, and M. Takano, *J. Surf. Anal*, **15**, 16 (2008).

[219] J. F. Moulder, W. F. Stickle, P. E. Sobol, and K. D. Bomben, *Handbook of X Ray Photoelectron Spectroscopy*, (*Physical Electronics; Reissue*, 1995).

[220] G.K.Wertheim and H.J.Guggenheim, *Phys. Rev. B*, **22**, 4680 (1980).

[221] M. Hara, K. Asami, K. Hashimoto, and T. Matsumoto, *Electrochimica. Acta.*, **28**, 1073 (1983).

[222] Herbert B. Michaelson, *J. Appl. Phys.*, **48**, 4729 (1977).

[223] T. Susaki, A. Makishima, and H. Hosono, *Phys. Rev. B*, **84**, 115456 (2011).

[224] X. Fang and T. Kobayashi, *Appl. Phys. A: Mater. Sci. Process.*, **A69**, S587 (1999).

[225] C. W. Jones, P. D. Battle, P. Lightfoot, and W. T.A.Harrison, *Acta Cryst.*, **C45**, 365(1989).

[226] K. J. Choi, M. Biegalski, Y. L. Li, A. Sharan, J. Schubert, R. Uecker, P.Reiche, Y. B. Chen, X. Q. Pan, V. Gopalan, L.-Q. Chen, D. G. Schlom, and C. B. Eom, *Science*, **360**, 1005 (2004).

[227] S. Y. Yang, L. W. Martin, S. J. Bymes, T. E. Conry, S. R. Basu, D. Paran,L. Reichertz, J. Ihlefeld, C. Adamo, A. Melville, Y.-H. Chu, C.-H. Yang, J. L. Musfeldt, D. G. Schlom, J. W. Ager Ⅲ , and R. Ramesh, *Appl. Phys. Lett.*, **95**, 062909 (2009).

[228] A. Sawa, T. Fujii, M. Kawasaki, and Y. Tokura, *Appl. Phys. Lett.*, **85**, 4073 (2004).

[229] J. J. Randall and R. Ward, *J. Am. Chem. Soc.*, **81**, 2629(1959).

[230] W. E. Bell and M. Tagami ., *J. Phys. Chem.*, **67**, 2432 (1963).

[231] D. Kan and Y. Shimakawa, *Cryst. Growth Des.*, **11**, 5483 (2011).

[232] H. N. Lee, H. M. Christen, M. F. Chisholm, C. M. Rouleau, and D. H. Lowndes, *Appl. Phys. Lett.*, **84**, 4107 (2004).

[233] F. Lichtenberg, A. Catana, J. Mannhart, and D. G. Schlom, *Appl. Phys. Lett.*, **60**, 1138 (1992).

[234] A. Callaghan, C. W. Moeller, and R. Ward, *Inorg. Chem.*, **5**, 1572 (1966).

[235] J. Randall and R. Ward, *J. Am. Chem. Soc.*, **81**, 2629 (1959).

[236] L. Walz and F. Lichitenberg, *Acta. Crysta.*, **C49**, 1268 (1993).

[237] Y.-W. Chung and W.B.Weissbard, *Phys. Rev. B*, **20**, 3456(1979).

[238] http://www.shinkosha.com/SrTiO3.html, 信光社株式会社.

[239] H. Kamimura, S. Sugano, Y. Tanabe, 配位子場理論とその応用, (*Syokabo, Tokyo, Japan*, 1990).

[240] T. Nakamura, T. Shimura, M. Itoh, and Y. Takeda, *J. Solid State Chem.*, **103**, 523 (1993).

[241] S. Kawasaki, K. Nakatsuji, J. Yoshinobu, F. Komori, R. Takahashi, M. Lippmaa, K. Mase, and A. Kudo, *Appl. Phys. Lett.*, **101**, 033910 (2012).

[242] T. Higuchi, T. Tsukamoto, K. Kobayashi, S. Yamaguchi, Y. Ishiwata, N. Sata, K. Hiramoto, M. Ishigame, and S. Shin, *Phys. Rev. B*, **65**, 033201 (2001).

[243] T. Higuchi, T. Tsukamoto, S. Yamaguchi, K. Kobayashi, N. Sata, M. Ishigame, S. Shin, *Phys.Res.*, **199**, 255 (2003).

[244] N. Nakajima, M. Deguchi, H. Maruyama, K. Ishiji, Y. Tezuka, *Jpn. J. Appl. Phys.*, **49**, 09ME04 (2010).

[245] K. Kresse, J. Hafner, *Phys. Rev. B*, **47**, 558 (1993).

[246] K. Kresse, J. Furthmuller, *Phys. Rev. B*, **54**, 11169 (1996).

[247] P.E. Blochl, *Phys. Rev. B*, **50**, 17953 (1994).

[248] G. Kresse, D. Joubert, *Phys. Rev. B*, **59**, 1758 (1999).

[249] H.J. Monkhorst, J.D. Pack, *Phys. Rev. B*, **13**, 5188 (1976).

[250] We obtained an optimized lattice constant of 3.903 A using a 1 × 1 × 1 SrTiO3 cell, 4 × 4 × 4 Monkhorst-Pack k-point mesh (the tetrahedron method with Bloechl corrections was applied) and a cut-off energy of 500 eV.

[251] J.P. Perdew, K. Burke, M. Ernzerhof, *Phys. Rev. Lett.*, **77**, 3865 (1996).

[252] J. Heyd, G.E. Scuseria, M. Ernzerhof, *J. Chem. Phys.*, **124**, 219906 (2006).

[253] H.C. Chen, C.W. Huang, J.C.S. Wu, and S.T. Lin, *J. Phys. Chem. C*, **116**, 7897 (2012).

[254] T. Higuchi, T. Tsukamoto, N. Sata, M. Ishigame, Y. Tezuka, S. Shin, *Phys. Rev. B*, **57**, 6978-6983. (1998).

[255] D.E. Ibbotson, T.S. Wittrig, W.H. Weinberg, *Surf. Sci.*, **110**, 313-328 (1981).

[256] W. Shockley and W.T. Reas, Jr., *Phys. Rev.*, **87**, 835-842 (1952).

[257] M. Dressel, *Electrodynamics of Solids, Cambridge University Press*, (2002).

[258] R. Ulbricht, E. Hendry, J. Shan, T. F. Heinz, and M. Bonn, *Rev. Mod. Phys.*, **83**, 543 (2011).

[259] H. Yasuda, Y. Yamda, T. Tayagaki, and Y. Kanemitsu, *Phys. Rev. B*, **78**, 233202 (2008).

[260] Y. Yamada, H. Yasuda, T. Takagaki, and Y. Kanemitsu, *Phys. Rev. Lett.*, **102**, 247401 (2009).

[261] Y. Kanemitsu, and Y. Yamada, *Phys. Status Solidi B*, **248**, 416 (2011).

[262] C. Lee, J. Destry, and J. L. Brebner, *Phys. Rev. B*, **11**, 2299 (1975).

[263] D. Ricci, G. Bano, and G. Pacchioni, *Phys. Rev. B*, **66**, 224105 (2003).

[264] Z. Hou, and K. Terakura, *J. Phys. Soc. Jpn.*, **79**, 114704 (2010).

[265] Y. Kozuka, Y. Hikita, C. Bell, and H.Y. Hwang, *Appl. Phys. Lett.*, **97**, 012107 (2010).

[266] S. Suzuki, T.Yamamoto, H.Suzuki, K. Kawaguchi, K. Takahashi, and Y. Yoshisato, *J. Appl. Phys.*, **81**, 6830-6836 (1997).

[267] T. Yamamoto, S. Suzuki, K. Kawaguchi, and K. Takahashi, *Jpn. J. Appl. Phys.*, **37**, 4737-4746 (1998).

[268] H.Yasuda et al., *Phys. Rev. B*, **77**, 193202 (2008).

[269] T. Susaki, Y. Kozuka, Y. Tateyama, and H.Y. Hwang, *Phys. Rev. B*, **76**, 155110 (2007).

[270] Y. Hikita, Y. Kozuka, T. Susaki, and H.Y. Hwang, *Appl. Phys. Lett.*, **90**, 143507 (2007).

[271] R. Takahashi, Y.Cho, and M. Lippmaa, *J. Appl. Phys.*, **117**, 014104 (2015).

[272] J. Yin, J. Ye, and Z. Zou, *Appl. Phys. Lett.*, **85**, 689-691 (2004).

[273] W.W. G*ä*rtner, *Phys. Rev.*, **116**, 84-87 (1959).

[274] T. Minemoto and M. Murata, *J. Appl. Phys.*, **116**, 054505 (2014).

[275] A.E. Delahoy, Z.Cheng, and K.K.Chin, *27th European Photovoltaic Solar Energy Conference and Exhibition, Frankfurt, Germany,*, 2837-2842 (2012).

[276] J. Robertson, *J. Appl. Phys.*, **93**, 1054-1059 (2003).

[277] H. Liu, H. Dong, X. Meng, and F. Wu, *Chem. Phys. Lett.*, **555**, 141-144 (2013).

[278] S.W. Bae, P.H. Borse, and J.S. Lee, *Appl. Phys. Lett.*, **92**, 104107 (2008).

[279] H.-C. Chen, C.-W. Huang, J.C.S. Wu, and S.-T. Lin, *J. Phys. Chem. C*, **116**, 7897-7903 (2012).

[280] R.U.E. 't Lam, L.G.J. de Haart, A.W. Wiersma, A.H.A. Tinnemans, and A. Mackor, *Mat. Res. Bull.*, **16**, 1593-1600 (1981).

[281] A. Rothschild, W. Menesklou, H.L. Tuller, and E.I.-Tiffee, *Chem. Mater.*, **18**, 3651-3659 (2006).

[282] E.D. Jeong, S.M.Yu, J.H. Yoon, J.S. Bae, C.R. Cho, K.T. Lim, P.H. Borse, and H.G. Kim, *J. Ceram. Proces. Res.*, **13**, 517-522 (2012).

[283] P. Li, C. Liu, G. Wu, Y. Heng, S. Lin, A. Ren, K. Lv, L. Xiao, and W. Shi, *RSC Adv.*, **4**, 47615-47624 (2014).

[284] T.-H. Xie, X. Sun, and J. Lin, *J. Phys. Chem. C*, **112**, 9753-9759 (2008).

[285] X. Zhou, J. Shi, and C. Li, *J. Phys. Chem. C*, **115**, 8305-8311 (2011).

[286] M.O. Selme, P. Pecheur, and G. Toussaint, *J. Phys. C: Solid State Phys.*, **19**, 5995-6007 (1986).

[287] M. O. Selme, and P.pecheur, *J. Phys. C: Solid State Phys.*, **21**, 1779-1790 (1988).

[288] M. Matsumura, M. Hiramoto, and H. Tsubomura, *J. Electrochem. Soc.*, **130**, 326-330 (1983).

[289] H. Paul Maruska, and A.K. Ghosh, *Solar Energy Materials*, **1**, 237-247 (1979).

[290] B. Modak, K. Srinivasu, S. K. Ghosh, *Phys. Chem. Chem. Phys.*, **16**, 24527-24535 (2014).

[291] B. Modak, S. K. Ghosh, *J. Phys. Chem. C*, **119**, 23503-23514 (2015).

[292] B. Modak, S. K. Ghosh, *J. Phys. Chem. C*, **119**, 7215-7224 (2015).

[293] C. Ye, Y. Wang, Y. Ye, J. Zhang, and G.H. Li, *J. Appl. Phys.*, **106**, 033520 (2009).

[294] T. Takata, and K. Domen, *J. Phys. Chem. C*, **113**, 19386-19388 (2009).

[295] A. I. Lebedev, *Phys. Solid State*, **51**, 362-372 (2009).

[296] M.F.M. Taib, M.K. Yaakob, F.W. Badrudin, T.I.T. Kudin, O.H. Hassan, and M.Z.A. Yahya , *Ferroelectrics*, **459**, 134-142 (2014).

[297] M.F.M. Taib, M.K. Yaakob, O.H. Hassan, and M.Z.A. Yahya, *Integrated Ferroelectrics*, **142**, 119-127 (2013).

[298] J. Wang, H. Li, H. Li, S. Yin, and T. Sato, *Solid State Sciences*, **11**, 182-188 (2009).

[299] P. Jing, W. Lan, Q. Su, and E. Xie, *Beilstein J. Nanotechnol.*, **6**, 1281-1286 (2015).

[300] X. Qiu, M. Miyauchi, H. Yu, H. Irie, and K. Hashimoto, *J. Am. Chem. Soc*, **132**, 15259-15267 (2010).

[301] Y. Nosaka, S. Takahashi, Y. Mitani, X. Qiu, and M. Miyauchi, *Appl. Catal. B: Environ.*, **111-112**, 636-640 (2012).

[302] K. Nogami, K. Yoshimatsu, H. Mashiko, E. Sakai, H. Kumigashira, O. Sakata, T. Oshima, and A. Ohtomo, *Appl. Phys. Express*, **6**, 105502 (2013).

[303] T. Okumura, T. Inoue, Y. Tasaki, E. Sakai, H. Kumigashira, and T. Higuchi, *J. Phys. Soc. Jap.*, **81**, 094705 (2012).

[304] S. Hara, M. Yoshimizu, S. Tanigawa, L. Ni, B. Ohtani, and H. Irie, *J. Phys. Chem. C*, **116**, 17458-17463 (2012).

[305] M.R. Balasubramanian, *J. Mater. Sci.*, **19**, 1890-1896 (1984).

[306] K.A. Muller, M. Aguilar, W. Berlinger, and K.W. Blazey, *J. Phys.:Condens. Matter*, **2**, 2735-2741 (1990).

[307] J.-P. Zou, L.-Z. Zhang, S.-L. Luo, L.-H. Leng, X.-B. Luo, M.-j. Zhang, Y. Luo, and G.-C. Guo, *Inter. J. Hydrogen Energy*, **37**, 17068-17077 (2012).

[308] T. Higuchi, T. Tsukamoto, K. Kobayashi, S. Yamaguchi, Y. Ishiwata, N. Sata, K. Hiramoto, M. Ishigame, and S. Shin, *Phys. Rev. B*, **65**, 033201 (2001).

[309] T. Higuchi, T. Tsukamoto, N. Sata, M. Ishigame, Y. Tezuka, and S. Shin, *Phys. Rev. B*, **57**, 6978 (1998).

[310] L. Chen, S. Zhang, L. Wang, D. Xue, and S. Yin, *Journal of Crystal Growth*, **311**, 735-737 (2009).

[311] A.I.J. Joseph, and S. Thiripuranthagan, *RSC Adv.*, **5**, 9792-9805 (2015).

[312] H.W. Kang, S.N. Lim, S.B. Park, *Inter. J. Hydrogen Energy*, **37**, 5540-5549 (2012).

[313] A. Jia, Z. Su, L.-L. Lou, S. Liu, *Solid State Sciences*, **12**, 1140-1145 (2010).

[314] P. Koidl, K.W. Blazey, W. Berlinger, and K.A. Muller, *Phys. Rev. B*, **14**, 2703-2708 (1976).

[315] W. Huang, R. Nechache, S. Li, M. Chaker, and F. Rosei, *J. Am. Ceram. Soc.*, , 1-8 (2015).

[316] Y. Ham, T. Hisatomi, Y. Goto, Y. Moriya, Y. Sakata, A. Yamakata, J. Kubota, and K. Domen, *J. Mater. Chem. A*, DOI: 10.1039/c5ta04843e (2016).

[317] H. Irie, Y. Maruyama, and K. Hashimoto, *J. Phys. Chem. C*, **111**, 1847-1852 (2007).

[318] A. Kudo, H. Kato, and I. Tsuji, *Chem. Lett.*, **33**, 1534-1539 (2004).

[319] H. Yu, S. Yan, Z. Li, T. Yu, and Z. Zou, *Inter. J. Hydrogen Energy*, **37**, 12120-12127 (2012).

[320] R.B. Comes, P.V. Sushko, S.M. Heald, R.J. Colby, M.E. Bowden, and S.A. Chambers, *Chem. Mater.*, **26**, 7073-7082 (2014).

[321] S. Ouyang, H. Tong, N. Umezawa, J. Cao, P. Li, Y. Bi, Y. Zhang, and J. Ye, *J. Am. Chem. Soc.*, **134**, 1974-1977 (2012).

[322] P. Reunchan, S. Ouyang, N. Umezawa, H. Xu, Y. Zhang, and J. Ye, *J. Mater. Chem. A*, **1**, 4221-4227 (2013).

[323] Q.I.Rahman, M. Ahmad, S.K. Misra, and M.A. Lohani, *J. Nanosci. Nanotechnol.*, **12**, 7181-7186 (2012).

[324] M.E. de A. Reyes, G.T. Delgado, R.C. Perez, J.M. Marquez, and O.Z. Angel, *J. Photochem. Photobio. A: Chemistry*, **228**, 22-27 (2012).

[325] Y. Iwazaki, Y. Gohda, and S. Tsuneyuki, *APL Mater.*, **2**, 012103 (2014).

[326] Y. Iwazaki, T. Suzuki, and S. Tsuneyuki, *J. Appl. Phys.*, **108**, 083705 (2010).

[327] H. Yukawa, K. Nakatsuka, and M. Morinaga, *Solid State Ionics*, **116**, 89-98 (1999).

[328] J. Wang, S. Yin, Q. Zhang, F. Saito, and T. Sato, *J. Mater. Chem.*, **13**, 2348-2352 (2003).

[329] T. Ohno, T. Tsubota, Y. Nakamura. and K. Sayama, *Appl. Catal. A*, **288**, 74-79 (2005).

[330] C. Zheng, Y. Jia, Y. Jing, Y. Yao, J. Ma, and J. Sun, *Phys. B*, **407**, 4649-4654 (2012).

[331] H. F. Liu, *Solid State Commun.*, **152**, 2063-2065 (2012).

[332] N. Li, and L. Yao, *AIP Adv.*, **2**, 032135 (2012).

[333] W. Wei, Y. Dai, M. Guo, L. Yu, H. Jin, S. Han, and B. Huang, *Phys. Chem. Chem. Phys.*, **12**, 7612-7619 (2010).

[334] S. Piskunov, O. Lisovski, J. Begens, D. Bocharov, Y. F. Zhukovskii, M. Wessel, and E. Spohr, *J. Phys. Chem. C*, **119**, 18686-18696 (2015).

[335] P. Liu, J. Nisar, B. Pathak, and R. Ahuja, *Inter. J. Hydrogen Energy*, **37**, 11611-11617 (2012).

[336] C. Zhang, Y. Jia, Y. Jing, Y. Yao, J. Ma, and J. Sun, *Comp. Mater. Sci.*, **79**, 69-74 (2013).

[337] Y. Guo, X. Qiu, H. Dong, and X. Zhou, *Phys. Chem. Chem. Phys.*, **17**, 21611-21621 (2015).

[338] P. Boutinaud, and E. Cavalli, *Chem. Phys. Lett.*, **503**, 239-243 (2011).

[339] Y. Ishida, R. Eguchi, M. Matsunami, K. Horiba, M. Taguchi, A. Chainani, Y. Senba, H. Ohashi, H. Ohta, and S. Shin, *Phys. Rev. Lett.*, **100**, 056401 (2008).

[340] K. Betsuyaku, H. Tanaka, H. Katayama, and T. Kawai, *Jpn, J. Appl. Phys.*, **40**, 6911-6912 (2001).

[341] C. Liu, N.P. Dasgupta, and P. Yang, *Chem. Mater.*, **26**, 415-422 (2014).

[342] Mor, G. K. et al., *Nano. Lett.*, **5**, 191-195 (2005).

[343] O. Khaselev, and J.A. Turner, *Science*, **280**, 425-427 (1998).

[344] Y. Lin et al., *Chem. Phys. Lett.*, **507**, 209-215 (2011).

[345] S. Oikawa, A. Takeo, T. Hikosaka, and Y. Tanaka, *IEEE Trans. Mag.*, **36**, 2293 (2000).

[346] T. Oikawa, M. Nakamura, H. Uwazumi, T. Shimatsu, H. Muraoka, and Y. Nakamura, *IEEE Trans. Mag.*, **38**, 1976 (2002).

[347] H. Zheng et al., *Science*, **303**, 661 (2004).

[348] G. Yu, J. Gao, J.C. Hummelen, F. Wudl, and A. Heeger, *Science*, **270**, 1789 (1995).

[349] H.M.-Ardabili et al., *Nature Materials*, **3**, 533 (2004).

[350] J. Shin, A. Goyal, C. Cantoni, J.W. Sinclar, and J.R. Thompson, *Nanotech.*, **23**, 155602 (2012).

[351] D.H. Kim *etal*., *Adv. Func. Mater.*, **25**, 3091 (2015).

[352] A. Watanabe, K. Ikemiya, A. Chikamatsu, Y. Hirose, and T. Hasegawa, *Chem. Lett.*, **43**, 225-227 (2014).

[353] J. Kano, T. Kizuka, F. Shikanai, and S. Kojima, *Nanothech.*, **20**, 295704 (2009).

[354] Y. Nishihata *etal*., *Nature*, **418**, 164 (2002).

[355] M. Haruta, S. Tsubota, T. Kobayashi, H. Kageyama, M. J. Genet, and B. Delmon, *J. Catal.*, **144**, 175-192 (1993).

[356] V. Moshnyaga *etal*., *Phys. Rev. B*, **66**, 104421 (2002).

[357] Y. Yamada *etal*., *Appl. Phys. Lett.*, **87**, 132502 (2005).

[358] S. Kang *etal*., *Science*, **311**, 1911-1914 (2006).

[359] J.L. MacManus-Driscoll, P. Zerrer, H. Wang, H. Yang, J. Yoon, A. Fouchet, R. Yu, M.G. Blamire, and Q. Jia *Nat. Meter.*, **7**, 314-320 (2008).

[360] A. Imai, X. Cheng, H.L. Xin, E.A. Eliseev, A.N. Morozovska, S.V. Kalinin, R. Takahashi, M. Lippmaa, Y. Matsumoto, and V. Nagarajan, *ACS Nano*, **7**, 11079-11086 (2013).

[361] W. Zhang, R. Ramesh, J.L. MacManus-Driscoll, and H. Wang, *MRS Bull.*, **40**, 736-745 (2015).

[362] J.L. MacManus-Driscoll, A. Suwardi, and H. Wang, *MRS Bull.*, **40**, 933-942 (2015).

[363] Y. Ichino, A. Tsuruta, S. Miura, Y. Yoshida, M. Yoshizumi, and T. Izumi, *IEEE Trans. Appl. Supercond.*, **25**, 6604506 (2014).

[364] T. Koji *etal*., *Adv. Mater.*, **23**, 3320 (2011).

[365] Z.Wang, T. Miyadera, T. Yamanari, and Y. Yoshida, *ACS Appl. Mater. Interfaces*, **6**, 6369 (2014).

[366] W.M. Haynes,*Handbook of Chemistry and Physics 94th Ed.*, *CRC Press*, (2013).

[367] Y.R.Luo, Bond Dissociation Energies, *Bond Dissociation Energies*,(2009).

[368] A.S. Darling, *Int. Mater. Rev.*, **18**, 91-122 (1973).

[369] M. Peuckert, *J. Phys. Chem*, **89**, 2481-2486 (1985).

[370] R. Takahashi *etal.*, *Adv. Func. Mater.*, **16**, 485-491 (2006).

[371] S.J. Tauster, S.C. Fung, and R.L. Garten, *J. Am. Chem. Soc.*, **100**, 170-175 (1978).

[372] Y. Gao, Y. Liang, and S.A. Chhambers, *Surf. Sci.*, **365**, 638-648 (1996).

[373] R. Moos, and K.H. Härdtl, *J. Am. Ceram. Soc.*, **80**, 2549 (1997).

Publication and Presentation list

Publication

1. Seiji Kawasaki, Kan Nakatsuji, Jun Yoshinobu, Fumio Komori, Ryota Takahashi, Mikk Lippmaa, Kazuhiko Mase, and Akihiko Kudo,
"Epitaxial Rh-doped $SrTiO_3$ thin film photocathode for water splitting under visible light irradiation"
Appl. Phys. Lett., **101**, 033910, (2012).

2. Seiji Kawasaki, Kazuto Akagi, Kan Nakatsuji, Susumu Yamamoto, Iwao Matsuda, Yoshihisa Harada, Jun Yoshinobu, Fumio Komori, Ryota Takahashi, Mikk Lippmaa, Chikako Sakai, Hideharu Niwa, Masaharu Oshima, Katsuya Iwashina, and Akihiko Kudo,
"Elucidation of Rh-Induced In-Gap States of Rh:$SrTiO_3$ Visible-Light-Driven Photocatalyst by Soft X-ray Spectroscopy and First-Principles Calculations",
J. Phys. Chem. C, **116**, 24445-24448, (2012).

3. Seiji Kawasaki, Ryota Takahashi, Kazuto Akagi, Jun Yoshinobu, Fumio Komori, Koji Horiba, Hiroshi Kumigashira, Katsuya Iwashina, Akihiko Kudo, and Mikk Lippmaa,
"Electronic Structure and Photoelectrochemical Properties of an Ir-Doped $SrTiO_3$ Photocatalyst"
J. Phys. Chem. C, **118**, 20222-20228, (2012).

4. Kouichi Hayashi, Naohisa Happo, Seiji Kawasaki, Mikk Lippmaa, Koji Kimura, Shinya Hosokawa, and Hiroo Tajiri
"Observation of nanostructures in advanced materials by X-ray fluorescence holography"
Proceedings of 10th International Symposium on Atomic Level Characterizations for New Materials and Devices ' 15, in-press.

5. Seiji Kawasaki, Ryota Takahashi, Takahisa Yamamoto, Jun Yoshinobu, Fumio Komori, Akihiko Kudo, and Mikk Lippmaa,
"Photoelectrochemical water splitting enhanced by self-assembled metal nanopillars embedded in an oxide semiconductor photoelectrode", submitted.

Keynote and Invited Talk

1. (招待講演) 川崎聖治, リップマーミック
   「Rh ドープ $SrTiO_3$ エピタキシャル薄膜の光電気化学特性」
   創成光分子科学セミナー, 2012 年 10 月, 神戸大学

2. (招待講演（講演奨励賞受賞記念講演）) 川崎聖治, 水光俊介, 高橋竜太, 大西洋, リップマーミック
   「周波数変調型原子間力顕微鏡による光触媒上の水和構造観察」
   第 61 回応用物理学関係連合講演会, 18a-E8-1, 2014 年 3 月, 青山学院大学

3. (Keynote Lecture) Seiji Kawasaki, Shunsuke Suiko, Ryota Takahashi, Hiroshi Onishi, and Mikk Lippmaa,
   "Pt-cocatalyst Effect on the Hydration Structure of $SrTiO_3$ Photocatalyst Surface Analyzed by FM-AFM"
   Photocatalysts for energy (PHOTO4E), October (2014), Lyon, France

4. (Invited) Seiji Kawasaki, Ryota Takahashi, Takahisa Yamamoto, Jun Yoshinobu, Fumio Komori, Akihiko Kudo, and Mikk Lippmaa,
   "$SrTiO_3$ photoelectrodes with embedded metal nanopillars for solar water splitting"
   First International Symposium on Recent Progress of Energy and Environmental Photocatalysis (Photocatalysis1), September (2015), Noda, Chiba, Japan

5. (Invited) Seiji Kawasaki and Mikk Lippmaa,
   "Photoelectrochemical Water Splitting Enhanced by Metal Nanopillars in Metal-doped $SrTiO_3$"
   EMN meeting on Photocatalysis, U04, November (2015), Las Vegas, USA

International Conference

1. (Oral) Seiji Kawasaki, Kan Nakatsuji, Susumu Yamamoto, Iwao Matsuda, Fumio Komori, Jun Yoshinobu, Yoshihisa Harada, Mikk Lippmaa, Kazuto Akagi, Akihiko Kudo
   "In-situ Observation of Occupied and Unoccupied States of a Photocatalyst in Water"
   IUMRS-International Conference on Electronic Materials 2012, B3-O27-001, September (2012), Yokohama, Kanagawa, Japan

2. (Oral) Seiji Kawasaki, Ryota Takahashi, Akihiko Kudo, and Mikk Lippmaa,
"Spontaneous Surface Nanodot Formation and Enhanced Photoelectrochemical Properties of Ir:$SrTiO_3$"
JSAP-MRS, September (2013), Kyoto, Japan

3. (Poster) Seiji Kawasaki, Shunsuke Suiko, Ryota Takahashi, Hiroshi Onishi, and Mikk Lippmaa,
"Hydration Structure on a Photocatalyst $SrTiO_3$ Observed by FM-AFM"
ACSIN-12 and ICSPM-21, 5PN-42, September (2013), Tsukuba, Ibaraki, Japan

4. (Poster) Seiji Kawasaki, Kazuto Akagi, Ryota Takahashi, Kan Nakatsuji, Susumu Yamamoto, Iwao Matsuda, Fumio Komori, Jun Yoshinobu, Yoshihisa Harada, Akihiko Kudo, and Mikk Lippmaa,
"Photocatalytic activity and electronic structure of Rh- and Ir-doped $SrTiO_3$ for solar water splitting"
Materials Research Society Fall Meeting, AA9.44, December (2013), Boston, USA

5. (Poster) Seiji Kawasaki, Shunsuke Suiko, Ryota Takahashi, Hiroshi Onishi, and Mikk Lippmaa,
"Photo-induced Hydration Structure Change Observed on a $SrTiO_3$(100) Photocatalyst Surface Using FM-AFM"
NC-AFM 2014, PW06, August (2014), Tsukuba, Ibaraki, Japan

6. (Poster) Seiji Kawasaki, Kazuto Akagi, Ryota Takahashi, Iwao Matsuda, Fumio Komori, Jun Yoshinobu, Yoshihisa Harada, Akihiko Kudo, and Mikk Lippmaa,
"Dopant Sites in Noble Metal Doped Photocatalysts"
588. WE-Heraeus Seminar, April (2015), Bonn, Germany

7. (Poster) Seiji Kawasaki, Ryota Takahashi, Takahisa Yamamoto, Jun Yoshinobu, Fumio Komori, Akihiko Kudo, and Mikk Lippmaa,
"Spontaneous Epitaxial Metal Nanopillar Formation in $SrTiO_3$ Thin Films for Enhanced Photoelectrochemical Water Splitting"
STAC-9, PS-1-29, October (2015), Tsukuba, Ibaraki, Japan

8. (Oral) Seiji Kawasaki, Ryota Takahashi, Takahisa Yamamoto, Jun Yoshinobu, Fumio Komori, Akihiko Kudo, and Mikk Lippmaa,
"Photoelectrochemical Water Splitting Enhanced by Implantation of Metal Nanopillars in a $SrTiO_3$ Photoelectrode"
Materials Research Society Fall Meeting, QQ1.10, December (2015), Boston, USA

Domestic Conference

1. (口頭発表) 川崎聖治, 岩品克哉, 高橋竜太, 中辻寛, 小森文夫, 吉信淳, 工藤昭彦, リップマーミック
「Rh ドープ $SrTiO_3$ 薄膜内の Rh の価数制御」
第 58 回応用物理学関係連合講演会, 25a-BA-6, 2011 年 3 月, 神奈川工科大学

2. (口頭発表) 川崎聖治, 岩品克哉, 高橋竜太, 中辻寛, 小森文夫, 吉信淳, 工藤昭彦, リップマーミック
「Rh ドープ $SrTiO_3$ 薄膜の水分解光電極への応用」
第 72 回応用物理学会学術講演会, 30p-ZK-9Z, 2011 年 8 月, 山形大学

3. (ポスター発表) 川崎聖治, 中辻寛, 山本達, 松田巌, 小森文夫, 吉信淳, 原田慈久, 赤木和人, 工藤昭彦, リップマーミック
「XES/XAS による可視光応答光触媒 Rh ドープ $SrTiO_3$ の電子状態観測」
第 7 回放射光表面科学部会/顕微ナノ材料科学研究会合同シンポジウム, P4, 2011 年 11 月, 大阪電気通信大学

4. (ポスター発表) 川崎聖治, 中辻寛, 山本達, 松田巌, 小森文夫, 吉信淳, 原田慈久, 赤木和人, 工藤昭彦, リップマーミック
「Rh ドープ $SrTiO_3$ の電子状態観測」
第 59 回応用物理学関係連合講演会,15a-GP3-5, 2012 年 3 月, 早稲田大学

5. (ポスター発表) 川崎聖治, 中辻寛, 山本達, 松田巌, 小森文夫, 吉信淳, 原田慈久, 赤木和人, 工藤昭彦, リップマーミック
「M:$SrTiO_3$(M=Rh,Ir) の光電気化学特性」
第 73 回応用物理学会学術講演,12p-PB5-3, 2012 年 9 月, 愛知大学・松山大学

6. (口頭発表) 川崎聖治, 高橋竜太, リップマーミック, 工藤昭彦
「Ir:$SrTiO_3$ 表面ナノドットの自発的成長とその光電気化学特性」
第 60 回応用物理学関係連合講演会, 要旨投稿済, 2013 年 3 月, 神奈川工科大学

7. (口頭発表) 川崎聖治, 水光俊介, 高橋竜太, 大西洋, リップマーミック
「FM-AFM による光触媒 $SrTiO_3$ 上の水和構造観察」

第 74 回応用物理学会学術講演会, 17a-D3-6, 2013 年 9 月, 同志社大学

8. (ポスター発表) 川崎聖治, 水光俊介, 高橋竜太, 大西洋, リップマーミック
「周波数変調型原子間力顕微鏡による光触媒 $SrTiO_3$(001) 上の水和構造観察」
短期研究会「エネルギーと新材料の物性・物質科学」, P04, 2013 年 11 月, 東京大学物性研究所

9. (ポスター発表) 川崎聖治, 赤木和人, 松田巌, 小森文夫, 吉信淳, 原田慈久, 工藤昭彦, リップマーミック
「M ドープ $SrTiO_3$ (M = Rh, Ir) の光触媒活性と電子状態の関係性」
元素戦略プロジェクト・大型研究施設連携シンポジウム, P-56, 2014 年 2 月, 東京大学物性研究所

10. (口頭発表) 川崎聖治, 高橋竜太, 山本剛久, 工藤昭彦, リップマーミック
「Ir 金属ナノピラーを利用した Ir:$SrTiO_3$ の光電気化学特性の増強効果」
第 61 回応用物理学関係連合講演会, 20a-E8-1, 2014 年 3 月, 青山学院大学

11. (ポスター発表) 川崎聖治, 赤木和人, 松田巌, 小森文夫, 吉信淳, 原田慈久, 工藤昭彦, リップマーミック
「遷移金属ドープ $SrTiO_3$ の電子状態と光触媒活性」
第一回「3D 活性サイト科学」公開ワークショップ, P21, 2014 年 11 月, CIVI 研修センター新大阪東

12. (ポスター発表) 川崎聖治, 水光俊介, 高橋竜太, 大西洋, リップマーミック
「光触媒 $SrTiO_3$ 上の水和構造観察」
機能物性融合科学研究会「光機能」, P07, 2014 年 12 月, 東京大学物性研究所

13. (ポスター発表) 川崎聖治, 高橋竜太, 山本剛久, 吉信淳, 小森文夫, 工藤昭彦, リップマーミック
「金属ナノピラーを利用した光電気化学特性の高効率化」
機能物性融合科学研究会「反応と輸送」, P01, 2015 年 6 月, 東京大学物性研究所

14. (口頭発表) 川崎聖治, 水光俊介, 高橋竜太, 大西洋, リップマーミック
「金属ナノピラーを利用した水分解光電極特性の増強効果」
触媒学会若手会「夏の研修会」, O-6, 2015 年 8 月, ホテルニュー伊香保

15. (口頭発表) 川崎聖治, 高橋竜太, 山本剛久, 吉信淳, 小森文夫, 工藤昭彦, リップマーミック
「酸化物薄膜内部の金属ナノピラーの自発的形成」
第 76 回応用物理学会秋季学術講演会, 15p-2J-5, 2015 年 9 月, 名古屋国際会議場

16. (口頭発表) 川崎聖治, 高橋竜太, 大西洋, リップマーミック
「酸化物単結晶の表面における親水性」
第 76 回応用物理学会秋季学術講演会, 13p-4E-2, 2015 年 9 月, 名古屋国際会議場

Awards

1. 優秀ポスター賞, 第 7 回放射光表面科学部会/顕微ナノ材料科学研究会合同シンポジウム, 2011 年 11 月
2. Award for Encouragement of Research in Materials Science, *IUMRS-International Conference on Electronic Materials 2012*, September (2012)
3. 修士論文優秀賞, 東京大学 新領域創成科学研究科 物質系専攻, 2013 年 3 月
4. 講演奨励賞, 第 35 回応用物理学会, 2013 年 9 月
5. 優秀口頭発表賞, 触媒学会若手会「夏の研修会」, 2015 年 8 月
6. Gold Poster Award, *STAC-9*, October (2015)

Fellowships

1. 一般財団法人 丸文財団 国際交流助成受領, 2013 年 12 月
2. 東京大学 統合物質科学リーダー養成プログラム MERIT, 2012 年 12 月ー 2016 年 3 月
3. 日本学術振興会 特別研究員 DC2, 2014 年 4 月ー 2016 年 3 月

Acknowledgment

I would like to express my sincere gratitude to Prof. Mikk Lippmaa for his excellent guidance, advice, and help with my research in the past six years. He has given me an opportunity to study oxide thin films for photocatalyst applications since I was a bachelor student of Tokyo University of Science. His unmeasurable support always helped my study and kindled my scientific ideas. I am deeply grateful to Dr. Ryota Takahashi. He also took care of me in Lippmaa laboratory and gave me valuable advice in my life as well as in my research.

I am also grateful to Prof. Akihiko Kudo who has given me an unusual chance to study photocatalysts since my third grade at Tokyo University of Science. His sincere attitude toward the practical application of photocatalytic water splitting always provided strong motivation for my research. I also appreciate the members of Kudo laboratory, especially Dr. Katsuya Iwashina, who helped with the fabrication and characterization of powdered photocatalysts at Kudo laboratory in Tokyo University of Science and gave me a lot of valuable advice in photocatalyst study.

I really appreciate Prof. Hiroshi Onishi for collaboration to study water/photocatalyst interfaces by advanced FM-AFM. He kindly took care of my study in his laboratory and gave me valuable scientific advice. Discussion with him always deepened my understanding of physical chemistry. Dr. Yuki Araki, Mr. Shunsuke Suiko, Mr. Yusuke Tanaka, Mr. Hiroyuki Kataoka are acknowledged for optimizing the conditions of FM-AFM. I stayed in Kobe for 2 months in total during my PhD life.

Prof. Adam Foster gave me a beneficial opportunity to study theoretical simulations in his group at Aalto University in Finland. It is generally very rare for experimental scientists to study theoretical simulations. I was very happy to stay there for three months and study simulations on water/oxides interfaces. I am grateful to the group members, Dr. Ville Loukonen, Dr. Hugo Pinto, Ms. Tiziana Musso, Mr. John Tracey, and Ms. Lidija Zivanovic. Especially, Dr. Peter Spijker kindly helped me study MD simulations and gave me a lot of valuable advice. I am also grateful to Dr. Eero Holmström. He computed DFT-MD simulations on water/$SrTiO_3$ interface and had a lot of discussion with me on the comparison between experiments and simulations.

I thank Prof. Hiroshi Okamoto, my assistant supervisor, for fruitful discussion on photocarrier dynamics. He and Mr. Masato Soutome collaborated with me on the measurement

of photocarrier lifetimes of Rh:$SrTiO_3$ by ultrafast transient absorption spectroscopy, which clarified the role of impurity levels in photocarrier dynamics.

This research was supported by many collaborators. Prof. Fumio Komori, Prof. Jun Yoshinobu, Prof. Yoshihisa Harada, Prof. Iwao Matsuda, Prof. Kan Nakatsuji, Prof. Kazuhiko Mase, Prof. Koji Horiba, Prof. Hiroshi Kumigashira, Prof. Masaharu Oshima, Prof. Kouichi Hayashi, Prof. Naohisa Happo, Prof. Shinya Hosokawa, Prof. Fumihiko Matsui, Prof. Hiroshi Daimon, Dr. Hiroo Tajiri, Dr. Tomohiro Matsushita, Dr. Hideharu Niwa, Dr. Chikako Sakai, and Dr. Koji Kimura are gratefully acknowledged for supporting my experiments at the synchrotron facilities, SPring-8 and Photon Factory. I am also grateful to Prof. Kazuto Akagi who helped me to clarify the electronic structure of doped $SrTiO_3$ from the view point of theoretical calculations. He calculated the density of states of Rh- and Ir-doped $SrTiO_3$, which was essential for the elucidation of the impurity levels. The priceless experience of working with many collaborators always stimulated my passion toward scientific research.

All of my research collaborators supported my research work and helped me to decide to continue studying in academia. Thanks to their support, I was be able to receive six awards in my master and PhD courses. I am sincerely grateful to all collaborators.

I would also like to thank my defense committee members, Prof. Maki Kawai, Prof. Akira Ohtomo, Prof. Yuji Matsumoto, and Prof. Hiroyuki Matsuura for fruitful discussions. They gave me a number of critical advices from viewpoint of their expertise, helping to develop my understanding and the thesis.

I sincerely appreciate the graduate school "MERIT" program coordinated by Prof. Masashi Kawasaki. The program gave me many valuable opportunities to communicate with leading researchers and engineers working in industry, academia, and government. Each coursework, including camp, colloquium, special lectures, joint-research, and overseas training helped me broaden my view and build deeper understanding of materials science. The program also supported my travel to study at Aalto University in Finland for three months. There are actually many 'merits' for my life. The experiences in the program helped me to decide to continue my future career in academia.

I thank all members of Lippmaa laboratory, Dr. Kazunori Nishio, Dr. Mikko Matvejeff, Dr. Takayuki Harada, Dr. Esko Avenniemi, Dr. Takumi Ohtsuki, Mrs. Junko Kawamura, Mr. Ken Sasamura, Mr. Hikaru Misumi, Mr. Masahiro Ogawa, Mr. Thomas Peltier, Mr. Akira Yoshida, Mr. Hou Xiuyi, Mr. Daiki Shono, Mr. Naoyuki Osawa, Ms. Jiyeon Lee, and Ms. Mihee Lee. The research life with them was really interesting and a valuable experience in my life. Each of them has an individual personality which always impressed me.

Finally, I would like to express my deepest gratitude to my family, especially to my wife Mrs. Kumiko Kawasaki, for their kind support and encouragement in my life.